Configuration Manual
Polarized Proton Collider at RHIC [1]

I. Alekseev (ITEP) C. Allgower (ANL) M. Bai (Indiana U., ANL, BNL)
Y. Batygin (RIKEN) L. Bozano (U. Genova) K. Brown (BNL) G. Bunce (BNL)
P. Cameron (BNL) E. Courant (BNL) S. Erin (IHEP) J. Escallier (BNL)
W. Fischer (BNL) R. Gupta (BNL) K. Hatanaka (RCNP, Osaka U.)
H. Huang (BNL) K. Imai (Kyoto U.) M. Ishihara (RIKEN) A. Jain (BNL)
V. Kanavets (ITEP) T. Katayama (INS, U. Tokyo) T. Kawaguchi (RIKEN)
E. Kelly (BNL) K. Kurita (RIKEN, BNL) S. Y. Lee (Indiana U.) A. Luccio (BNL)
W. W. MacKay (BNL) G. Mahler (BNL) Y. Makdisi (BNL) F. Mariam (BNL)
W. McGahern (BNL) G. Morgan (BNL) J. Muratore (BNL)
M. Okamura (RIKEN, BNL) S. Peggs (BNL) F. Pilat (BNL) V. Ptitsin (BINP)
L. Ratner (BNL) T. Roser (BNL) N. Saito (RIKEN) H. Satoh (KEK)
Y. Shatunov (BINP) H. Spinka (ANL) D. Svirida (ITEP) M. Syphers (BNL)
S. Tepikian (BNL) T. Tominaka (RIKEN) N. Tsoupas (BNL) D. Underwood (ANL)
A. Vasiliev (IHEP) P. Wanderer (BNL) E. Willen (BNL) H. Wu (RIKEN)
A. Yokosawa (ANL) A.N. Zelinski (BNL)

Spokesperson: T. Roser
Project Manager: W. W. MacKay

March 2001, Rev. 1 (in progress)

[1]Work was performed under the auspices of the U.S. Department of Energy and was supported by grants from the U.S. National Science Foundation and funds from The Institute for Chemical and Physical Research (RIKEN), Japan.

Contents

1 Introduction **1**
1.1 Physics Motivation . . . 1
1.2 Spin Dynamics and Siberian Snakes . . . 6
1.3 Polarized Proton Acceleration at RHIC . . . 7

2 Polarized Proton Injector **13**
2.1 Polarized Ion Source . . . 13
2.2 Acceleration in the Booster and AGS . . . 15

3 AGS-to-RHIC Transfer Line **23**
3.1 AtR Sections Affecting the Proton Beam Polarization . . . 23
3.2 Calculation of Stable Spin Direction at RHIC Injection Point . . . 26
3.2.1 Stable Spin Direction at AGS . . . 27
3.2.2 Stable Spin Direction at RHIC Injection Point . . . 28
3.2.3 Optimization of Stable Spin Direction with Energy . . . 30
3.2.4 Conclusions . . . 32

4 Snakes and Spin Rotators in RHIC **35**
4.1 General Layout . . . 35
4.2 Siberian Snake and Spin Rotator Design . . . 36
4.3 Effects on RHIC Operation . . . 37
4.4 Compensation for Detector Solenoids . . . 43

5 Polarized Proton Acceleration in RHIC **45**
5.1 Depolarizing Resonance Strengths . . . 45
5.2 Effectiveness of Siberian Snakes . . . 46
5.3 Sextupole Depolarizing Resonances . . . 49
5.4 Spin Tune Spread and Modulation . . . 49
5.5 Betatron Tune Spreads and Modulations . . . 50
5.6 Tuning of Siberian Snakes . . . 51
5.7 Spin Tracking Calculations . . . 51
5.8 Closed Orbit Correction Schemes . . . 54

6 Accelerator Systems Hardware **59**
6.1 Helical Dipole Magnets . . . 62
6.1.1 Conductor . . . 70
6.1.2 Mechanical Construction . . . 70
6.1.3 Electrical Design . . . 73

6.1.4 Quench Performance of Early Model . . . 73
6.2 Prototype Measurements and Final Magnet Design . . . 74
6.2.1 Quench Results . . . 74
6.2.2 Harmonic Measurements . . . 75
6.2.3 Rotation Angle . . . 78
6.2.4 Modification of End Design . . . 83
6.3 Snake and Rotator Assemblies . . . 83
6.3.1 Snake/Rotator Coldmass . . . 84
6.3.2 Cryostat Assembly . . . 86
6.4 Other Accelerator Systems Hardware . . . 91
6.4.1 Power Supplies and Controls . . . 91
6.4.2 RHIC Vacuum and Cryogenics Interface . . . 91

7 Collision of Polarized Protons in RHIC 93
7.1 Polarization Lifetime . . . 93
7.2 Beam-Beam Interactions . . . 95
7.3 Luminosity of Polarized Proton Collisions . . . 96
7.4 Spin Reversal of Stored Beams . . . 97

8 Measuring Beam Polarization in RHIC 103
8.1 Introduction . . . 103
8.2 p-C elastic scattering in CNI Region . . . 104
8.3 Experimental Test of p-Carbon CNI Polarimeter . . . 105
8.4 Overall Design . . . 107
8.5 Carbon Ribbon Target . . . 110
8.6 Event Rates and Emittance Blowup . . . 111
8.7 Commissioning Experience . . . 113
8.8 New DAQ system . . . 116

9 Commissioning and Operational Issues 119
9.1 Operational Modes of RHIC for Polarized Proton Running . . . 119
9.2 Commissioning . . . 119
9.2.1 Commissioning Steps–One Ring Only . . . 120
9.3 Physics Running–Issues . . . 122
9.3.1 Bunch pattern . . . 122
9.3.2 Frequency of Spin Flip . . . 123
9.3.3 Recogging . . . 123
9.3.4 Systematic Errors . . . 123
9.3.5 Beam Polarization Measurements . . . 124

A Toroidal Polarimeter Design 127
A.1 Toroidal Magnets, Pion Exit Windows . . . 129
A.2 Pion Production Target . . . 132
A.3 Acceptance, Event Rates and Emittance Blowup . . . 132
A.4 Polarimeter Detectors . . . 134

B Measuring Beam Polarization in RHIC **137**
B.1 Introduction . . . 137
B.2 Measuring the Pion Asymmetry at the RHIC Injection Energy . . . 139
B.3 Scaled Down Day-one Pion Production Polarimeter . . . 141
B.3.1 Target Box, Beam Pipe, Pion Exit Windows . . . 141
B.3.2 Pion Production Target . . . 145
B.3.3 Acceptance, Event Rates and Emittance Blowup . . . 145
B.3.4 Polarimeter Detectors . . . 149
B.4 p-Carbon CNI Polarimeter . . . 150

C Bibliography **159**

Chapter 1

Introduction

In the chapters that follow, we present our design to accelerate and store polarized protons in RHIC, with the level of polarization, luminosity, and control of systematic errors required by the approved RHIC spin physics program. Below, we provide an overview of the physics to be studied using RHIC with polarized proton beams, and a brief description of the accelerator systems required for the project.

1.1 Physics Motivation

The Relativistic Heavy Ion Collider (RHIC)[1] at Brookhaven will collide gold nuclei to create very high density and temperature, and explore a regime of the possible deconfinement of quarks and gluons in the colliding nuclei. RHIC will also collide intense beams of polarized protons[2], reaching transverse energies where the protons scatter as beams of polarized quarks and gluons.

The polarized proton program at RHIC will open a unique laboratory. W and Z boson production are expected to maximally violate parity. This parity violation will be used to measure the quark polarization in polarized protons by individual flavor: W^+ production will give the u and $\bar{d}$ quark polarization, and W^- production will give d and $\bar{u}$ polarization in the polarized proton. Direct photon production with colliding polarized protons measures the gluon polarization in the polarized proton. These examples use perturbative QCD to explore the spin structure of the proton. Searches for other parity violation is sensitive to new physics. For example, a parity violation can arise from interactions from quarks with substructure, or from a new right-handed Z boson.

RHIC provides an optimal energy range for this study. Collisions may be studied from 50 to 500 GeV center of mass energy. For these energies the transverse momentum reach is well into the perturbative QCD regime. For example, jets will be studied with $p_T = 50$ GeV/c. At the highest energy, W and Z will be copiously produced. At the same time, the fraction of the proton energy carried by the quarks and gluons that collide will be relatively large, typically $x > 0.1$. For large momentum fraction, SLAC and CERN have measured that the quarks that participate in the collisions will have large polarization. When we are investigating, for example, gluon polarization using direct photon production, the asymmetry that

we measure is proportional to the product of the gluon polarization and the quark polarization. If the quark polarization is high, we are more sensitive to the gluon polarization.

The RHIC polarized proton luminosity is expected to be high: 2×10^{32} cm^{-2}s^{-1} for $\sqrt{s} = 500$ GeV. This is possible because of the compression of the protons in the Booster/AGS into bunches which are then stored in RHIC. The luminosity requires an emittance of 20 π mm mrad (95%, normalized), and this is an important issue in the approaches used to maintain polarization through acceleration in the AGS. The major RHIC accelerator and beam parameters for achieving polarized proton collisions are found in Table 1.1.

Parameter	
Peak c.m. energy	500 GeV
Initial luminosity	2×10^{32}cm^{-2}sec^{-1}
Interactions per crossing (60 mb)	1
Protons per bunch	2×10^{11}
Bunches per ring	120
Normalized emittance (95%)	20 π mm mrad
β^*	1 m
Average polarization	70%
Stable Spin direction at Interaction Point	vert. or long.
RF voltage per turn	6 MV
RF harmonic number	2520
Long. emittance (95%)	0.3 eV sec
Beam Momentum Spread	2.6×10^{-4}
Beam-beam tune spread (per IR)	0.007

Table 1.1: RHIC Spin Accelerator Parameters.

Several experiments have used polarized electrons or muons scattering from polarized protons to study the quark spin contribution to the proton. These experiments have found that when quarks carry most of the momentum of a polarized proton, they are also very polarized.[3] This is important for the RHIC sensitivity to the gluon polarization. The experiments have also found, however, that the average contribution of the quarks to the proton spin is small: $27\% \pm 10\%$ from E143 proton data and $22\% \pm 14\%$ from SMC proton data. The remaining contribution must be from gluons, angular momentum, or both. A number of programs have been proposed to measure the gluon polarization: COMPASS at CERN, SLAC, HERA, and RHIC. The process and sensitivity for the proposals are given in Tables 1.2 and 1.3.[4] The RHIC program is more sensitive to the gluon polarization than the others. If the gluons in a polarized proton are significantly polarized, one would want to understand the origin of this nonintuitive result.

The electron and muon programs measure an average quark contribution to the proton spin, without distinguishing the quark flavor (semi-inclusive scattering can separate flavor, with a severe penalty for

Experiments Planned To Measure ΔG			
EXPERIMENT	**SLAC**	**COMPASS @CERN**	**RHIC**
Quantity Measured	$\mathcal{A}^{c\bar{c}}_{\vec{\gamma}\vec{N}} + \mathcal{A}^{J/\psi}_{\vec{\gamma}\vec{N}} + \mathcal{A}^{Bet-Heit}_{\vec{\gamma}\vec{N}}$+... 4 (e$^-$ beam) energies	$\mathcal{A}^{\mu c\bar{c}}_{\vec{\mu}\vec{N}}$ up to 4 ν bins	$\mathcal{A}^{\gamma jet}_{\vec{p}\vec{p}}$ several x_G bins
Processes	$\vec{\gamma} + \vec{N} \to c\bar{c}$ $c \to \mu$ (BR= 8%) $\mu^+\mu^-$ & μ (high p_T)	$\vec{\mu} + \vec{N} \to \vec{\mu} + c\bar{c}$ $c \to D^0 \to K^-\pi^+$ (BR= 4%) Also $D^{*+} \to \pi^+ D^0$	$\vec{p} + \vec{p} \to \gamma$+jet
Kinematical range	Bremsstrahlung $\gamma's$, Q$^2 = 0$ $E_\gamma^{min} < E_\gamma < 48.5$ $0.10 < x_G < 0.25$	Quasi-real $\gamma's$ Q$^2 \approx 0$ $35 < \nu < 85$ $0.06 < x_G < 0.35$	$0.0 < x_G < 0.4$
Theoretical Basis & Uncertainties	LO available, NLO in progress For $\vec{\gamma} + \vec{N} \to c\bar{c}$	For $\vec{\mu} + \vec{N} \to \vec{\mu} + c\bar{c}$	For $qg \to \gamma(qjet)$ Background from $q\bar{q} \to \gamma(gjet)$; Should know Δq
	c quark mass uncertainty		
Kinematical Constraints	Cuts on $p_T^{\mu\mu'}$, $M^{\mu\mu'}$ and p_T^μ	Events at D^0 mass	$5 < p_T < 30$
Experimental Difficulties	Disentangle $\mathcal{A}^{c\bar{c}}_\gamma$ from background asymmetry	Combinatorial background from K/π $B/S \approx 4$	Identify direct $\gamma's$; Contamination from $\pi^o \to \gamma\gamma$
Statistical Error on $\mathcal{A}$	$\delta\mathcal{A}^{c\bar{c}}_\gamma = 0.01 - 0.02$	$\delta\mathcal{A}^{\mu c\bar{c}}_\gamma = 0.05$ for full data	$\delta\mathcal{A} = 0.002 - 0.04$
on $\Delta G/G$	$\delta(\Delta G/G) = 0.02 - 0.08$	$\delta < \Delta G/G >= 0.10$	$\delta(\Delta G/G) = 0.01 - 0.3$
Systematics	Contribution of backgrounds and randoms to $\mathcal{A}^{c\bar{c}}_\gamma$	Beam & target polarizations $\pm 4\%$	Beam polarization $\pm 6\%$ False asymmetries small
Status	pre-proposal stage	Approved by SPSLC	RHIC complete with Siberian snakes in 1999
Time scale	$<$ Year 2000	$\geq$ Year 2000	Accelerator and detectors ready after year 2000
Remarks	Data taking : few months	Apparatus shared with hadron program	Apparatus shared with heavy ion program

Table 1.2: Gluon polarization experimental proposals.

Experiments Planned To Measure ΔG			
EXPERIMENT	**POLARIZED HERA**		**HERA-N**
	Inclusive	**Exclusive (2-jets)**	
Quantity Measured	$g_1^p(x)$ wide x-Q^2 range	$\mathcal{A}_{\vec{e}\vec{p}}^{e(2\ jets)}$ several x_G bins	$\mathcal{A}_{\vec{p}\vec{N}}^{\gamma jet}$ & $\mathcal{A}_{\vec{p}\vec{N}}^{J/\psi jet}$ several x_G bins
Process	Polarized inclusive e,p DIS	$\vec{e}+\vec{p}\rightarrow 2$ jets Photon-Gluon-Fusion $(80-90\%)$	$\vec{p}+\vec{N}\rightarrow\gamma(J/\psi)+jet$ Internal $\vec{N}$ target
Kinematics Range	$1.8<Q^2<(1.8\times 10^4)$ $(5.5\times 10^{-5})<x<1$	$5<Q_G^2<100,\ \sqrt{s_{ij}}>10$ $0.002<x_G<0.2$	$0.1<x_G<0.4$
Theoretical Basis & Uncertainties	$\Delta G(x,Q^2)$ & $\int\Delta G$ from pQCD at NLO minimum uncertainties	LO calculations for $\mathcal{A}_{\vec{e}\vec{p}}^{e(2\ jets)}$ Lack of NLO calculations for polarized cross sections and for Monte Carlo	Onset of pQCD for $\gamma+(X)$; pQCD for $J/\psi+(X)$ Should know Δq
Kinematical Constraints	$y>0.01\ \theta_{e'}>3^o$ $Q^2>1,\ E_{e'}>5$	$p_T>5,\ \mid\eta\mid<2.8$ $0.3<y<0.8$	$2\leq p_T\leq 8$ $-1.5\leq\eta\leq+1.5$
Experimental Problems	Polarization of 820 GeV protons in HERA and measurement of proton polarization		
		Gluon Compton 2-jet background	Identify direct $\gamma's$
Statistical Error on $\mathcal{A}$	for $\mathcal{L}=200$ $\delta\mathcal{A}=10^{-3}$ to 0.1	for $\mathcal{L}=200$ $\mathcal{A}=$ few%, $\delta\mathcal{A}<(0.2\ to\ 1\%)$	
on $\Delta G/G$	Relative error on $\int\Delta G$ 25(20)% with $\mathcal{L}=200(1000)$	$\delta(\Delta G/G)\ 0.10-0.50$	for $\mathcal{L}=250$ $\delta(\Delta G/G)<0.1$
Systematics	Measurement of P_e, P_p $(\pm 5\%)$. False asymmetries small since can provide any sign of P_p for any bunch, and with a spin rotator can change P_p sign of all bunches.		
Status	Study of polarized protons at HERA; pre-proposal stage		
Time Scale	$\geq$ Year 2003 HERA operational with 27 GeV $\vec{e}$; H1 & ZEUS detectors operational		
Remarks Conclusions	Low x behavior of $g_1^p(x,Q^2)$ of great interest	x_G is directly measured over a wide kinematic range	Need (new) HERA-B type detector

Table 1.3: Gluon polarization experimental proposals (cont'd).

rate; the CERN experiment SMC has done this). With both proton and neutron results, the s-quark contribution has been isolated to be $-10\% \pm 4\%$ (E143) of the proton spin.[3] This implies that the sea quarks may have significant polarization. The RHIC program will measure $\bar{u}$ and $\bar{d}$ polarization, as well as u and d-quark polarization using parity violation in W production.

The RHIC program will measure asymmetries in the production of photons, jets, and W and Z bosons with longitudinal polarization and with transverse polarization. Longitudinal polarization is required for the proton spin content studies discussed above. The asymmetries are a difference in production between left and right handed protons divided by the sum, normalized by the beam polarizations. For parity violation, we compare the production with one beam polarized, with the other beam unpolarized (or summing over both polarization states of the other beam):

$$A_L = \frac{1}{P}\,\frac{N_+ - N_-}{N_+ + N_-}. \tag{1.1}$$

N_+ and N_- represent the number of particles observed from right and left handed polarized protons, respectively, normalized for luminosity. P is the polarization of the beam. The error in the asymmetry is proportional to $1/\sqrt{N_+ + N_-}$ and to $1/P$. The RHIC Spin proposal is based on 70% polarization. If the polarization were smaller, say 50%, the experiments would need to run twice as long to obtain the proposed sensitivity for parity violation experiments. The direct photon experiments measure a two-spin asymmetry,

$$A_{LL} = \frac{1}{P^2}\,\frac{N_{++} - N_{+-}}{N_{++} + N_{+-}}. \tag{1.2}$$

N_{+-} represents the production for right handed polarized protons colliding with left handed polarized protons. Both beams have the polarization P. For this case, a 50% beam polarization would lead to a four times longer run to obtain the proposed sensitivity. Similar arguments point to the importance of excellent knowledge of the beam polarization. We expect to know the beam polarization to $\pm 7\%$ of itself.

The asymmetry is proportional to the polarization of the quarks or gluons that collide and to the analyzing power of the subprocess:

$$A_{LL} = \frac{\Delta a(x_a)}{a} \times \frac{\Delta b(x_b)}{b} \times \widehat{a}\,(a + b \to c + d)\,. \tag{1.3}$$

$\Delta a(x_a)/a$ is the polarization of quark or gluon a, which carries the fraction x_a of the proton momentum, for a proton polarization of 100%. b represents the other colliding quark or gluon. Here we assume that only one subprocess is involved. The analyzing power of the subprocess is typically of order 1. For direct photon production, which is dominated by gluon-quark scattering, the analyzing power for the subprocess is $\widehat{a} = 0.6$ for production near 90°. The large subprocess analyzing power is a result of angular momentum conservation. We see that to make a sensitive measurement of the polarization of the gluon, say $\Delta a/a$, it helps if the polarization of the quark b is large. This is the case for $x_b > 0.1$, which is true for the RHIC energy range.

The measured raw asymmetry is the product of the beam polarizations, the quark/gluon polarizations, and the subprocess analyzing power. These raw asymmetries will typically be small, and the measurement will need excellent control of systematic errors such as different detection efficiency for different beam polarization sign. These systematic errors will need to be controlled to reach proposed sensitivity.

1.2 Spin Dynamics and Siberian Snakes

To achieve high energy polarized proton collisions polarized beams first have to be accelerated which requires an understanding of the evolution of spin during acceleration and the tools to control it. The evolution of the spin direction of a beam of polarized protons in external magnetic fields such as exist in a circular accelerator is governed by the Thomas-BMT equation[5],

$$\frac{d\vec{P}}{dt} = -\left(\frac{e}{\gamma m}\right)\left[G\gamma\vec{B}_{\perp} + (1+G)\,\vec{B}_{\parallel}\right] \times \vec{P} \tag{1.4}$$

where the polarization vector $\vec{P}$ is expressed in the frame that moves with the particle. This simple precession equation is very similar to the Lorentz force equation which governs the evolution of the orbital motion in an external magnetic field:

$$\frac{d\vec{v}}{dt} = -\left(\frac{e}{\gamma m}\right)\left[\vec{B}_{\perp}\right] \times \vec{v}. \tag{1.5}$$

From comparing these two equations it can readily be seen that, in a pure vertical field, the spin rotates $G\gamma$ times faster than the orbital motion. Here $G = 1.7928$ is the anomalous magnetic moment of the proton and $\gamma = E/m$. In this case the factor $G\gamma$ then gives the number of full spin precessions for every full revolution, a number which also called the spin tune ν_{sp}. At top RHIC energies this number reaches about 400. The Thomas-BMT equation also shows that at low energies ($\gamma \approx 1$) longitudinal fields $\vec{B}_{\parallel}$ can be quite effective in manipulating the spin motion, but at high energies transverse fields $\vec{B}_{\perp}$ need to be used to have any effect beyond the always present vertical holding field.

The acceleration of polarized beams in circular accelerators is complicated by the presence of numerous depolarizing resonances. During acceleration, a depolarizing resonance is crossed whenever the spin precession frequency equals the frequency with which spin-perturbing magnetic fields are encountered. There are two main types of depolarizing resonances corresponding to the possible sources of such fields: imperfection resonances, which are driven by magnet errors and misalignments, and intrinsic resonances, driven by the focusing fields.

The resonance conditions are usually expressed in terms of the spin tune ν_{sp}. For an ideal planar accelerator, where orbiting particles experience only the vertical guide field, the spin tune is equal to $G\gamma$, as stated earlier. The resonance condition for imperfection depolarizing resonances arises when $\nu_{sp} = G\gamma = n$, where n is an integer. Imperfection resonances are therefore separated by only 523 MeV energy steps. The condition for intrinsic resonances is $\nu_{sp} = G\gamma = kP \pm \nu_y$, where k is an integer, ν_y is the vertical betatron

tune and P is the superperiodicity. For example at the Brookhaven AGS, $P = 12$ and $\nu_y \approx 8.8$. For most of the time during the acceleration cycle, the precession axis, or stable spin direction, coincides with the main vertical magnetic field. Close to a resonance, the stable spin direction is perturbed away from the vertical direction by the resonance driving fields. When a polarized beam is accelerated through an isolated resonance, the final polarization can be calculated analytically[6] and is given by

$$P_f/P_i = 2e^{-\frac{\pi|\epsilon|^2}{2\alpha}} - 1, \tag{1.6}$$

where P_i and P_f are the polarizations before and after the resonance crossing, respectively, ϵ is the resonance strength obtained from the spin rotation of the driving fields, and α is the change of the spin tune per radian of the orbit angle. When the beam is slowly ($\alpha \ll |\epsilon|^2$) accelerated through the resonance, the spin vector will adiabatically follow the stable spin direction resulting in spin flip. However, for a faster acceleration rate partial depolarization or partial spin flip will occur. Traditionally, the intrinsic resonances are overcome by using a betatron tune jump, which effectively makes α large, and the imperfection resonances are overcome with the harmonic corrections of the vertical orbit to reduce the resonance strength ϵ [7]. At high energy, these traditional methods become difficult and tedious.

By introducing a 'Siberian Snake' [8], which generates a 180° spin rotation about a horizontal axis, the stable spin direction remains unperturbed at all times as long as the spin rotation from the Siberian Snake is much larger than the spin rotation due to the resonance driving fields. Therefore the beam polarization is preserved during acceleration. An alternative way to describe the effect of the Siberian Snake comes from the observation that the spin tune with the Snake is a half-integer and energy independent. Therefore, neither imperfection nor intrinsic resonance conditions can ever be met as long as the betatron tune is different from a half-integer.

Such a spin rotator is traditionally constructed by using either solenoidal magnets or a sequence of interleaved horizontal and vertical dipole magnets producing only a local orbit distortion. Since the orbit distortion is inversely proportional to the momentum of the particle, such a dipole snake is particularly effective for high-energy accelerators, e.g. energies above about 30 GeV. For lower-energy synchrotrons, such as the Brookhaven AGS with weaker depolarizing resonances, a partial snake[9], which rotates the spin by less than 180°, is sufficient to keep the stable spin direction unperturbed at the imperfection resonances. A 5% (i.e., 9° rotator) partial snake has been successfully used in the AGS as described in Section 2.2.

1.3 Polarized Proton Acceleration at RHIC

By using Siberian Snakes the stage is set for the acceleration of polarized proton beams to much higher energies. Polarized protons from the AGS are injected into the two RHIC rings to allow collisions at center of mass energies up to 500 GeV with both beams polarized. Fig. 1.1 shows the lay-out of the Brookhaven accelerator complex highlighting the components required for polarized beam acceleration.

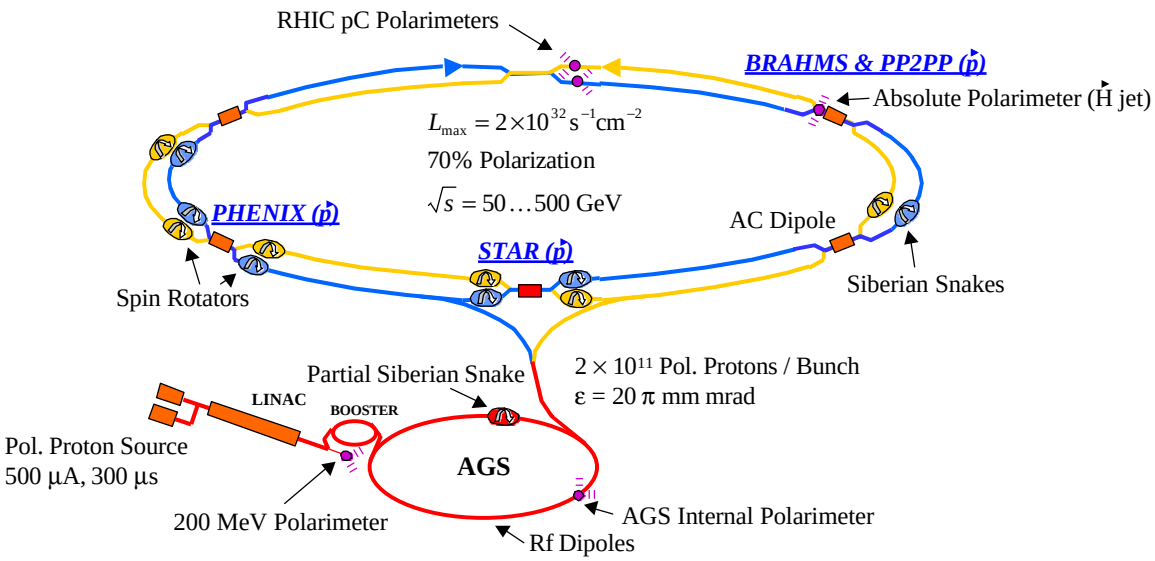

Figure 1.1: The Brookhaven hadron facility complex, which includes the AGS Booster, the AGS, and RHIC. The RHIC spin project will install two snakes per ring with four spin rotators per detector for achieving helicity-spin experiments.

To maintain polarization during the acceleration process, two full Siberian Snakes are inserted on opposite sides of the RHIC lattice for each of the two counter-rotating rings. In addition to these Snakes other magnetic components – spin rotators – are located on each side of the two major interaction points (again, for each ring) which allow the spin orientation to be altered from the vertical plane to the longitudinal plane. These devices are the primary magnetic components of the polarized beam project at RHIC. In addition, "spin flip" devices will be inserted to allow for the manipulation of the spin through 180° during a store, as well as polarimetry instrumentation. Fig. 1.2 shows all the major components that are required for the acceleration of polarized beams to RHIC top energy. The feasibility of accelerating polarized protons in RHIC was the basis of the proposal the RHIC Spin Collaboration (RSC) submitted to the Brookhaven PAC in October 1992 [10] and approved in 1993.

A summary list of the major hardware components for the acceleration of polarized protons in RHIC is provided in Table 1.4. The major elements required for this project are the superconducting magnets for the Siberian Snakes and the Spin Rotators. Each Siberian Snake consists of a set of four superconducting helical dipole magnets. The magnets will be capable of producing a central field of up to 4 T which spirals through 360° over a length of approximately 2.4 m. Four such magnets, each independently powered, can generate a spin rotation from vertically up (the nominal stable spin direction for the synchrotron) to vertically down, with no net excursions of the particle trajectory. This is the function of the Snake. The Spin Rotator is similarly constructed; by altering the "handedness" of two of the helical magnets, and

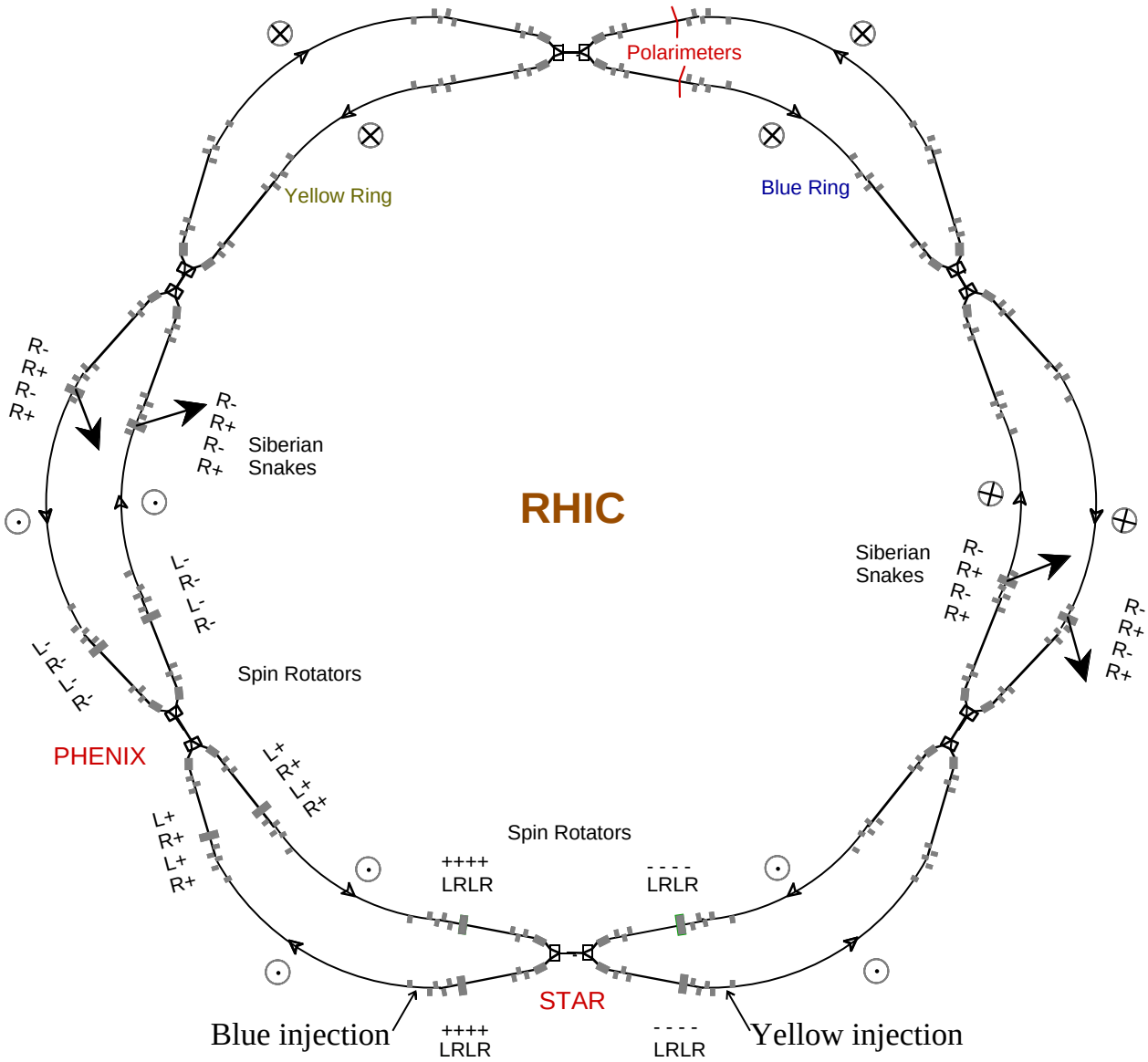

Figure 1.2: View of RHIC overemphasizing the interaction regions to show the location of the Siberian Snakes and the spin rotators placed around the collider experiments STAR and PHENIX. Also shown are the polarization directions around the rings and around the detectors for collisions with longitudinal polarization.

using slightly different fields, the spin can be made to rotate from the vertical to the longitudinal direction.

With one or two Snakes all depolarizing resonances should be avoided since the spin tune is a half-integer independent of energy. However, if the spin disturbance from small horizontal fields is adding up sufficiently between the Snakes, depolarization can still occur. This is most pronounced when the spin rotation from all the focusing fields add up coherently which is the case at the strongest intrinsic resonances. At RHIC two Snakes can still cope with the strongest intrinsic resonance.

Item	**No.**
Snakes	4
Helical Dipoles	16
Rotators	8
Helical Dipoles	32
Spin Flippers	2
Polarimeters	2
Toroids	16

Table 1.4: RHIC Polarized Beams Systems Hardware

To provide RHIC with polarized beams capability, a total of 4 Snakes and 8 Rotators are required. Thus, 48 individual full-helical dipole magnets will be constructed. The four magnets needed to create one Snake or one Rotator will be mounted inside of a standard RHIC Dipole Magnet cryostat. Since it is desirable to independently power the four magnets within the cryostat, the required current should be minimized in order to keep the heat leak due to the power leads as small as possible. Thus, hundreds of turns are required. This poses a technical challenge to the construction of these high-field magnets. The parameters of the Snake and Rotator helical dipole magnets are shown in Tables 1.5 and 1.6. The field strengths of the Snake magnets are held constant during the acceleration process, while the appropriate fields in the Rotator magnets are beam energy dependent, and are only powered during beam storage.

Helical Magnets			Field [Tesla]
	length[m]	handedness	
1	2.4	righthanded	1.19
2	2.4	righthanded	−3.86
3	2.4	righthanded	3.86
4	2.4	righthanded	−1.19

Table 1.5: Parameters of the Siberian Snake magnets

During the course of a polarized colliding beams experiment, it is desirable to adiabatically reverse the direction of the spin to eliminate the possibility of systematic errors. By introducing an oscillating field on resonance with the natural spin precession frequency, such a "spin flip" can occur. A discussion of the

Helical Magnets			Field [Tesla]	
	length[m]	handedness	@ 25 GeV	@ 250 GeV
1	2.4	righthanded	2.05	3.38
2	2.4	lefthanded	2.65	3.14
3	2.4	righthanded	2.65	3.14
4	2.4	lefthanded	2.05	3.38

Table 1.6: Parameters of the Spin Rotator magnets

hardware used to perform this task is described in Section 7.4. In addition to their use for the experiments, the spin flip devices can be used to accurately measure the spin precession frequency (or, "spin tune") and so will be used during commissioning of the Snakes.

Another major component is the instrumentation used to measure the beam polarization. Polarimetry has two functions: relative and absolute polarization measurements. Relative measurements may use a spin-sensitive process which has a high rate, but is uncalibrated. Our plan for RHIC is to use proton-carbon elastic scattering in the Coulomb-nuclear interference (CNI) region to measure the polarization, with the assumption that hadronic spin-flip amplitudes are not important. Finally, Italian collaborators have applied for funds to develop an intense polarized proton jet target. The polarization of the jet would be known, and a process such as CNI proton-proton scattering could be calibrated with the jet. Our goal is to have an absolute polarization measurment accurate to $\Delta P/P = \pm 5\%$. The pC-CNI polarimeters use carbon ribbon targets in each beam, with wide-angle detectors to measure the time of flight and pulse height of the recoiling carbon nucleus. Details of the polarimeter system can be found in Chapter 8.

The other various accelerator systems which are part of the project include power supplies, controls, and installation. Some modifications to the RHIC cryogenic hardware in the tunnel is necessary to provide the proper interface to the Rotators which are located in otherwise warm straight sections near the interaction points. The Snakes are to be located in cold straight sections which are already the appropriate length for a standard RHIC Dipole Magnet and hence no tunnel hardware modifications are necessary. As much as possible, standard RHIC accelerator systems hardware will be utilized throughout the project.

Chapter 2

Polarized Proton Injector

To meet the required bunch intensity of 2×10^{11} protons per bunch in RHIC, the AGS as the polarized proton injector will need to reach a bunch intensity of about 4×10^{11} to allow for some losses during the transfer to RHIC for acceleration. Although it would be possible to use the old polarized proton source[11] by accumulating up to twenty source pulses in the Booster, a new optically pumped polarized ion source (OPPIS) has been installed. The new polarized H^- source should produce $500\mu A$ in a single $300\mu s$ pulse, which corresponds to 9×10^{11} polarized H^-. This is sufficient intensity to eliminate the need for the accumulation in the Booster. The polarized H^- ions are accelerated to 200 MeV with an RFQ and the 200 MHz LINAC with an efficiency of about 50%. The pulse of H^- ions is strip-injected and captured into a single bunch in the AGS Booster. The bunch in the Booster will then contain about $N_B = 4 \times 10^{11}$ polarized protons with a normalized emittance of about $\epsilon_N = 10\pi$ mm-mrad. The single bunch of polarized protons is accelerated in the Booster to 1.5 GeV kinetic energy and then transferred to the AGS, where it is accelerated to 25 GeV. Fig. 2.1 shows the components of the AGS complex used for polarized proton acceleration.

2.1 Polarized Ion Source

The new RHIC optically pumped polarized H^- source (OPPIS) was constructed at TRIUMF from the KEK OPPIS source. The goal is to provide a DC beam of 1.5 mA H^- with a pulsed polarization of 80% in 100 μs pulses at a repetition rate of 7.5 Hz. The polarized injector for RHIC must produce at least 0.5 mA H^- ion current with 80% polarization during the 300 μs pulse, within a normalized emittance of 2π mm mrad. This is an ideal application for the ECR-type OPPIS. A pulsed laser is used to optically pump the rubidium vapor.

The first ECR-type OPPIS was constructed at KEK[12]. Polarized beam is not presently required at KEK, and so the source was upgraded at TRIUMF to meet the RHIC requirements. It was installed at BNL for the 2000 commissioning run along with a low energy transport between the source and the RFQ. Table 2.1 compares the RHIC requirements with what was previously demonstrated on the TRIUMF

Polarized Proton Experiments in the AGS with a Partial Siberian Snake (E880)

(ANL,BNL,INDIANA,TRIUMF,KEK,RIKEN,IHEP)

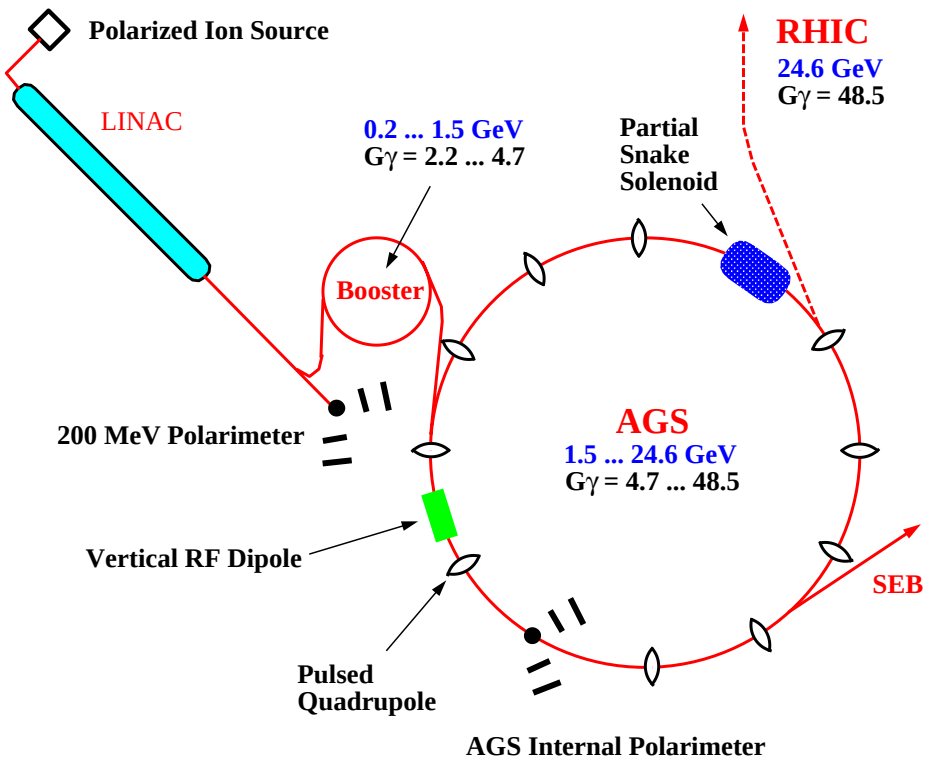

Figure 2.1: Schematic of the AGS complex for polarized proton acceleration.

OPPIS, and with the estimated KEK OPPIS parameters. (The KEK source was previously operated for polarized D^- production[13]). The table shows that the existing TRIUMF design meets the RHIC requirements if 300 μs pulses are extracted, even with CW laser pumping. However, 100 μs pulse durations with peak currents of 1.5 mA would be preferred, since that would improve injection efficiency. The preference for the higher current, combined with the much lower cost of pulsed lasers relative to CW lasers, dictates the use of pulsed optical pumping. In previous tests at TRIUMF, near 100% Rb polarization was measured in a 2 cm diameter Rb cell having a vapor thickness of 1×10^{14} atoms cm^{-2} and a length of 30 cm, using a pulsed Ti:sapphire laser[14].

The KEK OPPIS as delivered to TRIUMF used a pulsed 18 GHz ECR proton source and CW laser pumping. At TRIUMF the KEK OPPIS is being optimized using a DC 28 GHz ECR proton source.

	KEK	TRIUMF	RHIC
Current (mA)	0.1	0.5	0.5 – 1.5
Pulse duration (μs)	100	DC	100 – 300
Charge/pulse (mA μs)	10	150 (in 300 μs)	$\geq$150
Polarization (%)	75	85	$\geq$80
Normalized emittance (mm mrad)	2π	2π	$\leq 2\pi$
Repetition rate (Hz)	25	DC	7.5

Table 2.1: RHIC OPPIS parameters and comparison with KEK and TRIUMF designs.

Preliminary results give 520 μA of H^- DC current, using a 121-aperture extraction electrode with an overall diameter of 13 mm. This already satisfies the minimum RHIC beam current requirements, and a 199-aperture system will do proportionally better.

A new Na-jet negative-ionizer target is being developed, which has some advantages over the original canal and condensation chambers arrangement. A jet target can be shorter and the beam apertures larger, since Na vapor is more effectively confined. The condensed Na is recycled. Large apertures reduce secondary electron emission caused by the intense polarized atomic hydrogen beam striking the cell, and therefore may allow biasing the Na cell up to 32 kV. If so, a 35 keV beam from the source will be injected into an RFQ, without requiring that the whole source be placed on a high voltage platform.

The flashlamp-pumped pulsed Ti:sapphire laser produces pulse durations of 80 μs (FWHM) at a repetition rate of 1 Hz, using a simple power supply. The laser cavity is tuned with a 2-plate birefringent filter and a 0.5 mm thick etalon, producing a laser bandwidth of less than 20 GHz. The peak power density is more than 33 W/cm^2 over the 3 GHz Doppler broadened absorption width of Rb, for a 2 cm diameter laser beam. Previous results have shown that 14 W/cm^2 is enough to produce nearly 100% Rb polarization in a similar target[15]. Future development will concentrate on extending the pulse duration and repetition rate of the laser, mainly by increasing the capacitance of the power supply. Longer pulses may require the use of a different laser crystal, or two consecutive pulses.

2.2 Acceleration in the Booster and AGS

During acceleration, the polarization may be lost when the spin precession frequency passes through a depolarizing resonance. These resonances occur when the number of spin precession rotations per revolution $G\gamma$ (G=1.793 is the anomalous magnetic moment of the proton, $\gamma = \frac{E}{m}$) is equal to an integer (imperfection resonances) or equal to $kP \pm \nu_y$ (intrinsic resonances). Here P=12 is the superperiodicity of the AGS, $\nu_y \approx$ 8.8 is the vertical betatron tune and k is an integer. The depolarization is caused by the small horizontal magnetic fields present in all circular accelerators which, at the resonance condition, act coherently to move the spin away from the stable vertical direction. Imperfection resonances are due to the horizontal fields

caused by the vertical closed orbit errors and intrinsic resonances are caused by the horizontal focusing fields which are sampled due to the vertical betatron motion. The two weak resonances in the Booster ($G\gamma = 3$ and $G\gamma = 4$) are easily corrected by a harmonic correction of the closed orbit, since there are only two of them. Traditionally, the depolarizing resonances in the AGS were corrected by the tedious harmonic correction method for the imperfection resonances and by a tune jump method for the intrinsic resonances[16].

Three polarized beam test runs of experiment E-880 at the AGS have recently demonstrated the feasibility of polarized proton acceleration using a 5% partial Siberian Snake[17]. During the first run[18] in April 1994 it was shown that a 5% Snake is sufficient to avoid depolarization due to the imperfection resonances without using the harmonic correction method. The upper part of Fig. 2.2 shows the evolution of the beam polarization as the beam energy and therefore $G\gamma$ is increased. As predicted the polarization reverses sign whenever $G\gamma$ is equal to an integer. The lower part of Fig. 2.2 shows that no polarization was lost at the imperfection resonances. The only polarization loss occurred at the location of the intrinsic resonances for which the pulsed quadrupoles are required for the tune jump method. During the first run the pulsed quadrupoles were not available. Although some depolarization at intrinsic resonances are expected, the level of the depolarization does not agree with a simple model calculation. A spin tracking study was then performed and it showed that there is another resonance adjacent to the intrinsic resonance which causes further depolarization. Since the solenoidal 5% partial snake introduces considerable linear coupling between the two transverse betatron motions, the vertical betatron motion has a component with the horizontal betatron frequency. As a consequence, the beam will see an additional resonance, the so-called coupling resonance.

During the second run of E-880 in December 1994 it was shown that it is possible to use the tune jump method in the presence of the partial Snake. A new record energy for accelerated polarized beam of 25 GeV was reached with about 12% beam polarization left. Again no polarization was lost due to the imperfection resonances and depolarization from most intrinsic resonances was avoided with the tune jump quadrupoles. However, as can be seen from Fig. 2.3, which shows the achieved polarization as a function of beam energy, significant amount of polarization was lost at $G\gamma = 0 + \nu_y, 12 + \nu_y$ and $G\gamma = 36 + \nu_y$. The first two of these three resonances were successfully crossed previously and it is believed that the losses are partially due to the coupling resonances. The tune jump method changes the vertical betatron tune within less than one revolution to effectively make the resonance crossing speed very fast. However, the coupling resonance is still crossed at the normal crossing speed and can cause polarization loss. The strength of the tune jump quadrupoles is not sufficient to jump the third resonance. We attempted to induce spin flip at this resonance but were only partially successful. This is again due to the coupling resonance and the observed large momentum spread at this high energy. Table 2.2 summarizes the polarized proton beam parameters achieved in the AGS and also the requirements for RHIC.

A novel energy-jump method was used to cross the coupling resonance in the third run of E-880 and

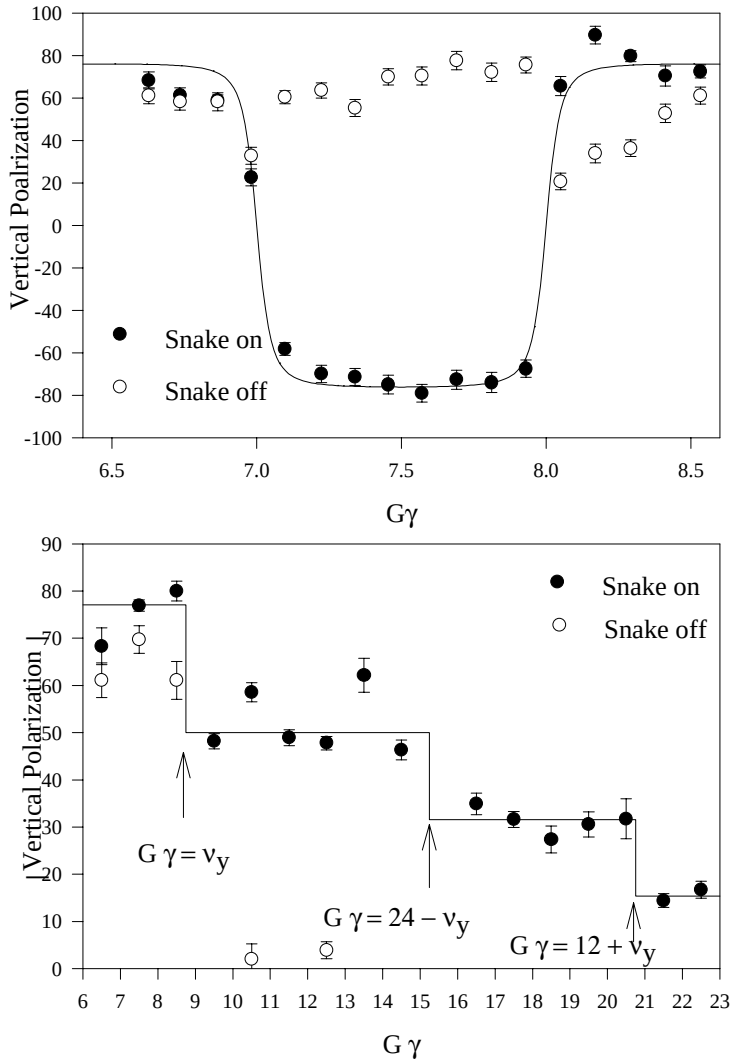

Figure 2.2: The upper figure shows the measured vertical polarization as a function of spin tune $G\gamma$ for a 10% Snake (solid dots) and without the Snake (open circles). Note that partial depolarization at $G\gamma = 8$ is avoided by using the 10% Snake. The lower figure shows the absolute value of the vertical polarization at $G\gamma = n + \frac{1}{2}$ up to $G\gamma = 22.5$ (solid dots). Note that partial depolarization only occurs due to the intrinsic resonances.

the results are summarized in Fig. 2.4. The energy-jump was accomplished by rapidly changing the beam circumference by 88 mm using the powerful AGS rf system. Because of the large momentum spread of the beam indicated as a hashed band in the lower part of Fig. 2.4, not all the beam particles are crossing the resonance during the jump unless the jump timing is carefully adjusted. From the beam momentum distribution, the ratio of the final to the initial polarization as a function of jump timing T_{jump} can be

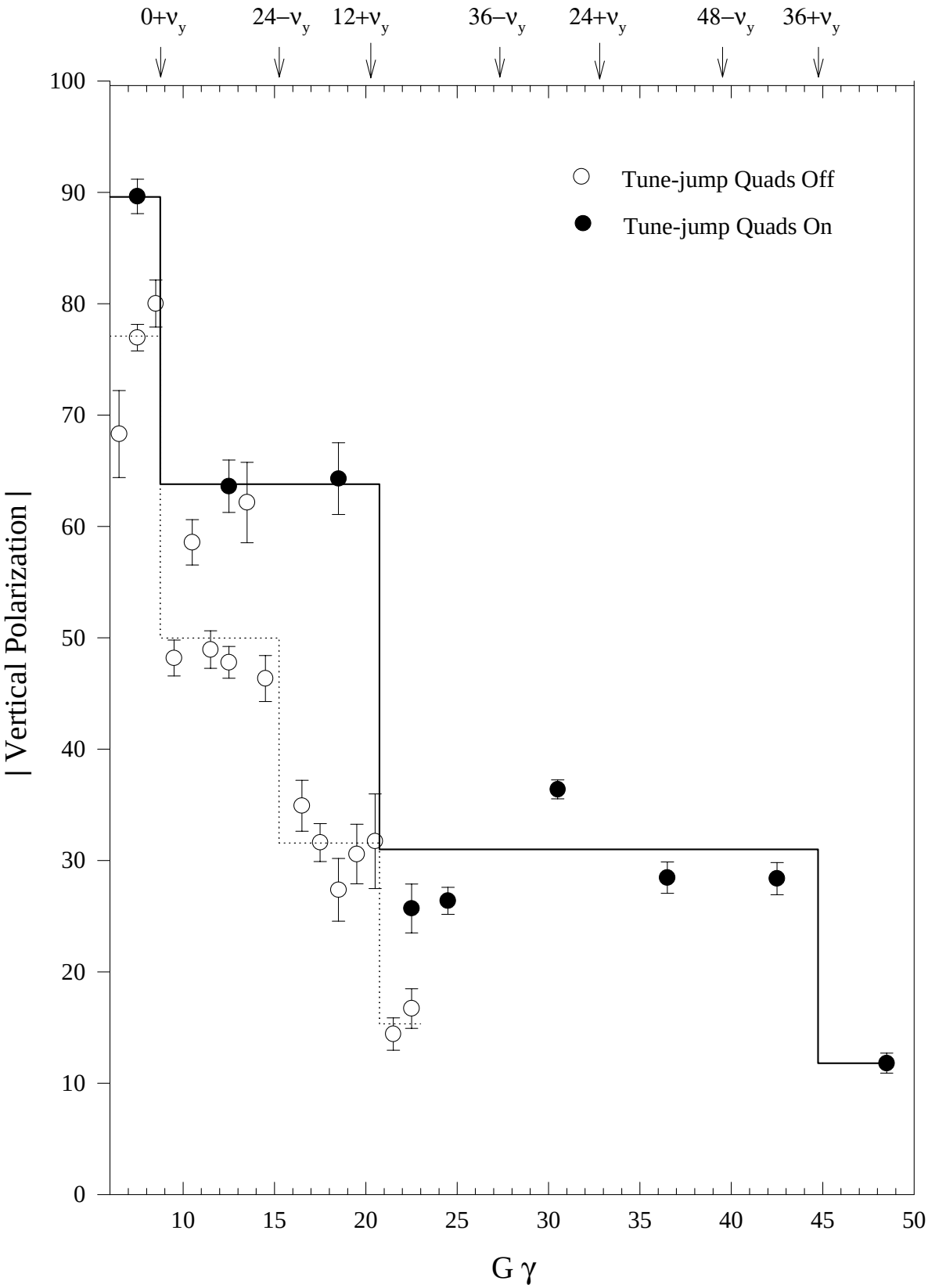

Figure 2.3: The absolute value of the vertical polarization is shown as a function of energy for the April 1994 run (open circles) and the December 1994 run (solid dots). Note that during the December run most intrinsic resonances were successfully crossed with significant depolarization only at the intrinsic resonances $G\gamma = 0 + \nu_y, 12 + \nu_y$ and $36 + \nu_y$.

	Intensity	**Polarization**	**Emittance**	**Momentum**
1988	1.8×10^{10}	65%		up to 13.3 GeV/c
		42%		up to 21.7 GeV/c
1994	0.5×10^{10}	64%	30π mm mrad	up to 10.7 GeV/c
		31%	30π mm mrad	up to 23.3 GeV/c
		12%	30π mm mrad	up to 25.4 GeV/c
RHIC	$2 - 4 \times 10^{11}$	70 – 80%	$10 - 20\pi$ mm mrad	up to 25.4 GeV/c

Table 2.2: AGS polarized beam parameters. The 1988 data reflects the result of the many year effort to accelerate polarized beam in the AGS using pulsed quadrupoles and numerous correction dipoles. The 1994 date comes from the first two test runs of E-880 testing the Partial Siberian Snake in the AGS. The RHIC data shows the required beam parameters for the RHIC spin program.

predicted and is shown as the solid line in the top half of Fig. 2.4. It shows good agreement with the data. It clearly demonstrates that the novel energy-jump method can successfully overcome coupling resonances and weak intrinsic resonances.

In July and November 1997 a novel scheme of overcoming strong intrinsic resonances using a radiofrequency dipole magnet was successfully tested[19]. Full spin flip can be achieved with a strong artificial rf spin resonance excited by an rf dipole at a modulation tune ν_m. If we choose the rf spin resonance location $K_{rf} = n \pm \nu_m$ near the intrinsic spin resonance, the spin motion will be dominated by the rf resonance and the spin near the intrinsic resonance will adiabatically follow the spin closed orbit of the rf spin resonance. With the rf dipole, a new dominant resonance near the intrinsic resonance is introduced to flip the spin, instead of enhancing the intrinsic resonance which also enhanced the coupling resonance strength as has been proposed earlier[20]. Fig. 2.5 shows the new record proton beam polarization achieved during the last E-880 run. The rf dipole was used to completely flip the spin at the four strong intrinsic resonances $0 + \nu_y$, $12 + \nu_y$, $36 - \nu_y$, and $36 + \nu_y$. The lower curve shown going through the data points was obtained from a spin tracking calculation simulating the experimental conditions. Most of the residual polarization loss is caused by the coupling resonances. A new AGS partial Snake using a helical dipole magnet would eliminate all coupling resonances[21]. Spin tracking simulations of this condition are depicted by the upper curve in Fig. 2.5. The depolarization from the two weak intrinsic resonances $24 + \nu_y$ and $48 - \nu_y$ will be avoided using the energy jump method described above.

At 25 GeV, the polarized protons are transferred to RHIC. At this energy the transfer line between the AGS and RHIC is spin transparent[22]. If the last resonance, $G\gamma = 36 + \nu_y$, cannot be crossed without significant polarization loss it is possible to transfer the polarized protons to RHIC before crossing this resonance in the AGS at an energy of 22.4 GeV ($\gamma \approx 25$). This is discussed in the following chapter.

We estimate that the overall efficiency of the acceleration and beam transfer is better than 50%, giving 2×10^{11} protons per bunch. With proper care the normalized emittance of the bunch is expected to be much less than 20π mm-mrad. During the last E-880 run the vertical beam emittance was tuned to less than 10π mm-mrad. We repeat the process until all 120 bunches of each ring are filled. Since each bunch

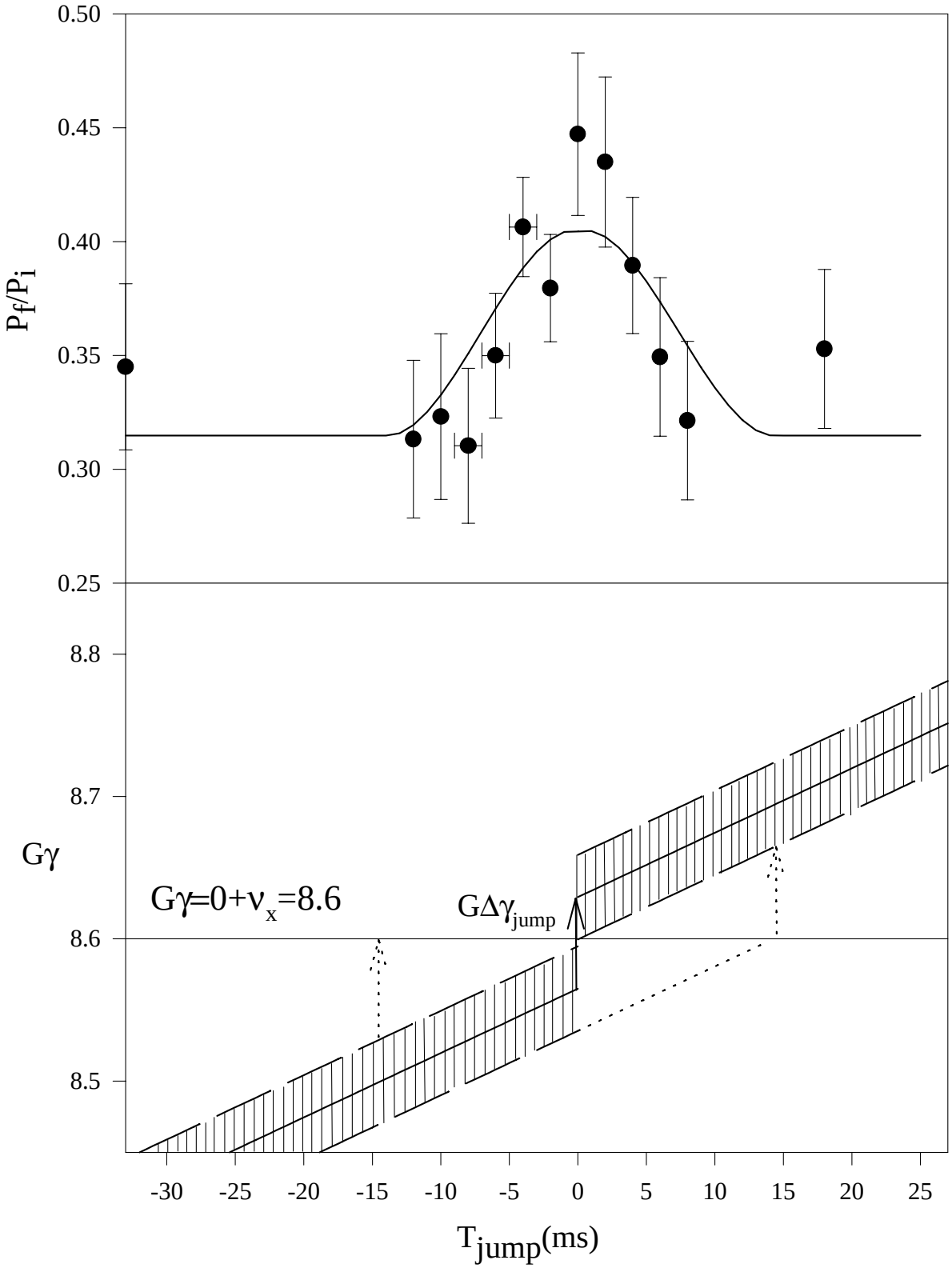

Figure 2.4: Energy jump data and schematics. In the top half, solid points are the experiment data, the solid line is the predicted curve. Bottom half shows the energy jump scheme.

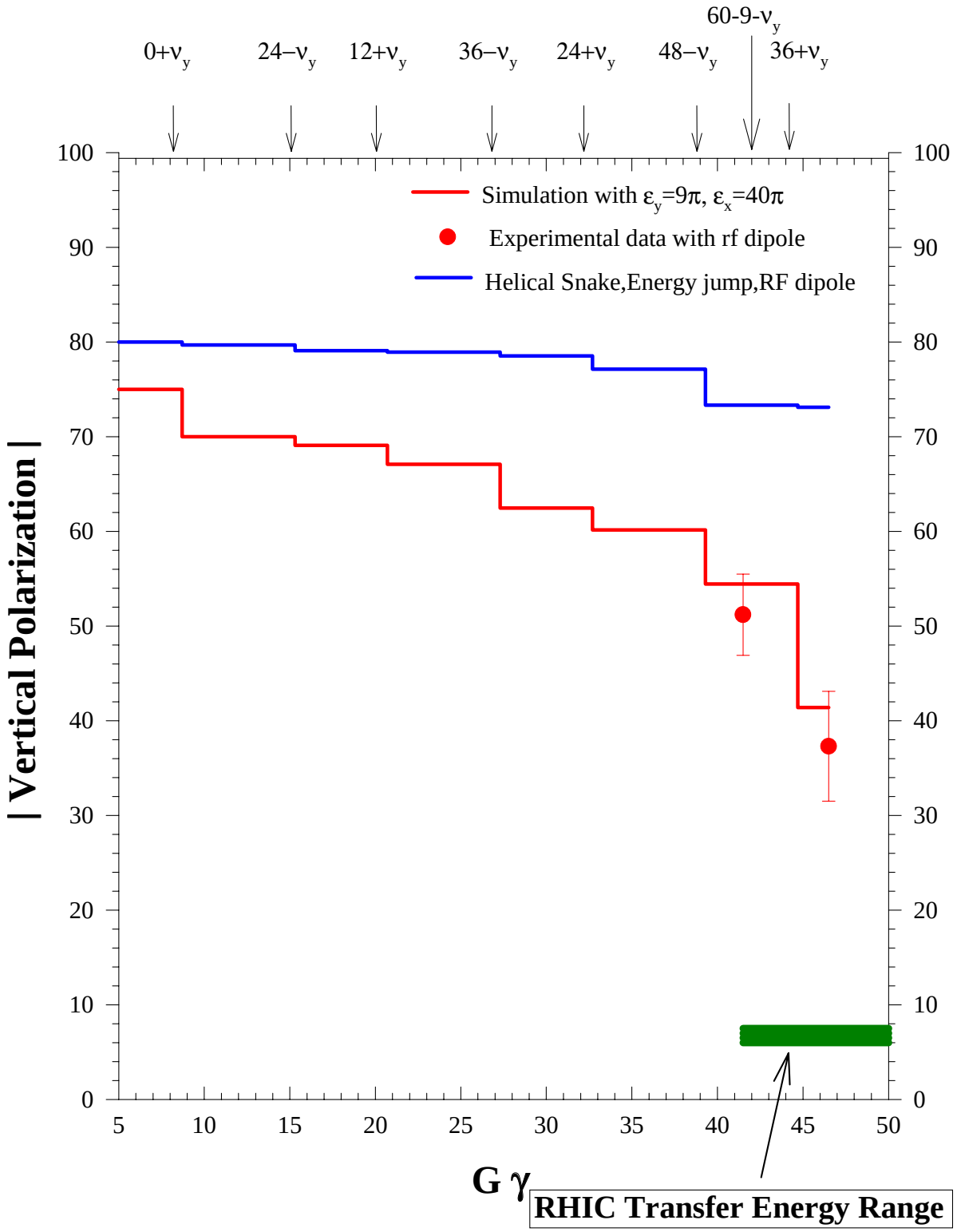

Figure 2.5: Vertical polarization versus $G\gamma$ measured during the November 1997 run of E-880. The lower curve is the result of a spin tracking calculation for the experimental conditions. The upper curve simulates the use of a helical partial Snake in the AGS.

is accelerated independently, we have the option of preparing the polarization direction of each bunch independently. Filling both RHIC rings with 120 bunches each and acceleration to full energy will only take about 10 minutes which is short compared to the expected lifetime of the stored polarized proton beams in RHIC of many hours.

Chapter 3

AGS-to-RHIC Transfer Line

The AGS to RHIC (AtR) transfer line[23] has been designed to transport proton beams in the energy range, from 20.58 GeV (just above the RHIC transition Energy) to a maximum injection energy of 28.3 GeV. This range of injection energies is not however applicable for a polarized proton beam which is confined to a shorter range of injection energies. The range of energies of a polarized proton beam to be injected from the AGS to RHIC via the AtR transfer line has been studied before[22], but a more detailed and complete study is the subject of this chapter. The study consists of calculating the stable spin direction of a polarized proton beam from AGS, at the RHIC injection point (defined below), as a function of the proton energy. This energy dependence of the stable spin direction of an injected polarized beam from AGS to RHIC is due to the relative location of the horizontally and vertically bending magnetic elements of the AtR line. In addition a modification of the AtR line is proposed. This modification of the AtR transfer line can increase the energy range that a polarized proton beam can be transferred into RHIC machine with optimum polarization transfer.

3.1 AtR Sections Affecting the Proton Beam Polarization

The layout of the (AtR) transfer line is shown in the schematic diagram of Fig. 3.1. In the AtR transfer line there are two sections of the beam line where the beam direction is not parallel to the horizontal plane but makes an angle below the horizontal plane. The first of the sections is located in the W-line (see Fig. 3.1) within the 20° bend. The second section is located at the end of the Y-line in the RHIC injection section (see Fig. 3.1). A schematic diagram of the first of these two sections is shown in Fig. 3.2 and will be referred to in this chapter as the "12.5 mrad vertical bend."

The "12.5 mrad vertical bend" consists of a -12.51 mrad vertically bending magnet located after the second horizontally bending magnet of the 20° W-line[23] (see also Fig. 3.1) followed by six combined-function dipole magnets which bend the beam horizontally to the right by 15°, and finally a +12.46° mrad vertically bending dipole which restores the beam direction to the horizontal plane. A schematic diagram of the second vertical bend is shown in Fig. 3.3. and will be referred to in this chapter as the "3.0 mrad

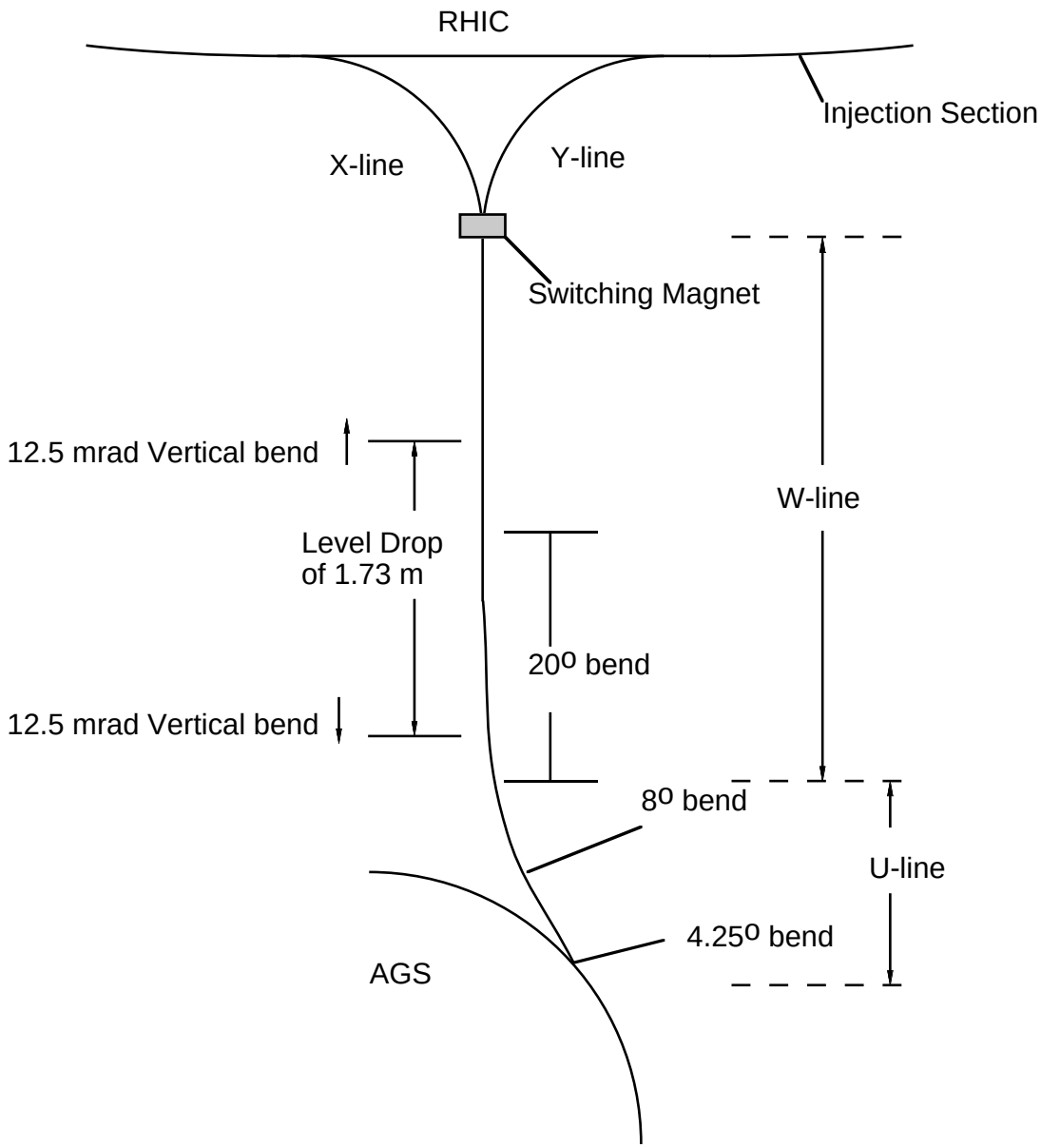

Figure 3.1: Schematic diagram of the AGS to RHIC (AtR) transfer line. The 12.51 mrad vertical bend is located at the region of the 20° horizontal bend. The 3 mrad bend is located at the end of the RHIC injection section shown in the figure.

vertical bend."

The "3.0 mrad vertical bend" is located at the end of the injection section of the AtR transfer line and begins with a −3.0 mrad vertically bending magnet (see Fig. 3.3) followed by a Lambertson septum

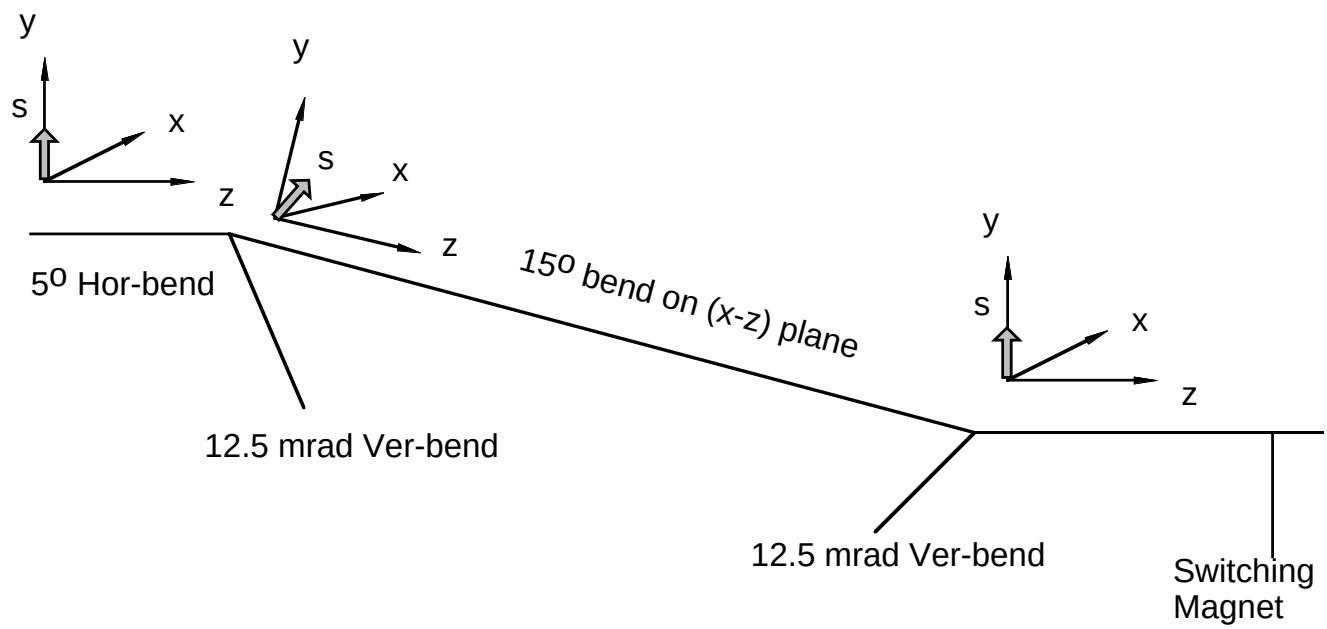

Figure 3.2: Schematic diagram of the "12.5 mrad vertical bend." A -12.51 mrad vertical bend is followed by a 15° horizontal bend and $+12.46°$ vertical bend. (Note that the small difference in vertical bends is used to correct for the earth's curvature.)

magnet[24] which bends the beam 38.0 mrad to the right, then a RHIC quadrupole (focusing) – dipole (left-bend) – quadrupole (defocusing) and finally the vertically bending RHIC injection kicker which deflects the beam by +1.73 mrad which restores the injected beam onto the RHIC plane. The strength required for the vertical injection kicker to restore the beam back to the horizontal plane has been reduced down to 1.73 mrad because part of the vertical bend has been accomplished by the two RHIC quadrupoles. (For the injection into the clockwise beam circulating ring, the polarity of both, the Lambertson injection magnet and RHIC dipole have to be inverted.) The exit point of the RHIC injection kicker is defined here as the "RHIC injection point." It is the arrangement of the bending magnets in these two vertical bends (vertical bend followed by horizontal bend and then vertical) that affects the stable spin direction of a polarized proton beam.

The small difference in the two vertical pitching magnets, +12.51 and -12.46 mrad is to correct for the earth's curvature; the planes of the AGS and RHIC rings are not quite parallel, since the center of RHIC is more than a kilometer north of the AGS ring. Both the AGS and RHIC tunnels were designed to be level. An additional vertical correction of 10μrad was made just after the extraction from the AGS.

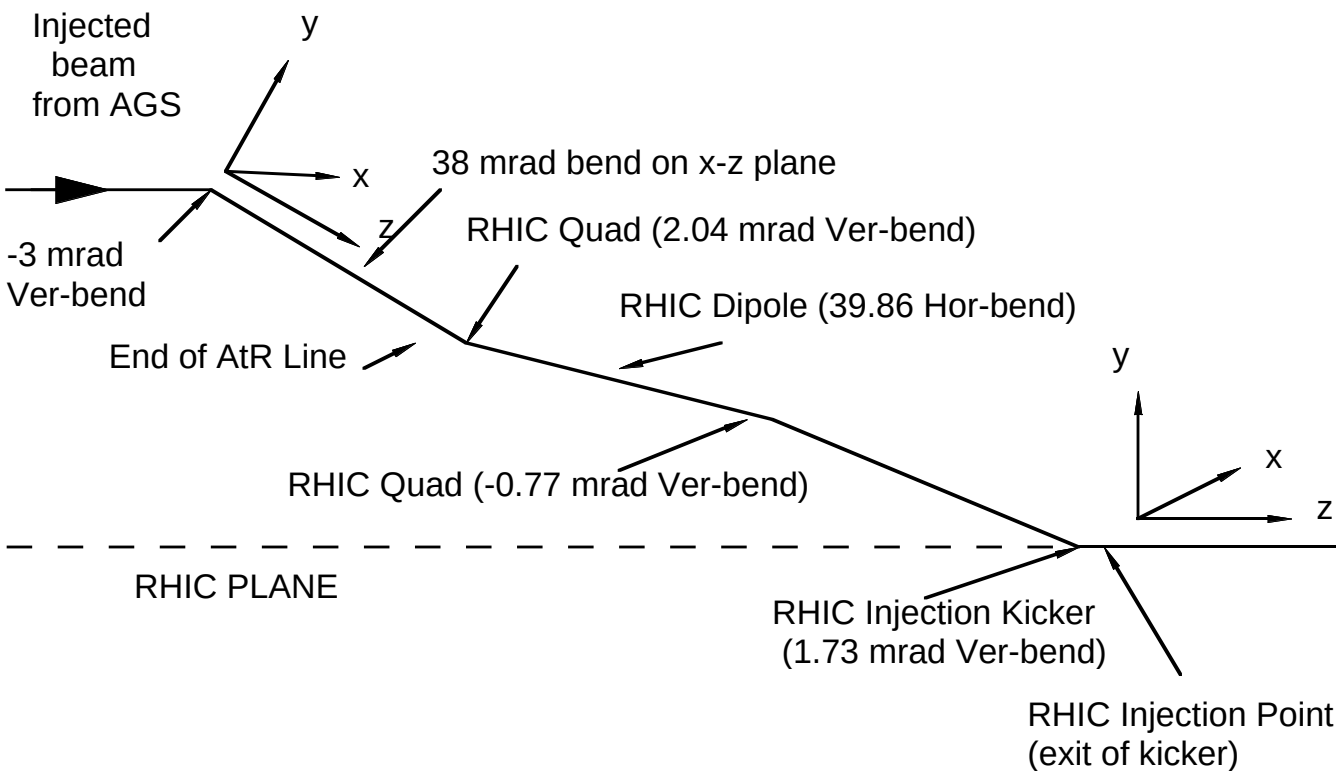

Figure 3.3: Schematic diagram of the "3.0 mrad vertical bend." The beam is injected off axis with respect to the two RHIC quadrupoles which act also as vertical bending magnets. This injection geometry reduces the required strength of the vertical injection kicker, to a value of 1.73 mrad.

3.2 Calculation of Stable Spin Direction at RHIC Injection Point

The stable spin direction at the exit of the "12.5 mrad vertical bend" has been calculated[22] earlier. In those calculations the initial stable spin direction had been assumed to be vertical and the effect of the "3.0 mrad vertical bend," discussed above, was not included in the calculations since the "3.0 mrad vertical bend" was introduced in the AtR line after the calculations. In the present calculations, the stable spin direction was calculated at the "RHIC injection point" (see Fig. 3.3) and the following items were included in the calculations.

1. *A section of the AGS machine (from the center of the straight section C10 of AGS to the H13 fast extraction point) followed by the AtR line (see Fig. 3.1).* The inclusion of this section of the AGS (C10 to H13) in the calculations makes it possible to take into account the effect of the AGS extraction bumps, the extraction kicker at G10 straight section, and the extraction septum at H10 straight section[25].

2. *The energy dependence of the stable spin direction of a polarized proton beam circulating in the AGS machine.* This energy dependence is due to the partial Snake. For a given strength of the AGS partial Snake, the stable spin direction of a polarized proton beam in the AGS, is well defined anywhere along a closed beam orbit in the AGS. The center of the C10 straight section has been chosen as the starting location of all the required ray trace calculations. This starting location has been chosen because of item 1 above.

3. *The finite beam size and momentum spread of the beam.* In order to calculate the spread of the stable spin direction at the "RHIC injection point," the shape of the beam ellipsoid at the location "C10" of the AGS machine is required. Closed orbit calculations[25] based on measured magnetic field maps of the combined function magnets of the AGS were performed for the AGS machine. From these calculations the beam parameters at any given point along a closed orbit in AGS machine were calculated, and for a given emittance, the beam ellipsoid at the location C10 of the AGS was calculated.

The calculations to determine the stable spin direction at the "RHIC injection point" were based on the numerical integration of two equations: the differential equation of motion (Eq. 3.1) of a charged particle moving in static magnetic and electric fields, and the spin precession equation (Eq. 3.2) of a particle with magnetic moment in the same electric and magnetic field:

$$\frac{d\mathbf{v}}{dt} = \frac{e}{m\gamma}\left(\mathbf{v}\times\mathbf{B} + \mathbf{E} - \frac{(\mathbf{v}\cdot\mathbf{E})\,\mathbf{v}}{c^2}\right) \tag{3.1}$$

$$\frac{d\mathbf{s}}{dt} = \frac{e}{m\gamma}\left((G\gamma+1)\,\mathbf{s}\times\mathbf{B} + (\gamma-1)\,G\frac{(\mathbf{v}\cdot\mathbf{B})\,(\mathbf{v}\times\mathbf{s})}{v^2} + \left(G\gamma + \frac{1}{1+\frac{1}{\gamma}}\right)\frac{\mathbf{s}\times(\mathbf{E}\times\mathbf{v})}{c^2}\right) \tag{3.2}$$

In (Eq. 3.1) and (Eq. 3.2), above B and E are the magnetic and electric fields in the laboratory system, e, m, and v are the charge, rest mass, and the velocity of the proton, $\gamma = (1 - v^2/c^2)^{1/2}$, $G = (g-2)/2$ (g = gyromagnetic ratio of the proton magnetic moment), and $\mathbf{s}$ is the spin vector from the relation $\mu = g(e/2m)s$ where μ is the magnetic moment of the proton. The computer code which performed the integration of the differential equations of motion (Eq. 3.1) and (Eq. 3.2), as the particles pass through the various magnetic elements of the AtR transfer line, comes under the name RAYTRACE_SPIN and is a modified version of the RAYTRACE computer code[26].

3.2.1 Stable Spin Direction at AGS

The stable spin direction in the AGS is normally along the vertical direction. However, the introduction of the partial Snake makes the stable spin direction depend on the azimuthal location of the beam in the AGS and the beam energy. In particular, at the location of the middle of the C10 straight section which

is located 180° from the partial Snake, the directional cosines of the stable spin direction are given by:

$$n_{\text{rad}} = 0 \tag{3.3}$$

$$n_{\text{vert}} = \frac{1}{N}\sin(\pi G\gamma)\cos(\delta) \tag{3.4}$$

$$n_{\text{long}} = \frac{1}{N}\sin(\delta) \tag{3.5}$$

where: $N = [1 - \cos^2(\pi G\gamma)\cos^2(\delta)]^{\frac{1}{2}}$ and δ is the spin rotation angle introduced by the Snake, referred to as the Snake strength. When $\delta = 0$ the stable spin direction is along the vertical, independent of the beam energy.

3.2.2 Stable Spin Direction at RHIC Injection Point

With the knowledge of both the stable spin direction and the beam parameters at the middle of the straight section C10 of the AGS, the calculations to obtain the stable spin direction at RHIC injection point proceeded as follows.

a) A given beam energy (corresponding to the AGS closed orbit particle) was chosen.

b) The AtR line was tuned to transport protons with energy equal to the energy of the closed orbit particle in AGS.

c) The closed orbit particle starting from the AGS location C10 was traced (trajectory and spin) down to the H10 extraction section of the AGS, followed by the AtR line to the "RHIC injection point" where the directional cosines of the stable spin direction were recorded.

d) Following the closed orbit particle, step (c) above was repeated for another 999 particles which were randomly selected from the beam ellipsoid of the AGS location C10 and traced down to the "RHIC injection point."

e) From the distribution of the 1000 particles traced, the average value $< S_y >$ and the standard deviation $< (S_y - < S_y >)^2 >^{1/2}$ of the vertical spin direction S_y was calculated at the "RHIC injection point."

The procedure (1) to (5) was repeated for an injected beam with different proton energy.

Stable Spin Direction at RHIC injection point (AGS partial Snake off)

The vertical component S_y of the stable spin direction, at the RHIC injection point, is shown in Fig. 3.4 as a function of $G\gamma$. The empty squares are the S_y components of the central trajectory particle. The filled squares are the average vertical spin projection $< S_y >$, as calculated from the distribution of the S_y component of the 1000 injected particles. The error bars are one standard deviation of the vertical spin

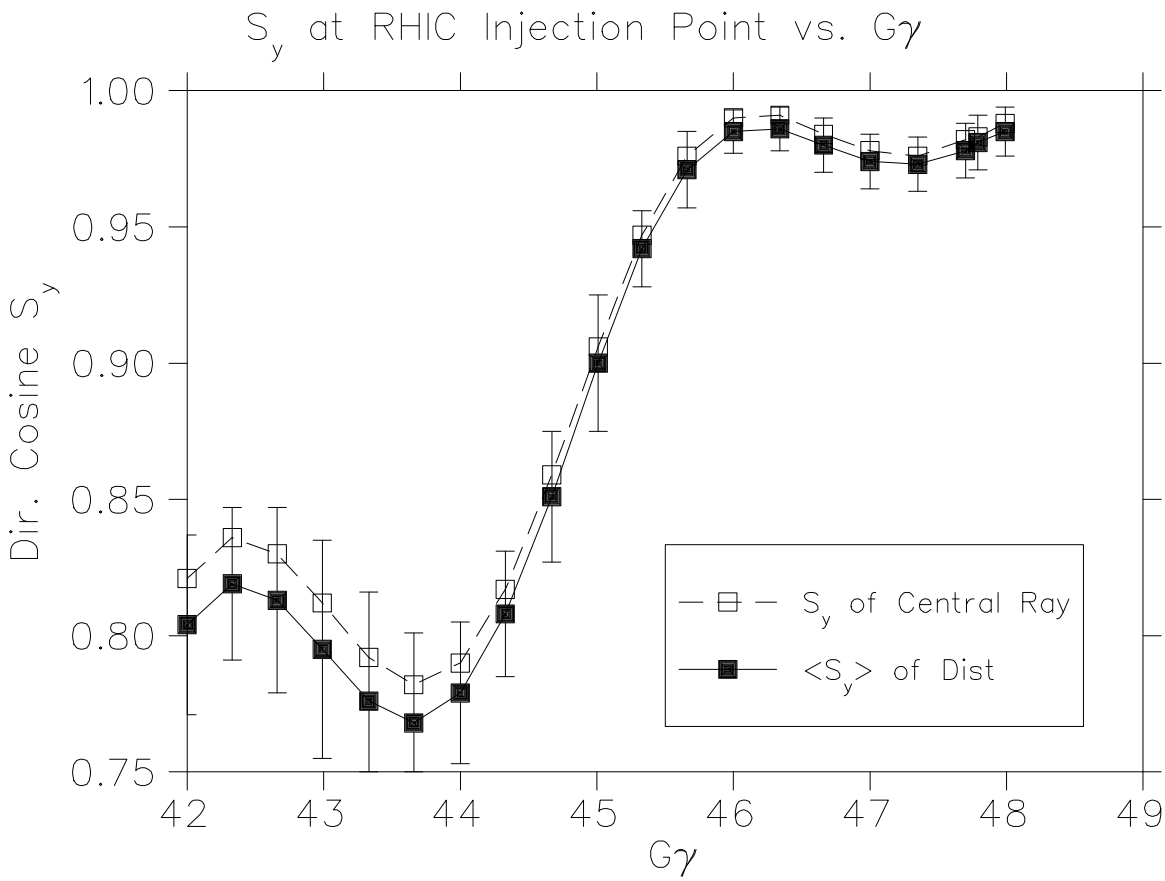

Figure 3.4: The S_y component of the stable spin direction at the RHIC injection point. The empty squares correspond to the central trajectory particle. The filled squares to the average S_y of the spin distribution. The error bars correspond to one standard deviation of the S_y component of the spin distribution. The initial spin direction at AGS has been assumed vertical. (AGS Snake off.)

projection S_y and contains over 90% of the final spin distribution which is not Gaussian and represent a measure of the spread of the stable spin direction at the RHIC injection point. This spread of the stable spin direction at the RHIC injection point is due to the off central trajectory particles which are experiencing the non vertical fields of the various quadrupoles and combined function magnets (dipole plus quad) of the AtR transfer line. The random sampling of the particles was taken from a beam with a normalized beam emittance of 10 π mm mrad for both vertical and horizontal planes, and one standard deviation of the beam momentum spread $\Delta p/p = \pm 0.05\%$.

The calculations performed to obtain the results shown in Fig. 3.4 assumed that the initial stable spin direction was along the vertical. In a realistic injection of a polarized proton beam the assumption that the spin direction is along the vertical will not be valid, at least at the range of energies covered by the Fig. 3.4. This is because of the partial Snake, the effect of which is discussed next.

Stable Spin Direction at RHIC injection point (AGS partial Snake on)

The vertical component S_y of the stable spin direction at the RHIC injection point when the partial Snake in the AGS is on at a 9° strength, is shown in Fig. 3.5 as a function of the $G\gamma$. The empty squares are the S_y components of the central trajectory particle. The filled squares are the average vertical spin projection $< S_y >$, as calculated from the distribution of the S_y component of the 1000 particles injected. The error bars are $\pm$ one standard deviation of the vertical spin projection S_y and contain over 90% of the final spin distribution which is not Gaussian. The spread of the stable spin direction at the RHIC injection point as it appears in Fig. 3.5 is due to the off central trajectory particles as mentioned in the previous section. In addition the initial stable spin direction, which is defined by the strength of the partial Snake in the AGS, has a profound effect not only in the spread but also on the average value of the stable spin direction itself at the RHIC injection point. Likewise, as mentioned in the previous section, the random sampling of the particles was taken from a beam with a normalized beam emittance of 10 π mm mrad for both vertical and horizontal planes, and the beam momentum spread with a standard deviation $\Delta p/p = \pm 0.05\%$.

The stable spin direction of a polarized proton beam circulating in RHIC which will operate with two full Snakes, is along the vertical. Therefore the stable spin direction of the injected polarized beam should be along the vertical if possible. The results in Fig. 3.5 will serve as a guide to help choose the injection energy which will provide the maximum vertical components of the stable spin direction with minimum spread. At injection proton beam energies corresponding to $G\gamma = integer$ the stable spin direction at AGS is not well defined and neither is the stable spin direction at the RHIC injection point. (See Fig. 3.5.)

3.2.3 Optimization of Stable Spin Direction with Energy

The preceding two sections suggest that the optimum energy range for injection of a polarized proton beam into RHIC corresponds to values of $G\gamma$ from $\sim$45 to 48. However it is possible to alter the energy range for optimum polarization transfer of an injected beam into RHIC by employing three additional horizontally bending dipole magnets in the AtR transfer line. A schematic diagram of the the section of the AtR transfer line which includes the three added dipoles, is shown in Fig. 3.6.

The first of the three dipoles is placed in front of the second 12.5 mrad vertically bending magnet of the 20° bend of the ATR line (see Fig. 3.6). The second dipole shown in Fig. 3.6 is to be placed just after the second 12.5 mrad vertically bending magnet with the center of the third dipole placed downstream from the center of the second dipole, at a distance equal to the distance of the centers of the first two horizontally bending dipoles. This dipole arrangement is not dispersive, and will only affect the stable spin direction after the vertical magnet shown in Fig. 3.6. The beam trajectory will be restored at the entrance of the WQ3 quadrupole (Fig. 3.6) and the beam parameters will be practically the same as before the inclusion of the dipoles. The next two sections present and discuss the results of the stable spin direction at the RHIC injection point when the three horizontal dipoles shown in Fig. 3.6 are excited to 1.5 Tesla

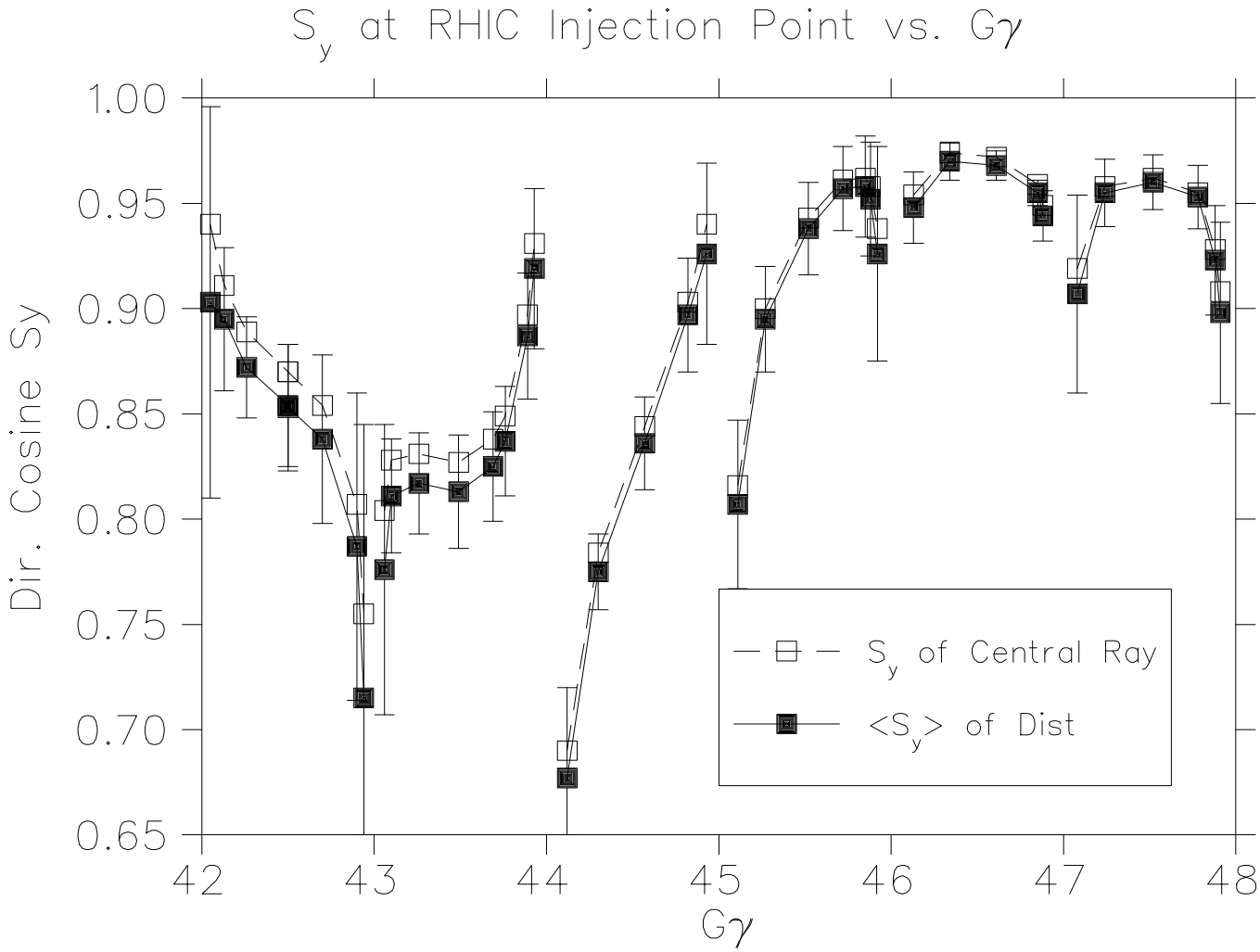

Figure 3.5: The S_y component of the stable spin direction at the RHIC injection point as a function of $G\gamma$. The empty squares correspond to the central trajectory particle. The filled squares are the average S_y of the spin distribution. The error bars correspond to one standard deviation of the S_y component of the spin distribution. The initial spin direction at AGS is defined by the partial Snake in the AGS.

each in a direction such that the first dipole will bend the beam to the right, the second to the left, and the third one to the right.

Stable Spin Direction (AGS partial Snake off; AtR modified)

With the AtR transfer line modified by the insertion of the three dipoles mentioned in the previous subsection, the calculation for the stable spin direction at the RHIC injection point was repeated. The vertical component S_y of the stable spin direction at the RHIC injection point is shown in Fig. 3.7 as a function of $G\gamma$.

Comparing Fig. 3.4 with Fig. 3.7, the shift of the optimum stable spin direction to lower energies is

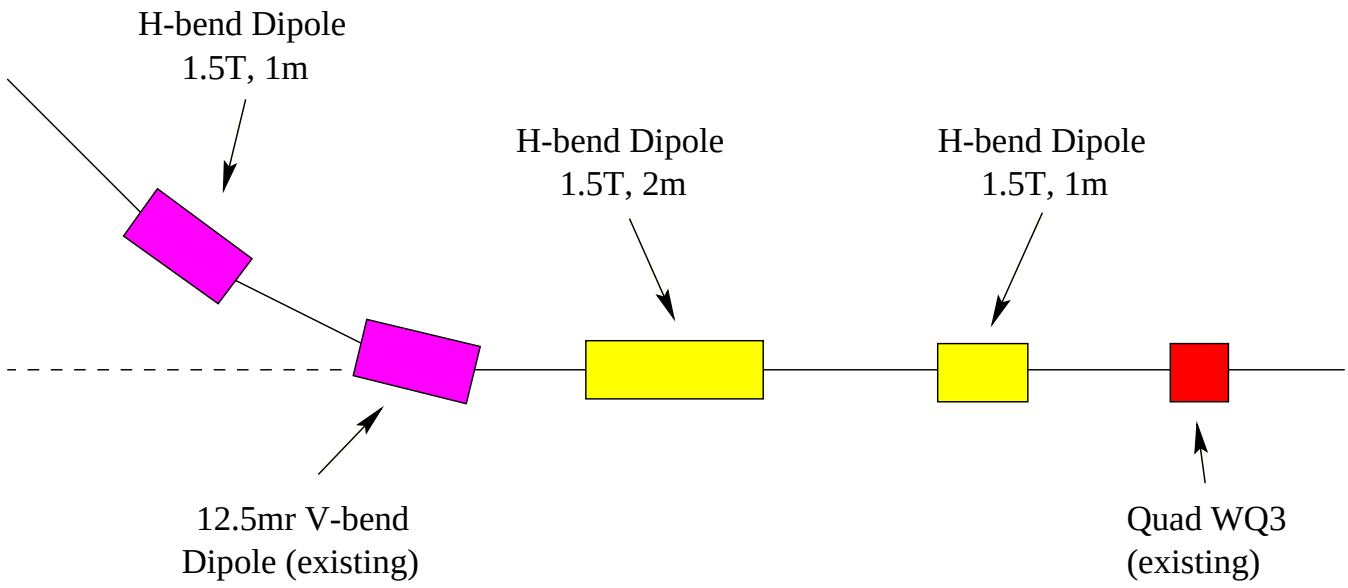

Figure 3.6: Schematic diagram of the section of the AtR transfer line with the three horizontally bending magnets which can optimize the AtR polarization transfer at various proton injection energies.

obvious. The assumption made in the calculation to obtain the results shown in Fig. 3.4 are also valid in obtaining the results of Fig. 3.7

Stable Spin Direction (AGS partial Snake on; AtR line modified)

In these calculations the AtR transfer line is modified as mentioned earlier, and the AGS partial Snake is turned on at a 9° strength. The vertical component S_y of the stable spin direction at the RHIC injection point when the partial Snake in AGS is on, is shown in Fig. 3.8 as a function of $G\gamma$.

Comparing Fig. 3.5 with Fig. 3.8 the shift of the optimum stable spin direction to lower energies is again obvious.

3.2.4 Conclusions

The stable spin direction of a polarized proton beam at the RHIC injection point, has been studied as a function of proton energy. It is shown that the stable spin direction at the RHIC injection point depends upon the injected proton energy. Optimum polarization transfer can be defined as the condition where the average stable spin direction of the protons at the RHIC injection point is "almost" vertical with the minimum possible spread among the particles of the bunch.

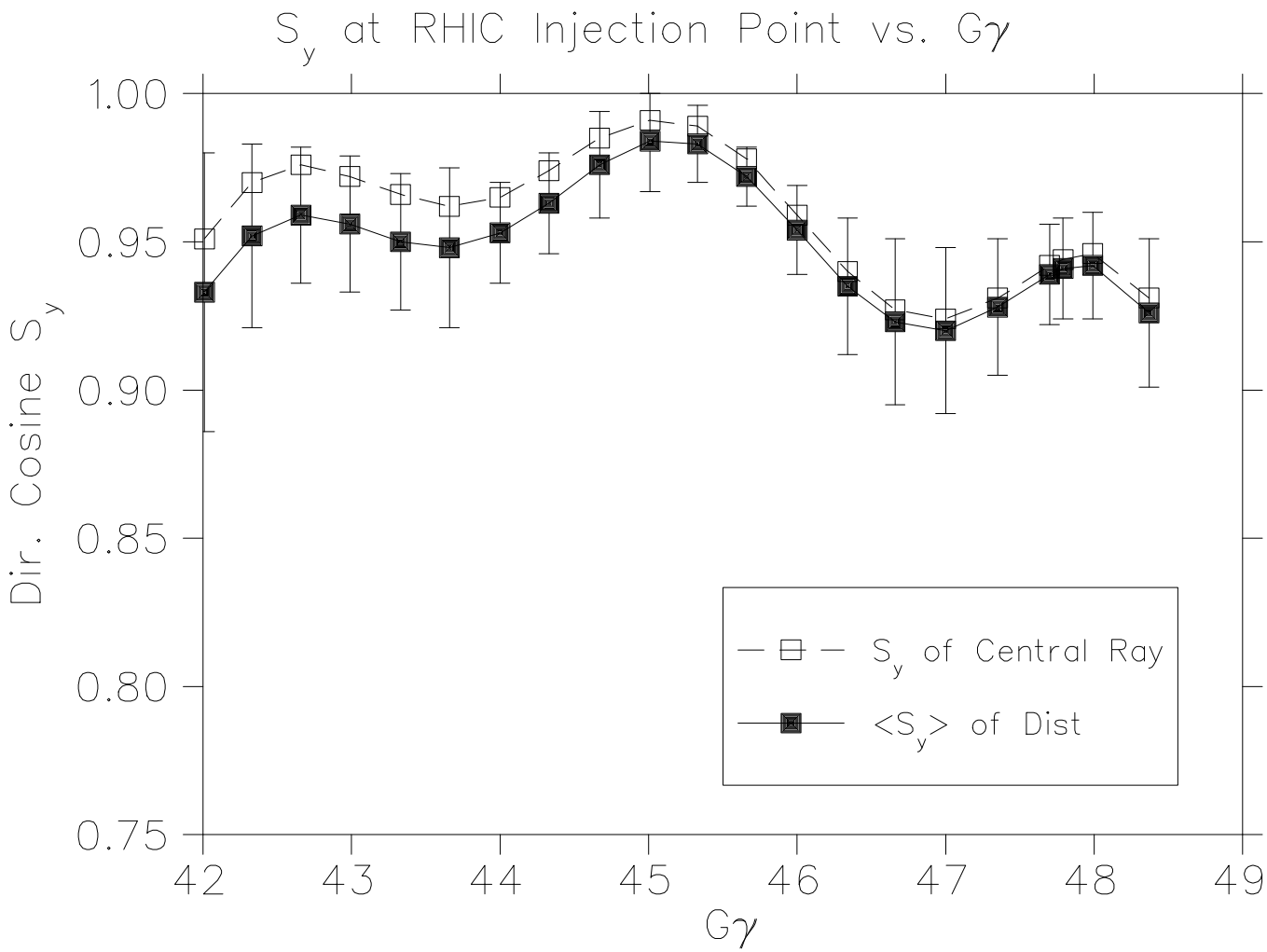

Figure 3.7: The S_y component of the stable spin direction at the RHIC injection point. The empty squares correspond to the central trajectory particle. The filled squares to the average S_y of the spin distribution. The error bars correspond to one standard deviation of the S_y component of the spin distribution. The initial spin direction in the AGS has been assumed vertical. (Partial Snake is off.) The three dipoles of Fig. 3.6 are excited to 1.5 T each.

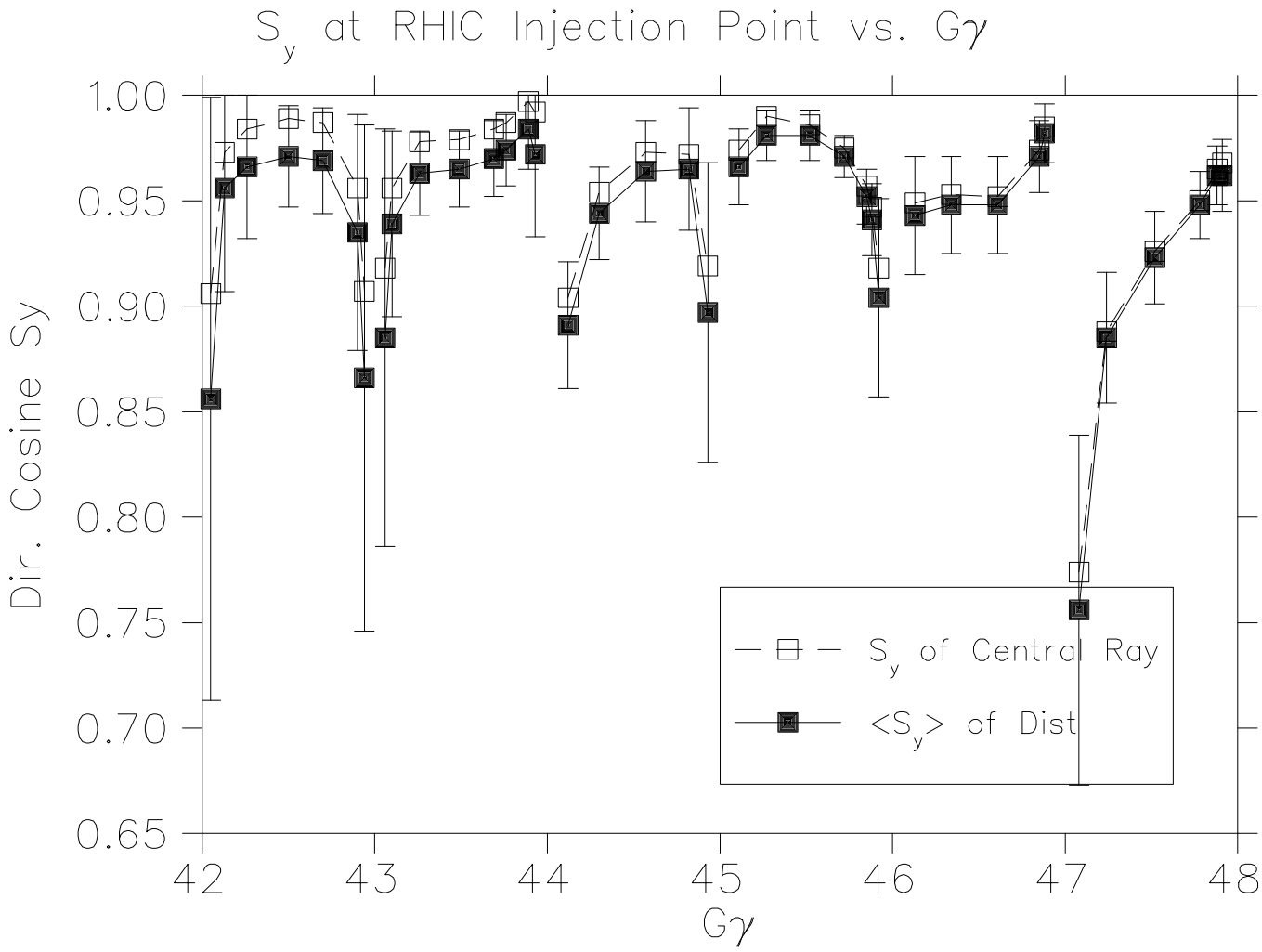

Figure 3.8: The S_y component of the stable spin direction at the RHIC injection point as a function of $G\gamma$. The empty squares correspond to the central trajectory particle. The filled squares is the average S_y of the spin distribution. The error bars correspond to one standard deviation of the S_y component of the spin distribution. The three dipoles of Fig. 3.6 are excited to 1.5 T each. The initial spin direction at AGS is defined by the partial Snake in AGS.

Chapter 4

Snakes and Spin Rotators in RHIC

To fit within existing straight sections in RHIC, it is important to find the most compact design for Siberian Snakes and Spin Rotators which could produce the desired spin rotation in the shortest space. A particularly elegant solution was proposed by V. Ptitsin and Y. Shatunov.[27] Their solution is based on helical dipole magnet modules, each having a complete 360° twist. Using helical dipole magnets minimizes orbit excursions which is most severe at injection energy. This allowed for a more modular design, where similar superconducting helical magnets could be used for both Snakes as well as Spin Rotators near the interaction points in RHIC.

4.1 General Layout

Two full Siberian Snakes on opposite sides of each of the two RHIC rings serve to avoid depolarization from imperfection and intrinsic depolarizing resonances up to the top energy of 250 GeV. In addition, Spin Rotators are required at the intersection points used by PHENIX and STAR to allow for measurements of spin effects with longitudinally polarized protons. The Spin Rotators rotate the polarization from the vertical direction into the horizontal plane on one side of the interaction region and restore it to the vertical direction on the other side.

The Siberian Snakes introduce a 180° spin rotation without generating a net orbit distortion. The Spin Rotators placed around the experiments rotate the spin by 90° to provide longitudinal polarization at the interaction region again without generating net orbit distortions. In both cases the spin rotation is accomplished with a sequence of constant field, superconducting helical dipole magnets.

Each Snake rotates the spin by 180° around a horizontal axis and the two axes of the two Snakes of each ring have to be perpendicular to each other. We are planning to use pairs of Siberian Snakes with one Snake rotating the spin around an axis that points 45° to the outside and the other Snake rotating around an axis that points 45° to the inside of the ring. In this case all Snakes can be constructed in the same way. Also, the two Snakes of each ring have to be installed on opposite sides of the ring. In fact, the beam direction in one Snake has to be exactly opposite to the beam direction in the other Snake to within

0.3 mrad. The following is a summary for the locations and construction of the Siberian Snakes and the Spin Rotators (see Fig. 1.2):

- Two pairs of full Siberian Snakes, one pair in each ring, are installed in the 3 o'clock and 9 o'clock sections of RHIC as shown in Fig. 1.2. These Snakes rotate the spin around axes that point 45° to the inside or outside of the ring. We are planning to install the Siberian Snakes in the 13 m long, cold straight sections between Q7 and Q8.

- The two pairs of Spin Rotators, one set for PHENIX at the 8 o'clock region and another set for STAR at the 6 o'clock region, are installed in the 40 m long straight sections between Q3 and Q4 on either side of the interaction region. The beam direction in the straight sections is different from the direction in the collision area by 3.67 mrad which introduces a spin rotation that is larger by a factor of $G\gamma$. This means that the Spin Rotators have to prepare a horizontal polarization direction such that after this spin rotation the desired longitudinal polarization direction is obtained at the interaction point.

4.2 Siberian Snake and Spin Rotator Design

For both the Siberian Snakes and the Spin Rotators we are planning to use four helical magnets[27]. Helical field magnets have some distinctive advantages over more conventional transverse Snakes or rotators: (i) the maximum orbit excursion is smaller, (ii) orbit excursion is independent from the separation between adjacent magnets, and (iii) they allow an easier control of the spin rotation and the orientation of the spin precession axis.

In an ideal helical dipole magnet to be used for our purposes, the central dipole field should rotate through a complete 360° from one end of the magnet to the other. In a real magnet, of course, the fields at the ends of the magnet will also contribute to the particle dynamics. The plan is to design a magnet in which the field integrals $\int B_x d\ell$ and $\int B_y d\ell$ are both equal to zero (for some particular energy). The maximum body field will thus rotate through an angle less than 360° along the axis of the magnet. Moreover, in order to simplify the construction of the Snakes/Rotators, a solution has been found with all magnetic modules identical in both devices. The only variation is that the helix of some magnets is right-handed and others left-handed.

Snake parameters are listed in Table 4.1. The parameters are a result of an optimization using an orbit and spin tracking program that includes the effects of fringe fields[28], [29]. The integration is performed by interpolation through the magnetic field numerically calculated and mapped on a 3-dimensional grid. The result of the orbit and spin tracking is shown in Fig. 4.1. To produce these results, it was found that the central body field of the helical magnets should rotate through approximately 340°, with the ends contributing the necessary remaining field. Naturally, the exact amount of rotation depends upon the

Number of helical magnets				4
Total length				10.56 m
Magnet bore				100 mm
Helical Magnets				
	Length (effective)	Field helicity	Field orientation at entrance/exit	Field strength
1	2.40 m	right-handed	Vertical	1.3 T
2	2.40 m	right-handed	Vertical	-4.0 T
3	2.40 m	right-handed	Vertical	4.0 T
4	2.40 m	right-handed	Vertical	-1.3 T
Max. orbit excursion (hor./ver.)			(25 GeV)	15 mm / 33 mm
Total field integral				24 T-m
Orbit lengthening			(25 GeV)	2 mm

Table 4.1: Parameters for the Siberian Snake magnets. All helical magnets are right-handed, and begin and end with vertical fields. The central field strengths were optimized to include end effects of the magnets.

model used to describe the ends, and final magnet parameters will be a result of actual magnet tests and measurements.

All helical magnets may be powered by separate power supplies. This allows for an adjustment of the spin tune to 1/2 and of the direction of the rotation axis to compensate for the effect of the detector solenoids. This is shown in Fig. 4.2.

Spin Rotator parameters are listed in Table 4.2. The result of the orbit and spin tracking is shown in Fig. 4.3. Since in RHIC the direction of the Spin Rotator beam line is at a horizontal angle $\theta = 3.674$ mrad with the direction of the adjacent insertion, the spin should emerge from the rotator in the horizontal plane and at an angle $G\gamma\theta$ with the rotator axis in order to obtain a longitudinal polarization through the insertion region. The needed rotation is therefore dependent on the beam energy. The values of the field needed to provide a longitudinal polarization at different energies are shown in Fig. 4.4.

4.3 Effects on RHIC Operation

Calculations of the changes to the RHIC lattice parameters generated by the helical dipole magnets show minimal effects on the RHIC lattice parameters. Because of the spiral trajectory within the magnets, the Snakes and rotators introduce coupling into the RHIC accelerators. Both computer modeling and analytical calculations have shown that this effect is also small, with a minimum tune separation due to coupling of $\Delta\nu = 0.004$ with two Snakes and 4 Spin Rotators present at RHIC injection.[30],[31]

The effects on RHIC operation of helical dipole magnet error fields and misalignments have also been studied.[32] In contrast to a "regular" dipole magnet error which can be thought of as producing a kink in the slope of the particle trajectory at the source of the error, a "helical dipole" error will introduce a step in the trajectory. To keep the vertical orbit distortions under control, the helical dipole field errors

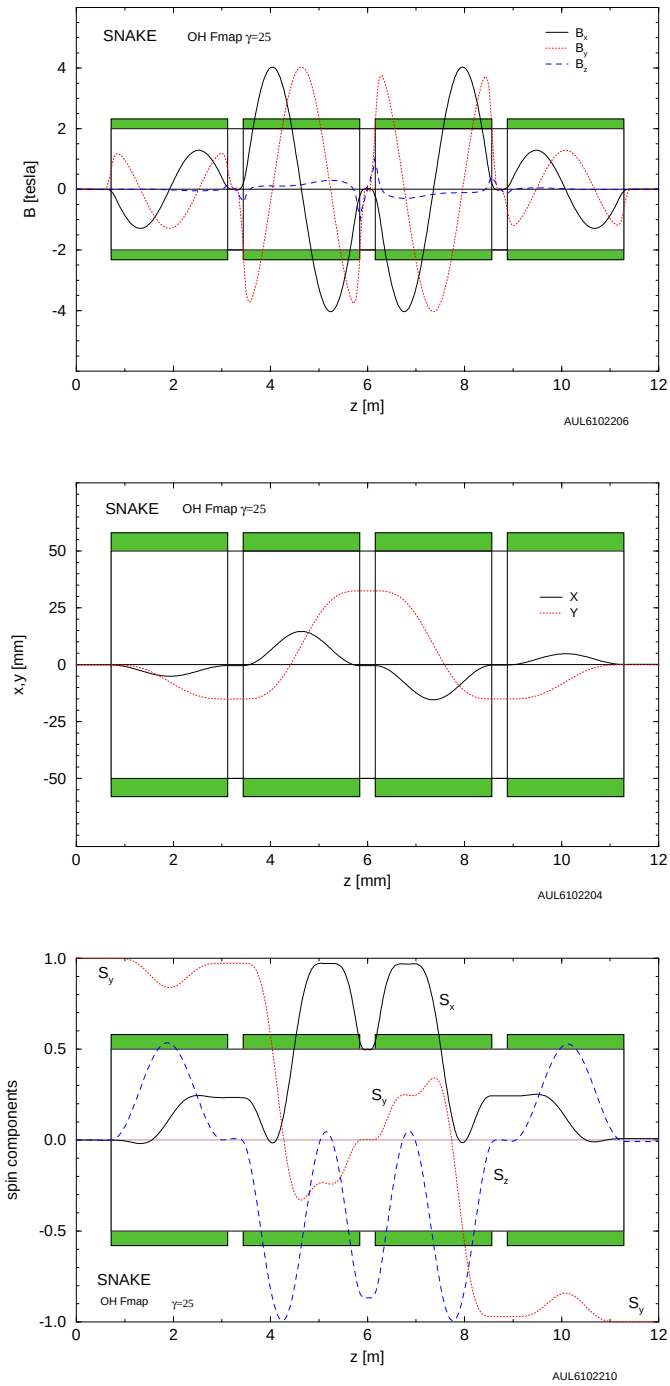

Figure 4.1: Field, orbit, and spin tracking through the four helical magnets of a Siberian Snake at $\gamma = 25$. The spin tracking shows the reversal of the vertical polarization.

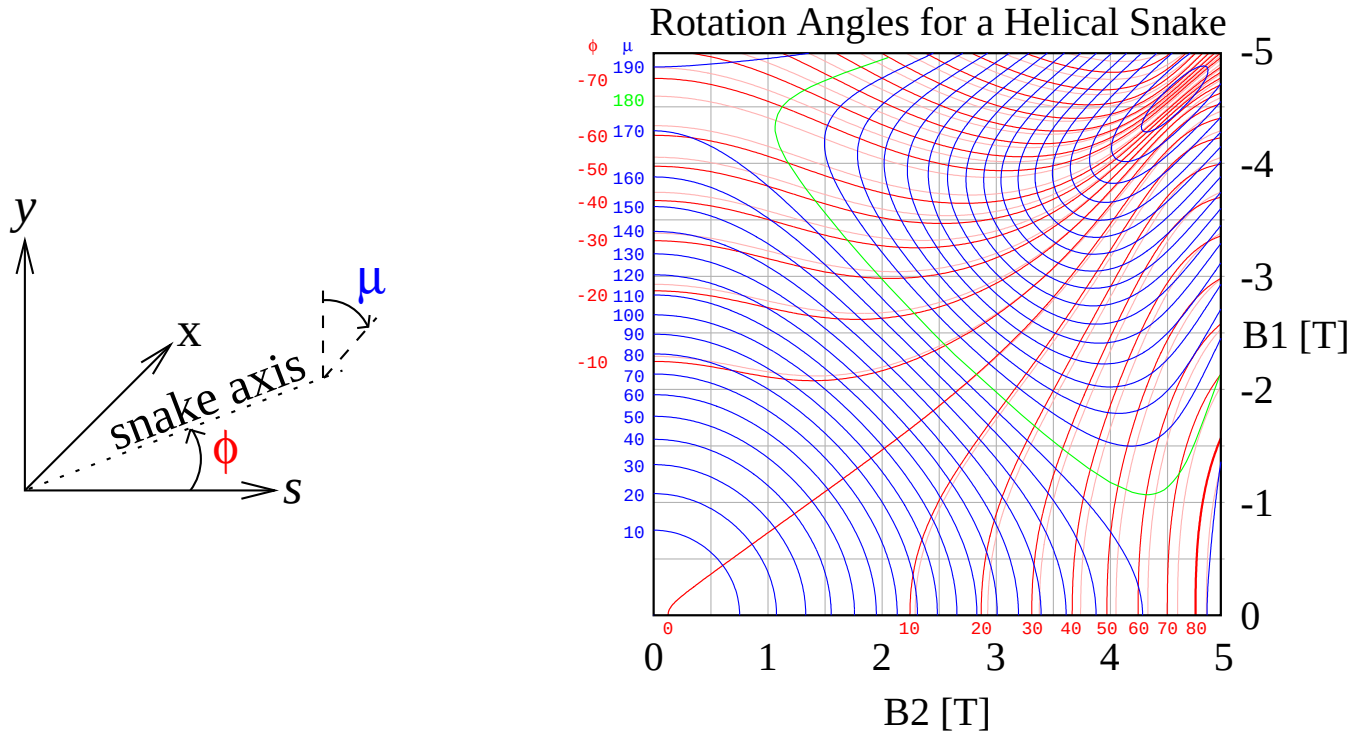

Figure 4.2: Change of the direction of the Snake rotation axis as a function of magnet excitation. This calculation uses a simplified analytical expression for the Snake magnetic field. The rotation axis of the snake is ϕ, and μ is the rotation angle. Note that the ϕ contours shift slightly from injection (red) at 25 GeV to storage (pink) at 250 GeV.

Number of helical magnets				4	
Total length				10.56 m	
Magnet bore				100 mm	
Helical Magnets					
	Length (effective)	Field helicity	Field orientation at entrance/exit	Field (25 GeV)	Field (250 GeV)
1	2.40 m	right-handed	Horizontal	2.1 T	3.5 T
2	2.40 m	left-handed	Horizontal	2.8 T	3.1 T
3	2.40 m	right-handed	Horizontal	2.8 T	3.1 T
4	2.40 m	left-handed	Horizontal	2.1 T	3.5 T
Max. orbit excursion (hor./ver.)			(25 GeV)	25 mm / 10 mm	
Total field integral				23 T-m	
Orbit lengthening			(25 GeV)	1.4 mm	

Table 4.2: Parameters for the Spin Rotator magnets. Helical magnets alternate right-handed and left-handed, and all begin and end with horizontal fields. The central field strengths were optimized to include end effects of the magnets, and are calculated for longitudinal polarization at the beam collision point.

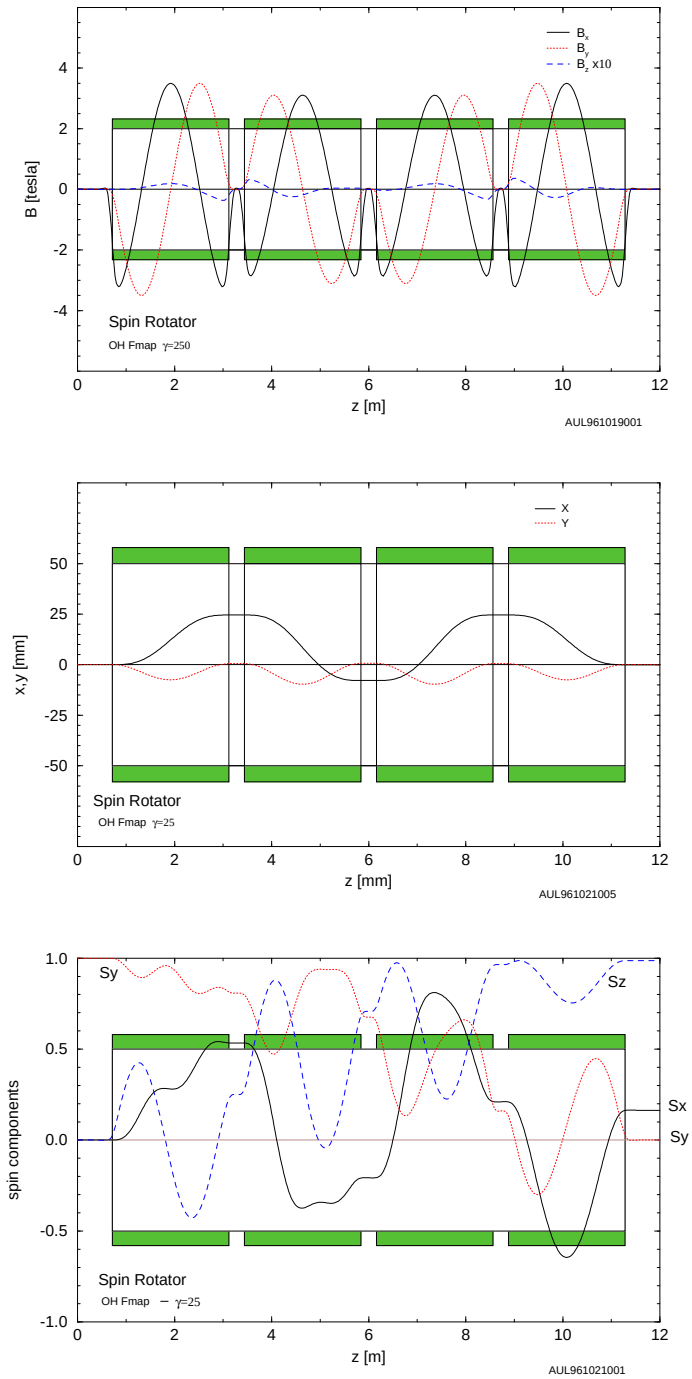

Figure 4.3: Field, orbit, and spin tracking through the four helical magnets of a Spin Rotator at $\gamma = 25$. In this example, the spin tracking shows how the polarization is brought from vertical to horizontal.

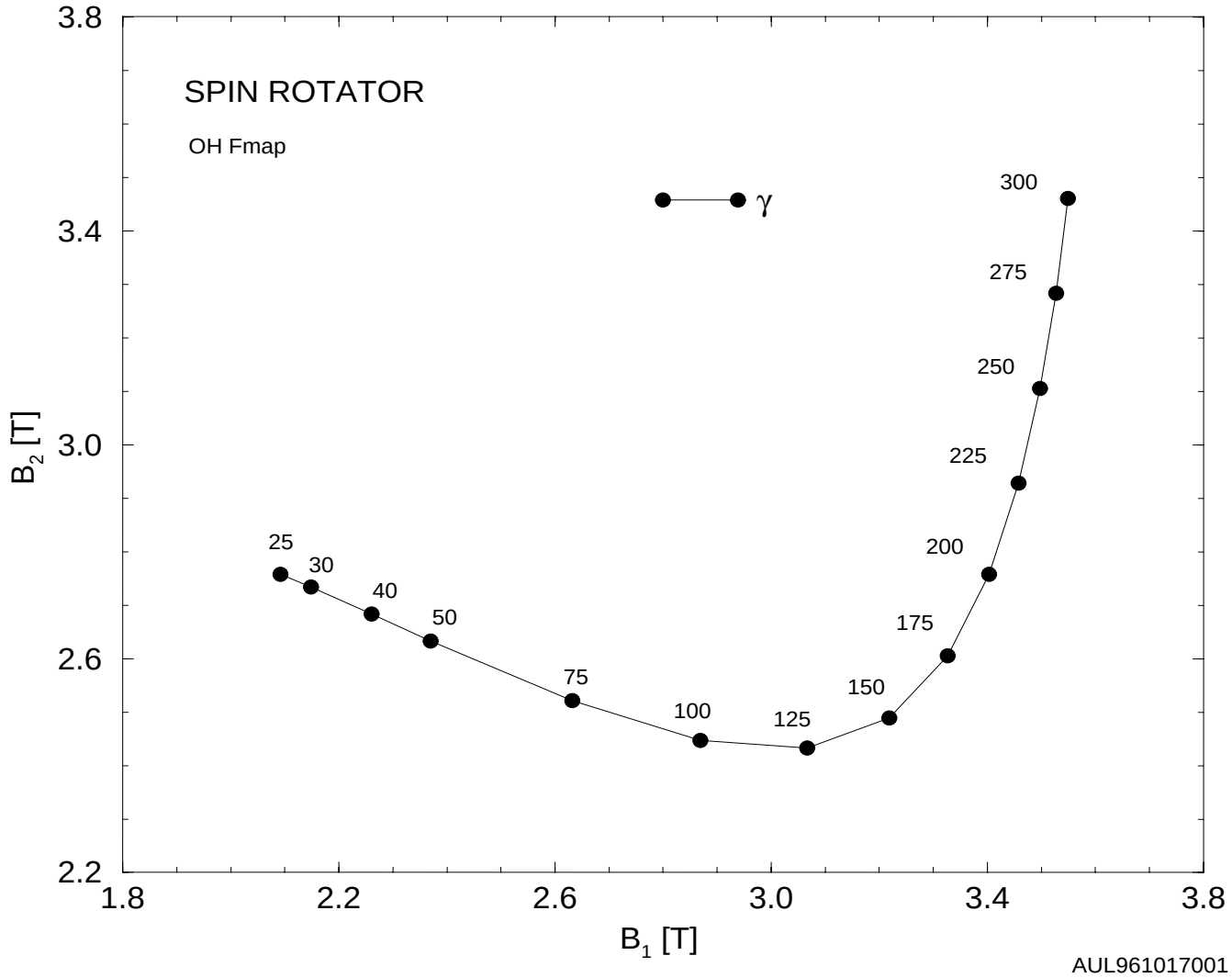

Figure 4.4: Excitation of the two pairs of helical magnets in the rotator to achieve longitudinal polarization in the insertion of RHIC, for various beam energies.

$\Delta(B\ell)/(B\ell)$ should be kept reasonably below 1%, and rotational misalignments should be less than about 10 mrad. The more important parameter will be the total integrated field strength ($\int B_x ds$, $\int B_y ds$) which should be zero, or equivalently the total equivalent integrated twist of the magnet should be 360°. This last requirement is especially sensitive in the case of the Rotator magnets (horizontal fields at the entrance and exit of the magnets). The Rotators, however, are only used at storage energy, where their effects on the orbit are smaller. With two Snakes on throughout injection and acceleration, the orbit distortions generated by their twist errors can easily be corrected using standard RHIC dipole correctors. The total twist angle and its tolerance are 360° ± 2°.[33] The ends of the magnets have been carefully designed to obtain not only the desired integrated field strength but also the desired total field twist well within this tolerance.[34], [35]

Field quality is also an issue for the helical magnets, though not as central an issue as for the normal bending magnets in the accelerator. The intrinsic helical nature of the field will itself produce nonlinear terms in the field expansion. In particular, Maxwell's equations dictate that the helical dipole field will be of the form

$$B_x \approx -B_0 \left\{ [1 + \frac{k^2}{8}(3x^2 + y^2)] \sin kz - \frac{k^2}{4} xy \cos kz \right\} \tag{4.1}$$

$$B_y \approx B_0 \left\{ [1 + \frac{k^2}{8}(x^2 + 3y^2)] \cos kz - \frac{k^2}{4} xy \sin kz \right\} \tag{4.2}$$

$$B_z \approx -B_0 k \left\{ 1 + \frac{k^2}{8}(x^2 + y^2) \right\} [x \cos kz + y \sin kz] \tag{4.3}$$

where the repeat period of the helical field is $\lambda = 2\pi/|k|$. In the above, we have assumed a field which is "vertical" (i.e., positive y direction) at the entrance to the magnet. The sign of k determines the handedness of the field. To first order, the transverse fields are just $B_y = B_0 \cos kz$, $B_x = -B_0 \sin kz$ as desired. However, we see that for significant displacements, there are nonlinear terms which will contribute to the particle motion.

In addition to this intrinsic nonlinear feature, magnet design and construction errors will add nonlinearities to the field as well. While the nonlinear field components tend to average to zero over the length of the helical dipole, the protons follow a trajectory which is not centered within the magnet. (This is illustrated in Fig. 4.5, in which the choice of the name "Snake" is readily apparent.) Thus, one expects to see feed-down effects due to this trajectory. For example, a sextupole component in the magnet will generate a tune shift due to the off-centered orbit. Analytical estimates indicate that the intrinsic tune shift at 25 GeV due to two Snakes in RHIC is on the order of $\Delta\nu \approx 0.015$, and that a sextupole component in the magnet design of strength $b_2 \approx 2 \times 10^{-4}/\text{cm}^2$ (or, approximately 20 "units" measured at 3.1 cm) will give approximately the same tune shift.[36],[37] Particle tracking results are in qualitative agreement with these estimates.[38] The magnet design has a much smaller b_2 component, and so should not pose a problem in this regard.

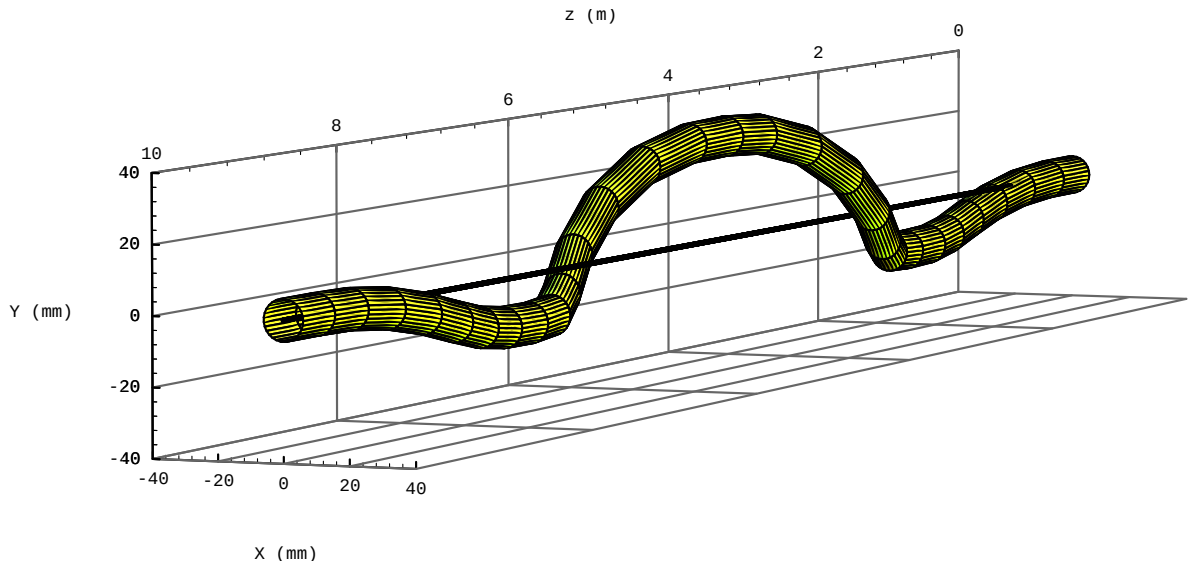

Figure 4.5: Three dimensional view of the trajectory through a RHIC Snake.

4.4 Compensation for Detector Solenoids

The STAR and PHENIX detectors use solenoid magnets as spectrometers. With transverse polarization at the collision point the solenoid contributes to the imperfection resonance strength,

$$\epsilon_{imp,sol} = \frac{1+G}{2\pi} \frac{\int B_{\|} d\ell}{B\rho} \tag{4.4}$$

For a 5 Tesla-meter integrated solenoid field strength, the resulting spin resonance strength is about 0.02 at the injection energy and 0.003 at 250 GeV/c.

With longitudinal polarization at the collision point the longitudinal field rotates the polarization around its axis and thus changes the spin tune. The spin tune is changed by 0.03 to 0.003 at 25 GeV and 250 GeV, respectively, by a 5 T-m solenoid. This can be compensated by adjusting the direction of the axes around which the Snakes rotate the spin. By adjusting up to $\pm 5^\circ$ the spin tune can be adjusted for energies down to 25 GeV.

Chapter 5

Polarized Proton Acceleration in RHIC

5.1 Depolarizing Resonance Strengths

Without Siberian Snakes there are numerous depolarizing resonances in RHIC, both intrinsic and imperfection resonances. The strengths of the intrinsic resonances can be calculated quite accurately from the appropriate integral over the horizontal focusing fields. Fig. 5.1 shows the result for the RHIC lattice with

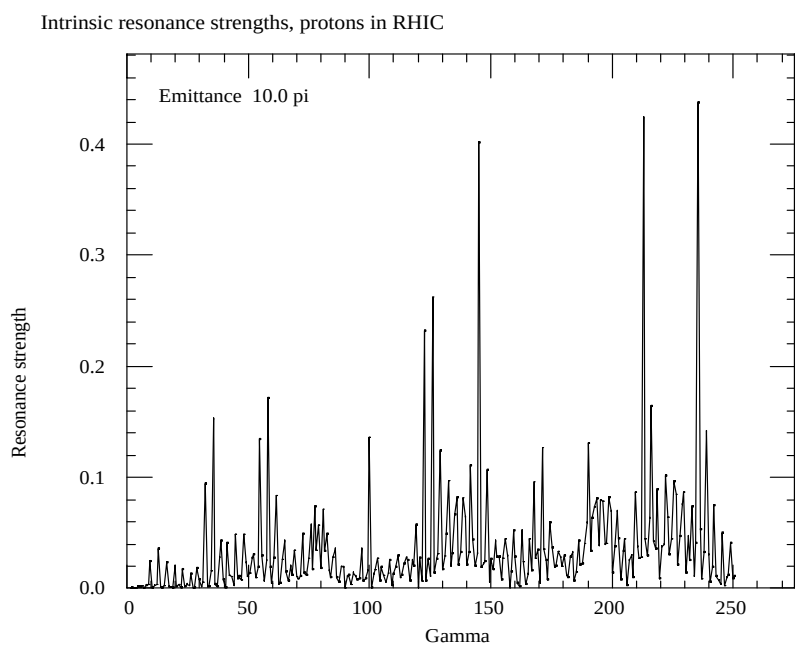

Figure 5.1: Strengths of the intrinsic depolarizing resonances in RHIC calculated for the RHIC lattice and for both $\beta^* = 10$ m and $\beta^* = 1$ m at all six intersection points. There is no noticeable difference of the calculated strengths for the two values of β^*.

$\beta^* = 10$ m at all intersections. A calculation with $\beta^* = 1$ m gave only a slightly different result. The calculation was performed for a particle with a normalized Courant-Snyder invariant of ε_0 =10 π mm mrad. For a different value of the invariant the strength scales according to

$$\epsilon = \epsilon_0 \sqrt{\frac{\varepsilon}{\varepsilon_0}} \tag{5.1}$$

where ϵ_0 is the resonance strength for the invariant ε_0.

Important intrinsic spin resonances are located at

$$G\gamma = kP \pm \nu_y \approx mPM \pm \nu_B, \tag{5.2}$$

where k and m are integers, P is the superperiodicity of the accelerator, M is the number of FODO cells per superperiod, and $2\pi\nu_B = 2\pi(\nu_y - 12)$ is the accumulated phase advance of all FODO cells, which contain bending dipoles. The locations of the 3 strongest intrinsic resonances are

$$G\gamma = 3 \times 81 + (\nu_y - 12), \qquad 5 \times 81 - (\nu_y - 12), \qquad 5 \times 81 + (\nu_y - 12) \tag{5.3}$$

$$E = \quad 136 \text{ GeV}, \qquad 203 \text{ GeV}, \qquad 221 \text{ GeV} \tag{5.4}$$

where 81 is the product of superperiodicity, 3, and the "effective" FODO cells per superperiod, 27, which includes dispersion suppressors. The strengths of all 3 strong resonances are less than 0.5.

Important imperfection resonances are located at an integer closest to strong intrinsic resonances. This is clearly shown in the top part of Fig. 5.2 which shows the calculated imperfection resonance strengths for an uncorrected closed orbit obtained from a random sample of magnet misalignments with a rms spread of ± 0.5 mm, dipole roll angles with a spread of ± 1 mrad, dipole field errors of $\pm 5 \times 10^{-4}$, and position monitor errors of ± 0.5 mm. After the closed orbit correction scheme MICADO[39] was applied, the vertical closed orbit was corrected to within 0.155 mm rms. The resonance strengths are greatly reduced as shown in the lower part for Fig. 5.2. The strengths of the imperfection resonances generally increase linearly with the beam energy and are bounded by

$$\epsilon_{imp} = 0.25 \, \frac{\gamma}{250} \, \sigma_y \tag{5.5}$$

where σ_y is the rms value of the residual closed orbit excursions in mm. The strength is smaller than 0.04 for all energies. Present alignment data from the RHIC CQS cold masses has shown monitor and quadrupole placement errors each well below 0.5 mm. The dipole roll angle is well below 0.5 mrad as well.[40]

5.2 Effectiveness of Siberian Snakes

With the installation of Siberian Snakes, which are local 180° spin rotators, the spin tune becomes 1/2, independent of the beam energy. Clearly the depolarizing resonance conditions cannot be met anymore as long as the fractional betatron tune $\Delta\nu_y \neq 1/2$ and therefore, in principle, no depolarization would occur.

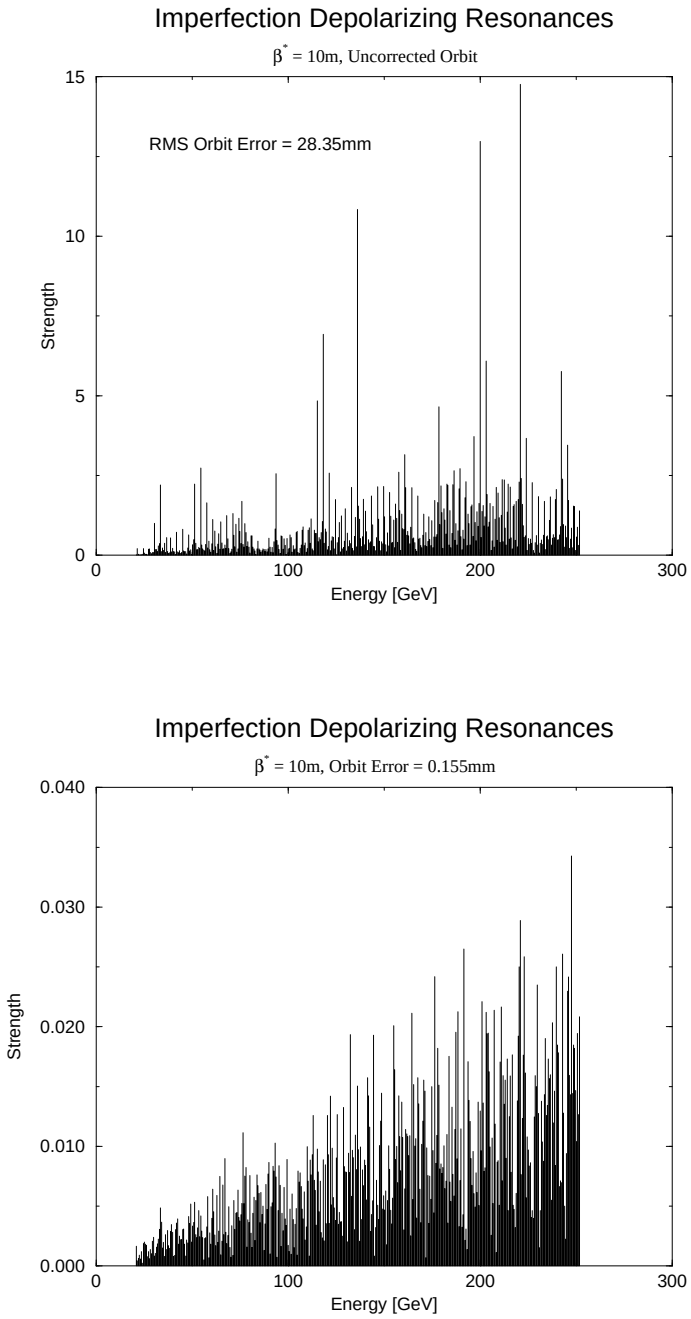

Figure 5.2: Strengths of the imperfection depolarizing resonances in RHIC calculated before and after the MICADO orbit correction scheme has been applied.

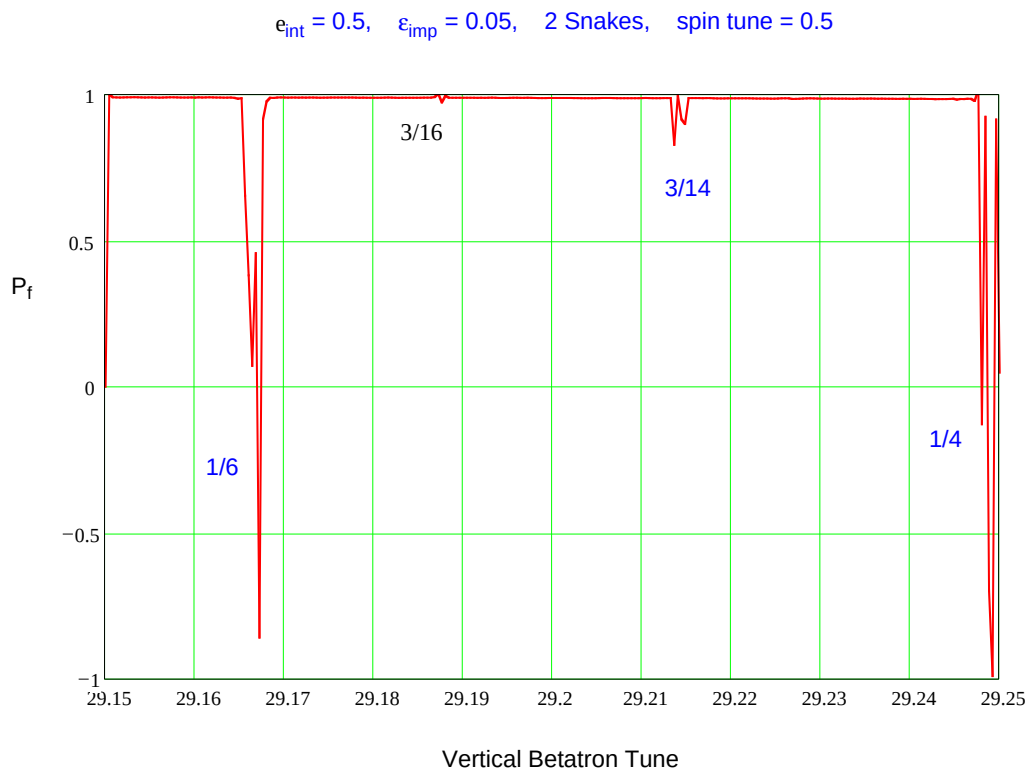

Figure 5.3: Vertical component of the polarization after acceleration through a strong intrinsic resonance and a moderate imperfection resonance shown as a function of the vertical betatron tune.

This is in fact true as long as the depolarizing resonances are not too strong. However, in the presence of strong resonances depolarization can occur from resonance conditions extended over more than just one turn. This leads to additional possible depolarizing resonance conditions:

$$\Delta\nu_y = \frac{\nu_{sp} \pm k}{n} \tag{5.6}$$

They are called Snake resonances[41] and n, the number of turns, is called the Snake resonance order. For two Snakes, as proposed here for RHIC, significant depolarization from Snake resonances only occurs for an intrinsic resonance strength of about 0.5 and even order Snake resonances require in addition an imperfection resonance strength of about 0.05. Fig. 5.3 shows the result of a simple 1-D spin tracking calculation through an energy region (using the RHIC acceleration rate) with an intrinsic resonance of strength 0.5 and an imperfection resonance of strength 0.05. There are clearly regions of the betatron tune that do not experience any depolarization. Since the betatron tunes of RHIC were chosen to be located between 1/6 and 1/5, the betatron tune could be placed between the Snake resonances $1/6 = 0.1667$ and $3/16 = 0.1875$. With the betatron tune including its spread located between 0.170 and 0.185, a 0.015 range, no depolarization will occur over the whole RHIC energy range up to the top energy. A more sophisticated

tracking calculation, using the spin tracking code *SPINK* to track through the strongest intrinsic resonance along a corrected RHIC orbit, is found in Section 5.8.

If the betatron tune spread is too large to fit into this range, some depolarization will be caused by the Snake resonance $\Delta\nu_y = 3/16$. Tracking calculations performed with an acceleration rate of $\dot{\gamma} = 3.9$/sec showed that a Gaussian beam with $\varepsilon_{N,95\%} = 20\ \pi$ mm mrad and with 10% of the beam overlapping the 3/16 Snake resonance less than 5% of the polarization is lost for each passage through one of the strong intrinsic resonances. The final polarization after passing all 3 strong resonances would then be at least 86% of the injected polarization. It is important to note that, unlike for electron beams, the betatron tune distribution within the proton beam is basically static and does not get mixed. This means that depolarization experienced by a part of the beam is confined to this part only and will not affect the whole beam. In other words, there is no diffusion of polarization.

5.3 Sextupole Depolarizing Resonances

Spin resonances arising from sextupoles are located at

$$\nu_{sp} = kP \pm \nu_x \pm \nu_y = mPM \pm (\nu_x - 6) \pm (\nu_y - 6) \tag{5.7}$$

with resonance strength given by,

$$\epsilon_K \approx \frac{1 + G\gamma}{8\pi}\sqrt{\frac{\varepsilon_x\varepsilon_y}{\pi^2}}\sqrt{\beta_x\beta_y}PM(|S_F| + |S_D|), \tag{5.8}$$

where S_F, S_D are respectively strengths of sextupoles located at the focusing and defocusing quadrupole locations. Because the emittance decreases with energy, the sextupole spin resonance strength is energy independent in hadron storage rings. For RHIC, the resonance strength is about 0.0003 at a normalized emittance of 20 π mm mrad. Such a sextupole driven resonance has been observed in the IUCF Cooler Ring.[42] However, because of their small spin resonance strength, depolarizing resonances due to sextupoles are not important as long as the betatron tunes are chosen to avoid the resonance condition, which for a spin tune of 1/2 is

$$\frac{1}{2} = kP \pm \nu_x \pm \nu_y. \tag{5.9}$$

The current working point for RHIC certainly avoids this condition.

5.4 Spin Tune Spread and Modulation

With snakes, the spin tune is independent of energy. Therefore the synchrotron motion does not give rise to spin tune spread. This has been verified indirectly in the snake experiment at the IUCF Cooler Ring, where one finds that there is no depolarization at the synchrotron side band for a 100% snake.[43] However the spin tune modulation may still arise from imperfect spin rotation in the snake, and imperfect orbital

angle between snakes. The errors in orbital angle may arise from survey error, closed orbit error, and/or betatron motion.

For an imperfection resonance strength $\epsilon = 0.05$ with two snakes, the perturbed spin tune shift is given by $\Delta\nu_{sp} = \pi|\epsilon|^2/4 = 0.002$. The error in the spin rotation angle of two snakes contributes also to the imperfection resonance strength. Assuming that the relative error of the integrated field strength of each snake magnet is 10^{-3}, the error in the spin rotation angle of a snake should be about $0.5°$. The effect of 2 snakes in the accelerator will give a resonance strength of the order $\epsilon_{imp}^{eq} \approx 0.004$, which is smaller than the imperfection resonances due to closed orbit errors.

The error $\Delta\theta$ in the orbital angle between the two snakes can give rise to a spin tune shift of $\Delta\nu_{sp} = G\gamma\Delta\theta/\pi$. Since the error in the orbital angle gives rise to spin tune shift and not a spin tune spread, one can compensate the effect by adjusting the spin rotation axes of the snakes. A survey error of about $\Delta\theta \approx 0.1$ mrad leads to a spin tune shift of 0.01 at the highest energy. For such a survey error, active compensation by adjusting the snake spin rotation axes is needed but is well within the tuning range of the Snake design.

The closed orbit can also cause an orbital angle error between snakes. Let us assume that the maximum closed orbit is about $\hat{a} \approx 6\sigma \approx 1.0$ mm. The angular deviation is of the order of $\Delta x'_{co} \approx \hat{a}/\sqrt{\beta\hat{\beta}}$, where $\hat{a}$ is the maximum orbit error and $\sqrt{\beta\hat{\beta}} \approx R/\nu$ is the average betatron amplitude function. The expected error is about $\Delta x'_{co} \approx 2 \times 10^{-5}$ for RHIC, which gives rise to a spin tune shift of 0.002.

Similarly a betatron oscillation can cause orbital angle modulations. The spin tune modulation is given by

$$\Delta\nu_{s,\beta} \approx \frac{1}{\pi} G\gamma \sqrt{\frac{\epsilon}{\beta}} = \frac{1}{\pi} G \sqrt{\frac{\gamma\epsilon_N}{\beta}}. \tag{5.10}$$

The resulting spin tune spread is about 0.007 for a beam with 20 π mm mrad normalized emittance at 250 GeV.

Combining all the possible sources, we expect that the total spin tune spread to be about 0.009 (imperfection resonance and betatron motion) and a correctable spin tune shift of 0.012 (Snake survey error and closed orbit error).

5.5 Betatron Tune Spreads and Modulations

In avoiding snake resonances up to the 13th order, the available tune space is about 0.015. With a spin tune spread of 0.009, the betatron tune needs to be controlled to better the 0.006. The tight requirements for the spin and betatron tune spread are only relevant while accelerating through the 3 strong intrinsic resonances when the beam-beam tune shift is negligible.

At the injection energy, the space charge tune spread can be as large as 0.02 for RHIC. However, the corresponding spin resonance strength at low energy is also about a factor of 3 smaller and therefore the available tune space is much larger.

5.6 Tuning of Siberian Snakes

The desired effect of the Siberian Snakes in RHIC is to effectively rotate the spin of a proton 180° about an axis in the horizontal plane. The amount of rotation, as well as the direction of the rotation axis, through a complete helical dipole magnet each depend upon the energy of the particle, and in fact are functions of the variable

$$\kappa \equiv \frac{1 + G\gamma}{B\rho} B_0 \tag{5.11}$$

where B_0 is the central field of the magnet. At high energies, where $G\gamma \gg 1$ then $\kappa \approx eGB_0/mc$ which is constant. At lower energy, the Snake magnets would have to be adjusted to perform "perfect" 180° rotations.

It would be desirable to run the Snakes at constant field, thus avoiding ramped superconducting magnets and power supplies. Simulations have shown that this indeed can be done.[44] For a "perfect" Snake, the fields in the inner and outer helical dipoles would need to change by approximately 3% in accelerating from 24 GeV to 250 GeV. Suppose the Snakes were tuned to operate at one of the strongest expected intrinsic resonances in RHIC, for instance the $G\gamma = 381.82$ resonance ($\gamma \approx 212$). At lower energies, the precession angle would deviate from 180° to approximately 178° at injection. Likewise, the direction of the precession axis would be off by about 3°. Spin tracking using *Spink* has shown that lower energy intrinsic resonances can be crossed effectively with the Snake set at high energy settings. Using lower energy settings when passing through higher energy resonances is less effective, though not disastrous. Thus, the operational procedure would be to optimize the Snakes for high energy resonances, and leave them at these settings throughout the acceleration cycle.

5.7 Spin Tracking Calculations

Spin behavior in RHIC in the presence of intrinsic and imperfection spin resonances has been studied with a numerical code, *Spink* [45], that reads the lattice of the machine created by the code *Mad* [46] and makes use of 6×6 orbit matrices and 3×3 spin matrices. The input to the code is a random distribution of polarized protons in the transverse and longitudinal phase spaces, within prescribed emittance contours. The helices of Siberian snakes and rotators are also represented by matrices that describe the orbit motion as well as the spin rotation. *Spink* includes acceleration and synchrotron oscillations.

To study imperfection resonances, one creates with *Mad* an output file containing a distorted closed orbit generated by a random distribution of position and field errors in the lattice elements.

The code has been extensively checked against standard theoretical results, where applicable. For example, in the case of an isolated resonance, *Spink* produces results in good agreement with the Froissart-Stora formula [6].

Among the spin tracking studies performed so far, notable are (i) acceleration scans through the full RHIC cycle, from $G\gamma = 50$ to 500, with snakes on (Fig. 5.4), that reproduce the known resonance spectrum

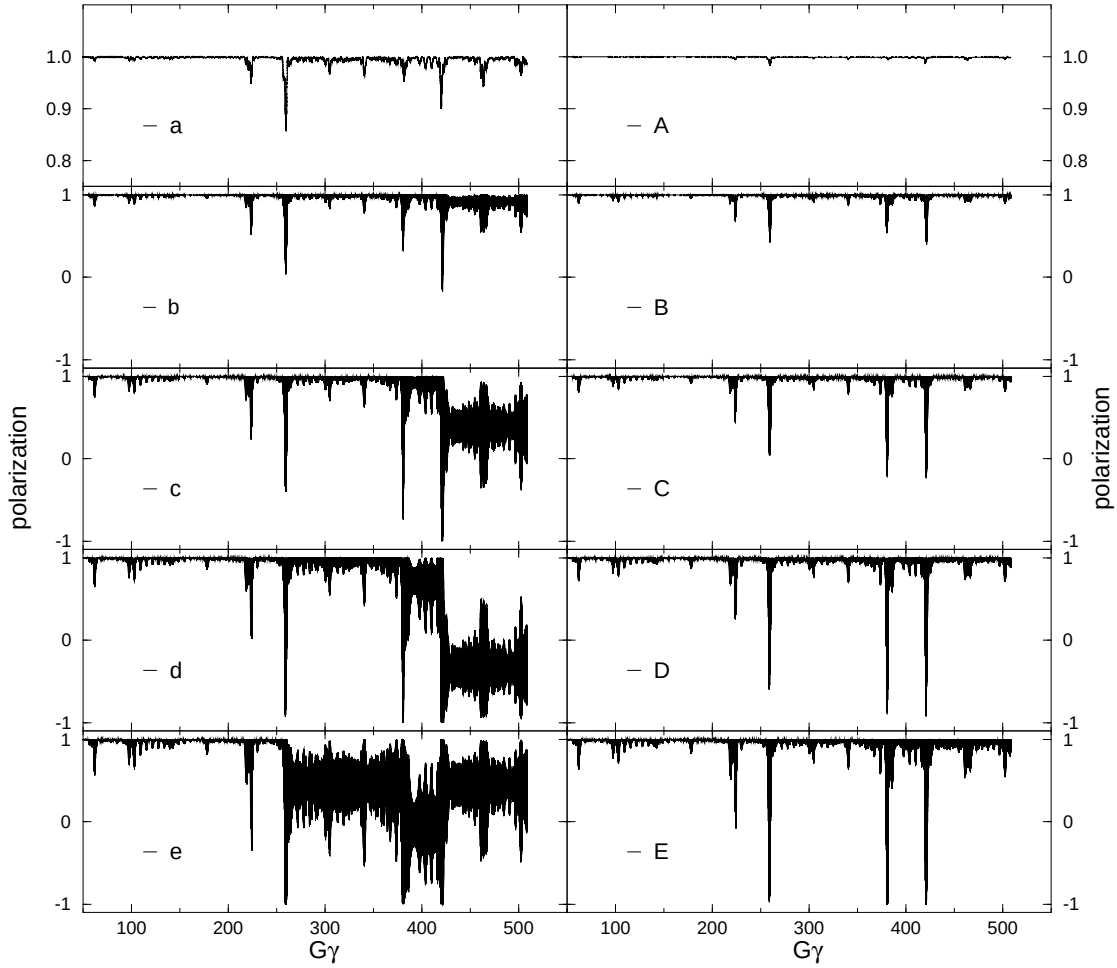

Figure 5.4: Tracking of single particle's spin in RHIC throughout the acceleration cycle. Snakes ON. Plots a - e are for vertical closed orbit deviations with rms 0.7 mm. Plots A - E are for vertical rms deviation of 0.2 mm. In each case, the horizontal orbit deviation is 0.7 mm rms. For plots a,A the particle's emittance is zero. For b,B, the particle's emittance is 5π mm-mrad. For c,C, 10π mm-mrad; d,D 15π mm-mrad; e,E, 20π mm-mrad. The RHIC tunes for this calculation are $\nu_x = 28.19$ and $\nu_y = 29.18$.

of Fig. 5.1; (ii) scan of a resonance line in storage mode (no acceleration) versus. vertical betatron tune, to find a good operating interval in tune space; (iii) test of a RF spin flipper, with rotating or oscillating magnetic field. A blow-up of a $G\gamma$ tracking interval, containing an intrinsic resonance, with snakes ON and snakes OFF is shown in Fig. 5.5.

The same code *Accsim* has also been extensively used to describe and interpret experimental results on polarized proton acceleration in the AGS [47].

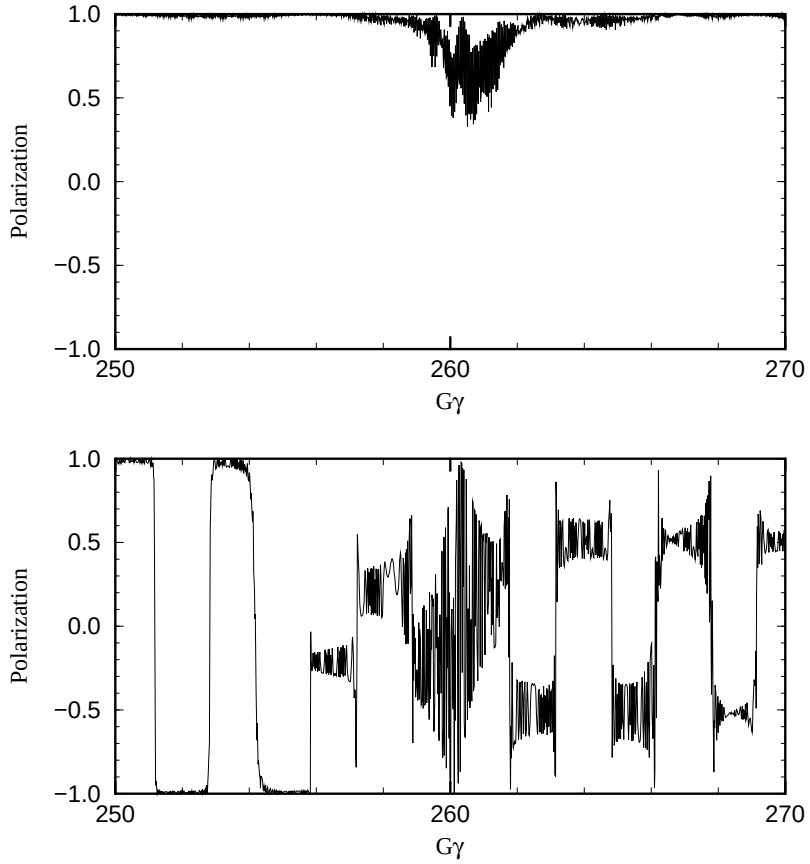

Figure 5.5: Tracking of spin through an isolated intrinsic resonance. Upper graph: snakes ON, lower graph: snakes OFF In this case, many other weak resonances show up). The tunes were again $\nu_x = 28.19$ and $\nu_y = 29.18$, and the single particle's emittance was 10π mm mrad.

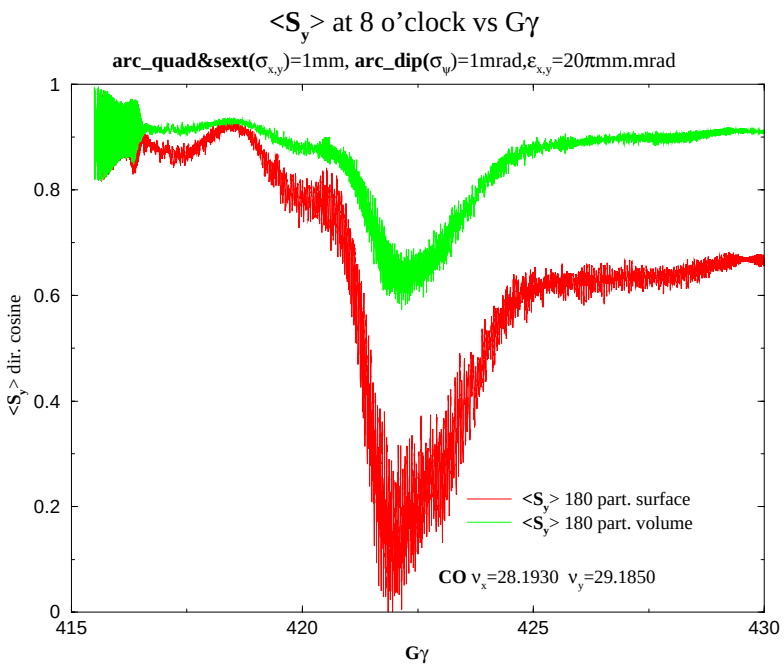

Figure 5.6: Tracking of spin through the intrinsic resonance $G\gamma = 422.18$. TOP: Average polarization of Gaussian beam (180 particles) with horizontal and vertical emittances (95%, normalized) of 20π mm-mr. BOTTOM: Average polarization of 180 particles, all with 20π emittance (horizontal and vertical).

5.8 Closed Orbit Correction Schemes

The *SPINK* computer code has been shown to reproduce the theoretically computed proton spin resonances, and their corresponding strength for an ideal RHIC machine (with magnetic elements not misaligned or having field errors). More recently, the *SPINK* code has been upgraded to allow for the study of spin resonances in the presence of random misalignments and/or field errors of magnetic elements. Two key issues can now be addressed with this version of the code. Firstly, tolerable field errors and misalignments of the magnetic elements of RHIC for which a 20π mm-mrad emittance proton beam will maintain its polarization can be explored through the various spin resonances during the acceleration cycle. Secondly, the most effective closed orbit correction scheme (MICADO, Harmonic Correction, 3-bump correction, for example) which minimizes the depolarization of the proton beam during resonance crossing can be explored.

As an example of the proton spin behavior while crossing the strongest spin resonance ($G\gamma = 422.18$) of RHIC is shown by the curves in Fig. 5.6. The top curve shows the average vertical spin component as a

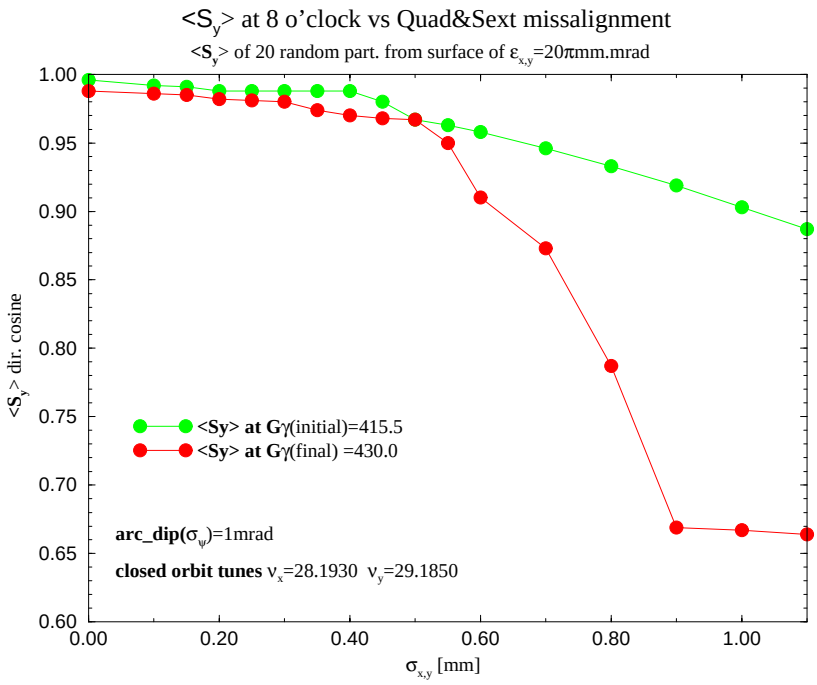

Figure 5.7: Resulting polarization through the strongest RHIC intrinsic resonance versus rms arc quadrupole and sextupole misalignment.

function of $G\gamma$ for 180 particles randomly selected from a Gaussian beam with normalized 95% emittances $\epsilon_x = \epsilon_y = 20\pi$ mm-mr). The bottom curve is the same average but the particles are randomly selected from the surface of a beam ellipsoid with $\epsilon_x = \epsilon_y = 20\pi$ mm-mr. Both curves correspond to a RHIC machine with the same arc-quadrupole and arc-sextupole misalignments of $\sigma_{x,y} = 1.0$ mm and arc-dipole rotational misalignments of $\sigma_\psi = 1$ mr. (Only errors within ± 2.5 times the chosen rms values were allowed in the simulations discussed here.) The MICADO algorithm was applied to correct the orbit prior to tracking the particle trajectories and spins through the resonance at the nominal RHIC acceleration rate. It is worth noticing that the average spin polarization shown by the top curve well after the resonance is almost the same as the average polarization well before the resonance. A closer look at the average polarization of particles selected from the surface of the 20π beam ellipsoid (lower curve) indicates that some of these particles do not track the stable spin direction during the resonance crossing. This polarization loss decreases with the rms error of the arc-quadrupole and sextupole displacements as shown in Fig. 5.7. In this figure, the initial (at $G\gamma = 415.5$) and final (at $G\gamma = 430.0$) average vertical spin components of 20 particles (randomly selected from the surface of 20π ellipsoid) are plotted as a function of the arc-

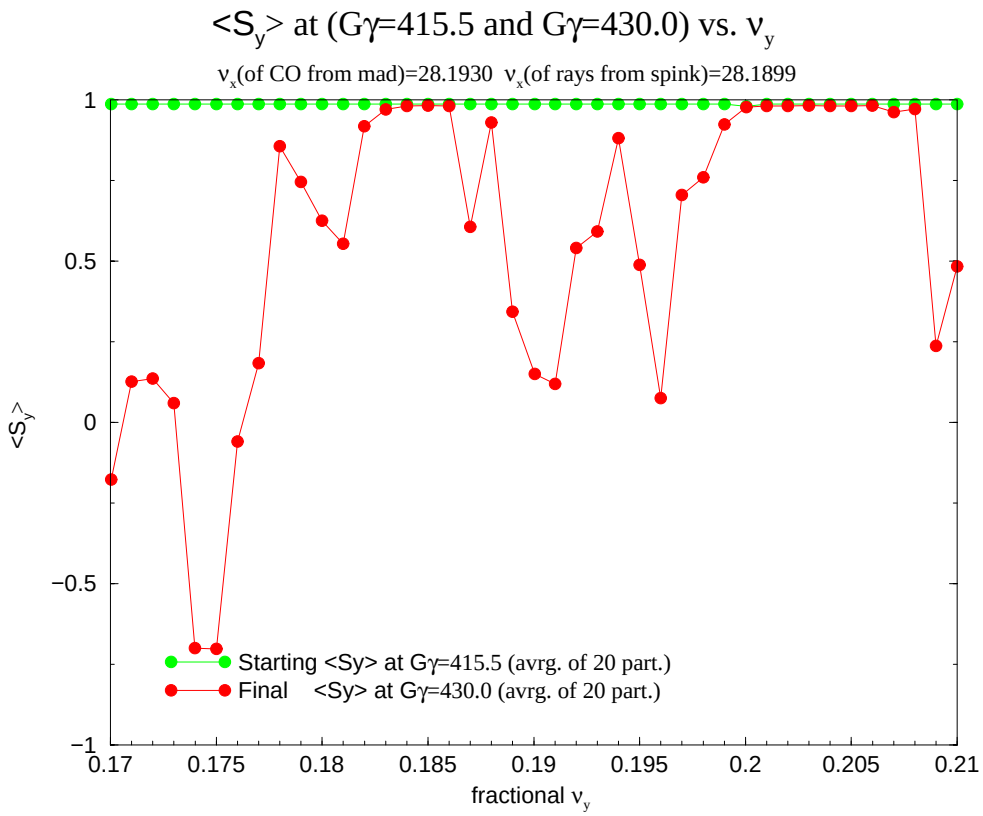

Figure 5.8: Resulting polarization through the strongest RHIC intrinsic resonance versus vertical betatron tune.

quadrupole and arc-sextupole misalignments. The arc-dipoles maintain the same random misalignment of $\sigma_\psi = 1$ mr. The maximum and minimum spin components of the distribution are also plotted. Care was taken to ensure that both the horizontal and vertical tunes of the closed orbit were the same for each calculation.

In all the calculations the MICADO formalism minimizes the closed orbit distortion at the location of the Beam Position Monitors (BPM's) which are located just next to the arc-sextupoles and are assumed to be free of errors. Similar calculations with appropriate BPM alignment errors produce the same results as in Figs. 5.6 and 5.7.

A study of the depolarization of a proton beam crossing the $G\gamma = 422.18$ RHIC spin resonance as a function of the vertical tune is shown in Fig. 5.8. In this figure, each point represents the ratio of the final average vertical spin component to the initial average for 20 particles randomly selected from the

surface of a beam ellipsoid with $\epsilon_x = \epsilon_y = 20\pi$ mm-mr. During these calculations the RHIC machine was misaligned with random arc-quadrupole and arc-sextupole rms displacements of $\sigma_{x,y} = 0.2$ mm, and arc-dipole rotations with standard deviation of σ_ψ =1 mr, and then corrected using MICADO. The horizontal tune of the closed orbit was kept at 28.1930 for each case. The first point corresponds to a vertical tune of 29.170 and the final point to 29.210 with the points in between differing by 0.001 units. There are clearly regions of betatron tune where depolarization does not occur.

Chapter 6

Accelerator Systems Hardware

The RHIC Spin Accelerator project requires 48 helical dipole magnets placed in special arrangements within the RHIC accelerator lattice to produce necessary manipulations of the particle spin. To maintain polarization while crossing resonances, "Siberian Snakes" are required, which will consist of 4 helical dipoles in succession, each with right-handed helical fields that begin and end with the dipole field vertical. At the two major interaction points, spin "Rotators" will also be installed, which consist of 4 helical dipoles in succession, each with dipole fields that begin and end horizontally; however, these magnets will have alternating helicity – right-handed, left-handed, right-handed, left-handed. The helicity is given in order as seen by the beam. Fig. 1.2 shows schematically the layout of these devices. The Rotators are located at a warm-to-cold interface within the Q3-Q4 straight section. Thus, the orientation of the cryogenic piping dictates that there be two additional categories of Rotator, namely one which follows the warm-to-cold transition with a right-handed helix, and one which follows the warm-to-cold transition with a left-handed helix. Figs. 6.1 and 6.2 show Snake assemblies located between quadrupoles Q7 and Q8 in the 3 o'clock and 9 o'clock sections or RHIC, while Figs. 6.3 and 6.4 sketch out the Rotator locations near the major detectors.

Using these figures, we can summarize basic magnet requirements as shown in Table 6.1, and requirements for the completed assemblies in Table 6.2. Parameters and tolerances for magnets are given in Table 6.3. A complete list of devices, including their Site Wide Names (used in the RHIC lattice database and other lists) and their characteristics, is provided In Tables 6.4 and 6.5.

Magnet Model	**Helicity**	**Field Orientation at Entrance and Exit**	**Quantity Required**
HSD1xx	Right-handed (forward)	Vertical	16
HSD2xx	Right-handed (reversed)	Vertical	16
HSD3xx	Right-handed (forward)	Horizontal	16
HSD4xx	Left-handed (reversed)	Horizontal	16

Table 6.1: Magnet quantities and types needed for Snakes and Rotators.

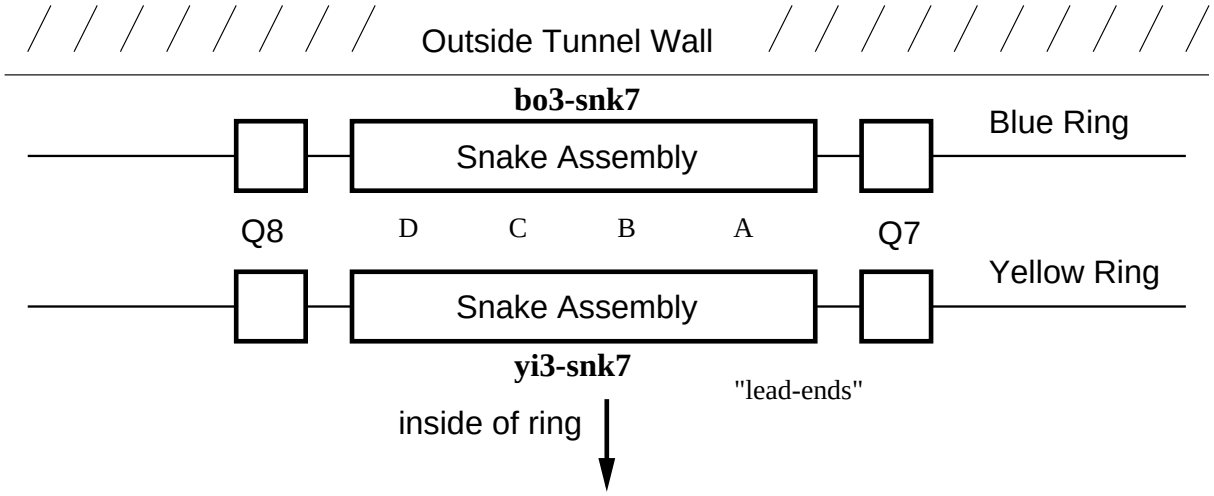

Figure 6.1: Schematic layout of Siberian Snake in the 3 o'clock Region of RHIC.

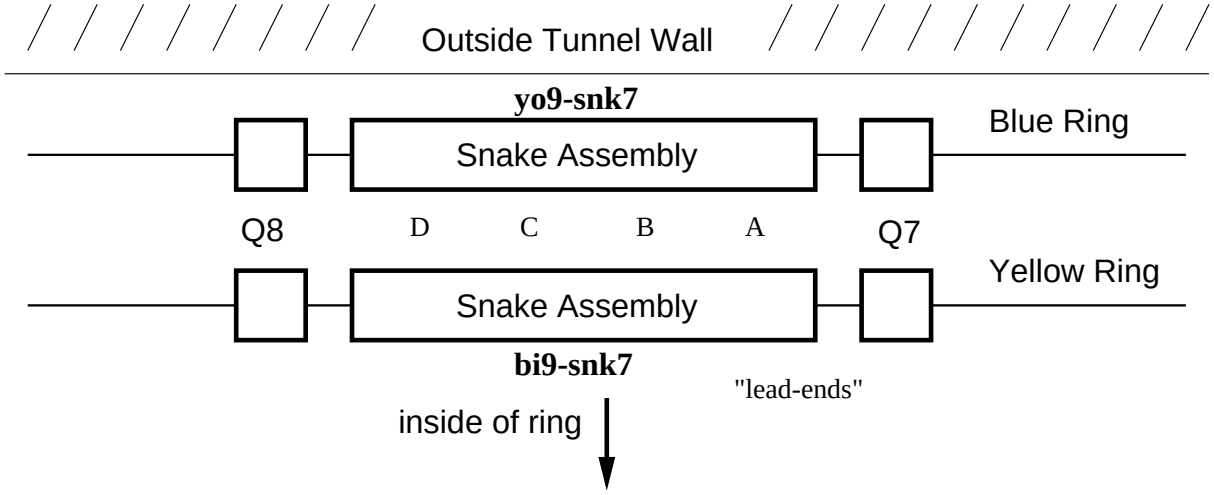

Figure 6.2: Schematic layout of Siberian Snake in the 9 o'clock Region of RHIC.

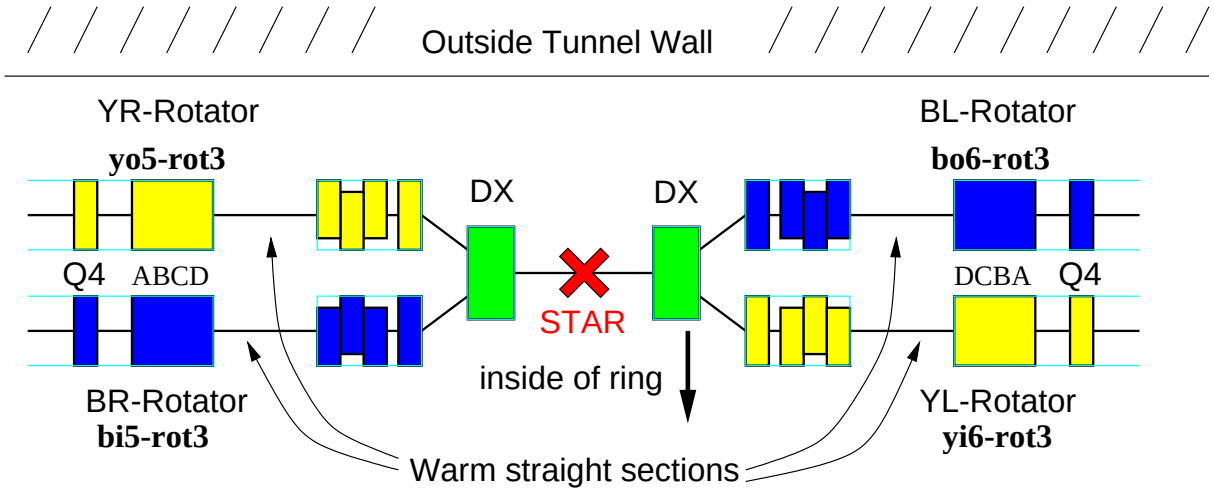

Figure 6.3: Schematic layout of Spin Rotators in the 6 o'clock Region of RHIC. The STAR detector is located at the interaction point. Further descriptions of the various Rotator units can be found in Table 6.2. The "lead-ends" are towards the Q4's.

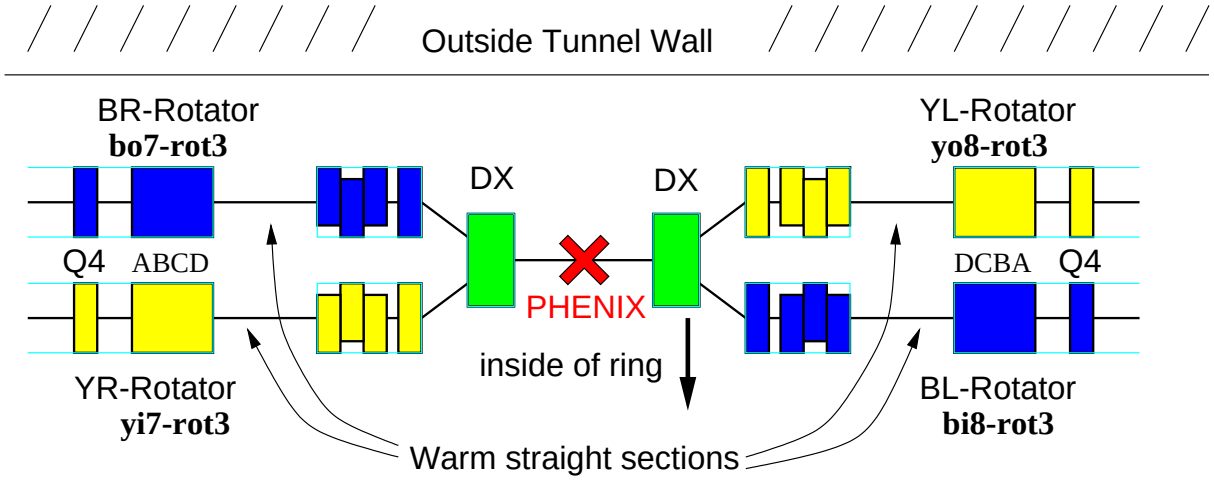

Figure 6.4: Schematic layout of Spin Rotators in the 8 o'clock Region of RHIC. The PHENIX detector is located at the interaction point. Further descriptions of the various Rotator units can be found in Table 6.2. The "lead-ends" are towards the Q4's.

Unit Type	**Field Orientation at Entrance/Exit**	**Helicity Pattern** (∗)	**Quantity Required**	**W-to-C transition** (∗∗)	**Unit Name**
Snake	Vertical	RH,RH,RH,RH	4	(none)	bo3-snk7 yi3-snk7 bi9-snk7 yo9-snk7
Rotator Sectors 5 & 7	Horizontal	RH,LH,RH,LH	4	RHS of unit	bi5-rot3 yo5-rot3 bo7-rot3 yi7-rot3
Rotator Sectors 6 & 8	Horizontal	RH,LH,RH,LH	4	LHS of unit	bo6-rot3 yi6-rot3 bi8-rot3 yo8-rot3

Table 6.2: Quantities and types of complete Snake and Rotator assemblies. (*)The helicity pattern is the pattern seen if standing at the inside wall of the tunnel, looking radially outward. (**)The Warm-to-Cold transition occurs either on the right-hand-side of the unit or on the left-hand-side, as seen if standing at the inside wall of the tunnel, looking radially outward.

6.1 Helical Dipole Magnets

Two methods for building helical magnet coils have been pursued. The first, called the "slotted" coil method, is based upon established BNL technology used to produce the RHIC sextupole magnets. It consists of a Kapton-wrapped, round cable placed into helical grooves that have been milled into a thick-walled aluminum cylinder. Thin sheets of epoxy-loaded fiberglass are placed between layers, and the entire assembly is cured at elevated temperature and with radial pressure to produce a compact, strong matrix. A first prototype coil using this technique was built and tested at BNL, and a full field, half length prototype magnet was completed late in 1996. Testing showed this to be a sound design, and it has been chosen as the design for production. A full length magnet is being built in 1998 using a newly developed automatic winding machine.

A second method for coil production was studied, called the "direct-wind" coil method. This method consists of the same type of cable as the slotted design applied by machine directly to the surface of a stainless steel tube in multiple layers. The surface of the Kapton-wrapped cable has a coat of adhesive. A very thin layer of epoxy-loaded fiberglass is placed between layers. The cable is applied in a helical pattern by a computer-controlled multiple-axis winding machine. A full field, half length prototype magnet using this direct-wind method was built by AML, Inc., in Palm Bay, FL and tested at BNL. Testing indicated the need for some design changes to increase the mechanical stability of the conductor, particularly in the ends of the magnet, in order to reach the required field level with sufficient operating margin.

Parameter		**Requirement**	**Tolerance (rms)**
Design Central Field	B_0	4 Tesla	
Operating Margin		15 %	
Design Magnetic Length	$\frac{1}{B_0}\int \lvert B\rvert dL$	240 cm	
Magnet Slot Length		260.65 cm	
Total Cryostat Assembly Length		1186.815 cm	
Integrated Field Strength	$\int \lvert B\rvert d\ell$	9.6 Tesla-meter	0.05 T-m
Integrated Field Components	$\int B_x d\ell,\ \int B_y d\ell$	0 Gauss-m	500 Gauss-m
Quadrupole Coefficient of main dipole field	b_1	0	2.0
Sextupole Coefficient of main dipole field	b_2	2.0	2.0
Octupole Coefficient of main dipole field	b_3	0	2.0
Decapole Coefficient of main dipole field	b_4	2.0	1.0
Skew Quadrupole Coefficient of main dipole field	a_1	0	2.0
Transverse Alignment(*)	$\Delta x, \Delta y$	0 mm	0.5 mm
Longitudinal Alignment(*)	Δz	0 mm	1.0 cm
Rotational Alignment(*)	$\Delta\phi$	0 mrad	1.0 mrad

Table 6.3: General parameters and tolerances for an individual Snake or Rotator magnet. Magnet multipole coefficients are in units of 10^{-4} at 3.1 cm reference radius. (*)Alignment is with respect to neighboring quadrupoles.

Site Wide Name	Magnet Name	Type	Inside/ Outside	Sector	Location Number	Handedness	Field Orientation at End
bo3-snk7							
bo3-hlx7.4	HSD206	Snk	o	3	7	R	V
bo3-hlx7.3	HSD107	Snk	o	3	7	R	V
bo3-hlx7.2	HSD202	Snk	o	3	7	R	V
bo3-hlx7.1	HSD108	Snk	o	3	7	R	V
bi5-rot3							
bi5-hlx3.4	HRDxxx	Rot	i	5	3	L	H
bi5-hlx3.3	HRExxx	Rot	i	5	3	R	H
bi5-hlx3.2	HRDxxx	Rot	i	5	3	L	H
bi5-hlx3.1	HRExxx	Rot	i	5	3	R	H
bo6-rot3							
bo6-hlx3.1	HRDxxx	Rot	o	6	3	R	H
bo6-hlx3.2	HRExxx	Rot	o	6	3	L	H
bo6-hlx3.3	HRDxxx	Rot	o	6	3	R	H
bo6-hlx3.4	HRExxx	Rot	o	6	3	L	H
bo7-rot3							
bo7-hlx3.4	HRDxxx	Rot	o	7	3	L	H
bo7-hlx3.3	HRExxx	Rot	o	7	3	R	H
bo7-hlx3.2	HRDxxx	Rot	o	7	3	L	H
bo7-hlx3.1	HRExxx	Rot	o	7	3	R	H
bi8-rot3							
bi8-hlx3.1	HRDxxx	Rot	i	8	3	R	H
bi8-hlx3.2	HRExxx	Rot	i	8	3	L	H
bi8-hlx3.3	HRDxxx	Rot	i	8	3	R	H
bi8-hlx3.4	HRExxx	Rot	i	8	3	L	H
bi9-snk7							
bi9-hlx7.4	HSD204	Snk	i	9	7	R	V
bi9-hlx7.3	HSD102	Snk	i	9	7	R	V
bi9-hlx7.2	HSD201	Snk	i	9	7	R	V
bi9-hlx7.1	HSD101	Snk	i	9	7	R	V

Table 6.4: RHIC Spin helical dipole magnet locations – **BLUE Ring**.

Site Wide Name	Magnet Name	Type	Inside/ Outside	Sector	Location Number	Handedness	Field Orientation at End
yi3-snk7							
yi3-hlx7.4	HSD208	Snk	i	3	7	R	V
yi3-hlx7.3	HSD106	Snk	i	3	7	R	V
yi3-hlx7.2	HSD207	Snk	i	3	7	R	V
yi3-hlx7.1	HSD109	Snk	i	3	7	R	V
yo5-rot3							
yo5-hlx3.4	HRExxx	Rot	o	5	3	R	H
yo5-hlx3.3	HRDxxx	Rot	o	5	3	L	H
yo5-hlx3.2	HRExxx	Rot	o	5	3	R	H
yo5-hlx3.1	HRDxxx	Rot	o	5	3	L	H
yi6-rot3							
yi6-hlx3.1	HRExxx	Rot	i	6	3	L	H
yi6-hlx3.2	HRDxxx	Rot	i	6	3	R	H
yi6-hlx3.3	HRExxx	Rot	i	6	3	L	H
yi6-hlx3.4	HRDxxx	Rot	i	6	3	R	H
yi7-rot3							
yi7-hlx3.4	HRExxx	Rot	i	7	3	R	H
yi7-hlx3.3	HRDxxx	Rot	i	7	3	L	H
yi7-hlx3.2	HRExxx	Rot	i	7	3	R	H
yi7-hlx3.1	HRDxxx	Rot	i	7	3	L	H
yo8-rot3							
yo8-hlx3.1	HRExxx	Rot	o	8	3	L	H
yo8-hlx3.2	HRDxxx	Rot	o	8	3	R	H
yo8-hlx3.3	HRExxx	Rot	o	8	3	L	H
yo8-hlx3.4	HRDxxx	Rot	o	8	3	R	H
yo9-snk7							
yo9-hlx7.4	HSD203	Snk	o	9	7	R	V
yo9-hlx7.3	HSD105	Snk	o	9	7	R	V
yo9-hlx7.2	HSD205	Snk	o	9	7	R	V
yo9-hlx7.1	HSD104	Snk	o	9	7	R	V

Table 6.5: RHIC Spin helical dipole magnet locations – **YELLOW Ring**.

A firm requirement for the helical magnet is that it reliably reach a field of 4 T at an operating temperature of 4.6 K. To ensure this capability for all the magnets that may be built, a margin of at least 15% is prudent. This margin allows for normal variations in component quality and size, quality of assembly, and variation in operational conditions.

The design of the slotted coil helical magnet follows principles that are derived from the operation of any superconducting magnet: that high forces be contained, that superconductor motion (particularly stick/slip motion) be minimized, that energy be safely extracted from the magnet at quench, that the ends of the magnet be restrained, that cooling be adequate for the operational conditions, etc. A number of concepts developed in the SSC and RHIC magnet programs are used, in particular the construction method used for the coils of the RHIC sextupole magnet. The basic structure of the helical coil uses a new concept: helical slots milled into thick-walled aluminum cylinders to give a $\cos\theta$ current distribution in a two-dimensional section when the slots are filled with conductor. In the initial models the cylinders are wound by hand. This could be done without a large tooling expense but would be too labor intensive for more than a few models. For production, a wiring machine that can place the cable directly into the slots has been built, and is shown in Fig. 6.5. This machine uses the ultrasonic wire bonding technique developed for the automatic wiring machines used to build the corrector coils for the RHIC Project. Two of these cylinders, concentric with one another, are used to give the required field of 4 T. A cross section of the design is shown in Fig. 6.6.

The Lorentz forces are contained initially by the strength of the aluminum cylinders and the compressive force exerted by the overwrap of Kevlar and fiberglass/epoxy around the circumference of each coil. At high field, the cylinders distort into an elliptical shape, growing outward on the midplane. After deflecting outward a fraction of a millimeter, they reach the stop provided by the next tube or the iron yoke. These small elastic motions are not expected to affect the quench performance of the magnet nor to distort the field in any significant way.

A number of features have been incorporated into the design that would ensure that the 4 T requirement is satisfied. In addition to including a sufficient number of turns, the design was optimized for a higher current (11/9) in all but the pole blocks of the outer coil — this is possible because the field is lower in these places and the superconductor is able to carry more current before reaching its quench point. In most two-layer superconducting magnet designs, the conductor is graded so that more turns can be placed in the second layer; here the expense of developing a second conductor was avoided by increasing the current requirement in the second layer. Also, the iron yoke was designed to be close to the coil to increase the field in the magnet aperture. However, these various design features lead to harmonics in the magnet that are unduly large if the magnet is powered with only one current. If only one current is sufficient to reach the required field, then a layer of turns can be removed from each of the inner coil and outer coil pole current blocks to give suitably small harmonics.

The quench performance and harmonic content (given in units: parts/10^4, at 31 mm radius) that were

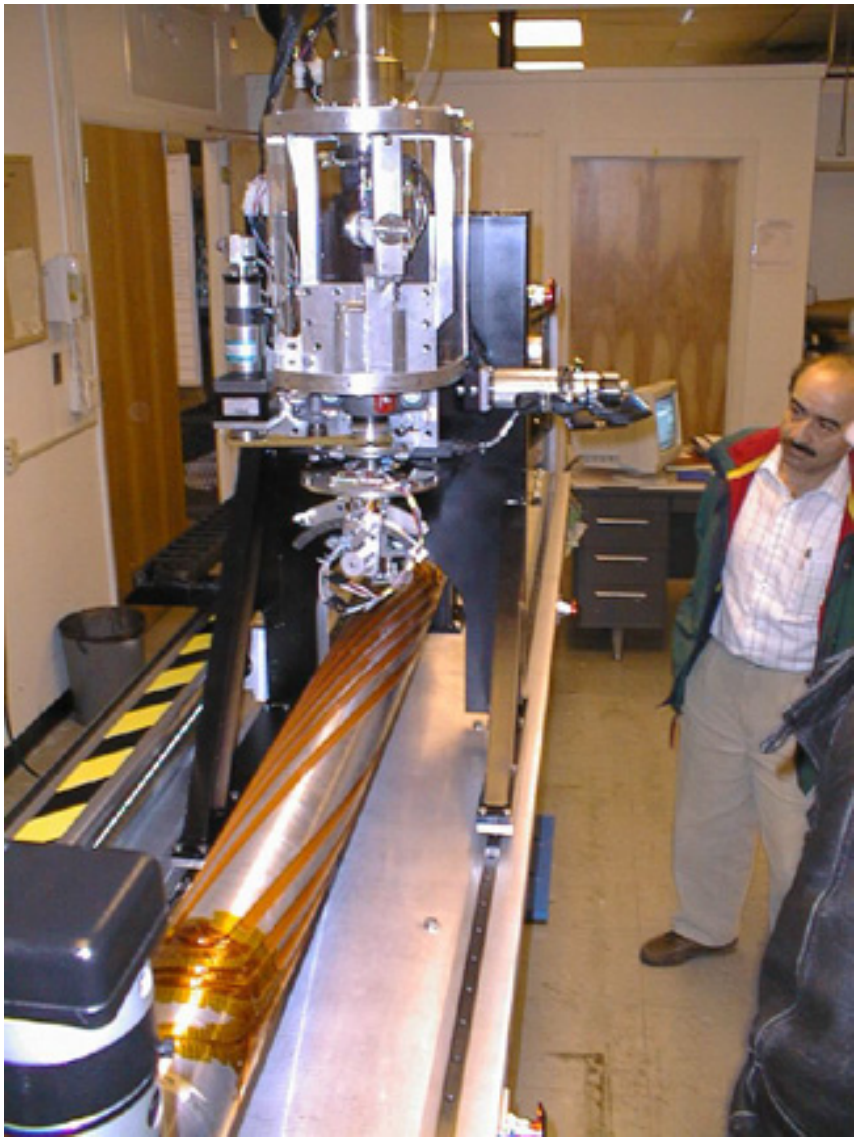

Figure 6.5: Automatic winding machine used for helical dipole coil production.

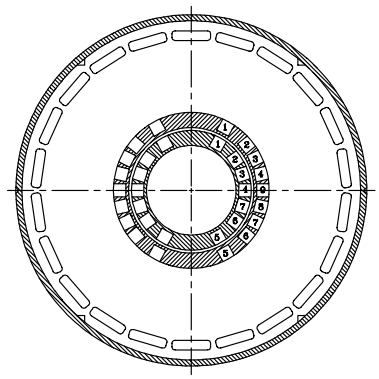

Figure 6.6: A cross section of the slotted coil helical magnet. The diameter of the iron yoke is 14 inches (355.6 mm).

expected in the prototype magnet as built when operated with just one current, and no holes in the iron yoke, are given in Tables 6.6 through 6.9. Fig. 6.7 shows the current versus. field characteristic for the prototype magnet, and for the superconductor that was used.

	B_{ss}, T @ 4.35 K	B_{ss}, T @ 4.6 K
Single current	5.0	4.55
Two currents	5.3	4.82

Table 6.6: Expected quench field (central field) in the prototype, slotted coil magnet, based on the short sample measurements made on the superconductor.

n	b_n (2-Dim)	b_n (Spiral)
2	-50.1	-2.9
4	5.4	0.73
6	0.4	-0.09
8	-7.5	0

Table 6.7: Expected values of the body harmonics for the one-current design. The "2-Dim" column gives the geometric harmonics assuming a straight coil, and the "Spiral" column gives the harmonics due to the spiral structure of the coils. Spiral harmonics have the x-dependence of the usual harmonic definition, but not the angular dependence — they have a dipole angular dependence.

n	b_n	a_n
2	0.2	164
4	0.04	19
6	0.04	3.8

Table 6.8: End harmonics in the lead plus return ends of the magnet, given in unit-meters.

I, A	B_0, T	δ(TF), %	b_2	b_4	b_6	b_8
50	0.68	-0.1	-50.3	5.4	0.4	-7.5
90	1.23	-0.2	-50.6	5.4	0.4	-7.4
200	2.71	-0.6	-52.9	5.3	0.4	-7.5
300	3.87	-5.6	-71.4	1.8	0.3	-7.7
400	4.81	-11.9	-82.7	2.4	0.4	-8.3
500	5.71	-16.3	-84.5	4.0	0.5	-8.9

Table 6.9: Single current dependence of the field and 2-dimensional harmonics in the prototype magnet due to the saturation of the iron yoke. A current of 314 A is estimated to give a central field of 4 T. The geometric harmonics given in Table 6.7, which are valid at any current, must be subtracted from these to obtain the harmonic changes due to saturation.

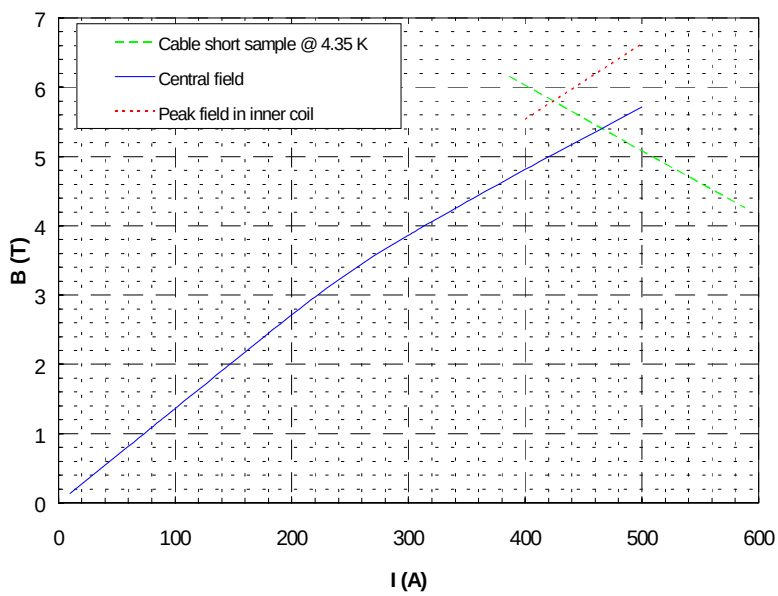

Figure 6.7: Field versus single current for the prototype slotted coil helical magnet. The central field is 4 T at 314 A. The peak field will determine the quench current, estimated at ∼420 A.

6.1.1 Conductor

The conductor is a cable that is made up of seven strands of the 0.330 mm superconductor wire developed for the RHIC corrector program. This cable, nearly 1 mm in diameter, carries 314 A to produce a 4 T field in the present design. Using a cable in the magnet is preferable to using a single wire: if a break in a wire of that cable should occur, the magnet would very likely still operate satisfactorily. In addition, a cable is more flexible than an equivalent wire and therefore eases the manufacturing of the coils. The required Kapton insulation is wrapped onto the cable in the cable-manufacturing operation. The superconductor parameters are given in Table 6.10.

	Parameter	**Units**	**Value**
Wire	Filament diameter	μm	10
	Filament spacing	μm	> 1
	Cu to non-Cu ratio		2.5:1
	Number of filaments		310±5
	Diameter, bare	mm	0.330
	Min I_c @ 5 T, 4.2 K	A	68
Cable	Number of Wires		7
	Cable style		6-around-1
	Diameter, bare	mm	0.991
	Diameter, insulated	mm	1.092
	Min I_c @ 5 T, 4.2 K	A	476

Table 6.10: Superconductor Parameters

The cable is made with a 6-around-1 geometry, which results in a cable in which the center wire is not transposed along the length of the cable. Eddy currents are generated in this wire when the magnet current is ramped. These eddy currents generate heat and have a measurable effect on quench performance above a ramp rate of 2 A/s. Since these magnets are not required to ramp in operation, this design feature is not detrimental to the required performance.

The Kapton wrap on the cable allows space for helium inside the wrap, in direct contact with the wires. This is a desirable feature for enhancing the stability of the superconductor. It is estimated that there are somewhat over 10% voids for helium inside the Kapton wrap.

6.1.2 Mechanical Construction

The cable is laid in an ordered pattern into the Kapton-lined slots milled into the aluminum cylinders. A piece of fiberglass cloth impregnated with a B-stage epoxy is placed between each layer of wires in the slots. The slots continue around the ends in a layout designed to minimize undesired harmonics. When all the turns have been wound into the slots, G10 fiberglass pusher plates 3.18 mm thick are placed on top the turns. Then the assembly is temporarily compressed with Kevlar that is wrapped onto the cylinder under

tension. The entire assembly is next placed into an oven for curing, thereby forming a series of current blocks around the cylinder in which each wire is firmly supported in a fiberglass/epoxy matrix. This design for supporting the cable turns is analogous to that developed for the wire turns in the RHIC sextupole magnet. After curing, any voids in the ends are filled with a mineral-loaded epoxy, a technique used in the SSC program for adding strength and rigidity to coil ends. A drawing of the inner coil is shown in Fig. 6.8.

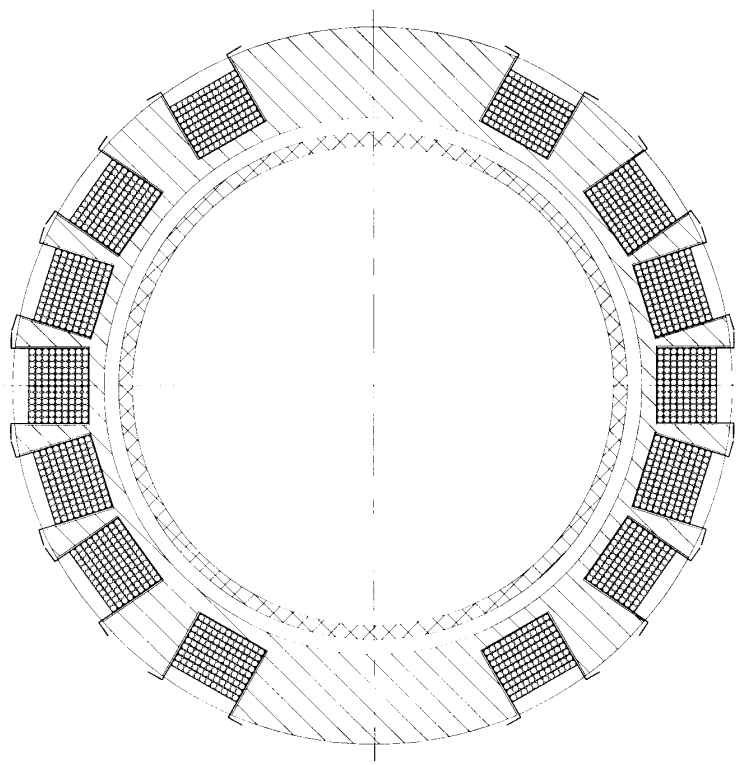

Figure 6.8: A detailed view of the inner coil of the slotted coil helical magnet. Each slot contains 108 turns of superconducting cable. The first layers of turns in the slots begin at a radius of 49.71 mm. The figure also shows the beam tube inside the coil.

The finished size of each cylinder is achieved by over-wrapping each cylinder with new Kevlar strand to compress the current blocks and then with bands of fiberglass/epoxy, followed by grinding to size after curing. The two cylinders are fitted into an iron yoke supported at one end by a plate that aligns the cylinders to a fixed position. Only a slight clearance exists between finished cylinders. The yoke is made up of one piece laminations having a ring of small holes on the outside perimeter. Tie-rods through these

holes in four places provide lateral restraint for the assembly (but are not required to restrain the axial Lorentz forces). Holes are also necessary for the passage of the helium coolant and the electrical buswork. The holes must be designed to minimize field irregularities as the field rotates along the length of the magnet. The inner radius of the yoke is increased in the ends to reduce the peak field on the conductor. A helium containment shell is welded in place around the yoke later when the entire unit is assembled into a complete helical Snake or Rotator.

This completed "storage unit" is now an independent, functional magnet, ready for installation into a cryostat (to be described later). The design at this point is similar to that of the arc CQS magnets for RHIC and the same concepts and methods from that construction are used as appropriate to complete the construction of the Snakes and Rotators. Mechanical parameters of the prototype storage unit are given in Table 6.11. Fig. 6.9 is a drawing of the length parameters that are relevant to an analysis of the fields in the prototype magnet.

	Parameter	Units	Value Inner, Outer
Coils	Number of cylinders		2
	Num of current blocks per cylinder		7,9
	Num of cable turns per layer		12, 12
	Num of layers per current block		9, 9
	Num of cable turns per block		108, 108
	Num of cable turns per cylinder		756, 972
	Total turns		1728
	Inner radius	mm	49.71, 68.63
	Outer radius	mm	60.02, 78.94
	Length, straight section	mm	1066.5
	Length including ends	mm	1371.6
	Effective length, low field	mm	1203.5
	Effective length, high field	mm	1222.7
	Helix, length	mm	1200
	Helix, rotation	deg	180
	Helix, pitch	deg/mm	0.15
Yoke	Inner radius in straight section	mm	84.46
	Outer radius	mm	177.80
	Length of lamination stack	mm	1029.1
	Inner radius at ends	mm	114.4
	Len of incr rad lam stack, ea end	mm	196.8
	Total length of lamination stack	mm	1422.8
Storage Unit	Weight	kg	795

Table 6.11: Selected mechanical parameters for the prototype slotted coil helical magnet. To optimize the design for single current operation, a layer of turns would be omitted from the pole-most current blocks in the inner and outer layers.

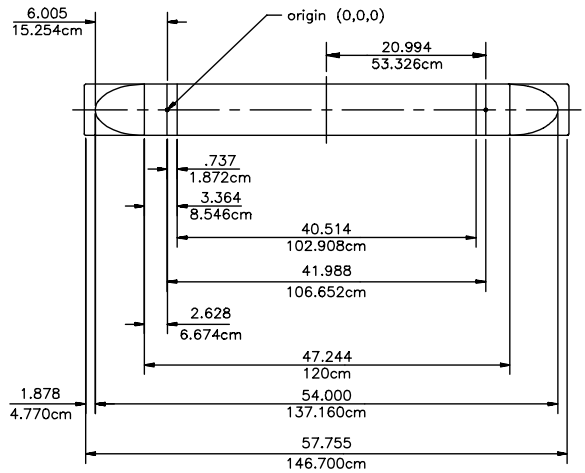

Figure 6.9: Length parameters of the prototype magnet. The inner and outer coils are the same in length. The ends begin at the point marked "origin." The effective length was intended to be 1200 mm, with a total spiral rotation of 180° over that distance; the effective length achieved will be measured when the prototype is tested.

6.1.3 Electrical Design

The 16 separate windings of the two coils are connected in series at the end of the storage unit. These interconnections generate a small but manageable amount of heat. It is planned to connect a low-resistance resistor across each of the windings for quench protection. Without these resistors, a quench in a winding could absorb too much of the stored energy of the magnet and possibly lead to conductor damage. Resistors will provide a current bypass as coil resistance builds up following a quench. Since these magnets do not have a ramp rate requirement, resistors are the best choice — diodes could be used if there were a need to ramp the magnets during operation. The stored energy of the prototype magnet at 4 T is 120 kJ (1.2 m effective length) and the inductance is 2.4 H.

6.1.4 Quench Performance of Early Model

A model coil of an earlier design was built and tested in 1995. It reached short sample after a few training quenches, though the exact value was somewhat ambiguous because a good calculation of the peak field in the conductor was not available. That coil had 630 turns of the same cable in a similar configuration of windings in a slotted aluminum tube. The self inductance of that coil was 250 mH. The coil was instrumented with voltage taps and spot heaters for starting quenches at several selected locations. In the standard $\int I^2 dt$ language, it was found that 60 Kiits gave a hot spot temperature at high current of between 200 to 300°C, depending on whether the quench occurred in the pole winding (lower temperature) or the

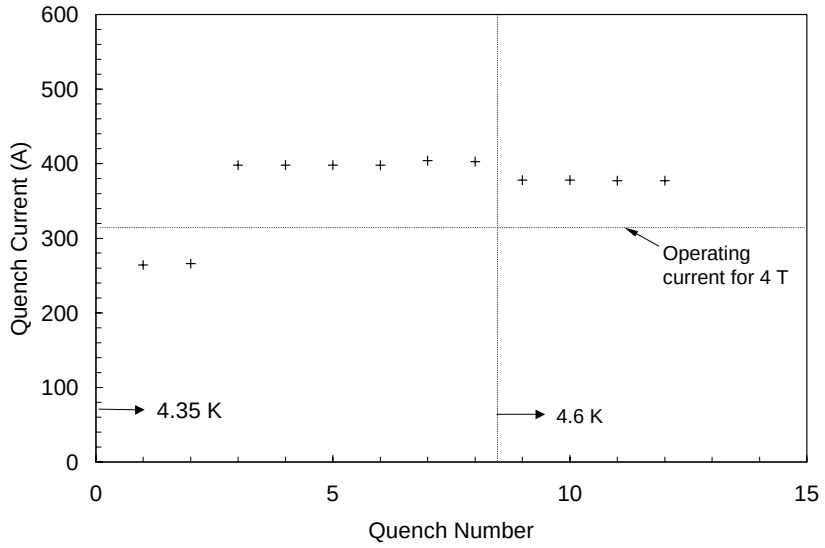

Figure 6.10: Quench performance of the prototype magnet. Following two low quenches, believed to have originated in the leads, the magnet quenched on a stable plateau following ramps at 0.1 A/s. Quenches 7 and 8 were slightly higher (6 A) because of the higher ramp rate used (1 A/s).

midplane winding. The maximum temperature recorded was for a midplane coil quench at 500 A: 490°C, 67 Kiits. These lower-than-calculated temperatures (calculations based on the amount of energy deposited in the windings) are the result of cooling from effects that are difficult to include in any calculation: effectiveness of cooling from helium, heat transfer to the surroundings, etc. Axial quench velocities in the windings were measured to be in the range 5-10 m/s for quenches with currents of 400-500 A. The short sample quench current for this coil was estimated at ∼620 A.

6.2 Prototype Measurements and Final Magnet Design

A half-length, full field magnet using the design discussed in the previous section was built and tested at BNL. The magnet was powered and quench tested, including thermocycle testing, and detailed field measurements were performed using both Hall probes and rotating coils. The results of the field measurements and corresponding 3-D magnetic field calculations of the design have been used to generate a final specification for the body field rotation angle and to improve upon the design of the ends of the magnet.

6.2.1 Quench Results

The half-length prototype magnet built at Brookhaven in 1996, labeled HRC001, was tested in February 1997. Its quench performance was excellent, as shown in Fig. 6.10. After two low quenches, believed to have originated in inadequately supported leads, the magnet quenched only at the level expected from prior

tests on the cable. A shift in dewar temperature, and a variation in ramp rate, both moved the quench current in the expected direction — independent confirmation that the magnet was operating at the short sample limit. The current for all four quenches at the nominal test temperature (4.35 K) and ramp rate (0.1 A/s) was 398 A (4.8 T). At 4.6 K, the magnet quenched at 378 A. Not shown are several quenches with a dual current configuration powering the coils that reached 5.0 T, indicating that the design is not mechanically limited.

Examination of the voltage traces from each of the current blocks in the magnet indicates that during a spontaneous quench of the type recorded here (quench current at or near the short sample limit of the magnet), a quench beginning in one block is quickly followed (typically within 100 msec) by quenching in all the other blocks, presumably because of strong magnetic coupling due to the high mutual inductances of the windings. The voltage traces have been studied and reproduced using the program MicroCap V to model the magnet. The fast spread of the quench throughout the magnet is desirable for reducing the energy dissipated at the quench point. However, the quench propagation speed at lower currents is not known and needs to be studied in a magnet that can be intentionally quenched via spot heaters in the coils.

6.2.2 Harmonic Measurements

A 9 inch long rotating coil and a Hall probe system were used to make magnetic measurements. The 9 inch long rotating coil is considered the more reliable measuring system and its results are taken as the measured field values. A correction factor is applied to the measured harmonic values to correct for the decreasing sensitivity to higher harmonics as the field rotates over the coil's 9 inch length. This sensitivity is 98% for the dipole field component, 87% for the sextupole, 66% for the decapole, etc. The corrected, measured field values are shown in Fig. 6.11 (dipole field transfer function, in T/kA) and in Fig. 6.12 through Fig. 6.15 (multipole moments). In these figures, a multipole "unit" is the field value from that multipole relative to the central dipole field measured at the reference radius of the rotating coil (31 mm) times 10^4.

Fig. 6.13 shows the measured sextupole field. At mid-range, the predicted value was -50.1 units for this harmonic, while the measured value is about -62 units. This is fairly good agreement considering the approximations involved in the calculations. The Hall probe system measured -76 units for the harmonic sextupole moment.

The Hall probe measurements have been more extensively analyzed and compared to a 3-D model calculation using TOSCA[48]. The z-dependence of the measurements and model results are in excellent agreement in the ends of the magnet, giving confidence that the calculation can be used to predict end behavior for changes in the design. The end design of the magnet is described in [49].

Because of the good quench performance of the prototype magnet, it is no longer necessary to consider operation with dual currents to achieve adequate field margin. However, single current operation gives

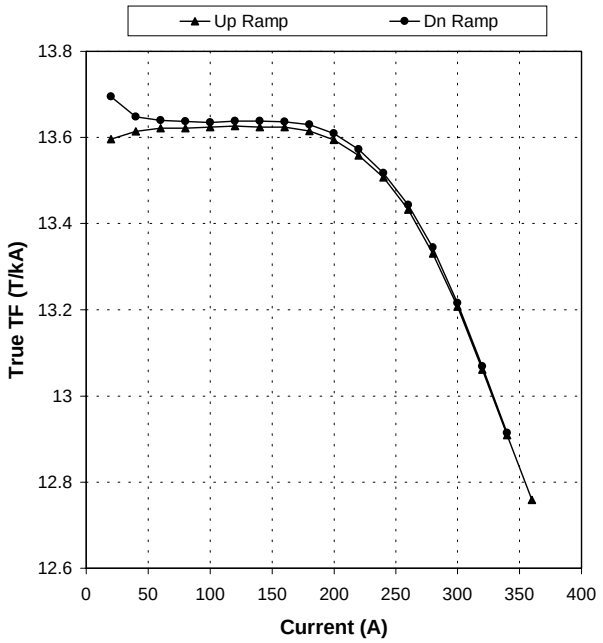

Figure 6.11: Measured dipole field transfer function for HRC001.

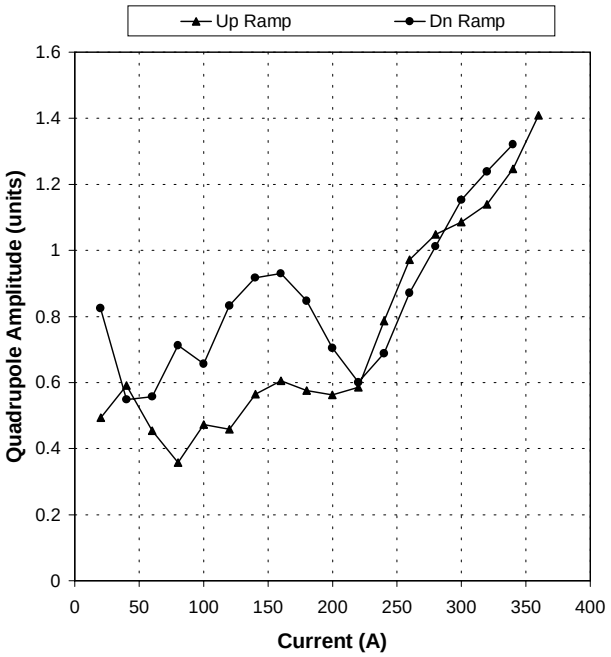

Figure 6.12: Measured quadrupole component for HRC001.

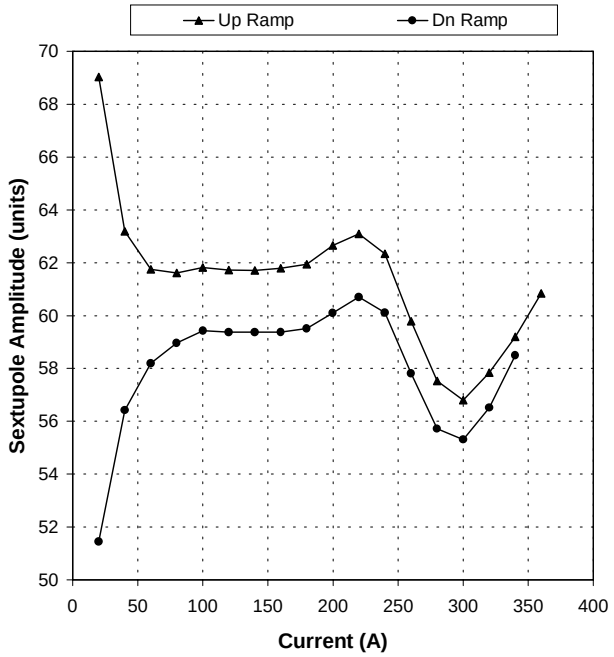

Figure 6.13: Measured sextupole component for HRC001.

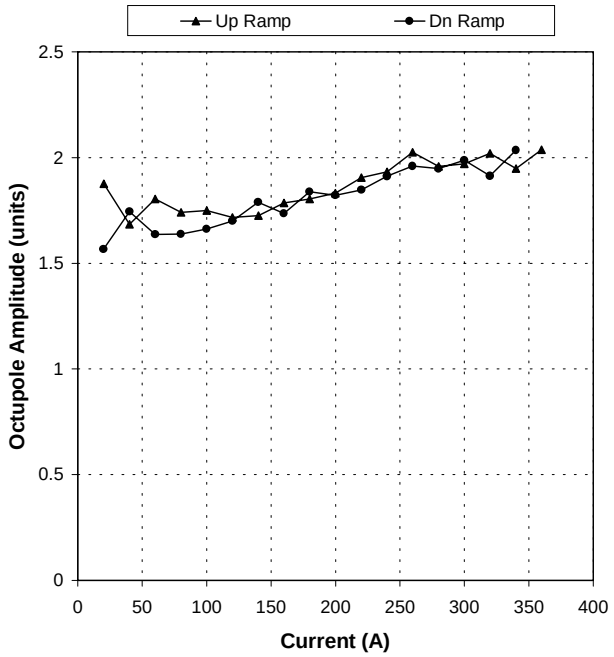

Figure 6.14: Measured octupole component for HRC001.

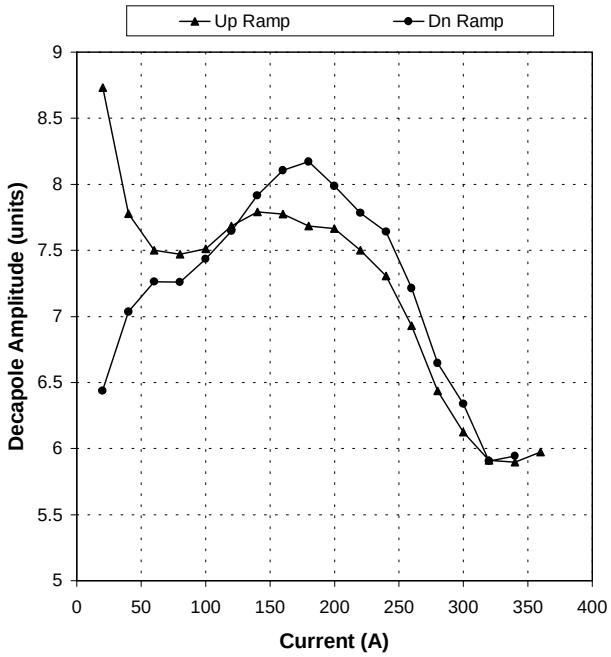

Figure 6.15: Measured decapole component for HRC001.

large harmonics. They could be reduced by relatively small changes in the current blocks. A suitable reduction is achieved by omitting a layer of turns in the pole-most blocks of both the inner and outer coils. With this change, the sextupole harmonic is predicted to be reduced to several units, with other harmonics also acceptably small. Future magnets will therefore be built with one less layer of turns (8 layers rather than 9) in the pole-most current blocks of both coils.

6.2.3 Rotation Angle

In the helical dipole magnets, the net deflection of the beam should be kept negligible.[1] In an oversimplified model, assuming a constant field strength over the magnetic length and zero field outside, the rotation angle of the field should be 360°. In practice, there are end regions where the field strength reduces gradually and the phase angle of the field changes very little. These end regions contribute to a net integrated dipole field, which must be compensated by an equal and opposite integrated dipole field from the body of the magnet. Due to lack of well defined boundaries, it is difficult to specify unambiguously a rotation angle. However, an effective rotation angle can be defined as the rotation angle in a simplified, "no ends" magnet, which will produce the same horizontal and vertical integrated dipole field as the real magnet. Thus, a magnet with zero integrated dipole field will be said to have an effective rotation angle of 360°.

If B_0 is the dipole field strength at the center of the magnet and θ_R is the effective rotation angle, then

[1]NOTE: This section contains excerpts from [35], where additional information may be found.

the integrated y and x components of the dipole field in the transverse direction are given by

$$\int_{-\infty}^{\infty} B_y(z)dz = \left(\frac{2B_0}{d\alpha/dz}\right)\cos\left(\alpha_0 + \frac{\theta_R}{2}\right)\sin\left(\frac{\theta_R}{2}\right), \tag{6.1}$$

$$\int_{-\infty}^{\infty} B_x(z)dz = \left(\frac{2B_0}{d\alpha/dz}\right)\sin\left(\alpha_0 + \frac{\theta_R}{2}\right)\sin\left(\frac{\theta_R}{2}\right), \tag{6.2}$$

where $(d\alpha/dz)$ is the rate of change of phase angle in the body of the magnet. The quantity $(\alpha_0 + \theta_R/2)$ depends upon the choice of reference frame, and can be interpreted as the phase angle at the center of the magnet, assuming symmetric ends. It is easy to see that for a rotation angle of 360° the integrals of both the components vanish. One can eliminate the dependence on the reference frame by examining the total amplitude of the integrated field, C_1, given by

$$C_1 = \left[\left(\int_{-\infty}^{\infty} B_y dz\right)^2 + \left(\int_{-\infty}^{\infty} B_x dz\right)^2\right]^{1/2} = \left(\frac{2B_0}{d\alpha/dz}\right)\sin\left(\frac{\theta_R}{2}\right). \tag{6.3}$$

Using Eq. 6.3, one can estimate the effective rotation angle from the integrated dipole amplitude. It is clear from Eq. 6.3 that the integrated field is zero for a 360° rotation, and has a maximum for 180°. A consequence of this fact is that the integrated field is least sensitive to the rotation angle in a magnet with 180° rotation. A small error in the measurement of the integral field will result in a rather large error in estimating the effective rotation angle for such a magnet.

Using a rotating system consisting of two Hall probes, axial scans of the field in HRC001 were carried out at two currents — 105 A and 220 A. These currents correspond to approximately 1.43 and 3.0 Tesla respectively in the body of the magnet. For various reasons the data at 220 A are much more reliable for the purpose of estimating the integral field, and hence the effective rotation angle. Fig. 6.16 shows the measured dipole field amplitude and the phase angle as a function of axial position at 220 A, measured by the Hall probe-2, located at a radius of 3.56 cm. The Z-positions are from the reference point of the probe transporter, which is at an arbitrary position outside the magnet. Also, the Z-positions increase from the lead end to the non-lead end of the magnet, which is inconsistent with a right-handed coordinate system. The phase angle is in a reference frame decided by the orientation of the probe. This orientation is also arbitrary with respect to the yoke. The dipole amplitude and phase are obtained from a Fourier analysis of the measured radial component of the field at 64 angular positions. The measured data have been shown to agree very well with a three dimensional numerical calculation using TOSCA[34].

In principle, one could calculate the integral of the field components, B_x and B_y, from the data shown in Fig. 6.16. These integrated values can be used to obtain the total integrated dipole amplitude, C_1, and the effective rotation angle, θ_R. Such a calculation yields a value of the integrated dipole amplitude of 2.286 T-m at a central field of 3.0083 T. The effective rotation angle calculated from this integrated field (see Eq. 6.3) is 173.8°. However, as pointed out above, the amplitude of the integrated field is not very sensitive to the effective rotation angle in a half-length magnet. Even small measurement errors could lead to very large error in the value of the effective rotation angle. For example, the integral dipole field

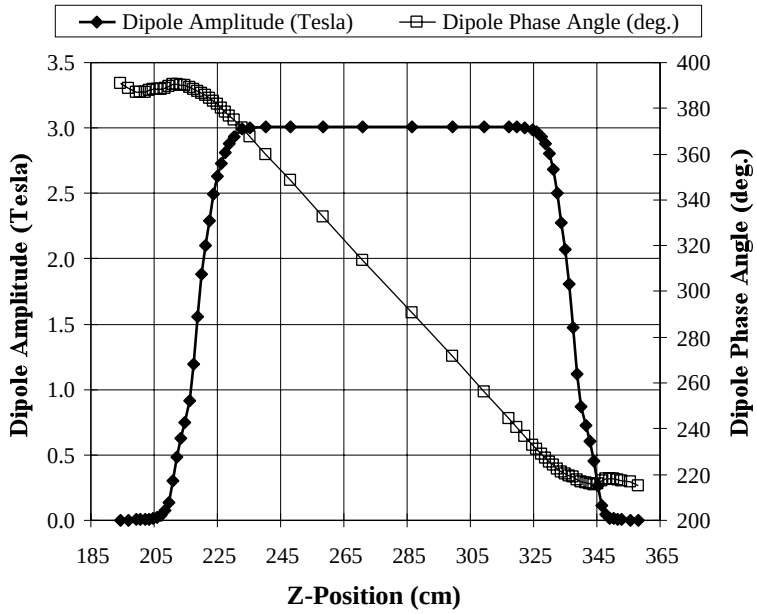

Figure 6.16: Measured dipole amplitude and phase at 220 A in HRC001.

expected for a 180° effective rotation angle instead of 173.8° is 2.289 T-m, which differs from the measured value by only 0.13%, well within the experimental errors.

A reasonable simulation of the actual full length magnet can be made by assuming that the ends of the magnet are identical to those in HRC001, but the straight section is longer by one half-period. The "experimental" data in such a full length magnet can be generated by dividing the actual data in HRC001 into two halves at any location in the body of the magnet, and then sandwiching a straight section with a uniform rate of twist and a constant dipole field amplitude between the two halves. The field amplitude of this extra section is given by the average amplitude over the central region of the prototype HRC001. The phase angle at various points in this region can be calculated from the nearest data point in HRC001 and the known rate of twist. With this extra half length sandwiched between the two halves of the measured data, the phase angles of the second half will be shifted by 180° from the actually measured values and the Z-positions will change by half a wavelength. In this way, one can generate a very good approximation to the experimental data that would have been recorded, had the magnet been of a full length.

Fig. 6.17 shows the simulated data at 220 A for a full length magnet, generated by a procedure as described above. In order to be consistent with the reference frame used in numerical simulations, the origin in the experimental data has been shifted to bring the magnet center at $Z = 0$. Also, the reference frame is rotated to make the integrated B_x component zero. Furthermore, the $Z-$axis is inverted to make the coordinate system right-handed. The two transverse components of the dipole field are shown in

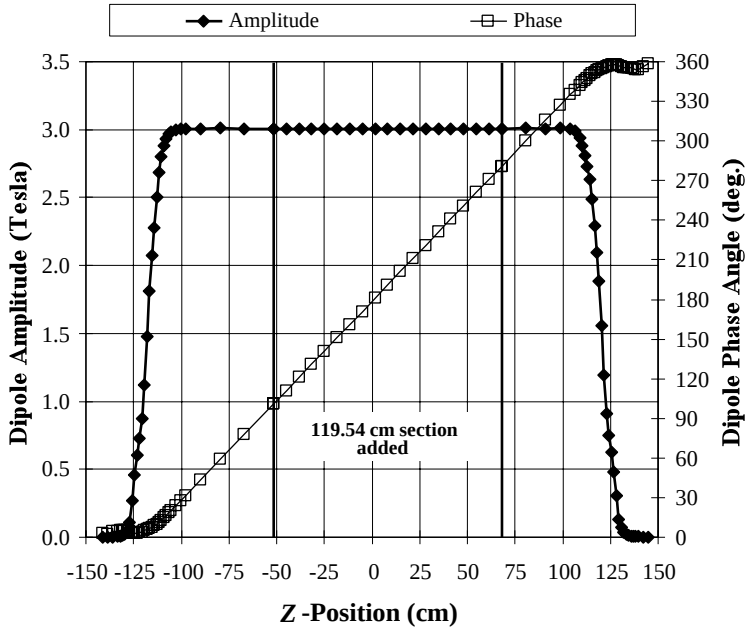

Figure 6.17: Simulated data at 220 A in a full length helical magnet. The Z-axis is inverted from the raw data in Fig. 6.16 to obtain a right handed coordinate system.

Fig. 6.18. It is seen that with this choice of reference frame, the dipole field is in the positive y-direction near the ends of the magnet ($\alpha_0 \approx 0$ in Eqs. 6.1 and 6.2). The length of the section added is 1.2 m at room temperature, or 1.1954 m at liquid helium temperature. A twist rate of 1.5057 degrees/cm gives a rotation of exactly 180° over this extra section.

The values of $\int B_y(z)dz$ and $\int B_y(z)dz$ are obtained by numerically integrating the data in Fig. 6.18. This integration was carried out in three separate regions — the two "end" regions made up of two halves of the actually measured data, and the "central" region consisting of the additional half length in the middle of the magnet. The integrated field in the "central" region can also be calculated analytically using Eqs. 6.1 and 6.2. The analytical result was used to check the accuracy of the numerical integration procedure. Since the measured data points are at non-uniform Z-intervals, it was convenient to use a piecewise linear approximation to the actual curve. Since the final result of integration is expected to be a small number, even small errors in integration can lead to large errors. Based on a comparison with the analytical value in the central region, a linear approximation between data points was found to be unsatisfactory. A 3-point integration formula for arbitrary increments was developed for a more precise integration. If the three distinct points are given by x_1, x_2, and x_3, then the integration of any function from x_1 to x_3 can be shown to be given by

$$\int_{x_1}^{x_3} f(x)dx \approx a_1 f(x_1) + a_2 f(x_2) + a_3 f(x_3), \tag{6.4}$$

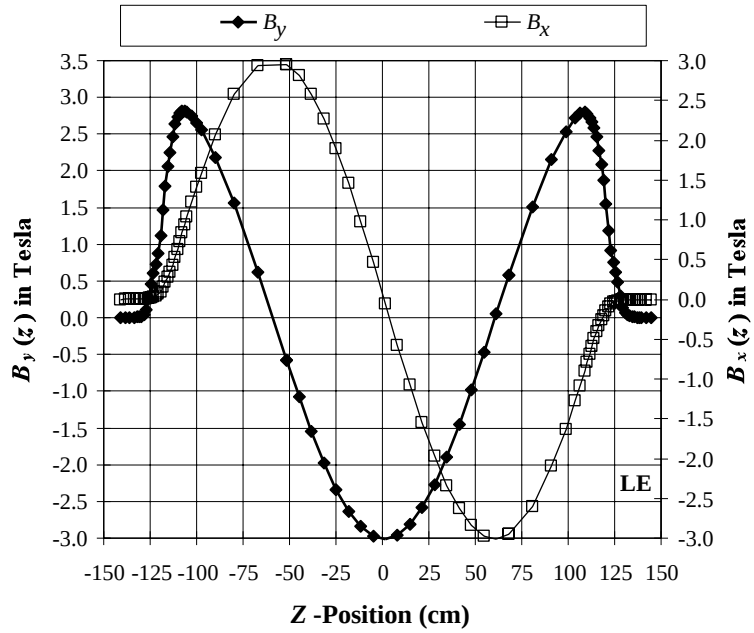

Figure 6.18: Simulated data for $B_x(z)$ and $B_y(z)$ at 220 A in a full length helical magnet.

where

$$a_1 = \frac{(x_3 - x_1)}{6(x_2 - x_1)}[2(x_2 - x_1) - (x_3 - x_2)], \tag{6.5}$$

$$a_2 = \frac{(x_3 - x_1)^3}{6(x_2 - x_1)(x_3 - x_2)}, \tag{6.6}$$

$$a_3 = \frac{(x_3 - x_1)}{6(x_3 - x_2)}[2(x_3 - x_2) - (x_2 - x_1)]. \tag{6.7}$$

Eq. 6.4 gives an exact integration for functions up to second order in x. This integration formula gave the correct integral field for the central region. The end regions were integrated numerically using Eq. 6.4, but the analytical value was used for the central region, even though a numerical integration also gave the same result.

The results of the calculations are summarized in Table 6.12. The integration of simulated data in

Current (A)	**Hall Probe**	**Central Field** B_0 (T)	$\int B_y(z)dz$ **Gauss-m**	$\int B_x(z)dz$ **Gauss-m**	**Integrated dipole Ampl.** C_1 (Gauss-m)	**Rotation Angle** θ_R (deg.)
220	1	3.007	208.06	0.00	208.06	361.04
220	2	3.008	193.96	0.00	193.96	360.97

Table 6.12: Summary of rotation angles calculated for a full length magnet.

Fig. 6.18, as described above, gave an integrated dipole field, C_1, of 193.96 Gauss-m at a central field

of 3 T, corresponding to an effective rotation angle of $\theta_R = 360.97°$. It should be recalled that the integrated x-component is made zero by an arbitrary choice of reference frame. It is interesting to estimate the uncertainty in the calculated value of the effective rotation angle. Assuming a $\pm 0.2\%$ error in the calculation of the integrated field strength (base on the 0.13% discrepancy seen in the half length magnet data), the maximum error in the effective rotation angle is only $\pm 0.002°$. Even if a rather large error of $\pm 10\%$ in the integral field is assumed, the error in the calculation of the effective rotation angle is only $\pm 0.10°$. This is in sharp contrast with the case of the half-length magnet where even a 0.1% uncertainty leads to an error of several degrees.

Even though the data at 105 A had problems, an analysis was nevertheless performed to obtain the effective rotation angle at this current as well. A value of 360.98° was obtained with the data from either of the two probes. These values are consistent with those obtained at 220 A.

A full three dimensional analysis of the field in the helical magnet has been carried out to optimize the rotation angle[50]. This analysis suggests that the effective rotation angle of the full length magnet with the present end design should be about 360.75°, which is close to the 360.97° estimated above from the simulated data. The value of 194 Gauss-m for the integral field at a central field of 3.0 T is well within the tolerance of 500 Gauss-m at 4.0 T[33]. Based upon the present analysis, no change in the length of the production magnets is necessary.

6.2.4 Modification of End Design

The ends of the magnet HRC001 had several current blocks where the wall between adjacent blocks was rather narrow. To ease problems in construction with these narrow walls, they will be widened in subsequent models. This design change has been modeled and the preliminary analysis shows that the effective rotation angle in the as-built full length magnet will be smaller by at least 0.25°[34]. This should significantly reduce the value of the integrated dipole field from the present estimate.

6.3 Snake and Rotator Assemblies

Each Snake and Rotator will be comprised of four superconducting helical dipole magnets making up a single cryostat assembly. With the Snake assemblies being located in the cold straight section between RHIC quadrupoles Q7 and Q8 (see Section 6.1), the cryostat for this assembly will be a modified "DU7" cryostat nominally used at these locations. The length of this cryostat (with the new nomenclature "DU3") is 11.876 m, slightly longer than a typical RHIC dipole magnet. This is due to the fact that the Q7 quadrupole, in the transition region between the arc and interaction region lattices, is slightly shorter than typical RHIC arc quadrupoles. Though the Rotators are located at the ends of a 30 m warm straight section, these assemblies will also reside in DU3 cryostats in order to make more efficient use of cryostat hardware. A sketch of the cold mass assembly within a DU3 cryostat is shown in Fig. 6.19 for the Snakes

and Fig. 6.20 for the Spin Rotators. Specifications for magnet placement and alignment were provided in Table 6.3.

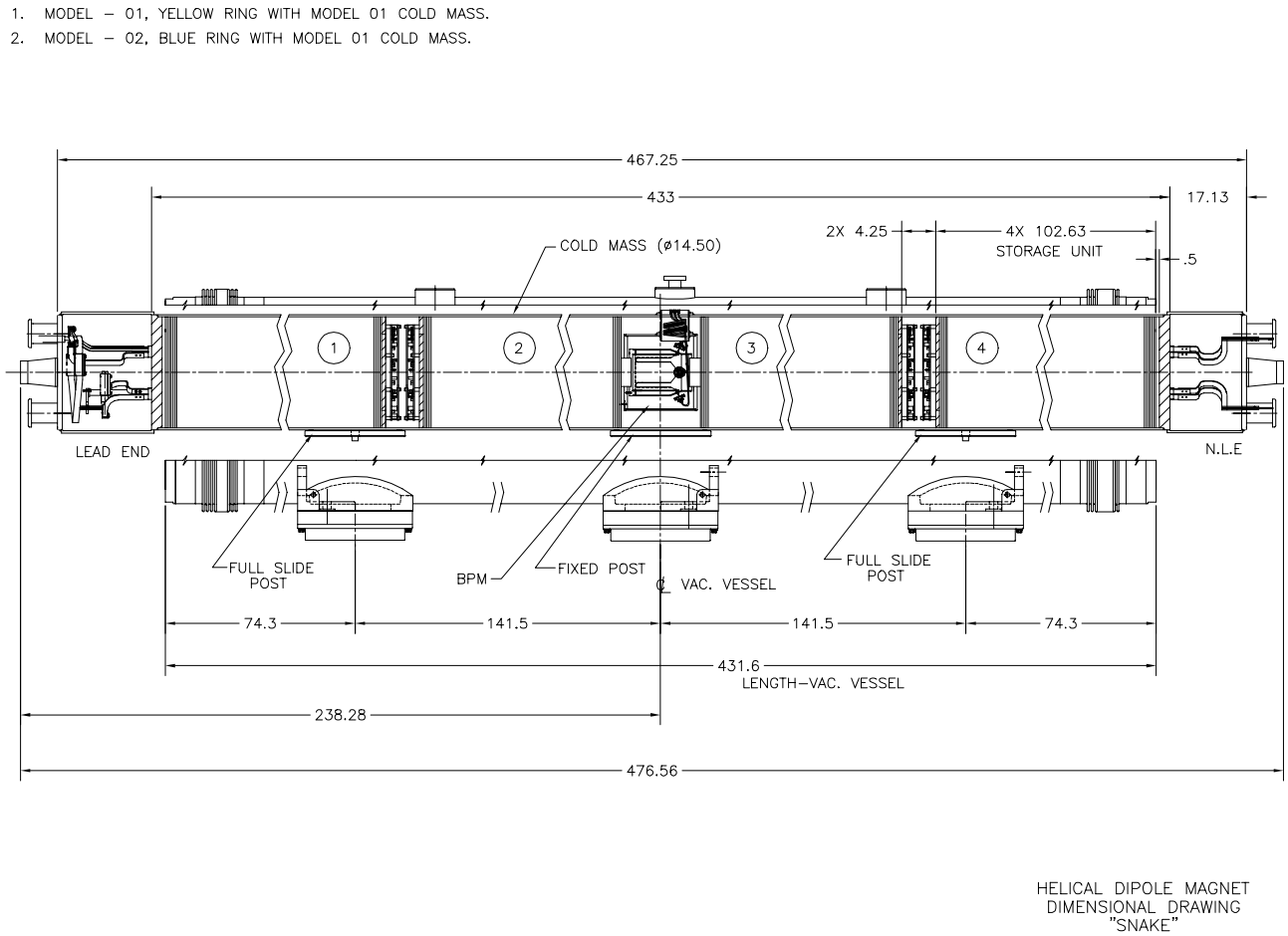

Figure 6.19: Sketch of Snake cryostat assembly. The four superconducting helical dipole magnets are located within a common cryostat. A dual-plane BPM is located near the center of the assembly.

6.3.1 Snake/Rotator Coldmass

Four individual helical cold masses, or "storage units," each ∼2.4 m long, are assembled into a single cold mass ∼10 m long. This is done by welding a stainless steel shell around the storage units as they are positioned on a fixture that gives accurate alignment of the units relative to one another. The beam position monitor that is required in the middle of this coldmass and the various electrical interconnections that must be made are completed before the shells are positioned. After the cylindrical shells are welded in place, end plates are welded to either end to terminate and align the assembly. The beam tube is welded

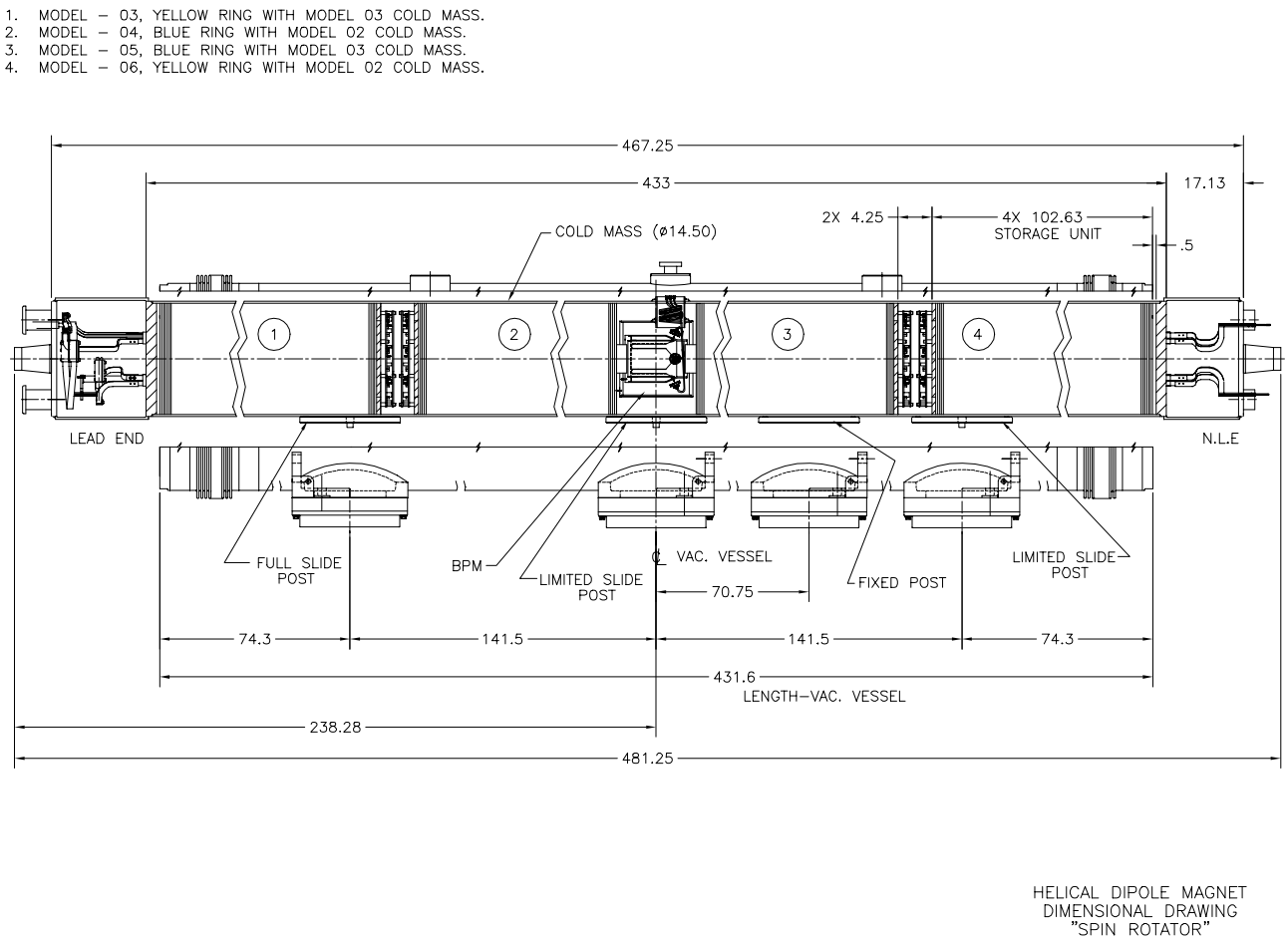

Figure 6.20: Sketch of Rotator cryostat assembly. This assembly, at the end of a cryo string, has different support post requirements than the Snakes.

to the end plates in order to enclose the helium volume. Its diameter increases from the nominal 7.30 cm diameter used in the RHIC arcs to the larger 9.05 cm diameter used in the helical magnets through a short cone-shaped transition piece, 8.89 cm long, at each end of the assembly.

A partial drawing of this assembly is shown in Fig. 6.21. Not shown are fiducial targets that reference the units to the outside.

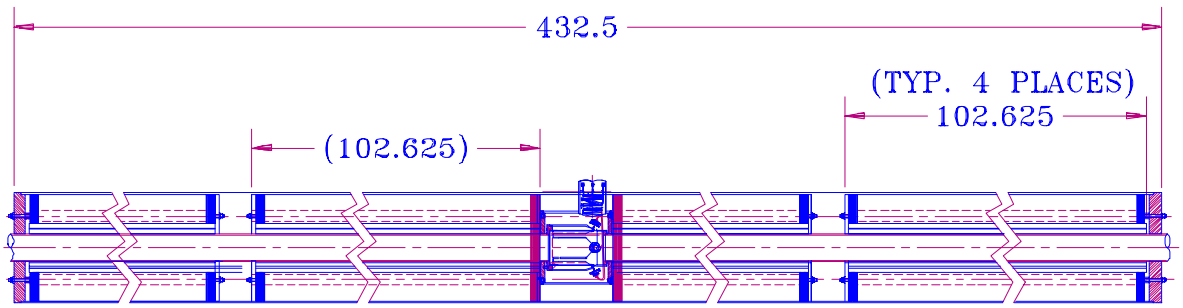

Figure 6.21: A Snake or Rotator cold mass consists of four individual helical cold masses, or "storage units," assembled into an integrated assembly as shown. Dimensions are shown in inches.

Before the coldmass can be installed into a cryostat, the electrical interconnects including bus expansion loops must be assembled in the ends. Busses to carry current for the RHIC arc magnet system must be installed through the slots that have been provided in the storage units. Finally, the ends are closed and made helium-tight with cylindrical containments welded to the end plates and terminating in the appropriate joints for interconnecting to the adjacent arc system. Power for the helical magnets is provided locally at each Snake or Rotator position through current feedthroughs that are welded to the shell in two locations along its length.

6.3.2 Cryostat Assembly

The coldmass is finally installed into a cryostat consisting of a vacuum tank, heat shield, and piping to carry the cryogens. Plastic posts similar to those used for the magnets in RHIC support the coldmass in three places and are designed to allow thermal motion with one anchor point. The vacuum tank is somewhat larger (∼50 mm) than the standard 610 mm tank used in RHIC in order to accommodate the larger diameter helical coldmass. Legs on the vacuum tank in two places support the assembly on stands in the tunnel. The cryogenic piping is necessarily somewhat rearranged with respect to the standard RHIC layout so that adapters are needed to connect the helical assembly to the neighboring magnets in RHIC. A cross section view of the cryostat assembly is shown in Fig. 6.22.

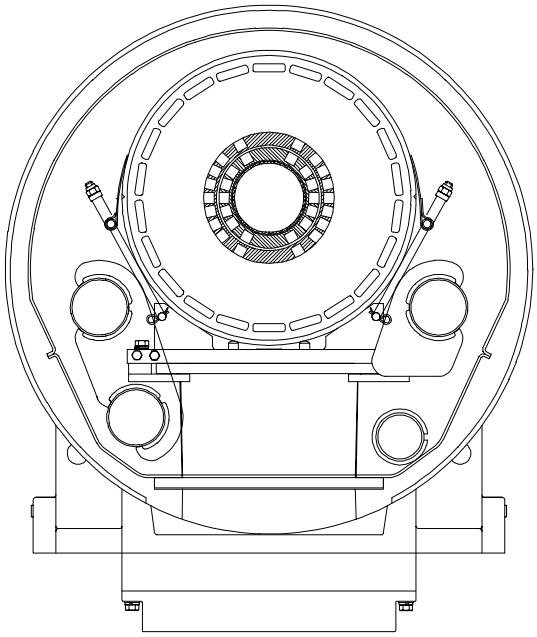

Figure 6.22: Helical magnet assembly in its cryostat. The outside diameter of the vacuum tank is 660 mm.

As seen in Figs. 6.19 and 6.20, some extra room is located between superconducting magnets at the center of the Snakes and Rotators for the internal Beam Position Monitor. Tolerances for the BPM alignment are indicated in Table 6.13. The layout of the internal BPM is sketched in Fig. 6.23.

Parameter	**Requirement**	**Tolerance (rms)**
Number of BPMs (each, hor. & ver.)	12	
BPM Transverse Alignment	0 mm	5 mm
BPM Longitudinal Alignment	0 mm	5 mm
BPM Rotational Alignment	0 mrad	25 mrad

Table 6.13: BPM position tolerances with respect to neighboring quadrupoles.

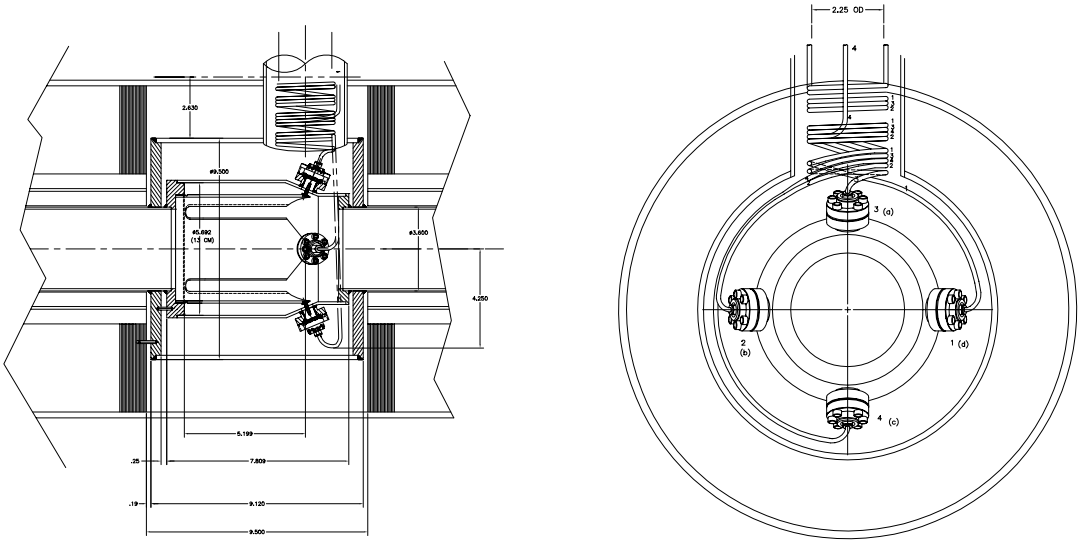

Figure 6.23: Sketch of internal BPM layout.

The internal BPMs will be a modified version of the RHIC triplet BPMs [51],[52]. The 11.2 cm aperture dual-plane detectors will be 13 cm long short-circuited 50 ohm strip transmission lines subtending 70 degrees. Their nominal transfer function is 0.46 dB/mm. To conform to the RHIC design rule which requires that insulating vacuum be interposed between liquid helium and weld joints which see beam vacuum, the snake BPMs will be nested within a vacuum envelope which is ported to the insulating vacuum. The port will also serve as a conduit for the BPM signal cables.

Unlike other BPMs in RHIC [51],[53], there will be no measurement of the snake BPM location relative

to the cryostat fiducials. The snake BPMs are not intended to provide an absolute measurement of beam position in the snakes, but rather simply a measurement of the difference in beam position with the snake magnets on and off. Also unlike other BPMs in RHIC, the normal operating condition for the snake BPMs will not be with the beam centered, but rather with it offset by several centimeters. This offset has significant impact upon the minimum and maximum signals which must be accommodated by the feedthroughs, signal cables, and electronics, and hence upon the accuracy and resolution of the position measurement [54]. This offset also greatly increases heating of the cryogenic signal cables by the beam image currents [55]. The maximum nominal deflection is 3.4 cm. For the purpose of a conservative design, a maximum offset of 4 cm has been used in calculations.

The accuracy and resolution of the position measurement is adversely affected by the beam offset. The offset affects both the raw signals coming from the BPM and the processing of the signals by the BPM electronics. Due to simple geometric considerations, the raw signals are not linear for large displacements. This non-linearity may be corrected by digital processing [56], using the mapped response of the BPM.

The primary limitation on the electronic accuracy of the position measurement is the linearity of the track and hold modules. As the beam moves off center the difference between the outputs of the opposing striplines increases, resulting in an increase in the effect of this non-linearity. Fig. 6.24 shows the result of a calculation of the effect of track and hold non-linearity for normal RHIC operating conditions [52]. The increase in error is approximately linear with offset, and for a 4 cm offset the error should be about an order of magnitude greater than that shown in the figure.

The primary limitation on resolution is noise injected in the track and hold modules. The BPM electronics performs a "difference over sum" measurement. As the beam moves off center the power to the more distant electrode is reduced, reducing the signal-to-noise ratio. Fig 6.25 shows the result of a calculation of the effect of noise on position measurement resolution for normal RHIC operating conditions [52]. The decrease in resolution is approximately linear with offset, and for 4 cm offset the resolution should be less than one order of magnitude worse than that shown in the figure.

If greater accuracy and resolution is required, the width of the input filter passband might be reduced. This would eliminate the possibility of measuring beam position on a bunch-by-bunch basis, but would result in considerable improvement in accuracy and resolution. In addition, there is also the possibility of calibrating a complete system of BPM plus electronics using the BPM mapping facility [51], and using this calibration in the digital processing.

The magnitude of the peak voltages and currents seen by the feedthroughs, signal cables, and electronics is affected by bunch length and by beam intensity and position. With possible future upgrade beam intensity of 2.5×10^{11} protons per bunch, and an rms bunch length of 15 cm, the maximum signal voltage will be in the range of 500 to 600 volts. This will require attenuation at the cryostat. Heating of the cryogenic signal cables within the cryostat will require that they be properly thermally anchored. Heating of the cable, and the corresponding variations in insertion loss resulting from the temperature dependent

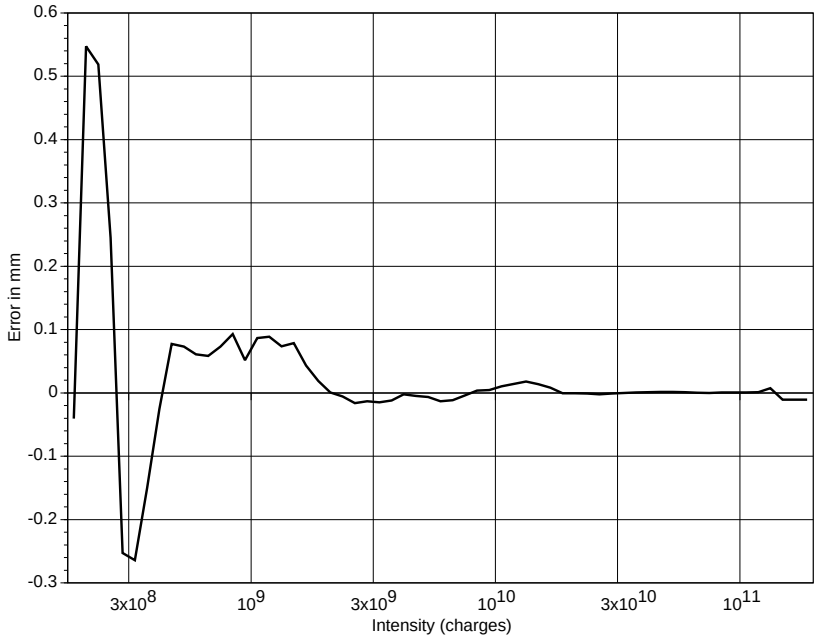

Figure 6.24: Measurement error of the internal BPM, assuming the beam is located near the center of the device. For expected large beam offsets, the error will be worse by roughly one order of magnitude.

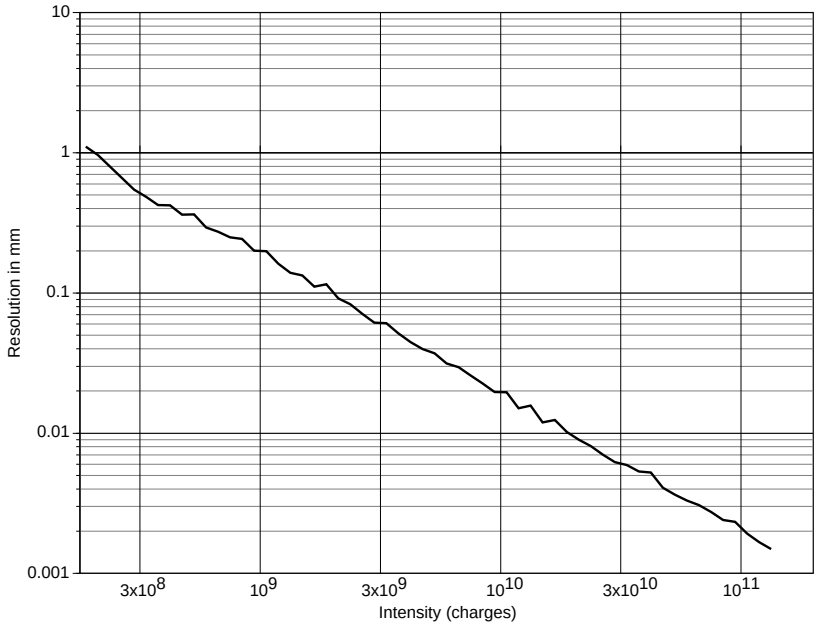

Figure 6.25: Position resolution of the internal BPM, assuming the beam is located near the center of the device. For expected large beam offsets, the resolution will be worse by less than one order of magnitude.

resistivity of the cable, can be compensated in the digital processing if necessary. With its large beam offsets the snake BPM might be a useful test platform for exploring the effects of signal cable heating in more detail.

6.4 Other Accelerator Systems Hardware

6.4.1 Power Supplies and Controls

The slotted helical dipole magnet design requires about 320 Amp for 4 Tesla operation. The power supplies for these magnets do not require many special features. The Snake magnets are run DC and at constant current throughout the acceleration cycle. The Rotator magnet settings are energy dependent, but the Rotators are not required to be on until the beams are in collision. It will be important for the Rotator magnet power supplies to be able to track each other when they are turned on, but because this is an adiabatic operation the ramp will be purposefully slow and the tracking requirements are very lenient. Standard RHIC control devices will enable all standard Snake and Rotator power supply operations.

Parameter	**Requirement**	**Tolerance (rms)**
Power Supply Current (I)	320 A	
Current Setting/Adjustment ($\delta I/I$)	0.5%	
Current Regulation/Stability ($\Delta I/I$)	0	0.01%
Ramp rate (dI/dt) (Rotator only)	1 A/sec	0.01 A/sec

Table 6.14: Snake/Rotator Power Supply requirements.

While the RHIC Spin system will introduce 24 new Beam Position Monitors (12 units with both horizontal and vertical position readout) to the RHIC ring, this will be a small perturbation to the RHIC BPM system which already has nearly 500 such devices. Standard RHIC signal processing and controls hardware will be employed in the Snake/Rotator BPM system.

6.4.2 RHIC Vacuum and Cryogenics Interface

The Snake and Rotator assemblies are contained within RHIC dipole-style cryostats with standard magnet interconnections to adjoining cryogenic devices. The one major change in the RHIC vacuum and cryogenics system which is to be incorporated as a consequence of the Spin system is at the Rotator locations. The Rotators reside in the warm straight sections between quadrupoles Q3 and Q4, immediately next to Q3. Thus, the length of the actual warm beam pipe at these locations and the associated cryogenics bypass need to be shortened. These modifications are indicated in Fig. 6.26. The modifications include shortening of the warm beam tube and of the cryogenic bypass assembly, while the end boxes and end connections remain standard.

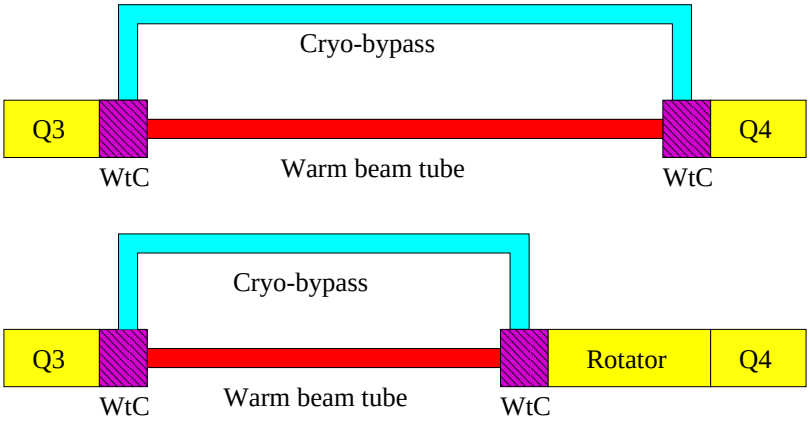

Figure 6.26: Sketch of cryo system modifications required at the Rotator locations in the RHIC tunnel.

Chapter 7

Collision of Polarized Protons in RHIC

7.1 Polarization Lifetime

In storage mode even a very small depolarizing resonance strength can in principle lead to significant depolarization. This was observed at the ZGS where the effect of high order depolarizing resonances were studied on a 1 second flat top as shown in Fig. 7.1[57]. In an accelerator without Snakes like the ZGS the

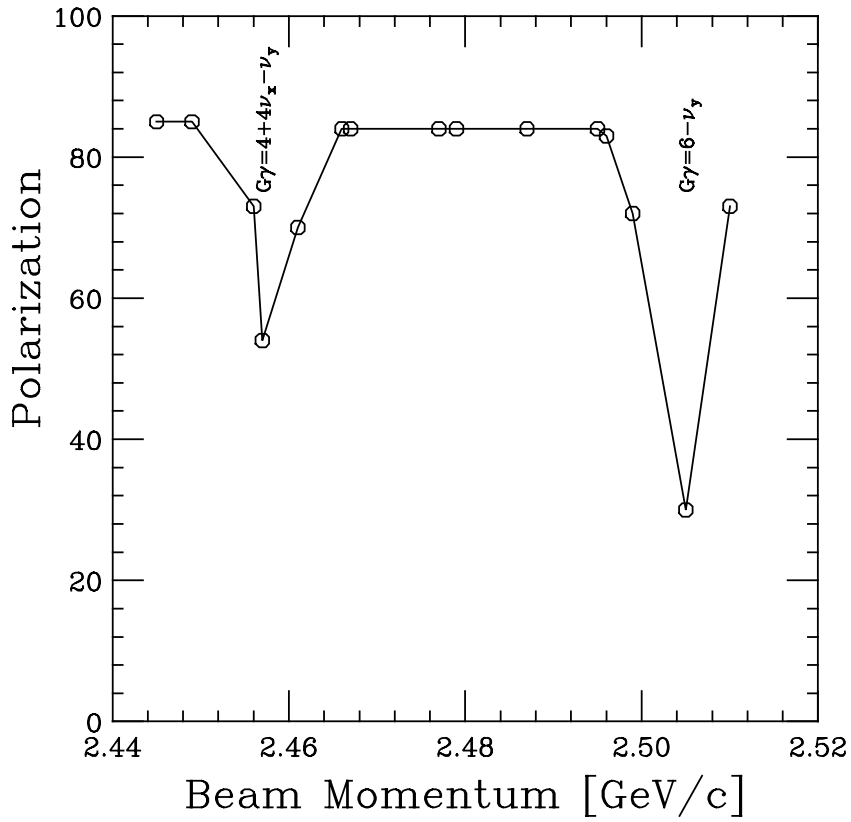

Figure 7.1: Depolarization on the 1 second flat top at the ZGS.

spin tune is energy dependent ($\nu_{sp} = G\gamma$) and therefore if the resonance condition is within the energy spread of the beam each proton will cross the resonance condition repeatedly and eventually the whole beam can be depolarized. With Snakes, however, the spin tune is energy independent and therefore all Snake resonance conditions are energy independent. As pointed out earlier and shown in Fig. 5.3 the beam can overlap higher order Snake resonances due to the betatron tune spread. Results of spin tracking calculations for a proton with $\Delta\nu_y = \frac{13}{16}$ and a Snake resonance strength of 0.15 showed that the spin vector is precessing about the vertical axis. [1] At a resonance strength of 0.15, the vertical projection is about 90%. This precession is in fact a spin closed orbit in a broader sense of 16 turns. Spin tracking calculations were calculated over 8×10^9 turns without significant deviations from this spin closed orbit. Only a small fraction of particles are located within the width of the resonance and therefore effective depolarization in the storage mode is small.

When the spin vector is acted on with an adiabatic modulation within the tolerable limit, the spin vector will follow the spin closed orbit adiabatically. Non-adiabatic processes, arising from rf noise at the spin precession frequency, can indeed cause beam depolarization. Let us consider that a single dipole with strength θ_k is modulated at $\nu_{sp} f_0$, which is about 39 kHz for RHIC. The corresponding induced spin precessing kick is $G\gamma\theta_k$. The number of turns that occur before the spin is perturbed to 80% of the original polarization is given by,

$$N_p = \frac{\cos^{-1}(0.8)}{G\gamma\theta_k} \tag{7.1}$$

Let us now consider the same angular kick to the orbital motion. If there is an rf source at $\nu_{sp} f_0$, one expects a similar angular kick at the frequency $q f_0$, where q is the fractional part of the betatron tune. The orbital survival turn number is given by

$$N_o = \frac{A}{\langle\beta\rangle\theta_k} \tag{7.2}$$

where $\langle\beta\rangle$ is the average betatron amplitude, and A is the dynamic aperture. Using $A = 0.01$ m, $\langle\beta\rangle = 20$ m for RHIC, we find that the orbital lifetime is only half as long as the polarization lifetime.

Indeed, any rf source at high frequencies around the synchrotron and betatron tunes, are dangerous to the orbital stability of particles in accelerators. Similarly, any rf source at the spin tune can cause beam depolarization. These high frequency rf sources should be addressed carefully in hardware design.

[1] In 1995, the RHIC operating point was changed. Since the spin dynamics is symmetric about the half-integer tune, many results found in this report are for the old tune values.

7.2 Beam-Beam Interactions

For round, Gaussian beams with rms beam size σ, the force experienced by a particle in one bunch due to its passage through an on-coming bunch is given by

$$F(r,s) = \frac{\lambda(s)\, e^2}{2\pi\epsilon_0} \left(1 + \frac{v^2}{c^2}\right) \frac{1 - e^{-r^2/2\sigma^2}}{r} \tag{7.3}$$

$$\approx \frac{\lambda(s)\, e^2}{2\pi\epsilon_0\sigma^2}\, r \tag{7.4}$$

where r is the transverse radial distance from the center of the bunch, $\lambda(s)$ is the local longitudinal particle density (particles per meter), and e is the proton charge. The last expression is for $r < \sigma$. The beam-beam interaction, for most of the protons in the center of the bunch, has a defocusing effect. Considering only one-dimensional (vertical, say) motion, a proton's trajectory would be altered by the other proton bunch by an amount

$$\Delta y' = \frac{\int (\partial F/\partial y) y\, ds}{pv} \tag{7.5}$$

$$= \frac{e^2}{4\pi\epsilon_0 mc^2} \frac{2\int \lambda(s) ds}{\gamma(\sigma^*)^2} \cdot y \tag{7.6}$$

$$= \frac{r_0 n}{\gamma(\sigma^*)^2} \cdot y \tag{7.7}$$

$$= \frac{6\pi r_0 n}{\beta^* \epsilon_N} \cdot y \tag{7.8}$$

$$\equiv \frac{1}{f^*} \cdot y \tag{7.9}$$

where n is the number of protons per bunch, r_0 is the classical radius of the proton, and σ^* is the rms beam size at the interaction point. The equivalent focal length, f^*, leads to the familiar beam-beam tune shift

$$\xi \equiv \frac{1}{4\pi}\frac{\beta^*}{f^*} = \frac{3r_0 n}{2\epsilon_N}. \tag{7.10}$$

The beam-beam interaction will thus precess the spin of a typical (rms-amplitude) particle by an amount

$$\Delta\phi \approx G\gamma\, \Delta y' \approx \frac{G r_0 n}{\sigma^*} = G r_0 n \sqrt{\frac{6\pi\gamma}{\beta^*\epsilon_N}} \tag{7.11}$$

which, for 2×10^{11} particles per bunch, 20π mm mrad emittance, and $\beta^* = 1$ m, corresponds to $\Delta\phi =$ 5 mrad. This precession will contribute to the intrinsic depolarizing resonance strength at storage. Since the resonance strength is given by

$$\epsilon_k = \frac{1 + G\gamma}{2\pi} \oint \sqrt{\frac{\beta(s)\epsilon_N}{6\pi\gamma}} \frac{\partial B_x(s)/\partial y}{B\rho} e^{ik\theta(s)} ds \tag{7.12}$$

we can compare $\sqrt{\beta^*}/f^*$ with the value $\sqrt{\beta_{max}}/F$ for a standard RHIC arc quadrupole to check the magnitude of the effect. We find that the contribution to the intrinsic resonance strength of the beam-

beam interaction is roughly 14% of the contribution from a single RHIC arc quad for the parameters above.

It is interesting to note that the beam-beam tune shift for the beam parameters used above is $\xi = 0.0073$ per crossing, or 0.015 for two IRs.

Analytical and numerical studies have been performed which indicate that the effect on spin of the beam-beam interaction is indeed small for RHIC.[58],[59]

7.3 Luminosity of Polarized Proton Collisions

The luminosity of RHIC is given by

$$\mathcal{L} = \frac{3 f_0 B N_B^2 \gamma}{2 \epsilon_N \beta^*} \tag{7.13}$$

where f_0 is the revolution frequency, B is the number of bunches in each ring, N_B is the number of particles per bunch, ϵ_N is the normalized emittance, β^* is the amplitude function at the interaction point, and $\gamma = E/mc^2$. For a β^* of 2 m, 20 π mm mrad emittance, 60 bunches, and 10^{11} protons per bunch (nominal RHIC proton parameters), the luminosity at 250 GeV is 1.5×10^{31} cm^{-2} s^{-1}. The above expression suggests a linear dependence of luminosity with beam energy. However, as the energy of the beam is decreased, the beam size in the interaction region triplet will increase. Hence, once a certain energy is reached (approximately 70 GeV in RHIC), the amplitude function at the interaction point must be optimized to maintain a maximum beam size in the low-beta triplet quadrupoles. With this scenario in mind, the luminosity at lower energies decreases more rapidly than linear.

The RHIC beam intensity can likely be raised to 2×10^{11} protons per bunch, and the interaction region optics is capable of generating a β^* of 1 m. In addition, the number of bunches can also be easily increased by a factor of two to 120. Thus the potential exists to produce a polarized proton luminosity at 250 GeV of 2×10^{32} cm^{-2} s^{-1}, which corresponds to about one interaction per crossing of the 120 bunches per ring. Even higher luminosity might possibly be achieved with lower emittance, or with higher beam current. The luminosity for polarized protons versus. energy is shown in Fig. 7.2. For this figure, we assume an emittance of 20 π mm mr emittance, 2×10^{11} protons per bunch, and β^* at high energy of 1 m. At 25 GeV, $\beta^* = 2.8$ m in order to maintain the required beam size in the triplet quadrupoles.

In the above analysis, the beam parameters were below the beam-beam tune shift limit of $\xi = 0.024$ typically observed in other hadron colliders (Tevatron, Sp$\bar{\text{p}}$S). If the beam emittance were improved to 10π mm mrad, for example, along with the "upgraded" parameters used above, the collider would become beam-beam limited. Fig. 7.3 shows the luminosity of the polarized proton collider at 250 GeV and for various emittances as a function of bunch intensity, assuming 120 bunches per ring, and $\beta^* = 1$ m. As the intensity is increased, the collider reaches the tune shift limit, and then the beam emittance would be increased in proportion to the bunch intensity to maintain this tune shift. The luminosity, at that point, would increase linearly with bunch intensity rather than quadratically.

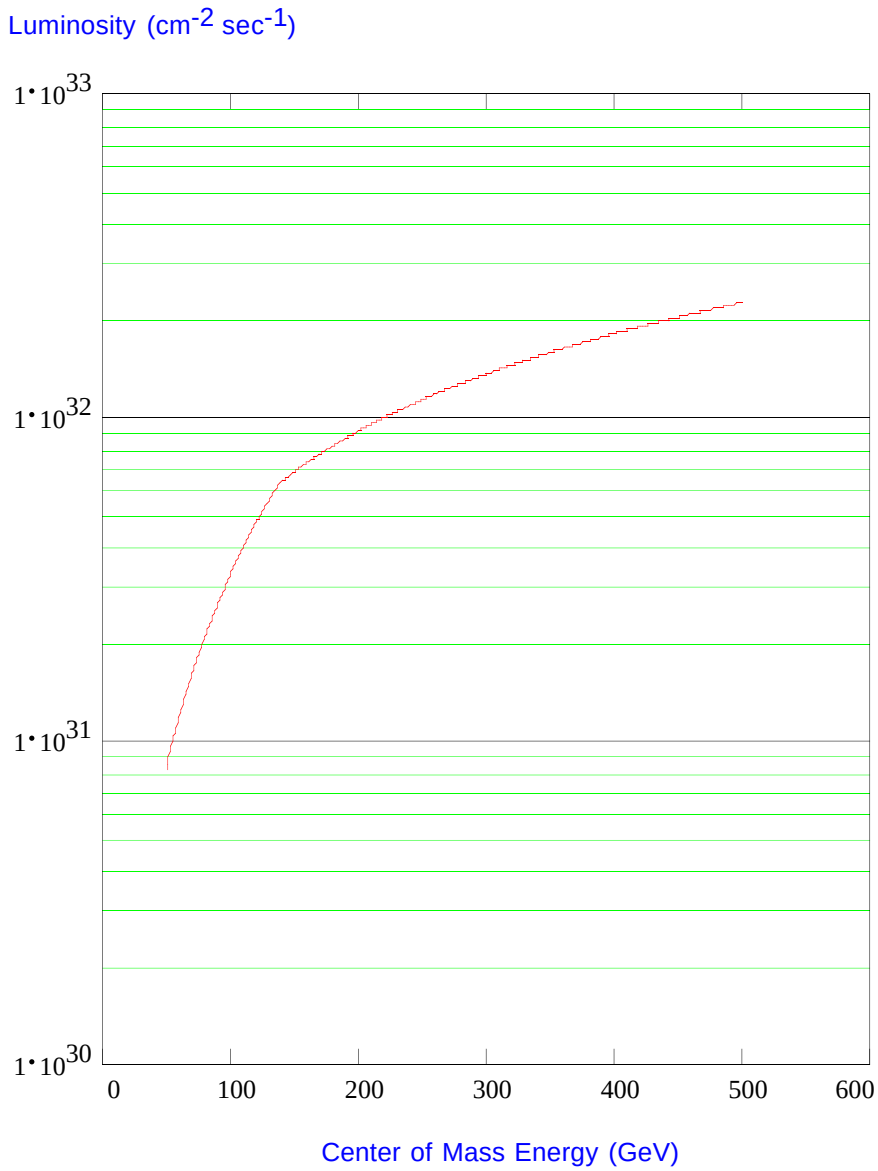

Figure 7.2: Polarized proton luminosity as a function of energy in RHIC. A normalized emittance of 20π mm-mr (95%), 120 bunches per ring, and a beam intensity of 2×10^{11} protons per bunch were used. A value of $\beta^* = 1$ m from 74 GeV to 250 GeV was assumed; at 25 GeV, β^* is 2.8 m.

7.4 Spin Reversal of Stored Beams

Since the proposed asymmetry measurements are high precision measurements, frequent polarization sign reversal is imperative to avoid systematic errors. Possible sources for systematic errors are luminosity variations, crossing angle variations, and detector efficiency variations. As mentioned earlier different bunches will have different polarization signs and therefore different bunch crossings will measure interactions with different combinations of incoming beam polarization signs. Although this will greatly reduce systematic

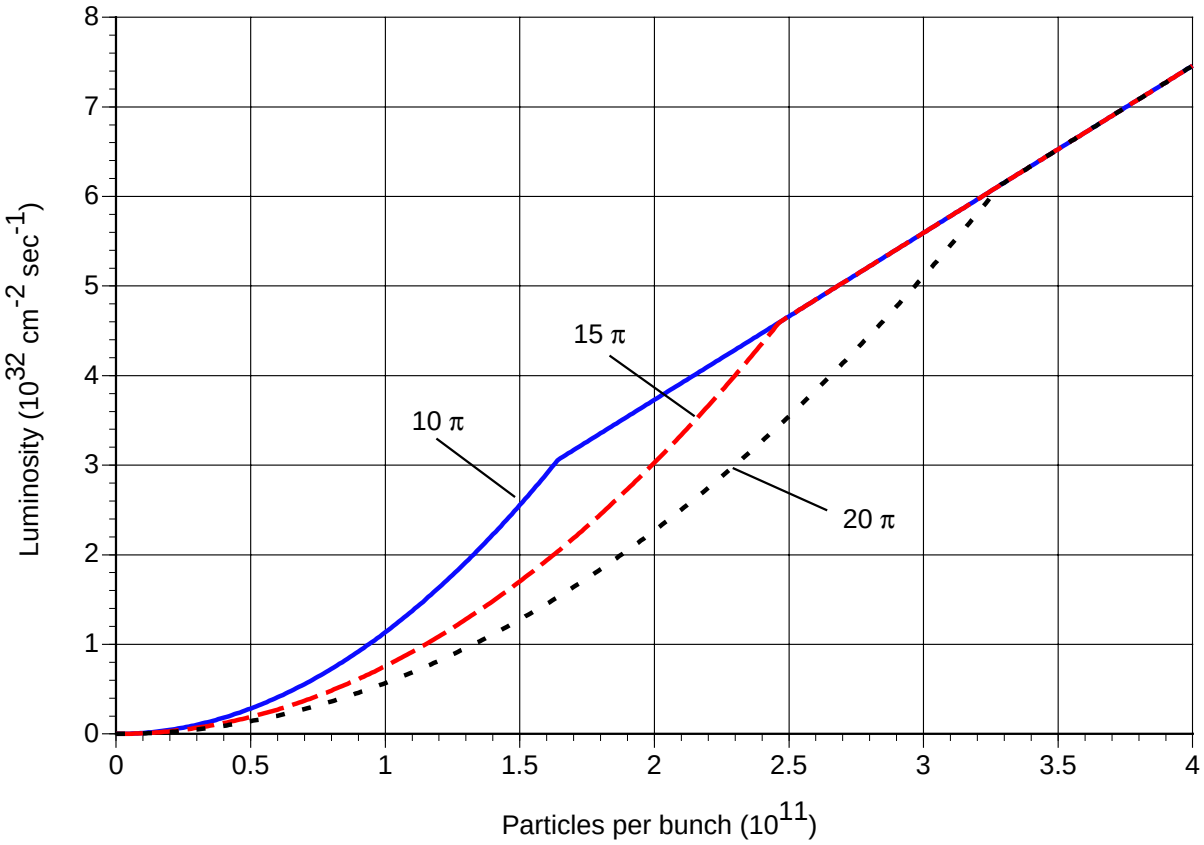

Figure 7.3: Polarized proton luminosity as a function of bunch intensity for normalized emittances of 10π, 15π, and 20π mm-mr (95%), using 120 bunches per ring, $\beta^* = 1$ m, and $E = 250$ GeV. A total (for two IRs) beam-beam tune shift limit of 0.024 was assumed.

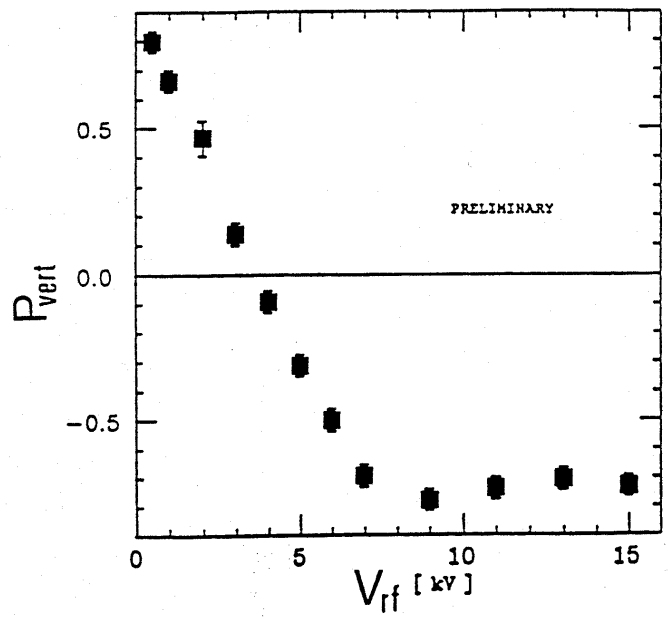

Figure 7.4: Adiabatic spin reversal of a stored beam of polarized protons at the IUCF Cooler ring. The RF voltage is proportional to the strength of the artificial spin resonance driving the spin reversal.

errors it is still true that one pair of bunches would always cross with the same combination of polarization signs during the whole lifetime of the stored beams which is at least several hours. To eliminate the possibility of systematic errors from this situation we propose to install a spin flipper in each ring which is capable of reversing the polarization sign of all bunches. The spin flippers consist of vertical dipole magnets[60] excited with about 40 kHz AC current. This would drive an artificial spin resonance which can be used to adiabatically reverse the polarization direction. Fig. 7.4 shows the result of a test of this concept performed at the Indiana University Cyclotron Facility (IUCF)[61]. We estimate that complete spin reversal would take less than 1 second. The same device will be used to accurately measure the spin tune by measuring the spin reversal efficiency as a function of the frequency of the spin flipper excitation. This is instrumental to adjust the spin tune to 0.500.

In most cases such a simple oscillating driving field is very effective in driving an artificial resonance since the oscillating field can be thought of as the sum of two counter-rotating fields, only one of which is in resonance with the beam precession frequency. However, with a Snake the spin tune is a half-integer and therefore the two counter-rotating fields are both in resonance and interfere so that effectively only half of the beam around the ring circumference sees a driving field. By designing a true rotating field the beam polarization can be fully flipped even with a half-integer spin tune.

Several designs have been proposed, all involving two sets of AC magnets with a 90° phase difference between them. The first design uses three strong DC magnets interleaved with four independently driven

Magnet	**Strength**	**Excitation**
1.Vertical magnet	0.01 Tm	$\sin \omega t$
2.Horizontal magnet	+4.2 Tm	DC
3.Vertical magnet	0.01 Tm	$-2 \sin \omega t + \cos \omega t$
4.Horizontal magnet	−8.4 Tm	DC
5.Vertical magnet	0.01 Tm	$\sin \omega t - 2 \cos \omega t$
6.Horizontal magnet	+4.2 Tm	DC
7.Vertical magnet	0.01 Tm	$\cos \omega t$

Table 7.1: Parameters for a spin flipper that produces a true rotating driving field. The excitation of the AC magnets indicates the relative phase shift between the four magnets.

vertical AC magnets. Table 7.1 shows the parameters of such a spin flipper, which could fit into a regular 12 m straight section. The DC magnets in this first design are quite strong and expensive. A less expensive design would utilize one of the two Siberian Snakes instead of special DC magnets. The two sets of vertical AC magnets are placed symmetrically around the Snake with one set generating a vertical bump of half a vertical betatron wavelength and the other one a full wavelength long. By driving the bumps with 40 kHz AC 90° out of phase a rotating driving field will be generated. Alternatively, and also least expensively, the spin tune can be simply moved away from the value of 0.5 during the spin flip operation using the tunability of the Snakes. To achieve full spin flip with less than 0.01% polarization loss per flip a field integral for the AC magnet of $\int Bdl = 0.01$ Tm and a flip time of about 1.0 s is required[62].

To avoid emittance growth from the oscillating vertical deflections, the dipole needs to be turned on and off slowly (adiabatically) as shown in Fig. 7.5. This scheme was successfully tested in the AGS where adiabatic build up of betatron oscillation amplitudes in excess of two beam sigma, and subsequent adiabatic turn off, has been demonstrated without emittance growth.[63]

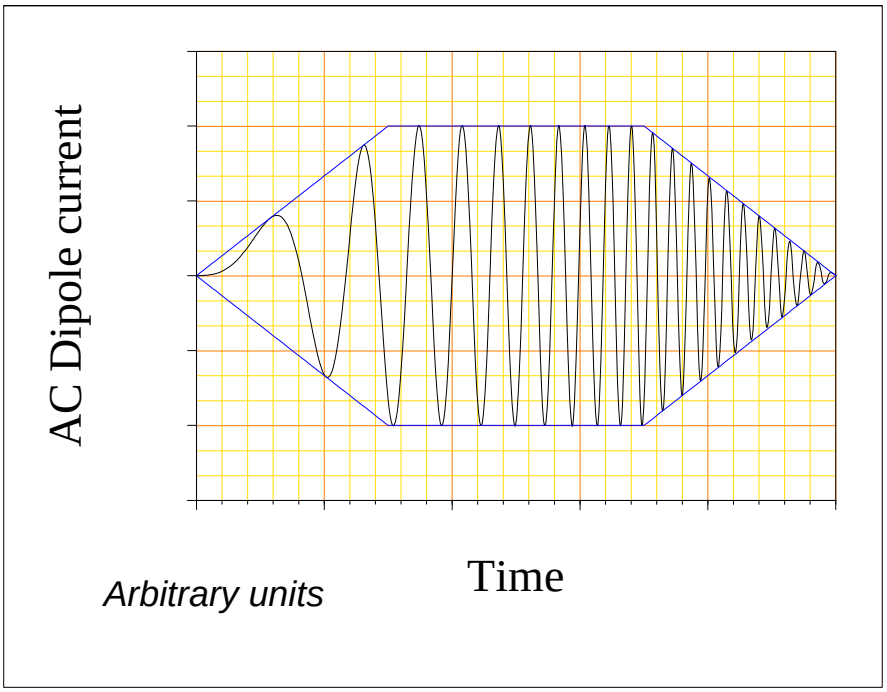

Figure 7.5: Schematic diagram of the excitation dipole current as a function of time. Note the increase of frequency with time. The trapezoidal curves are the amplitude envelopes to guide the eye.

Chapter 8

Measuring Beam Polarization in RHIC

Our approach of measuring the beam polarization is based on the asymmetry in p-Carbon elastic scattering in the Coulomb-Nuclear Interference (CNI) region. Originally, the inclusive pion production was chosen by the Polarization Measurement Working Group[64]. Toroid two-arm spectrometers[65] offer an attractive solution by providing left-right measurements that can cover the large energy range of RHIC and allow excellent cancellation of biases in polarization measurements. The details of this design can be found in Appendix A. Due to the funding constraints, a scaled down approach to providing a pion inclusive polarimeter system suitable for 25GeV to 100GeV was developed and can be found in Appendix B. Later on, the idea of using p-C elastic scattering in CNI region was picked up and tested successfully. In this chapter, a polarimeter based on p-Carbon scattering in CNI region is described. It is expected that the relative beam polarization can be determined by using a p-C CNI polarimeter to 10% for each measurement in seconds at full luminosity. The polarimeter can be calibrated using a polarized proton jet target later to 5% or by an inclusive π^- polarimeter, which shares the same carbon target (see Appendix B). Due to the simplicity of the detector system, the cost and development time of p-C CNI polarimeter are significantly less than other polarimeter options.

8.1 Introduction

In general, vertical beam polarization is measured by determining the asymmetry in the cross section for left and right scattering or particle production, using a reaction with a known analyzing power A_p:

$$P_B = \frac{1}{A_p(x_F, p_T)} \frac{Ed^3\sigma_L/dp^3 - Ed^3\sigma_R/dp^3}{Sum}. \tag{8.1}$$

$$P_B = \frac{1}{A_p} \frac{N_L - N_R}{N_L + N_R}. \tag{8.2}$$

P_B is the beam polarization, N_L and N_R are the number of scatters left and right normalized by luminosity. A_p can be known from experiment or theory.

A physics asymmetry is the raw (measured) asymmetry, normalized by the beam polarization. Examples are

$$A_L = \frac{1}{P_B}\frac{N_+ - N_-}{N_+ + N_-} \tag{8.3}$$

$$A_{LL} = \frac{1}{P_B^2}\frac{N_{++} - N_{+-}}{N_{++} + N_{+-}}. \tag{8.4}$$

A_L and A_{LL} are single and double spin longitudinal asymmetries. N_+ and N_{+-} are the number of scatters observed with the beam polarization helicity + (one beam + and the other beam - for N_{+-}) normalized by luminosity. The beam polarization P_B is taken as the same for both beams for A_{LL}. For those reactions with a high degree of statistical accuracy, the error in the physics asymmetry is

$$(\frac{\delta A_L}{A_L})^2 \sim (\frac{\delta P_B}{P_B})^2 \tag{8.5}$$

$$(\frac{\delta A_{LL}}{A_{LL}})^2 \sim 2(\frac{\delta P_B}{P_B})^2. \tag{8.6}$$

Thus, if the absolute beam polarization is known to 10%, for example, then the single spin asymmetry A_L is uncertain to 10% of itself. Similarly, for A_{LL} the error becomes 20%. The beam polarization error only becomes significant when the statistical precision reaches the same level, thus a 10σ or 5σ measurement respectively. We only anticipate a 10σ measurement for the u quark polarization in a polarized proton using parity violation of W^+ production, where the expected asymmetry A_L is quite large and, thus, the expected statistical contribution to $\delta A_L/A_L$ is small. Gluon polarization will be measured by direct photon production and the statistical contribution to $\delta A_{LL}/A_{LL}$ would approach 5σ only for maximal gluon polarization.

8.2 p-C elastic scattering in CNI Region

Small angle elastic scattering of hadrons in the Coulomb-Nuclear Interference(CNI) region has long been advocated for polarimetry. The predicted asymmetry is significant and largely independent of energy for energy above a few GeV. The prediction rests on hadronic spin flip being small, which is expected for high energies. The CNI process has been proposed for RHIC polarimetry using a hydrogen jet target and in collider mode using the *pp*2*pp* experiment [66]. Both would be *pp*CNI. It is also possible to use a carbon target, p-CCNI, which is simpler and cheaper than a hydrogen jet, and can be installed in the individual rings, vs. requiring collision of both rings as for the *pp*2*pp* experiment. In addition, carbon target is easier to handle in the vacuum. The analyzing power for p-CCNI is similar to *pp*CNI (both about 0.04) and the cross section is high, giving a very large figure of merit NA^2. However, for p-CCNI, a typical $(-t)$ value of 0.002 to 0.01 GeV^2 results at high energy in a very small angle of the forward scattered proton relative to the beam direction and also a very low kinetic energy of the Carbon recoil of about 0.1-1 MeV. It is impossible to measure the forward scattered proton without drastically reducing the beam divergence at

the target which would severely reduce the scattering rate and also cause unacceptable beam emittance growth. It will therefore be necessary to rely only on the measurement of the recoil Carbon nuclei to identify elastic scattering. The low energy carbon nuclei would stop in most targets. The very thin ribbon carbon targets developed at IUCF[67] is crucial to the p-CCNI polarimeter: both for survival in the RHIC beam and to get the carbon nuclei out of the target in the CNI region where the recoil carbon carries only hundreds of keV kinetic energy. The slowness of the recoil carbon makes detection difficult. However, the arrival time of the carbon can be set to be in between RHIC bunches, avoiding prompt background.

Elastic scattering in the small angle CNI region is predicted to have a calculable analyzing power of about 3-5% as well as a large cross section over the whole RHIC energy range from 24 GeV/c to 250 GeV/c [68]. The analyzing power is given by

$$A_N(t) = \frac{G t_0 t \sqrt{t}}{m_p(t^2 + t_0^2)}, \tag{8.7}$$

where G is the anomalous magnetic moment of the proton(1.7928), m_p the proton mass, and $t_0 = \frac{8\pi\alpha Z}{\sigma_{tot}}$. The total cross section σ_{tot} is only weakly energy dependent over the relevant energy range. Fig. 8.1 shows the calculated analyzing power for a hydrogen target ($Z = 1$, σ_{tot}=35mb) and a carbon target($Z = 6$, σ_{tot}=330mb[69]) as a function of $(-t)$. The uncertainty from a hadronic spin flip amplitude has been estimated to be smaller than 10% of the analyzing power from CNI. Using a carbon target will result in the high luminosity required for fast polarization measurements. The sizable analyzing power, the large cross section and the advantages of a solid ribbon target makes this process ideal for a fast primary polarimeter for RHIC.

8.3 Experimental Test of p-Carbon CNI Polarimeter

A series experiments were conducted before the actual RHIC polarimeter begin installed. The first test of such a polarimeter using silicon detectors had its first successful run in March 1998[70]. For low energy and kinematics where the recoil carbon is 0.1 to 1MeV, the forward proton scatters to a large angle, and can be seen by the Meyer forward detector system at IUCF[71]. The carbon energy range for this silicon detector was 150-400keV. For these data, the proton detector was used to trigger. We also successfully triggered on only the silicon detector energy, with the difficulty that a higher threshold was necessary (300keV) due to noise background.

Simultaneously, our collaborators at Kyoto University and RIKEN are conducting similar tests using Micro Channel Plate (MCP) detectors at the Kyoto 10 MeV proton Van de Graaff. The two detection techniques (MCP and SSD) were also successfully combined to give both timing as well as energy information [72].

The AGS Experiment E950 used AGS polarized proton beam to measure the asymmetry in p-C CNI process at 21.7 GeV/c. The experimental setup is shown in Fig. 8.2. The silicon strip detector (SSD) had a

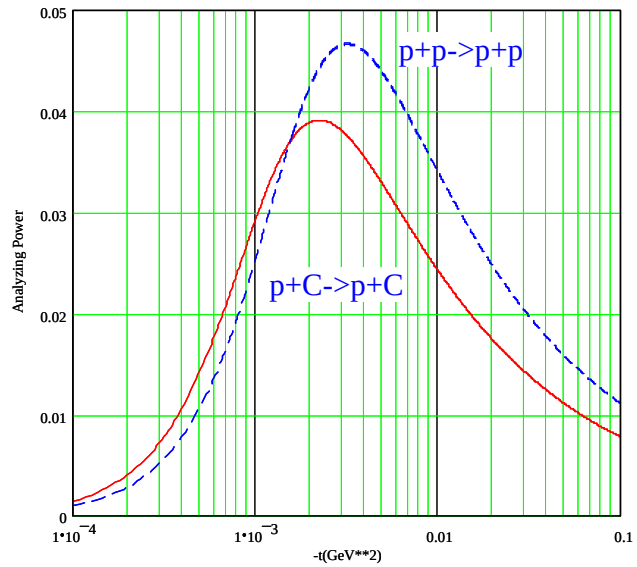

Figure 8.1: Coulomb-Nuclear interference analyzing power for pp and pC scattering.

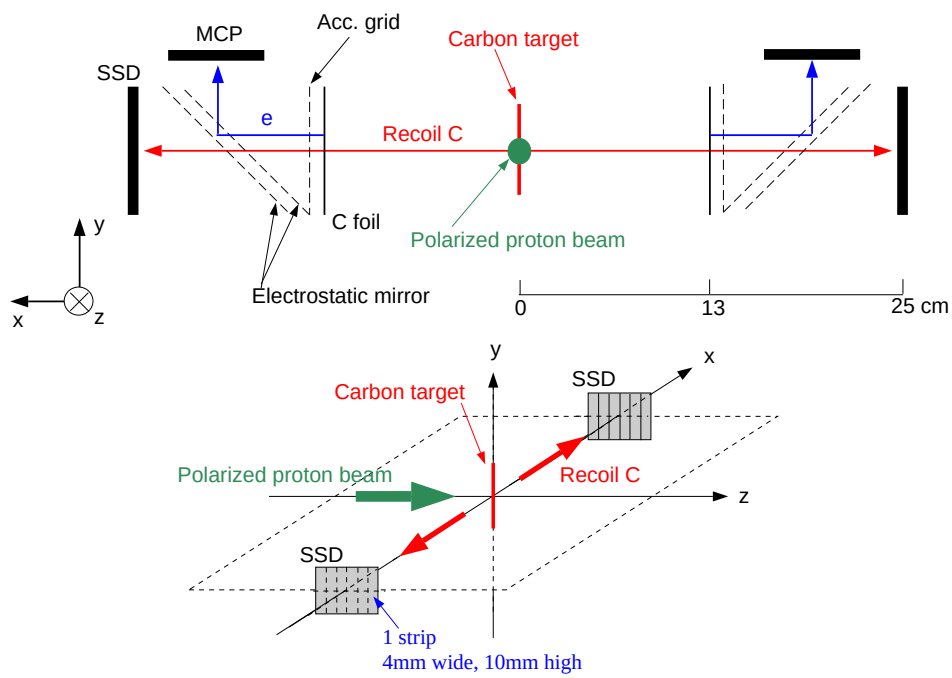

Figure 8.2: Schematic layout of the experimental setup (not to scale). Top: Side view of detectors, where beam is pointing into the paper. Bottom:Top view of detector setup(only SSDs are drawn).

thickness of 400 μm and was segmented into twelve strips. This segmentation provides angular information and also divided the events into segments, which is quite important due to the large cross section of the

scattering process. In the AGS E950, one segment consists of two strips and each segment was 4 mm wide and 10 mm high. The surface of the SSD had a special feature of a very thin Boron implantation with small aluminum wire electrodes so that low energy recoil carbons could penetrate the surface without being hindered by the electrodes. The micro channel plate (MCP) assembly, consisting of two layers of MCPs and a single anode, The experimental results show that the recoil carbons from CNI scattering can be detected with the SSDs. The *p-C* elastic scattering was identified by detecting only low energy recoil carbon nuclei. The analyzing power was successfully measured for the first time with high statistical accuracy. The asymmetry behavior follows the theory qualitatively [73]. The discrepancy suggests that the contribution from hardronic spin flip amplitude is larger than 10%, but this does not prevent us from using *p-C* CNI process as RHIC polarimetry. Although the micro channel plate (MCP) enhanced the time resolution, it complicated the detector system. The results showed that MCP was not necessary to get both energy and time information of the recoil Carbon nuclei. As the result, MCPs were not used in RHIC polarimeter. Given the success of AGS test, it was justified to develop a *p-C* CNI polarimeter for RHIC.

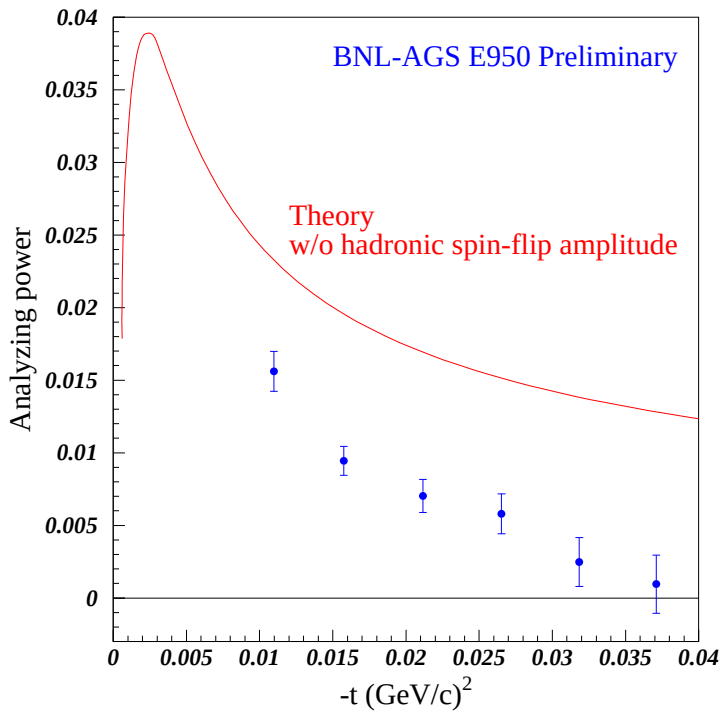

Figure 8.3: Preliminary results of the analyzing power for *p-C* elastic scattering in the CNI region. Error bars are statistical only. The theoretical curve in Eq. (8.7) are drawn for comparison.

8.4 Overall Design

The inclusive pion polarimeter was originally considered for RHIC [64] and a long straight section is needed. For easy maintenance, this has to be a warm straight section. The warm straight section between Q3 and

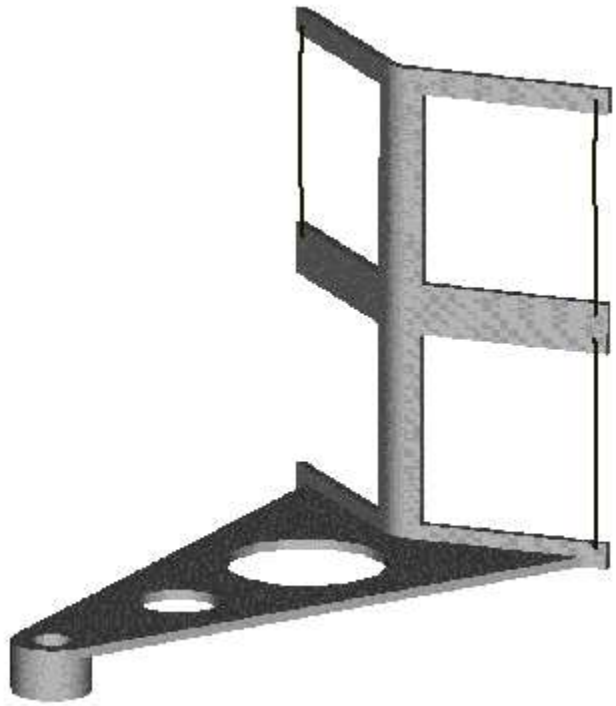

Figure 8.4: Metal target frame and the ceramic V plate. The ceramic plate reduces impedance impact. The holes in the V shape reduce the inertia of the target assembly. A typical target is a 5 μm, 5 μg/cm^2 ultra-thin carbon ribbon. It is 3 cm long.

Q4 at section 12 is assigned for both polarimeters in blue and yellow rings. Both target chambers are located near Q4 where the vertical and horizontal lattice β functions are small thus reducing the effect of multiple scattering on emittance dilution. Both target chambers are upstream of each other. Since beams are in opposite directions in the two rings, the detectors for both polarimeters are not in the scattering showers of each other. The target chamber for yellow ring is also close to Q4, which gives enough space for the one-arm inclusive pion polarimeter in the future(sharing the same target, see Appendix B).

It is desirable for the polarimeter to measure both horizontal and vertical beam polarization profiles, which requires separate targets scanning both vertically and horizontally. Since the thin carbon target has a relative short life time at the full RHIC beam luminosity, it would be advantageous to mount more than one ribbon on the driving mechanism (spaced so that the beam sees one ribbon at a time) to provide redundancy in case of ribbon breakage. The current design of target holder is capable of holding 4 targets. Three targets were mounted (a thick one and two thin ones), and one empty target holder is left for background check. The target holder drawing is shown in Fig. 8.4. Each target assembly has two motions: linear motion to move whole assembly in and rotary motion to move the desired target into the beam. A interlock relay system is in place to assure that at any time only one of the two assemblies can move into the beam.

The target box radius is 16.03 cm, which is minimum to host the target driving assembly. In manipu-

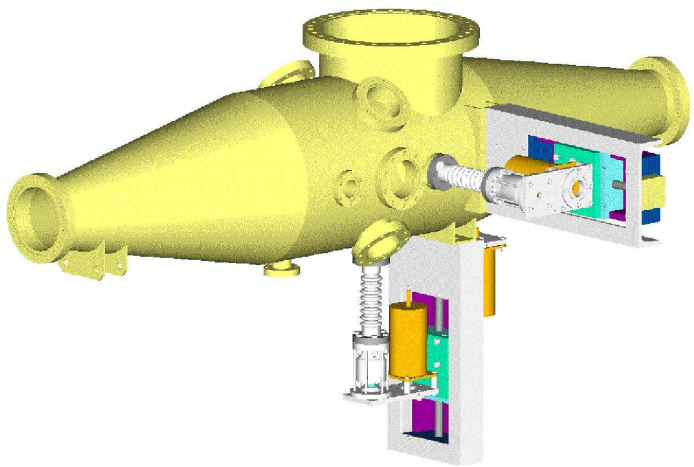

Figure 8.5: RHIC *p-C* CNI polarimeter target box. Top is assembly view and bottom is exploded view. Beam goes from the left to the right.

lating polarization in RHIC, information on both vertical and horizontal components of beam polarization are needed. In addition to one pair of detector sitting in the horizontal plane, two pairs of detectors sitting at 45° are added, which are capable of measuring both transverse components. When using these two pairs for either vertical or radial components, the analyzing power will drop by a factor of $\cos 45° = \sqrt{2}/2$. At full RHIC designed intensity, the bunch width is about 2 ns and bunch spacing is 106 ns. To avoid the prompt background, the carbon nuclei should arrive the detectors between two bunches, i.e., within 100ns. The Si detector can detect carbons with kinetic energy as low as 100keV, which can travel about 15cm in 100ns. The distance between detectors and interaction point is set as 15cm. This is slightly less than the radius of the chamber, so the detectors will be in socket shape and sunk into the cylinder chamber.

The minimum target box length is determined by the relative positions of target, view port and detector sockets, which is 50.8 cm. Due to the impedance constraint, two 5:1 transition sections are attached at both sides and give the total length of the target chamber as 1.6 m. The top view port is used for target installation and target position monitoring. Total of six silicon strip detectors can be used (only four of them were used in the fist commissioning). They are upstream of the target assemblies so there are less background due to forwarding scattering particles from targets. Due to the complicated shape of the target assemblies, the detector at horizontal plane on the driving motor side is partially blocked by the ceramic piece of the horizontal moving targets. So the 45° detectors will have to be used for these targets, which will be used for vertical beam polarization profile scan. On the other hand, the vertical moving targets are cleared for all detectors. The vertical moving targets should be the primary targets. The 3-D plots of the inside and outside of the target box are shown in Fig. 8.5.

To reduce the impact on beam impedance, the radius of the box should be as close as possible to that of the beam pipe, i.e., 6.5 cm. The extensive impedance has been done with MAFIA and can be found in

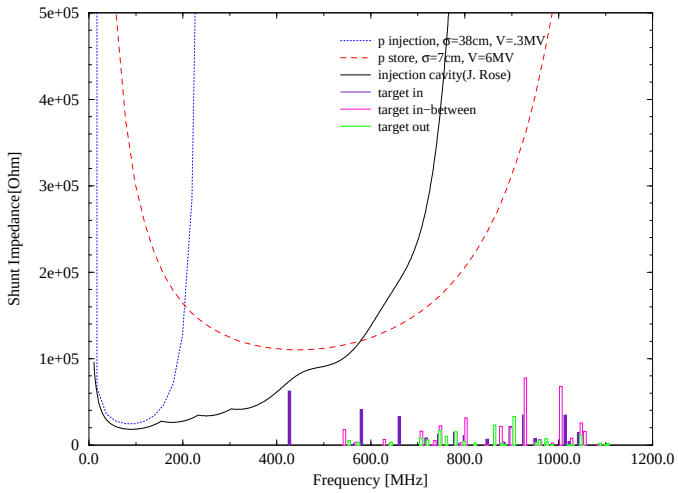

Figure 8.6: Comparison of simulations with different target positions. Three curves are various thresholds for different scenarios. MAFIA results for different target positions are shown as bars. Filled bars are impedances with target in, which is the worst case. It is desired that the impedances of all frequencies are below any of the three curves. Current design meets this requirement.

Ref [74]. Current design meets the RHIC impedance requirement as shown in Fig. 8.6.

8.5 Carbon Ribbon Target

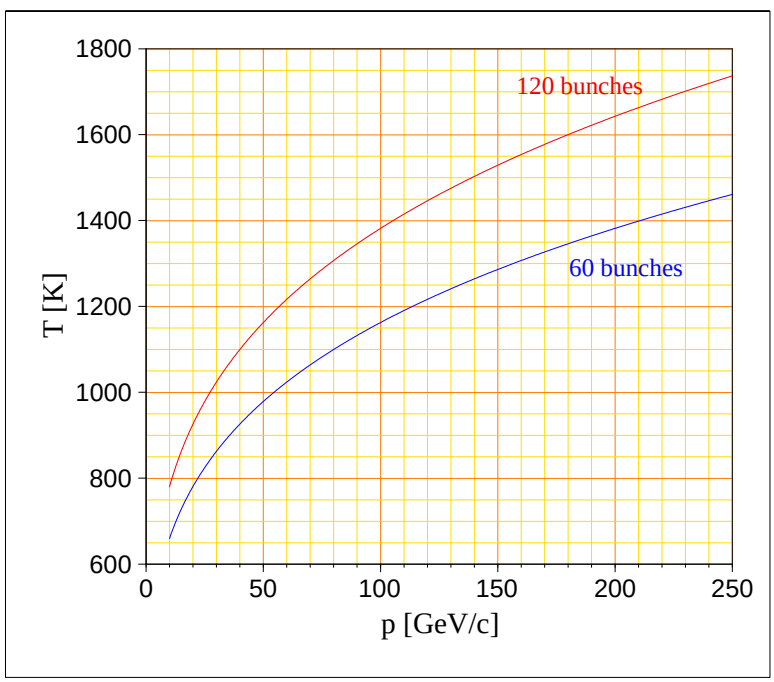

Figure 8.7: Equilibrium temperature of a 5 μg/cm^2 carbon ribbon for two beam currents. The beam parameters are: 2×10^{11} protons per bunch, $\epsilon_N = 10\pi$ μm.

For a solid target, target heating from beam is always a concern. Of the total ionization energy loss of the protons interacting with the carbon fiber, 30% is deposited on the target in the form of heat[75]. For a section of a horizontal fiber of length Δx intercepting the center of a Gaussian beam of rms width σ_x and σ_y in x and y, the heating power of the beam is

$$P_h = \frac{\epsilon_h f_r N_p \frac{dE}{dx} \rho d_t}{2\pi\sigma_x\sigma_y} [d_w \Delta x] \tag{8.8}$$

where N_p is the number of protons in the machine, $f_r = 78$ kHz is the beam revolution frequency, $dE/dx = 1.78$ MeV/gm/cm^2 is the ionization energy loss for carbon, $\rho = 1.75$ gm/cm^3 is the density , d_t and d_w are the thickness and width of the carbon ribbon, respectively. The fraction of the total energy loss that is converted to heat $\epsilon_h = 0.3$, which is from the CERN studies on carbon flying wires [75]. The radiated power is given by the Stefan-Boltzmann relation

$$P_{rad} = \epsilon_{rad}\sigma_{SB}(T^4 - {T_0}^4)\,[2d_w\Delta x] \tag{8.9}$$

where $\epsilon_{rad} \approx 0.8$ is the emissivity, σ_{SB} is the Stefan-Boltzmann constant, T is the fiber temperature and T_0 is the ambient temperature. The expression in square brackets in Eqs. (8.8) and (8.9) is the surface area of the element. The maximum equilibrium temperature is then,

$$T_{eq} = \left(\frac{\epsilon_h f_r N_p \frac{dE}{dx} \rho d_t}{4\pi\sigma_x\sigma_y\epsilon_{rad}\sigma_{SB}} + {T_0}^4\right)^{1/4} \tag{8.10}$$

Since the beam size depends on the energy the equilibrium temperature varies as ${p_{beam}}^{\frac{1}{4}}$. Fig. 8.7 shows the expected equilibrium temperature as a function of beam energy for a 5 μg/cm^2 carbon ribbon. It is generally inadvisable to run the fiber at temperatures exceeding 2000°K which is the onset of thermionic emission since this would shorten the life-time of the fiber. The result shows, with the ribbon target, heating is not a problem even with smaller beam emittance $\epsilon_N = 10\ \pi$ mm mrad.

8.6 Event Rates and Emittance Blowup

In the CNI interference region, the cross sections of elastic and inelastic scattering are comparable. One can use the elastic cross section to estimate the event rates. Each Si detector has twelve 0.1 cm × 1 cm strips and is away from beam by 15 cm. It is the same detector used in AGS E950 and the strips were designed to get angle information. From the experience in AGS E950, the angle information is not essential, the strips are mounted parallel to the beam direction in RHIC. The event rate of each strip will only be one twelveth of rate of the total detector.

As several quantities are used commonly for event rate estimation, following are a few formulae to calculate them. The luminosity is given by

$$L = f_r N_p \frac{d_w d_t}{\sqrt{2\pi}\sigma_y}\left[\frac{\rho N_A}{A_w}\right] \tag{8.11}$$

where d_t and d_w are the thickness and width of the carbon ribbon, respectively, $A_w = 12$ gm/mole is the atomic weight of carbon and $N_A = 6.022 \times 10^{23}$ atoms/mole is Avogadro's number.

The event rate per bunch crossing is given by,

$$R_{C,crossing} = L \cdot \delta\sigma = \frac{d_w d_t}{\sqrt{2\pi}\sigma_y} \left[\frac{\rho N_A}{A_w}\right] \delta\sigma \tag{8.12}$$

where $\delta\sigma$ is the instrumental cross section.

As the target sitting in the beam the emittance of the beam is increased due to multiple scattering. Total of 10^7 Carbons in the polarimeter is needed to obtain a 5% statistic error in polarization. It is useful to parameterize the resulting total emittance growth in terms of the total Carbon statistics N_C,

$$\Delta\epsilon_{(x,y)tot} = \frac{3\beta_{(x,y)}}{\beta^3\gamma} \frac{1}{L_{rad}} \left[\frac{0.0141}{0.938}\right]^2 \frac{N_C}{N_p} \left[\frac{A_w}{\rho N_A}\right] \frac{1}{\delta\sigma} [\pi] . \tag{8.13}$$

where $\beta_{(x,y)}$ is the (x,y) lattice beta function at the target location, β and γ are the usual relativistic factors and $L_{rad} = 18.8$ cm is the radiation length of the target material.

Detector Set	Energy(GeV)	Time(sec.)	$\Delta\epsilon$ (πmm-mrad)	event rate per bunch
2 detectors	25	154	1.63	0.138
	100	77	0.36	0.277
4 detectors	25	109	1.15	0.196
	100	54	0.25	0.391

Table 8.1: Rate estimates and emittance blowup for following running condition: $\epsilon_N = 10\pi$ mm mrad, protons/fill = 6 bunches at 1×10^{11} protons/bunch.

Detector Set	Energy(GeV)	Time(sec.)	$\Delta\epsilon$ (πmm-mrad)	event rate per bunch
2 detectors	25	3.85	0.02	0.277
	250	1.22	0.002	0.554
4 detectors	25	2.72	0.14	0.391
	250	0.86	0.0014	1.238

Table 8.2: Rate estimates and emittance blowup for full luminosity. Following parameters were assumed: $\epsilon_N = 10\pi$ mm mrad, protons/fill = 120 bunches at 2×10^{11} protons/bunch.

With the relations given above the event rates and measuring times are estimated as shown in Tables 1-2. A carbon ribbon target of 4 μg/cm^2 is assumed. For the six bunches scenario, the emittance growth at injection is about 16% for one measurement. Thus, the measurements at injection would be considered moderately destructive. On the other hand, the emittance increase at 100 GeV/c is negligible and such measurements can be parasitic. As can be seen from the table, measurement times are quite reasonable. With full intensity, the emittance blowup is negligible for the full energy range.

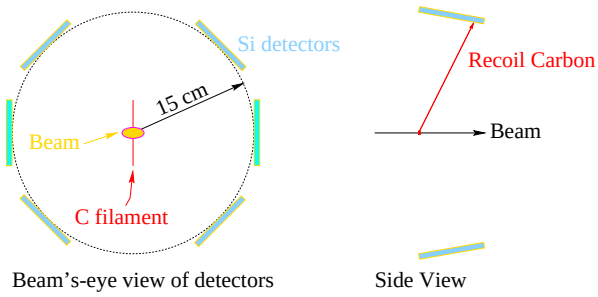

Figure 8.8: Cross section of the target chamber. Beam is going into the paper and hits the carbon target in the center of the beam pipe. The carbon target is 5.5 μg/cm^2 thick and 11.6μm wide. The thicker target was used to increase event rate. Note that for the initial commissioning run, the two horizontal detectors (cyan) were not installed.

8.7 Commissioning Experience

Only one helical Siberian snake[76] has been installed in year 2000. The stable spin direction is in the horizontal plane with snake on and in the vertical direction with snake off. The injected beam from AGS is in the vertical direction. It is necessary to have the snake off during injection and then have it adiabatically turned on so that beam polarization follows the stable spin direction and turns from vertical to horizontal. Four silicon detectors installed obliquely, as shown in Fig. 8.8, can measure both transverse components (another pair of detectors will be installed at left and right before next run). These detectors provide measurements of both vertical polarization (left-right)=((1+2)-(3+4)), and radial polarization (up-down)=((1+3)-(2+4)), with the detectors numbered as in Fig. 8.8.

The commissioning was done by injecting 6 proton bunches with alternating polarization, for example, $\uparrow\downarrow\uparrow\downarrow\uparrow\downarrow$. There were about 3 $\times 10^{10}$ protons per bunch with a separation of about $2\mu s$. Injection energy was 24.3 GeV ($G\gamma = 46.5$). The AGS E950 readout, FERA ADCs and TDCs, were used for this run. The trigger was a coincidence between the beam bunch crossing timing and any delayed Si strip hits. Triggers were rejected if no silicon detector strip was above threshold.

The identification of a carbon band is shown in Fig. 8.9 as energy vs. time-of-flight plots, for each of 12 strips on one silicon detector. All 48 silicon strips worked beautifully. In fact, there is very little background as shown for the reconstructed mass in Fig. 8.10. An alpha peak can be seen clearly (presumably quasi-elastic p-alpha scattering). The energy was calibrated using observed carbon and alpha mass peaks. The commissioning showed that p-C CNI scattering can be identified with little background.

When the data are combined as discussed above to measure vertical and radial polarization, the vertical polarization of the injected beam was observed (see plot A of Fig. 8.11). Reversing the injected beam polarization resulted the beam polarization reversed. As a cross-check, unpolarized beam was injected and zero polarization was observed in RHIC. Based on the preliminary analyzing power for p-C CNI polarimeter and AGS internal polarimeter, the polarization at RHIC injection was about 19 ± 1 % (statistical error only), which was less than the polarization measured at the AGS extraction, 33 ± 1% (statistical error

only). The polarization at injection is sensitive to the beam energy and betatron tunes. Due to the limited running time, no effort was devoted to explore the tune space and injection beam energy during the commissioning.

With one snake in the ring, it is necessary to turn it on after beam injection, so that the stable spin direction is then turned into the horizontal plane from vertical direction. The angle in the horizontal plane is determined by the beam energy, snake rotation axis and location of observation point relative to the snake. The polarimeter can only measure either vertical or radial components, so the beam energy was properly chosen to get radial component at the polarimeter. The expected radial polarization was observed after the snake was adiabatically turned on (see plot B of Fig. 8.11). This proved that the snake rotated the spin as expected. Polarized beam was accelerated to 25.1GeV ($G\gamma = 48$), past several resonances including a strong resonance with a strength of 0.02. Measured polarization reversed direction radially as expected and showed similar magnitude (see plot C of Fig. 8.11). Polarized beam was then accelerated to 29.2 GeV ($G\gamma = 55.7$), past many more resonances including two more strong resonances, and again was measured with the expected direction and no noticeable polarization loss (see plot D of Fig. 8.11). When polarized beam was accelerated to 31.6 GeV ($G\gamma = 60.3$) , just above a much stronger resonance with strength of 0.07, no significant polarization was measured (see plot E of Fig. 8.11). Most likely the depolarization is due to the strong snake resonances because the vertical closed orbit was too large and the betatron tune was moving around during acceleration. No time was spent in the commissioning to

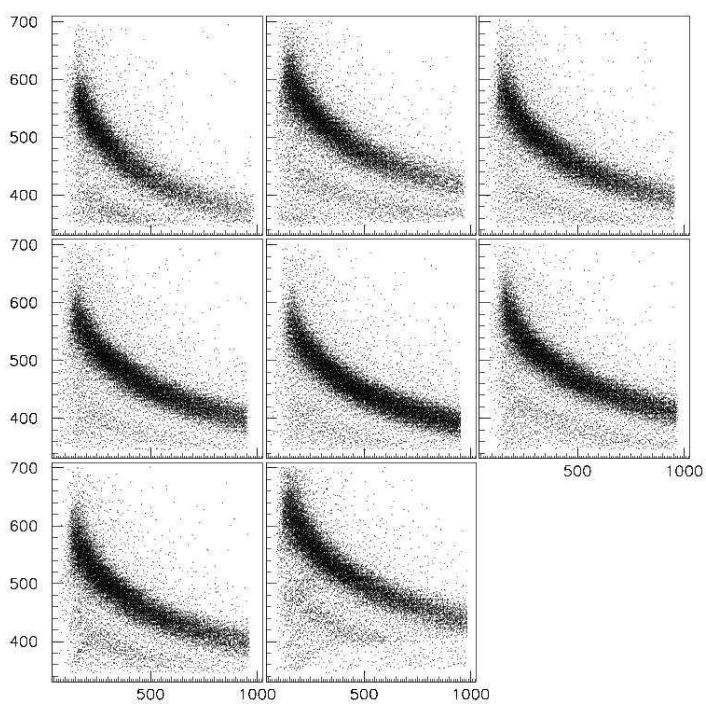

Figure 8.9: Scatter plot between the ADC values (horizontal axis) and the time of flight (vertical axis) for Si detector 1. Only center eight strips were used in the analysis.

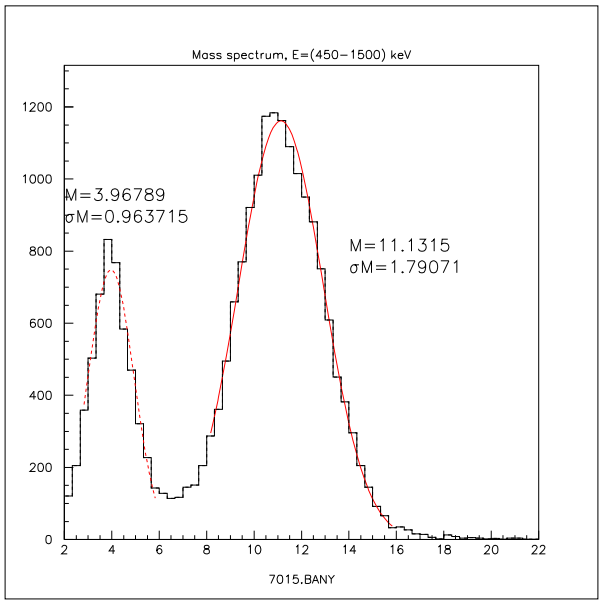

Figure 8.10: Mass spectrum. The horizontal axis is in the unit of GeV and vertical axis gives the event counts.

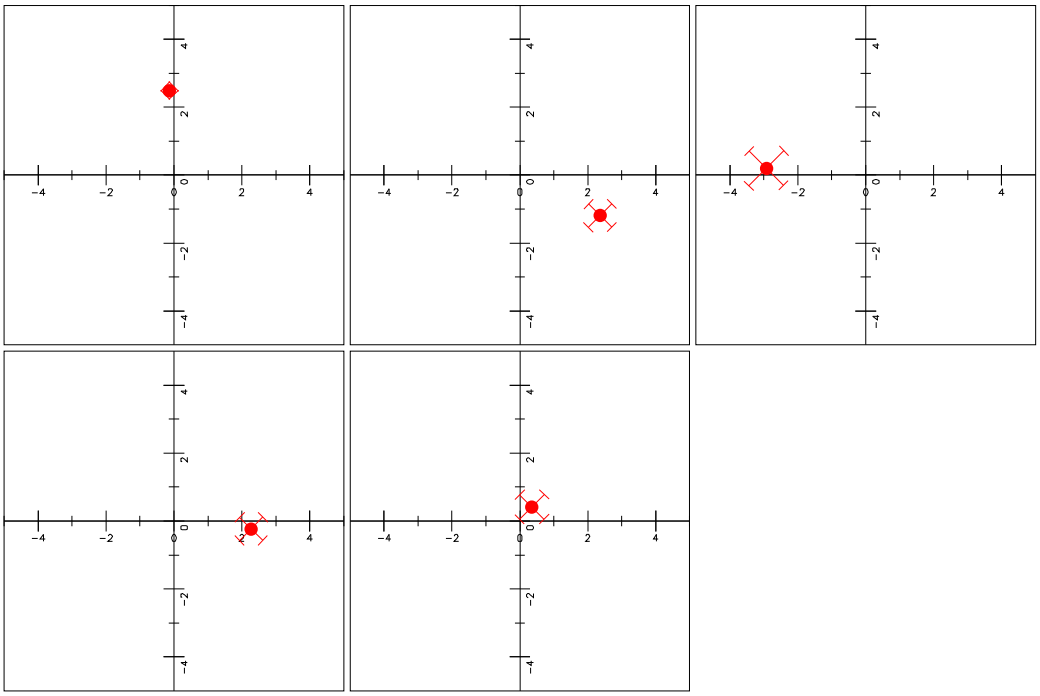

Figure 8.11: Plot of polarization vectors at various energies. Both horizontal and vertical axes are in units of asymmetry $\times 10^{-3}$. Top row from left to right: A) $G\gamma = 46.5$ and snake off; B) $G\gamma = 46.5$ and snake on; C) $G\gamma = 48$ and snake on; bottom row from left to right: D) $G\gamma = 55.7$ and snake on; E) $G\gamma = 60.3$ and snake on. The error bars reflect the fact that the asymmetries were derived from the 45° detectors.

correct them. In next run, our goal is to control the vertical betatron tune to better than .005 and the vertical closed orbit to better than 0.5 mm rms. Both of these requirements will be a major focus for the

preparations for next run but are quite feasible based on the operational experience with gold beams.

8.8 New DAQ system

With the E950 electronics, there was considerable dead time: readout of a full buffer took 1.5s. For next run, the first to take data with colliding polarized protons, There will be 60 bunches in each ring and expect 10^{11} polarized protons per bunch. The bunch spacing is 212 ns. The rates in this scenario compared to the commissioning will be about 10 times greater per bunch and 100 times greater overall. The deadtime in this situation for the AGS-type readout would be 99%, and it will not be possible to distinguish two hits in the same strip, which will occur at percent frequency. Considering the raw asymmetry is around a percent, with 2% average analyzing power and polarization of 50% expected, the two hits problem is a very serious problem.

A better method is to use Wave Form Digitizers (WFD). WFD provides the evolution of the pulse and its complete history. It also yields the shape of the pulse assisting in identification of the detected particle. WFD readout is ideal for this application, since no information other than energy and time on the event are available and needed. Therefore the WFD data is exactly what is needed and is complete. The clock frequency is set according to the rise time, which is set to be short to improve double pulse resolution. In future runs, WFD readout is planned. The plan is to take about 30 ns of data for each pulse, with digitization every 3 ns and no deadtime. A pulse is defined as a change in pulse height (differential measurement). A prototype WFD module was tested during the commissioning run and worked as expected. A digitized pulse is shown in Fig. 8.12.

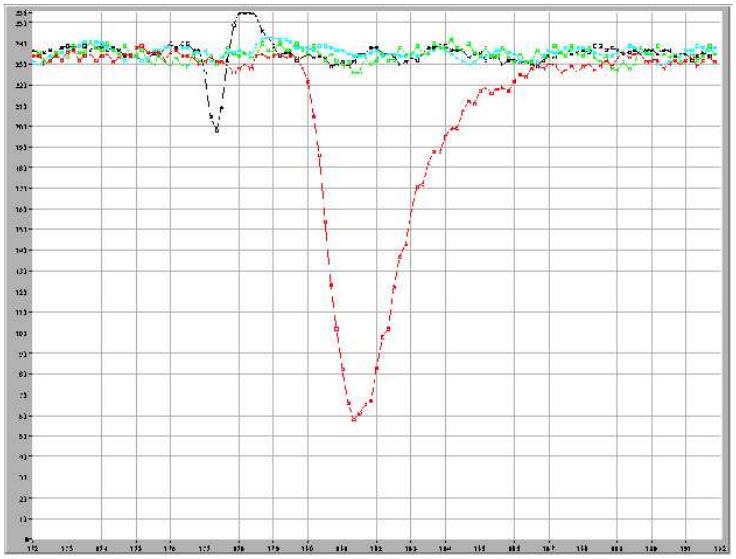

Figure 8.12: A wave form taken during the commissioning. Four traces corresponds to four different Si strips. One can see a smaller bipolar pulse followed by a large pulse. The bipolar pulse is pickup from the beam at prompt time, and the large pulse is a carbon signal. For the particular bunch crossing, there is one event from one of the four Si strips.

A major issue for the WFD is how to handle the large amount of data. It is under consideration of either writing to a local memory until the events needed for a measurement are collected (10^6 events, in tens of seconds for the 2001 run), or developing a fast asynchronous readout. Current plan is to program the WFD to obtain energy and time (also for multiple pulses), and to then sum for scalar type information the WFD hits in the carbon band. This then reduces the data size to minimal levels, and the need for a fast readout would be alleviated.

Chapter 9

Commissioning and Operational Issues

Our goal is to collide 70% polarized protons beams in RHIC with luminosity up to 2×10^{32} cm^{-2} sec^{-1}. A_{LL}, A_L, A_{NN}, and A_N are to be measured at STAR and PHENIX, and A_{NN} and A_N at $pp2pp$ and possibly other intersections. The statistical errors can be quite small — for example, 10^{-3} in asymmetry for jets with $p_T > 40$ GeV/c is desirable and achievable. Physics measurements will explore a wide energy range: $\sqrt{s} = 50$ to 500 GeV.

In this section we outline an approach to commissioning the polarized proton collider and we discuss several issues for physics running.

9.1 Operational Modes of RHIC for Polarized Proton Running

For normal operation no special operational modes of RHIC are required for the acceleration and storage of polarized protons. Since depolarizing resonances are driven predominantly by vertical orbit excursions, particular care has to be given to the corrected vertical closed orbit and the vertical beam emittance. This means that beam blow-up from beam-beam interactions and stop-bands should be minimized. To avoid depolarization from snake resonances the fractional vertical betatron tune including tune spread has to be kept well within $\frac{1}{6} = 0.1667$ and $\frac{3}{16} = 0.1875$, especially at the energies of the three strongest intrinsic resonances: $G\gamma = 3 \times 81 + (\nu_y - 12)$ [$E = 136$ GeV], $5 \times 81 - (\nu_y - 12)$ [$E = 203$ GeV], and $5 \times 81 + (\nu_y - 12)$ [$E = 221$ GeV]. Also the acceleration rate would have to be at least $\dot{\gamma} = 4.2$ sec^{-1}, which corresponds to $\frac{dB}{dt} = 0.05$ T/sec.

During commissioning, acceleration cycles that allow for polarization measurements at various energies are required, in particular at the injection energy, at energies below and above the 3 strongest intrinsic resonances, and at some intermediate energies: 25 GeV, 50 GeV, and 100 GeV.

9.2 Commissioning

The commissioning approach will be step-wise, beginning with one ring, no polarization, and advancing to both rings polarized at full energy. We expect to commission one ring to 100 GeV in FY2000. Com-

missioning both rings and to 250 GeV will be done in subsequent years. At the time that RHIC begins polarized proton studies, RHIC will have already been fully commissioned for heavy ions, and the AGS will be a well-understood injector for polarized protons. (E880, the partial snake experiment in the AGS, and E925, the polarimeter calibration at RHIC injection energy, will have been completed.)

It is important for efficient commissioning to optimize the measurement cycle, filling → polarization measurement → filling, and on-line polarization results are required. With an inclusive π^- polarimeter in each ring, we estimate that this cycle can be kept to about 10 minutes, with a 7% polarization measurement from each cycle. We set the spectrometer currents for the polarimeter at the desired kinematic region ($x_F = 0.5$, $p_T = 0.8$ GeV/c). We may also use a CNI polarimeter measuring proton-Carbon elastics. We expect, at the time of commissioning, to use 60 bunches per ring and to have 4×10^{10} protons per bunch. Emittance blow-up from polarization measurement during commissioning is not an important issue because we will measure the polarization at energies away from resonances. Emittance blow-up is largest at injection, and we will use a limit of an increase of $\Delta\varepsilon_N = 10\pi$ mm mrad. From Table B.2, we use a factor of 10 less beam for commissioning. The measuring time is then 180 seconds to make a 7% polarization measurement. The emittance blow-up is 3π mm mrad. Of the 60 bunches, half would be loaded with spin up and half with spin down, for each cycle. A pipeline readout would store the inclusive π^- tracks seen by the polarimeter, tagged for the spin direction of the bunches. Polarization is obtained nearly on-line as discussed in Chapter 8.

Besides the polarimeters, each ring will have an rf spin-flipper. This device can be used to measure the spin tune. At the resonant frequency of the device, the polarization can be adiabatically reversed. If left on for a longer time, the polarization will be driven to zero. In this way, the resonant frequency can be identified: by measuring the polarization at different frequencies. The spin tune is then the resonant frequency divided by the revolution frequency:

$$\nu_{sp} = \frac{f_{rf,res.}}{f_{rev}}. \tag{9.1}$$

The spin tune can be measured very accurately, and the tune should be 0.500 if the Siberian Snakes are set up properly.

9.2.1 Commissioning Steps–One Ring Only

A. Snakes off, establish bunched beam at 25 GeV to flat-top energy (100 GeV in FY2000) – perform closed orbit corrections, etc.

B. Turn on one snake, no polarization, 25 GeV

- adjust V, H, trim supplies for Snake to center beam using beam position monitors (BPMs)
- adjust tune to correct for Snake tune shift (use tune-meter)

– adjust multipole correction magnets for sufficient storage time (>10 min.) (use current transformer)

– Snake coupling correction using skew quads

– measure orbit excursion inside Snake (this uses the BPM at the center of the Snake)

C. Turn on second Snake in ring (alone), and repeat B.

– balance orbit excursion in both Snakes

D. Both Snakes on – check excursions and lifetime (don't anticipate a problem)

E. Polarimeter check-out

– target in/out, accidentals (polarimeter has been calibrated in E925 at RHIC injection energy)

F. Transverse polarization in one ring, 25 GeV, both Snakes on (note that the Snakes are not necessary to maintain polarization at 25 GeV)

– commission polarimeter – look for asymmetry

– no asymmetry? Check AGS polarization. If OK, vary transfer line.

– observe asymmetry. Check repeatability; put in $P = 0$, measure $P = 0$; turn off both Snakes, should measure $P = P_{AGS}$; turn off one Snake, should measure $P_y = 0$; small scan of (X, p_T) vs. NA^2 to optimize and check polarimeter.

– measure spin tune with rf spin flipper

– measure spin tune vs. energy – constant, 1/2 if the Snake settings are correct. Otherwise, there are several possible effects. If the spin tune depends on energy, then the Snakes would not be exactly 180° apart in ring field integral. This is not expected (and is not correctable). If the spin tune is independent of energy but not 1/2, two effects can contribute: the Snake axes are not orthogonal, or the Snake precession angles are not 180°. These can be explored and corrected by adjusting each separately.

– commission spin flipper

– at resonant rf frequency, measure polarization vs. time on to establish spin flip

– many spin flips – measure polarization loss from spin flipper

G. Accelerate – steps determined by spin resonances (measure just before/after expected resonance). Larger resonances at about 120, 140, 220, 240 GeV. (FY2000 will be below these resonances.)

- need to check spin tune at lower energies (expect different effective lengths of Snake magnets vs. orbit excursion)
- if the polarization is reduced or lost, measure spin tune and adjust Snakes
- also measure asymmetry in polarimeter at 200 GeV, the energy where the π^- asymmetry was measured at FNAL. This would give an absolute polarization for the beam. (FY2001)

H. Commission the spin rotators (FY2001)

- unpolarized beam: turn on each rotator and adjust so that there is no orbit shift, match the rotators by comparing BPMs in centers
- turn on each rotator, one at a time, and with polarized beam use polarimeters to measure the predicted P_y at the polarimeter position vs. different excitations of each rotator, and vs. energy
- with pairs of rotators energized, measure P_y at the polarimeter location (all polarization should be in the y direction)
- We do not have an approach to measure the longitudinal polarization at the intersection region. We could measure the absence of transverse polarization at the intersection, with the presence of vertical polarization at the polarimeter. Each experiment would need to evaluate the practicality of doing this.

For FY2001 and beyond, the above procedure would be repeated for the second RHIC ring. With two rings, relative luminosity measurements and polarization lifetime measurements would be performed.

9.3 Physics Running–Issues

9.3.1 Bunch pattern

Each bunch is to be injected independently, so the "pattern" of polarization direction for the 60 to 120 bunch positions in each ring can be arranged in an optimal way. At each intersection region the same pairs of bunches interact, but there are different pairs at each intersection. It is typically desirable to collide equal numbers of $(++, +-, -+, --)$ bunches at each experiment, where $+-$ represents a bunch in one beam with polarization up colliding with a bunch in the other beam with polarization down.

One solution which would satisfy all the intersections is to load the bunches of one ring $(++--++--++--$, etc.), and load the bunches of the other ring with $(+-+-+-+-+-+-$, etc.). The pattern and time of one bunch is given by RHIC to the experimenters. Each experiment chooses collisions to have complete sets of $(++, +-, -+, --)$. This is illustrated in Fig. 9.1.

It may be desirable to correct for polarized proton beam-gas scattering. This can be done with the empty bunches in the abort gaps of each ring, giving intersection combinations of $(0+, 0-, +0, -0)$.

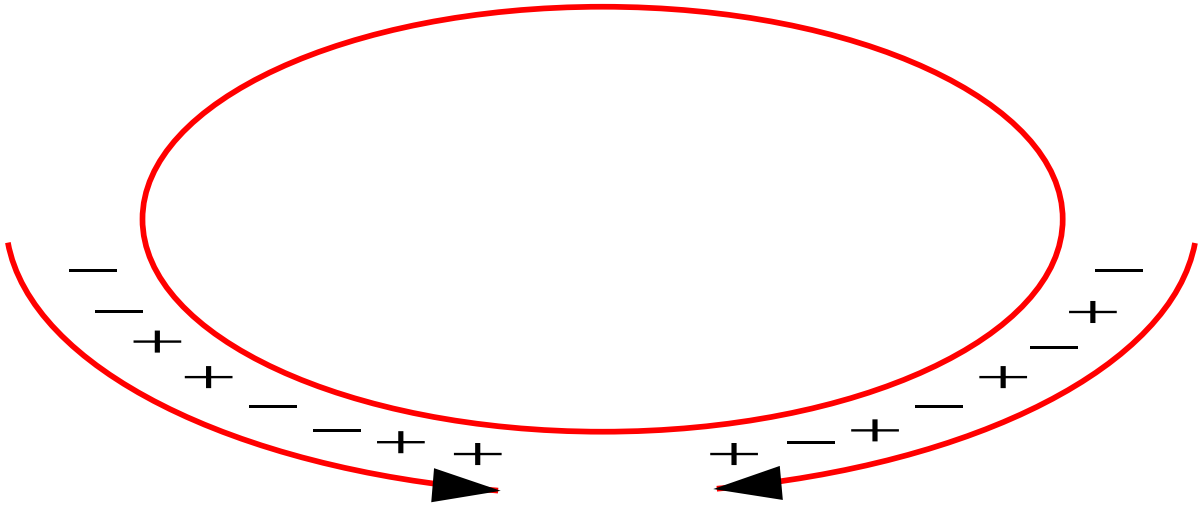

Figure 9.1: The pattern of the polarization signs of the bunches in the two counter-rotating beams in RHIC.

9.3.2 Frequency of Spin Flip

Because the same bunches collide for a given experiment, periodically reversing the spin will reduce systematic errors for asymmetry measurements even further. Polarization reversal will take about one second. The frequency of reversal depends on the effect on luminosity from emittance blow-up, and on polarization loss from the flipping process. Neither is expected to be large.

9.3.3 Recogging

Another tool available to reduce systematic errors is to recog the collisions. This can be done in one second, so that each experiment would then see different pairs of bunches collide. This could be used to randomize the order of the preparation of the bunches, as seen by the experiments. Recogging could also be used to move empty bunches so that each experiment can collect background data for part of the fill. In principle, recogging and spin-flipping can be used to give equal luminosity for $(++, +-, -+, --)$ combinations at an intersection region, although many steps are involved, as well as the assumptions that the number of protons in each bunch and the bunch polarization is unchanged by each step.

9.3.4 Systematic Errors

For each fill, the spin condition changes at each experiment every 100 nanoseconds or 3.6×10^{10} times per hour. In addition, the spin can be reversed for each crossing, possibly once per hour. The collisions can be recogged. And, finally, the pattern can be changed for each fill.

Experiments making particularly sensitive asymmetry measurements may desire to measure relative luminosity of individual bunch crossings. An asymmetry measurement to 10^{-3} requires that the overall

relative luminosity be known (or that the bunch luminosities be equal) to 10^{-4}. If the individual bunch crossing luminosities are independent of spin state *or* the spin flip process is independent of spin state, then the luminosities will be equal. If this is not assumed, the experiment can measure the bunch crossing relative luminosity with a factor of 100 more counts in a luminosity monitor than signal. If the signal counts are 10^6, collected over 10^6 seconds, the luminosity monitor must have a rate greater than 100 Hz.

9.3.5 Beam Polarization Measurements

The polarization measurements are unobtrusive at 250 GeV, with $< 0.1\%$ emittance growth to obtain a 7% polarization measurement. At 25 GeV, the emittance growth is 1-2% per measurement for full intensity beams (120 bunches and 2×10^{11} protons per bunch). The frequency of measurement depends on the stability of the system. We assume that a measurement would be made every hour, and the data for the previous hour would be thrown out if the polarization were lost.

The following two appendices cover earlier concepts of the polarimetry.

Appendix A

Toroidal Polarimeter Design

The two-arm polarimeter allows excellent cancellation of biases in polarization measurements. The toroids have little fringe field in the beam region and yet provide a large field integral for the pions. The result is a compact two arm device where one arm fits between the two RHIC rings and is upgradable to provide for possible up and down asymmetry measurements in case of radial polarization of the beam at the polarimeter location.

The toroidal design also naturally covers the required energy range without the need for adjusting magnet and detector positions. In the original dipole polarimeter we located the magnet at 30 m from the target and at 6.4 mrad angle for $p_{beam} = 250$ GeV/c; the magnet was relocated to 9.5 m and 64 mrad angle for $p_{beam} = 25$ GeV/c. Such readjustment of polarimeter position at the low energy was necessary in order to maintain a similar solid angle and rate. For a detector at a fixed distance from the target, the coverage in $\Delta\phi/2\pi$ is inversely proportional the scattering angle. However, for the toroids, scattered pions are bent in the r-z plane maintaining constant ϕ. At the lower energy it is possible to transport the pions scattered at 64 mrad to a detector at 30 m, maintaining the same coverage in $\Delta\phi/2\pi$ as for higher energy. Thus, with the toroidal design, it is only necessary to adjust the toroid fields to cover the full energy range and magnets and detectors do not move.

The layout of one polarimeter system is shown in Fig. A.1. Pions are produced by the interaction of polarized protons on a 5 μm carbon fiber target about 1.5 m downstream of Q4. A string of four toroids surrounds the warm beam line section between Q4 and Q3. The first toroid is 3 m long, the second and third are 1.5 m long all of the same cross-sectional geometry. The fourth toroid is 6 m long and its bore radius is 3 cm larger than that of the first three. The latter allows for placement of heating pads around the beam pipe. The inter-magnet drift regions of 1.4 m are for possible placement of collimators and detectors. This arrangement provides enough space for a collimator and a 6 m long Cerenkov counter as well as tracking detectors. If necessary a hadron calorimeter may be placed downstream of the Cerenkov counter. Each polarimeter has four arms that may be used to measure left-right and up-down asymmetry. The limited space between the two RHIC rings constrains detector sizes.

The production angle and selected spectrometer momentum depend on the beam energy; at RHIC

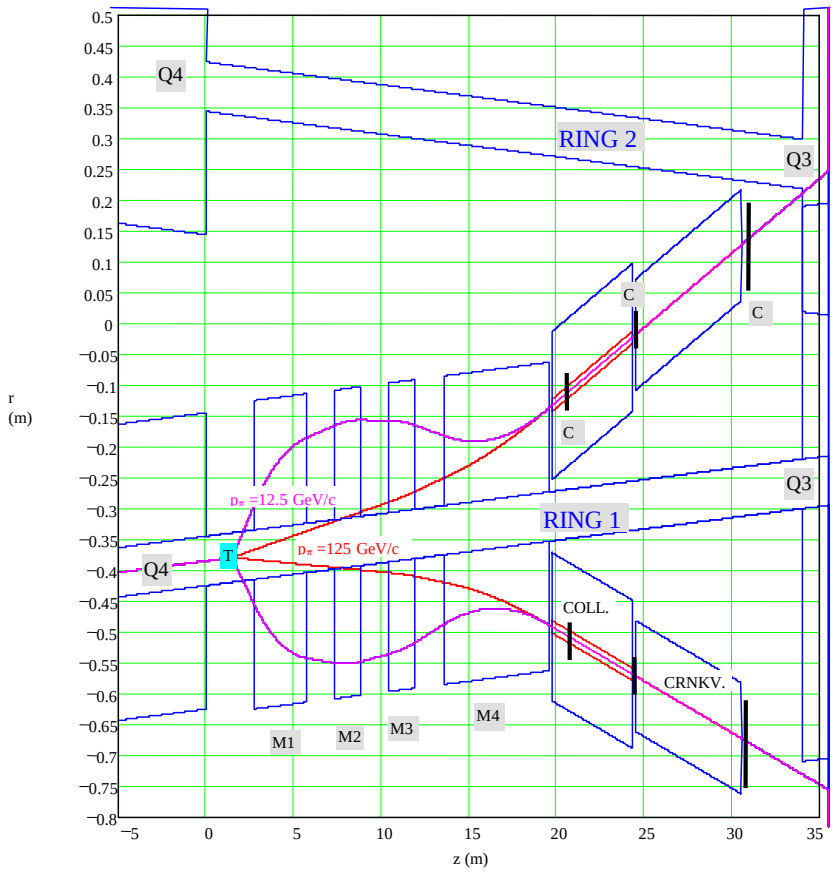

Figure A.1: Plan view of the two-arm polarimeter between Q4 and Q3 including the two RHIC beam lines. The two trajectories shown were calculated assuming hard edged magnets. The total bend angles for the 25 GeV/c and the 250 GeV/c tunes are 46 mrad and 12 mrad, respectively.

	Trgt	**M1**	**M2**	**M3**	**M4**	**Coll.**	**Crnkv**
Position (m)	1.5	2.75	7.35	10.45	3.55	19.75	24.55
Length (m)	0	3	1.5	1.5	6	4.6	6
23 GeV/c		-1	-1	-0.85	+0.380		
25 GeV/c		-0.99	-0.65	-0.4471	+0.3321		
100 GeV/c		-0.2	-1	-0.9	+0.782		
200 GeV/c		0	0	-0.275	+0.94		
250 GeV/c		0	0	+0.9	+0.9		

Table A.1: Parameters for the polarimeter layout. The positions of the elements are with respect to the end of Q4. The magnet settings are in fractions of the TOSCA design fields in Fig. A.3.

injection of 25 GeV/c, the production angle would be 64 mrad and the π momentum 12.5 GeV/c; at 250 GeV/c RHIC beam momentum, the production angle is 6.4 mrad and the π momentum is 125 GeV/c. For the smallest angle, 6.4 mrad, the spectrometer magnets will be set for near maximum deflection so that detectors behind the 2 cm slit collimator are shielded from straight-through neutrals. This fixes the positions of the collimator, the Cerenkov counter and all other possible detectors downstream of the collimator. For all other beam momenta, including injection at about 25 GeV/c, the four toroids can be set to guide pions with $x_F = 0.5$ and $p_T = 0.8$ GeV/c through the collimator. The apparatus thus allows measurement at various beam momenta without major readjustments to the detector positions. The details of the layout in Fig. A.1 are listed in Table A.1. The table also includes possible tunes at selected beam energies that will allow measurement in the desired kinematic range of $x_F = 0.5$ and $p_T = 0.8$ GeV/c.

A.1 Toroidal Magnets, Pion Exit Windows

Each toroid consists of four pie-shaped pole pieces with a 7° angular opening between adjacent poles (see Fig. A.2). The right and left arms measure vertical polarization, and, if necessary the steel wedges can be removed from the up and down arms and, with proper instrumentation, may be used to measure radial polarization. Several options were considered in the design of the toroidal magnets, and the parameters of a 2-dimensional TOSCA design are indicated in Table A.2. Bipolar power supplies are necessary for measurements with positive as well as negative pions and for flexibility in tuning. In order to achieve sufficient integrated field strength the beam pipe diameter was chosen to be 8 cm. Fig. A.3 shows the radial and azimuthal field configurations in the middle of the two types of magnets. Note that there are strong radial fields near the coil positions.

The four openings break the toroidal symmetry and give rise to octupolar fringe fields inside the RHIC beam pipe. The amplitude of the field at a radius of 1 cm is about 6 Gauss. A 5 mm thick iron shielding reduces the amplitude by more than a factor of 20 and the perturbation to the RHIC beam is negligible [77].

Multiple Coulomb scattering at the pion exit windows is an important issue that impacts the accuracy of track reconstruction. Even though the detailed mechanical design has not yet been completed, we envision providing a single thin window or set of multiple thin windows (3 mil Aluminum) over the 6 m section of the beam line spanning the pion production angles of 64 to 6.4 mrad. For a 3 mil aluminum window the multiple scattering angles are 0.13 mrad and 0.04 mrad at pion momenta of 12.5 GeV/c and 125 GeV/c, respectively. The multiple scattering angle is significantly less than the pion production angle and the bend angle by the spectrometer. The expected multiple scattering angles at the exit window are thus tolerable. The multiple window option carries the risk of not being able to measure the polarization at some energies where the desired production angle happens to take the pions through the thick sections of the beam pipe.

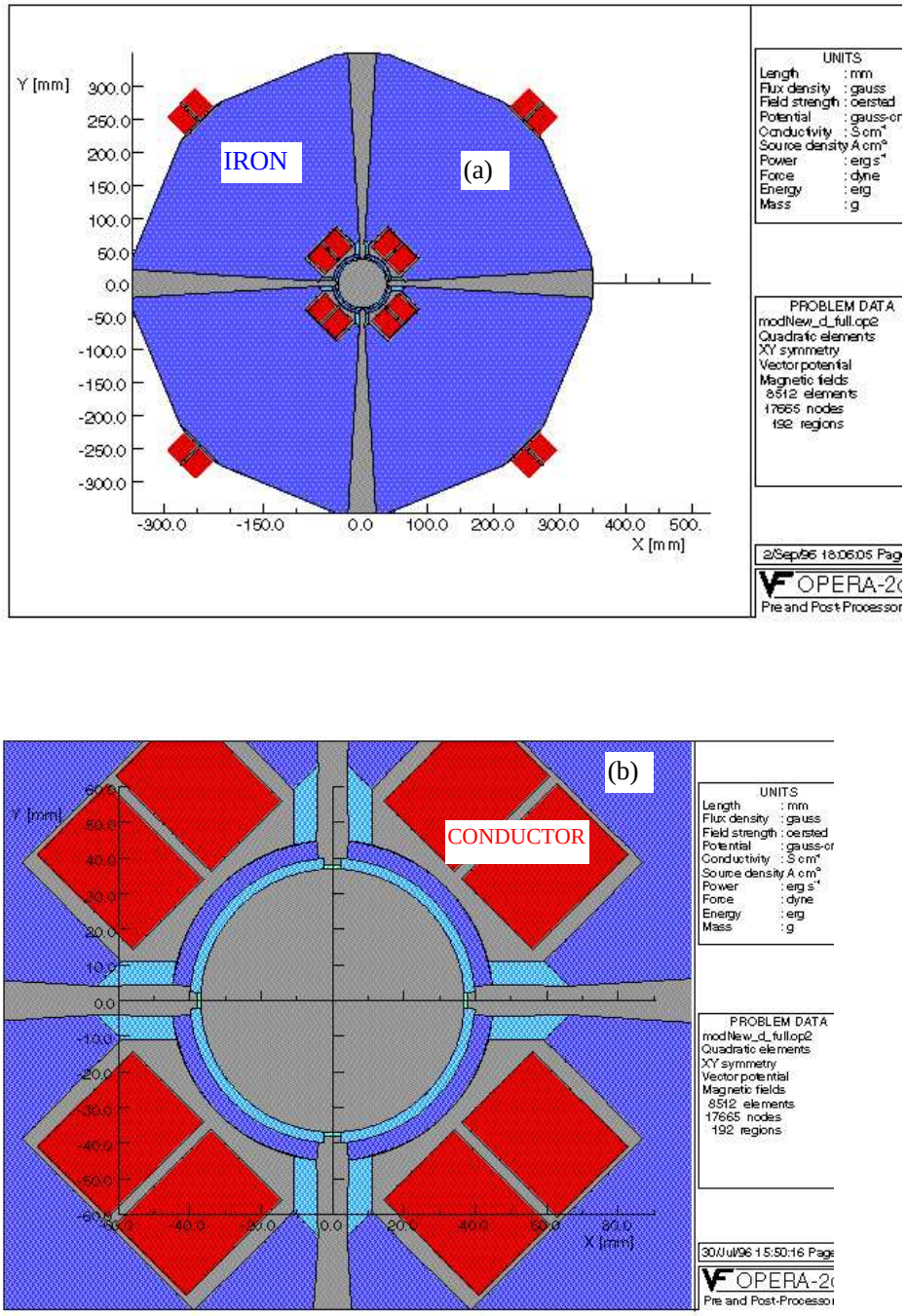

Figure A.2: Cross-sections of the toroidal magnets. The iron shield around the beam pipe reduces the field leakage by more than a factor of 20.

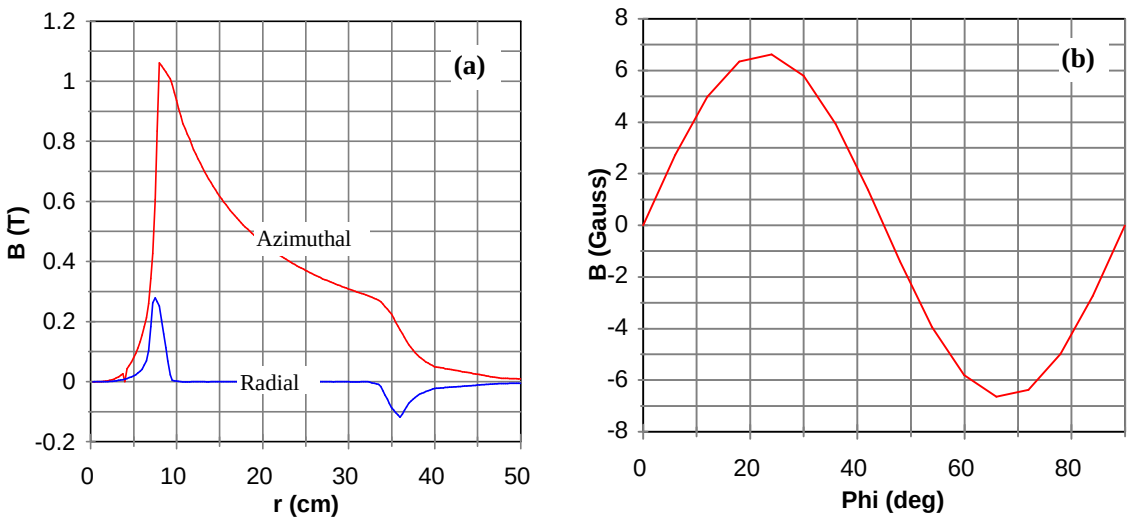

Figure A.3: (a) Expected azimuthal and radial magnetic field strength within the gaps in the toroid. The azimuthal field varies very little from the mid-plane to the half-angle limit of 3.5°. The radial field vanishes at the mid-plane and changes sign between the upper and lower halves of the 7° opening; the radial field plot shown is for a plane at 3° from the mid-plane. (b) The radial component of the leakage field inside the beam pipe at r=1 cm, as function of azimuthal angle with no magnetic shielding.

Turns per quadrant	31
Copper Conductor	9 mm × 9 mm, 5 mm hole
Max. Current Density	550 A/cm^2
Max. Current	332 A
Voltage	41 V for $L = 1.5$ m; 52 V for $L = 2$ m
Power Supply (bipolar)	15 KW for $L = 1.5$ m; 17 KW for $L = 2$ m

Table A.2: Parameters for a preliminary design of a toroidal magnet. Voltage specifications were estimated assuming that there will be no field ramping requirements.

p_{beam} (GeV/c)	Luminosity ($cm^{-2}s^{-1}$)	$N_{\pi/bunch}$	T_{meas} (sec)	$\Delta\epsilon_x$ ($\Delta\epsilon_y$) (π mm mrad)
250	4.5×10^{34}	5×10^{-4}	3.2	0.012 (0.013)
25	1.4×10^{34}	1.5×10^{-5}	7.2	0.8 (1.2)

Table A.3: Acceptance and rate estimates for the toroidal polarimeter. Also includes expected emittance dilution due to multiple scattering for collecting 10^4 pions. The following parameters were assumed: $\epsilon_N = 20\pi$ mm mrad, protons/fill = 120 bunches at 2×10^{11} protons/bunch, $d_f = 2.5 \times 10^{-8}$m, $d_w = 10\mu$ m, $p_T = 0.8$ GeV/c, $\delta p/p = 0.1$.

A.2 Pion Production Target

The toroid design utilizes the same production target as was described in Section B.3.2.

A.3 Acceptance, Event Rates and Emittance Blowup

We define ϕ as the angle between the magnet mid-plane and the pion production plane. For pions traversing the magnet gaps between the inner conductors, the ϕ-acceptance is determined by the strength and direction of the radial fields which are significant only near the conductor positions (see Fig. A.3). These fields are defocusing in ϕ if the polarity of the magnet is set to be radially focusing as is the case for the first three magnets in the 25 GeV/c tune. The position of the first magnet in Fig. A.1 was optimized such that pions with $p_L = 12.5$ GeV/c and $p_T = 0.8$ GeV/c do not pass between the inner magnet coils. Instead they enter the first magnet at $r > 8$ cm beyond which the radial fields are insignificant. This arrangement results in a ϕ-acceptance of about 6.4°. The high energy (125 GeV/c) pions, on the other hand, always have the full ϕ-acceptance of 7° because the radial fields encountered are always focusing in ϕ.

A simple estimate of the expected θ acceptance of the system was made by numerical evaluation of the range of production angles (or p_T) that are accepted by the 2 cm slit collimator. The plots in Fig. A.4 show the acceptance as a function of x_F at the 25 GeV/c and 250 GeV/c tunes. The acceptance is seen to extend to x_F and p_T values below the desired kinematic ranges of 0.5 and 0.8 GeV/c, especially for the high energy case. From the Fermilab and ZGS experiments, significant asymmetries can be expected only above $x_F > 0.45$ and $p_T > 0.7$ GeV/c. It is therefore necessary that the system be able to reject low momentum pions that do not carry significant analyzing power.

With the kinematic acceptance defined as $\delta x_F/x_F$ of 0.1 around x_F of 0.5, and using the p_T acceptance from Fig. A.4(c) we can estimate the event rates. The result is shown in Table A.3.

As in Chapter 8, we estimate the event rates and measuring times of the toroid system. These are listed in Table A.3.

Tracking studies at beam energy of 200 GeV/c have been done. The main concern in this study was the large pion multiplicity resulting from the interaction of one bunch in RHIC intersecting the Carbon target. These cannot be separated in time by electronic means in the polarimeter with either hodoscopes

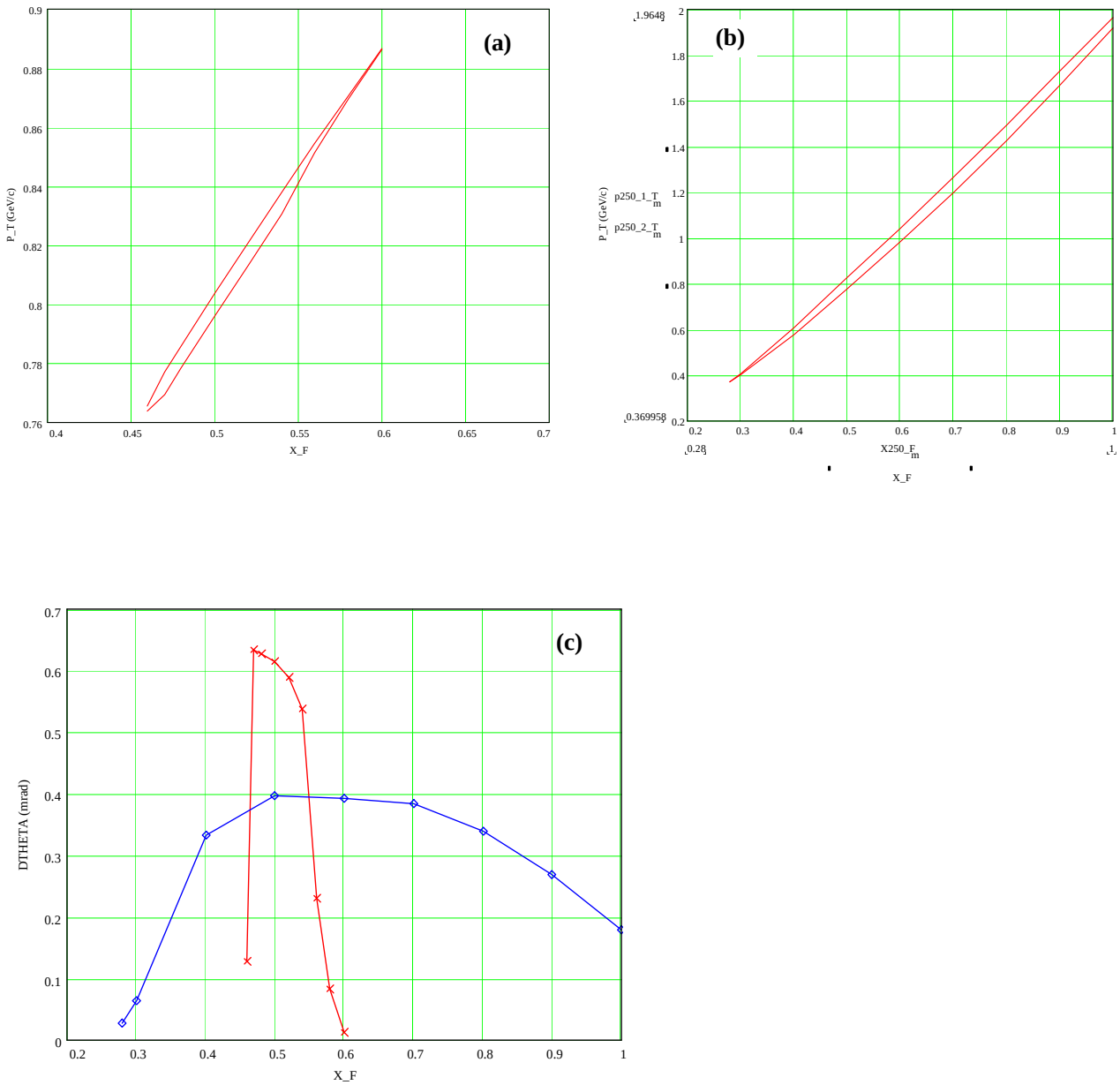

Figure A.4: Polarimeter acceptance for (a) the 12.5 GeV/c and (b) the 125 GeV/c, tunes in Table A.1. (c) The angular acceptance in the mid-plane derived from (a) and (b).

or calorimeter. The number of interactions in one crossing of the bunch with 5 μm target is of order 10^4. However, the planned Carbon ribbon target has a factor 500 lower collision rate. Simulations showed acceptable rates as for Chapter 8.

A.4 Polarimeter Detectors

The detectors will determine the (x_F, p_T) for each particle, and crudely measure the energy of each particle. If π^+ measurement becomes feasible, the Cerenkov counter will be used to identify pions. The(x_F, p_T) measurement will allow selection of pions with high analyzing power. We will want to choose pions with $x_F > 0.47$ and $p_T > 0.7$ GeV/c (see Fig. B.1)[78]. The acceptance of the toroids and collimator extends to lower (x_F, p_T) where pion production is significantly larger (see Fig. A.4) and the analyzing power lower. Therefore, the lower edge of (x_F, p_T) for the selected pions must be sharply defined. Particle identification (π^+ from p) is required for positives, although we may decide to use only π^- if the analyzing power for π^- production at the RHIC injection energy is found to be large in AGS experiment E925. We plan to use tracking to measure (x_F, p_T) and, in addition, hadron calorimeters to provide a cruder but independent measurement of the pion energy.

An important detector issue is to isolate the detectors out of the line of sight of the target. For this reason the collimator points downstream of the target, and the detectors will be downstream of the collimator. Therefore, to reconstruct the pion trajectories we use the target/beam location as an upstream point, and we measure the deflection (r) and track angle (Θ_{meas}) after the bending in the toroids, downstream of the collimator, (see Fig. A.1).

We plan to measure x_F to $\delta x_F = \pm 0.02$ and p_T to $\delta p_T = \pm 0.03$ GeV/c, which is similar to the E704 resolution. The binning in the E704 data was $\Delta x_F = 0.05$ and $\Delta p_T = 0.07$ GeV/c (full width). The δp_T resolution requires detection resolution of $\delta r = \pm 1.6$ mm and $\delta\Theta_{meas} = \pm 0.11$ mrad. The δx_F resolution requires similar resolution for Θ_{meas} and less stringent δr. The magnetic field integral should be known to $\delta p_{kick}/p_{kick} = \pm 0.02$, and the location of the bend center should be known to $\delta L_{bend}/L_{bend} = \pm 0.02$ so that these give negligible contributions.

The target point is defined by the beam width, and $\delta x_{target} = \pm 0.8$ mm at 200 GeV/c. We use an emittance of 20π mm-mrad and $\beta_x = 36\ m$ and $\gamma_x = 0.09$ m^{-1}. (We will use a radial carbon ribbon target with the pion source width defined by the beam radially. We can then bin the beam polarization vertically to measure any polarization dependence on y.) Therefore, the target source location will contribute a negligible error to δr. The beam radial divergence is $\delta\Theta_{r,beam} = \pm 0.04$ mrad, also contributing negligible error in $\delta\Theta_{meas}$.

Multiple Coulomb scattering in the pion exit window (0.003 inch/Θ_{prod}, aluminum) and 30 m of air give $\delta\Theta_{mult} = \pm 0.04$ mrad and $\delta r_{mult} = \pm 1$ mm at the location of the first tracking module, 25 m from the exit window, for 200 GeV/c beam (100 GeV/c pions).

We plan to use either wire chambers or scintillator hodoscopes with 2 mm pitch, and x, y, and u

planes for tracking. Three tracking modules will be spaced over 10 m, each covering an area of 3×3 cm^2. Resolution will be $\delta r_{meas} = \pm 1$ mm and $\delta\Theta_{meas} = \pm 0.1$ mrad, which satisfies the requirements above. If scintillator were used, 9 mm of scintillator in the first tracking module would give $\delta\Theta_{mult} = \pm 0.02$ mrad.

We have not designed the tracking modules at this time. For wire chambers, the drift time should be < 100 nsec, the bunch spacing in RHIC for 120 bunches per ring. The multiplicity downstream of the collimator is expected to be 0.0035/plane/bunch crossing for π^-, so that the granularity, 10 to 15 pixels/plane, is sufficient. We expect to use deadtimeless pipeline readout, and store the data during the measurement time. After the measurement, fast arithmetic processors can reconstruct the straight line tracks, obtaining (r, Θ_{meas}) for each event. A look-up table can then locate the event in (x_F, p_T). The data would then be binned according to the bunch polarization sign pattern in the ring, and polarimeter arm. The asymmetry is calculated similarly to the AGS internal polarimeter. Finally, the beam polarization is calculated using the known analyzing power. We expect that the processing time will be short, giving essentially instantaneous beam polarization information.

We plan to use a hadron calorimeter after the tracking modules. We do not have the space to completely contain the energy on the sides, so that we expect a resolution of $\delta E/E = (\pm 100\%)/\sqrt{E}$, or $\pm 10\%$ at 200 GeV/c beam (100 GeV/c pions). This will give an independent measurement of the energy, and provide both a cross-check of the tracking and a separate measure of the beam polarization without the track reconstruction. Both the Cerenkov and the calorimeter require that only one high energy track be in the acceptance.

Appendix B

Measuring Beam Polarization in RHIC

Our approach to measuring the beam polarization is based on the asymmetry in inclusive pion production as was chosen by the Polarization Measurement Working Group[64]. Toroid two-arm spectrometers[65] offer an attractive solution by providing left-right measurements that can cover the large energy range of RHIC and allow excellent cancellation of biases in polarization measurements. The details of this design can be found in Appendix A. Funding constraints have dictated a scaled down approach to providing a polarimeter system suitable for the initial FY2000 commissioning period. In this report, we describe a single arm pion spectrometer as well as a parallel effort to augment this with a second polarimeter based on p-Carbon scattering in the Coulomb-Nuclear Interference (CNI) region. If successful, the CNI polarimeter would be a simple, compact, and cost effective solution.

B.1 Introduction

In general, vertical beam polarization is measured by determining the asymmetry in the cross section for left and right scattering or particle production, using a reaction with a known analyzing power A_N:

$$P_B = \frac{1}{A_N(x_F, p_T)} \frac{Ed^3\sigma_L/dp^3 - Ed^3\sigma_R/dp^3}{Sum}, \tag{B.1}$$

$$P_B = \frac{1}{A_N} \frac{N_L - N_R}{N_L + N_R}. \tag{B.2}$$

P_B is the beam polarization, N_L and N_R are the number of scatters left and right normalized by luminosity. A_N can be known from experiment or theory.

For inclusive pion production, Fermilab E704 [79] has measured the analyzing power to $\Delta A_n/A_n = \pm 7\%$[1] for pion production with 200 GeV/c protons, with $x_F \sim p_\pi/p_{beam} = 0.5$ and $p_T > 0.7\ GeV/c$. For their measurement polarized protons were obtained from Λ hyperon decay and the polarization was known from the measured Λ weak decay asymmetry parameter α_Λ.

[1]The combined systematic and statistical error from E704 at 200 GeV/c is $\delta A_N/A_N = \pm 0.073$ if the statistics for both π^+ and π^- are used. If we used π^- only, the combined error is $\delta A_N/A_N = \pm 0.092$.

Recently, AGS experiment E925 measured the asymmetry at 22 GeV/c with a carbon target. Large asymmetries were observed in both π^+ and π^- production. The apparent x_F and p_t dependence of these asymmetries are consistent with the results from E704. The E925 data provide enough confidence to start construction of a relative inclusive pion polarimeter for RHIC. We may have to optimize the working kinematic region to maximize the analyzing power versus energy.

Inclusive pion production will provide an excellent polarization monitor for RHIC. A physics asymmetry is the raw (measured) asymmetry, normalized by the beam polarization. Examples are

$$A_L = \frac{1}{P_B}\frac{N_+ - N_-}{N_+ + N_-} \tag{B.3}$$

$$A_{LL} = \frac{1}{P_B^2}\frac{N_{++} - N_{+-}}{N_{++} + N_{+-}}. \tag{B.4}$$

A_L and A_{LL} are single and double spin longitudinal asymmetries. N_+ and N_{+-} are the number of scatters observed with the beam polarization helicity + (one beam + and the other beam - for N_{+-}) normalized by luminosity. The beam polarization P_B is taken as the same for both beams for A_{LL}. For those reactions with a high degree of statistical accuracy, the error in the physics asymmetry is

$$\frac{\delta A_L}{A_L} \sim \frac{\delta P_B}{P_B} \tag{B.5}$$

$$\frac{\delta A_{LL}}{A_{LL}} \sim 2\frac{\delta P_B}{P_B}. \tag{B.6}$$

Thus, if the absolute beam polarization is known to 10%, for example, then the single spin asymmetry A_L is uncertain to 10% of itself. Similarly, for A_{LL} the error becomes 20%. The beam polarization error only becomes significant when the statistical precision reaches the same level, thus at a 10σ statistical measurement for A_L and at a 5σ measurement for A_{LL}. We only anticipate a 10σ measurement for the u quark polarization in a polarized proton using parity violation of W^+ production, where the expected asymmetry A_L is quite large and, thus, the expected statistical contribution to $\delta A_L/A_L$ is small. Gluon polarization will be measured by direct photon production and the statistical contribution to $\delta A_{LL}/A_{LL}$ would approach 5σ only for maximal gluon polarization.

Our polarimeter utilizes the asymmetries (A_N, sometimes called A_p) in inclusive pion production at high x_F that were measured at the Argonne ZGS [80] at 12 GeV/c (see Fig. B.1), at Fermilab[79] at 200 GeV/c (see Fig. B.1), and recently at the AGS at 22 GeV/c. The asymmetries increase linearly with x_F and appear to be largely independent of the incident polarized beam momentum. Moreover, the ZGS data which were taken with both liquid hydrogen and deuterium targets, and the recent AGS data which were taken with carbon target, show little dependence on target nuclei. Since these polarimeters used a fixed target, these measurements cover most of the energy range of the RHIC beams. The pion asymmetry at the desired kinematic region measured at the AGS (E925) provides a direct measurement of the analyzing power at the RHIC injection energy.

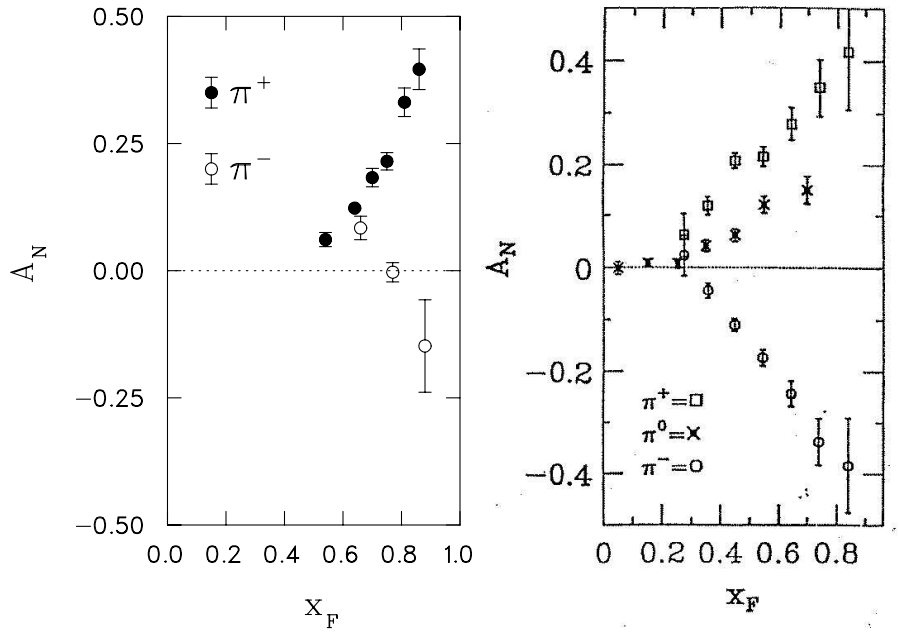

Figure B.1: Pion asymmetries measured at ZGS (left) and in Fermilab experiment E704 (right).

The polarimeters are designed to probe the kinematic region of 0.6 in x_F and 0.8 GeV/c in transverse momentum of the pions. This was optimized from the Fermilab data based on the fact that the asymmetry in this kinematic region rises linearly with x_F while the cross section is falling as $(1 - x_F)^2$, and that the error in the asymmetry measurement is the inverse of the square root of the total number of events.

At the present stage of design, the polarimeter will allow π^- measurements. It should be noted, that since π^- are a relatively large fraction of negatives, particle identification is not necessary. Due to the large proton background, measurement of π^+ asymmetry may be difficult. At the chosen parameters, the measured π^- asymmetry is 0.14 and the invariant cross section is about 100 μb/GeV^2 [81]. The polarimeters are designed to fit in the 35 m long straight sections of the RHIC machine between Q3 and Q4. The target is located near Q4 where the vertical and horizontal lattice β functions are small thus reducing the effect of multiple scattering on emittance dilution. For this reason also, the polarimeter is placed upstream of the interaction region (see Fig. 1.2).

B.2 Measuring the Pion Asymmetry at the RHIC Injection Energy

The RHIC inclusive pion polarimeter design (see Section B.3) will use carbon for the production target since it can survive beam heating. This presented some uncertainty as the available pion asymmetry data from the ZGS and Fermilab were collected using hydrogen and deuterium targets. The possibility that a nuclear target might present a large dilution of the observed asymmetries was a concern.

The AGS Experiment E925 was proposed to utilize an extracted polarized proton beam to provide a

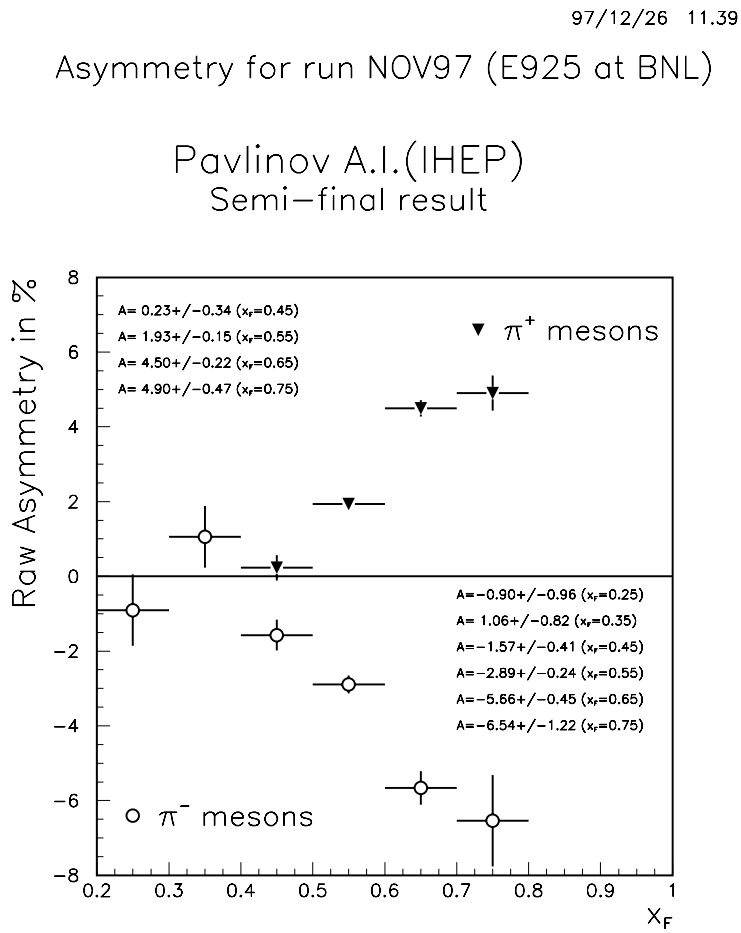

Figure B.2: The preliminary results from AGS E925 inclusive pion production.

statistically significant measurement of the asymmetry in pion production at the RHIC injection energy around 23 GeV, to compare the data from carbon and hydrogen targets, and to assure that negative pions exhibit the same kinematic dependence at lower energies as was observed in the Fermilab data.

The E925 proposal was approved by the AGS program advisory committee in October 1996, the apparatus was installed in the AGS B1 line in February and March 1997, took low energy unpolarized beam for tune up in April and May 1997 and ran parasitically for three days at 24 GeV. The apparatus ran for one week in November 1997 with polarized beam at 21.7 GeV and a carbon target. The average beam polarization was 0.30 as measured by the local *pp* elastic scattering polarimeter.

Preliminary results are shown in Fig. B.2. The data exhibit the mirror positive and negative pion asymmetries similar to what was seen at 200 GeV/c at Fermilab. This implies that we can use negative pions for the polarimeter as was discussed earlier. The magnitude of the asymmetry from a carbon target is (the raw asymmetries should be normalized to full beam polarization by a factor of 3.3) quite adequate for

use in the polarimeter. The dilution due to a nuclear target appears to be small. However, the comparison with production from hydrogen awaits the construction of a liquid hydrogen target which should be ready for the next polarized run scheduled for February 1999. The E925 results are quite encouraging and we are proceeding with the development of an inclusive pion polarimeter.

B.3 Scaled Down Day-one Pion Production Polarimeter

To reduce the cost, the day-one polarimeter will be a single arm spectrometer and will use modified existing apparatus. The layout is shown in Fig. B.3. It uses five existing dipole magnets, of which the first three will be on a movable platform to allow us to reach the desired energy range 23-100 GeV/c. Four scintillator hodoscopes from the E925 will be used, two are located between dipoles 3 and 4, and the other two are after dipole 5. Due to their limited sizes, the first two hodoscopes need to move transversely for different energies to cover the energy range. The first hodoscope can be attached to the first three dipoles and the second hodoscope needs to move 8 cm to cover 23-100 GeV/c. To save power, all five dipoles will be gapped down from the original gap size of 10 cm. The last hodoscope located 24 m away from the target defines the acceptance.

Pions are produced by the interaction of polarized protons on a 5 μg/cm ^{2} carbon ribbon target about 1.5 m downstream of Q4. The string of five dipole magnets lies on the outside of the warm beam line section between Q4 and Q3. The inter-magnet drift region of 5 m is for bending particles at different energies to the same final trajectory. This arrangement provides enough space for a 6 m long Cerenkov counter and a hadron calorimeter downstream of the Cerenkov counter, should we choose to run with π^+.

The production angle and selected spectrometer momentum depend on the beam energy; at RHIC injection of 23 GeV/c, the production angle would be 58 mrad and the π momentum 13.8 GeV/c; at 100 GeV/c RHIC beam momentum, the production angle is 13 mrad and the π momentum is 60 GeV/c. The details of the layout are listed in Table B.1. The table also includes the tunes at selected beam energies that will allow measurement in the desired kinematic range of $x_F = 0.6$ and $p_T = 0.8$ GeV/c.

B.3.1 Target Box, Beam Pipe, Pion Exit Windows

The asymmetric one-arm polarimeter gives rise to fringe fields inside the RHIC beam pipe. Only the fringe fields of the first magnet need to be considered. To save space, the first magnet has to be transversely as close to the beam pipe as possible and longitudinally as close to the target box as possible. With these constraints, there is little space for magnetic shielding. TOSCA simulations show that with a 0.05 in iron shielding and a stainless steel beam pipe (see Fig. B.4), the vertical field in the middle of the first dipole magnet is shown in Fig. B.5, and the fringe field in the beam pipe is shown in Fig. B.6. It shows that the fringe field in the beam pipe center is less than 1 Gauss which is quite acceptable.

One thin carbon ribbon target will be used for both CNI and inclusive pion production. The radius of the stainless steel target box will be about 26 cm and the radius of the beam pipe in this warm straight

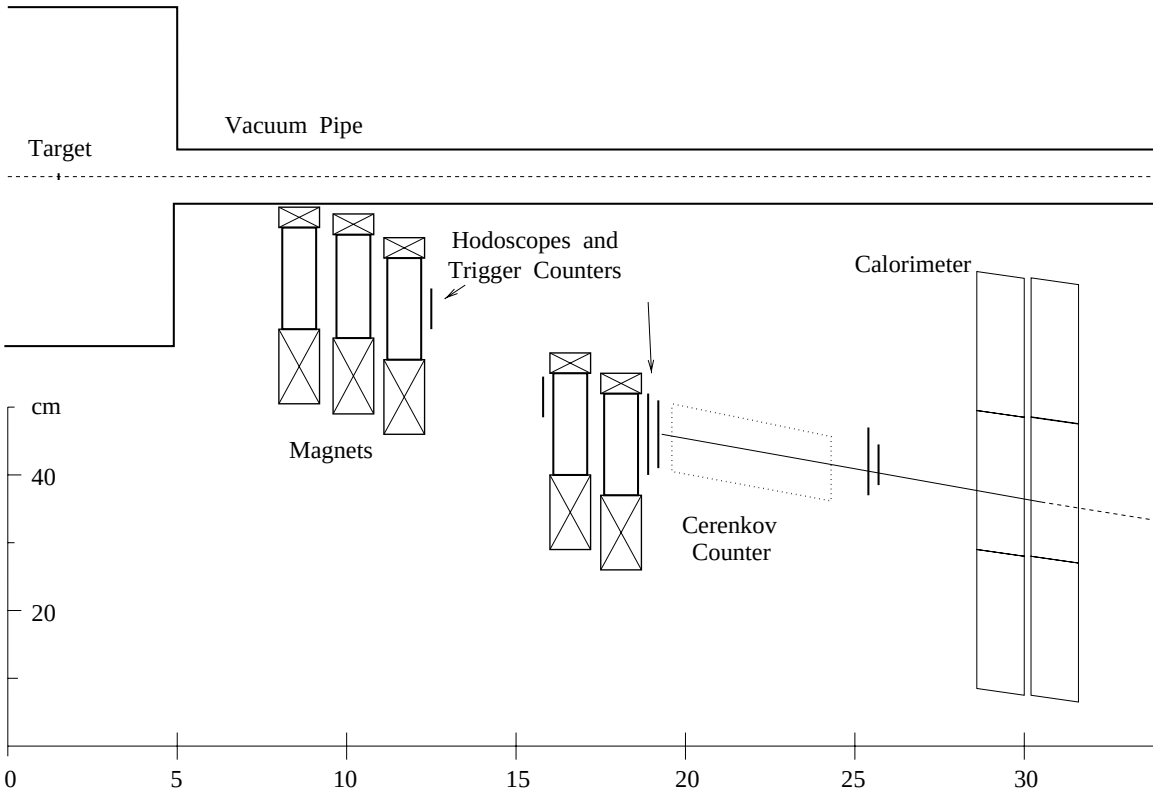

Figure B.3: Plan view of the the one-arm polarimeter between Q4 and Q3. The first 3 dipoles are in the position for 100 GeV/c. At lower energies, the first three dipoles will move out transversely. The first two hodoscopes will also move accordingly.

	Trgt	**M1**	**M2**	**M3**	**M4**	**M5**
Longitudinal Positions (m)	1.5	8.5	9.75	11.0	16.0	17.25
Length (m)		1	1	1	1	1
Full Gap (cm)		3.7	4.3	4.9	7.8	7.8
Current (A)		920	1070	1230	1950	1950
Power (kW)		41	56	74	185	185
Transverse Positions (cm):						
23 GeV/c		31	32	35	29	33
50 GeV/c		16	17	20	29	33
75 GeV/c		11	12	15	29	33
100 GeV/c		8	9	12	29	33
Settings:						
23 GeV/c		1	1	.15	−1	−1
50 GeV/c		0.36	0	0	−1	−1
75 GeV/c		−0.15	−0.2	−1	−1	−1
100 GeV/c		−1	−1	−1	−1	−1

Table B.1: Parameters for the polarimeter gaps and transverse positions. The transverse positions of the dipoles are with respect to the beam pipe center. The longitudinal positions of the dipoles are with respect to the end of Q4. The magnet settings are in fractions of the TOSCA design fields of 1.5T.

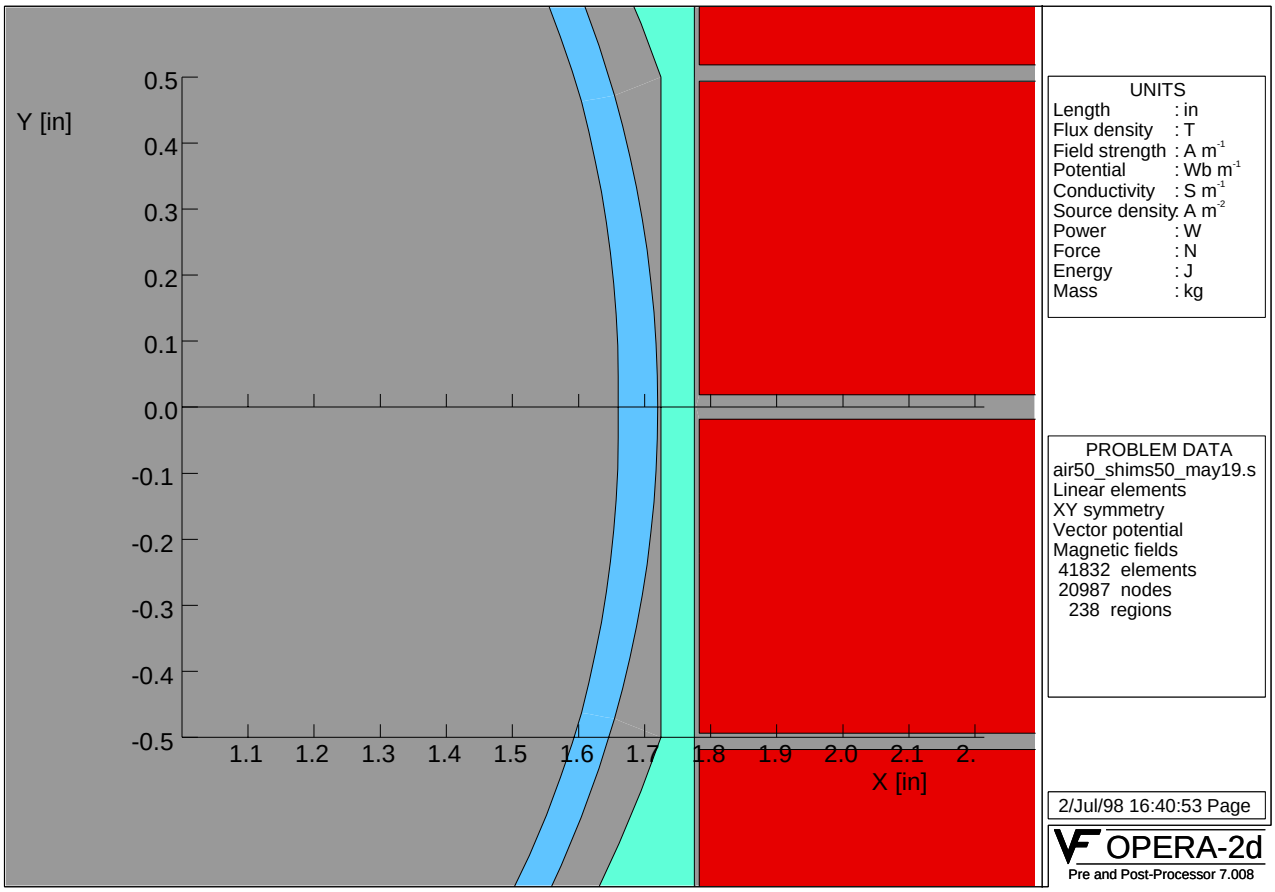

Figure B.4: Cross-section of the first dipole magnet. The iron shield around the beam pipe is 0.05 in thick and reduces the leakage field.

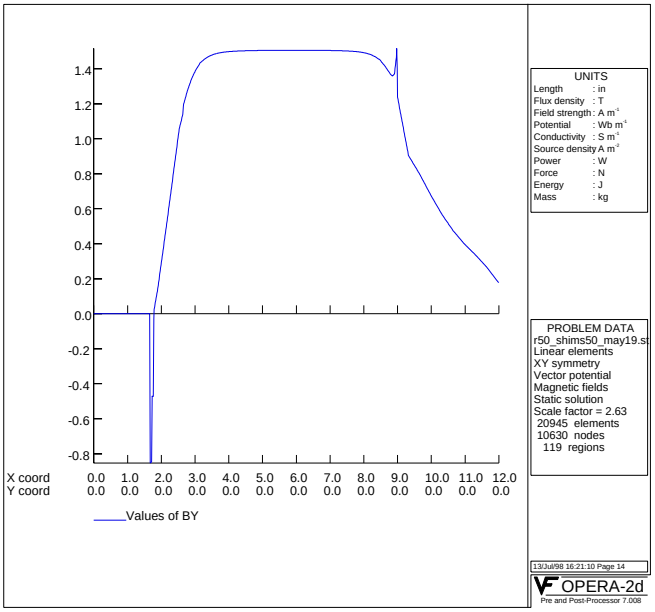

Figure B.5: Expected vertical magnetic field strength of the dipole magnet. The vertical axis is the field strength in Tesla and the horizontal axis is the distance from the beam pipe center in inches. Note that the negative spike at about 4.4 cm is in the shielding iron.

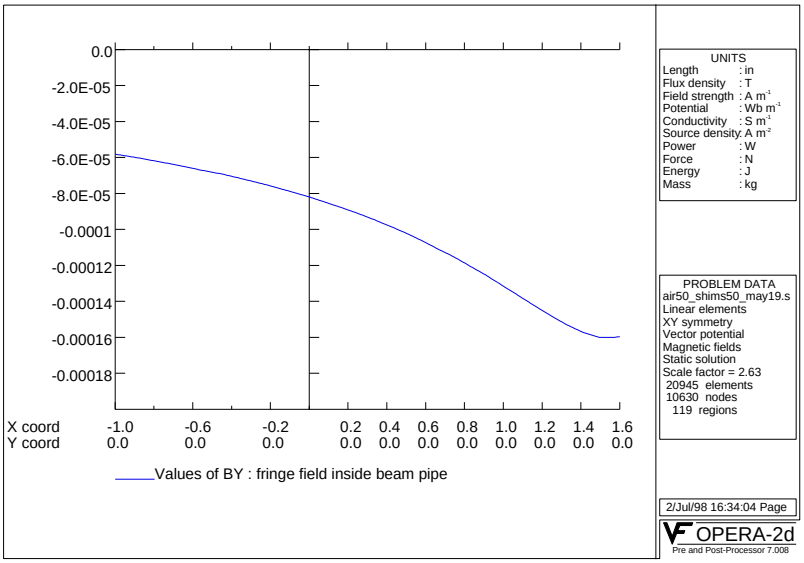

Figure B.6: Expected fringe field of the first dipole magnet inside the beam pipe. The vertical axis is the field strength in Gauss and the horizontal axis is the distance from the beam pipe center in inches.

section is 4 cm. The particle exit window is 22 cm long, 3 cm wide and 0.5 mm thick. Multiple Coulomb scattering at the pion exit windows is an important issue that impacts the accuracy of track reconstruction. It is estimated that the maximum acceptable thickness of the thin window is 1mm for stainless steel. We choose a thickness of 0.5 mm[82].

B.3.2 Pion Production Target

Of the total ionization energy loss of the protons interacting with the carbon fiber, 30% is deposited on the target in the form of heat[75]. For a section of a horizontal fiber of length Δx intercepting the center of a Gaussian beam of rms width σ_x and σ_y in x and y, the heating power of the beam is,

$$P_h = \frac{\epsilon_h f_r N_p \frac{dE}{dx} \rho t_f}{2\pi\sigma_x\sigma_y} [d_f \Delta x] \tag{B.7}$$

where N_p is the number of protons in the machine, $f_r = 78$ kHz is the beam revolution frequency, $dE/dx = 1.78$ MeV/gm/cm^2 is the ionization energy loss for protons, $\rho = 1.75$ gm/cm^3 is the density , t_f is the thickness of the carbon ribbon and d_f is the diameter of the carbon fiber. The fraction of the total energy loss that is converted to heat $\epsilon_h = 0.3$, is from the CERN studies on carbon flying wires [75]. The radiated power is given by the Stefan-Boltzmann relation

$$P_{rad} = \epsilon_{rad}\sigma_{SB}(T^4 - {T_0}^4)\,[2d_f\Delta x] \tag{B.8}$$

where $\epsilon_{rad} \approx 0.8$ is the emissivity, σ_{SB} is the Stefan-Boltzmann constant, T is the fiber temperature and T_0 is the ambient temperature. The expression in square brackets in Eqs. B.7 and B.8 is the surface area of the element. The maximum equilibrium temperature is then,

$$T_{eq} = \left(\frac{\epsilon_h f_r N_p \frac{dE}{dx} \rho t_f}{4\pi\sigma_x\sigma_y\epsilon_{rad}\sigma_{SB}} + {T_0}^4\right)^{1/4} \tag{B.9}$$

Since the beam size depends on the energy the equilibrium temperature varies as ${p_{beam}}^{\frac{1}{4}}$. Fig. B.7 shows the expected equilibrium temperature as a function of beam energy for a 5 μg/cm^2 carbon ribbon at full luminosity. For commissioning the heating will be less, but the target is to be used for any future polarimetry. It is generally inadvisable to run the fiber at temperatures exceeding 2000°K which is the onset of thermionic emission since this would shorten the life-time of the fiber. The result shows, with the ribbon target, heating is not a problem even with smaller beam emittance $\epsilon_N = 10\ \pi$ mm mrad. It would be advantageous to mount more than one ribbon on the driving mechanism (spaced so that the beam sees one ribbon at a time) since this would provide redundancy in case of ribbon breakage.

B.3.3 Acceptance, Event Rates and Emittance Blowup

We define ϕ as the angle between the magnet mid-plane and the pion production plane. A simple estimate of the expected θ acceptance of the system was made by numerical evaluation of the range of production

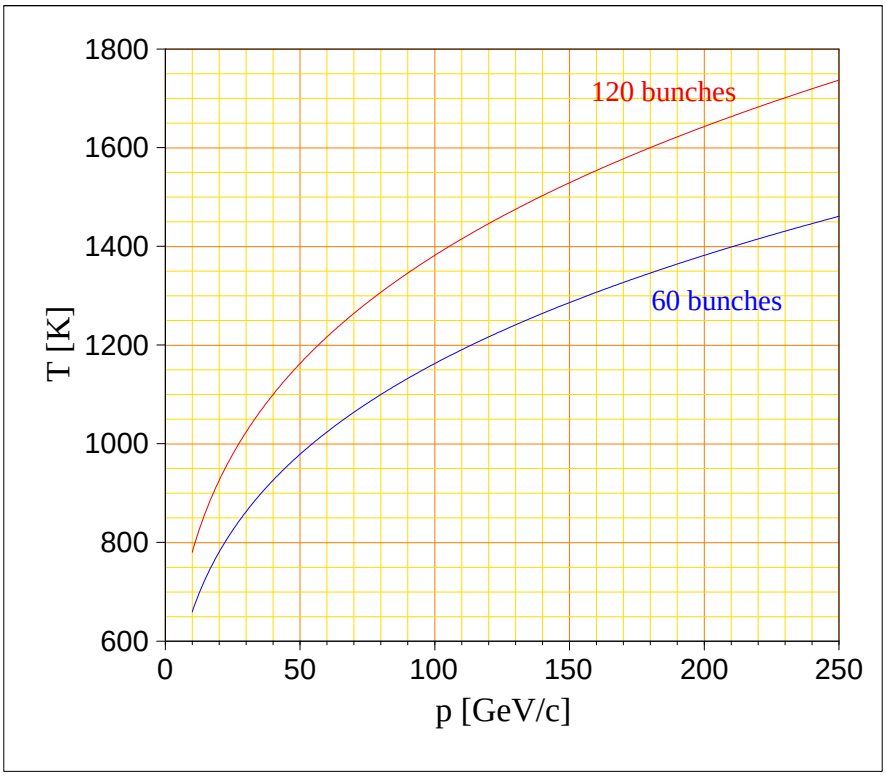

Figure B.7: Equilibrium temperature of a 5 μg/cm^2 carbon ribbon for two beam currents. The beam parameters are: 2×10^{11} protons per bunch, 120 bunches, $\epsilon_N = 10\ \pi$ mm mrad.

angles (or p_T) that are accepted by the 11 cm hodoscope located 24 m away from the target. The plots in Fig. B.8 show the acceptance as a function of x_F at several energy tunes. The acceptance is seen to extend to x_F and p_T values below the desired kinematic ranges of 0.6 and 0.8 GeV/c. From the ZGS, Fermilab and AGS experiments, significant asymmetries can be expected only above $x_F > 0.45$ and $p_T > 0.7$ GeV/c. It is therefore necessary that the system be able to reject low momentum pions that do not carry significant analyzing power. With the kinematic acceptance defined as $\delta x_F/x_F$ of 0.1 around x_F of 0.6, and using the p_T acceptance defined by the detectors we can estimate the event rates. The instrumental cross-section for a single polarimeter arm is

$$\delta\sigma = \left[E\frac{d^3\sigma}{dp^3}\right] p\delta p\delta\Omega \tag{B.10}$$

where $\left[E\ d^3\sigma/dp^3\right] \approx 100\ \mu\text{b/GeV}^2$ is the invariant cross-section for π^- of Ratner, et al.[81] and the solid angle $\delta\Omega$ is given by

$$\delta\Omega = \delta\theta_h\delta\theta_v \tag{B.11}$$

where $\delta\theta_h$ is the horizontal angular acceptance 0.11 m/24 m = 4.6 mrad and the vertical angular acceptance, $\delta\theta_v$ is given by

$$\delta\theta_v = 2\tan(\theta_\pi)\sin(\delta\phi) \tag{B.12}$$

with $\delta\phi$ the azimuthal acceptance half-angle of 4° and $\theta_\pi = (0.8\ \text{GeV/c})/p_L$ is the pion production angle. The number of pion events accepted in one second is given by,

$$N_{\pi,second} = f_r N_p \frac{d_w d_f}{\sqrt{2\pi}\sigma_y}\left[\frac{\rho N_A A_{nucl}}{A_w}\right]\delta\sigma \tag{B.13}$$

where d_f is the thickness of the carbon ribbon, d_w is the width of the carbon ribbon, $A_{nucl} = 12$ is the number of nucleons/atom, $A_w = 12$ gm/mole is the atomic weight of carbon and $N_A = 6.022 \times 10^{23}$ atoms/mole.

As the target sits in the beam the emittance of the beam is increased due to multiple scattering. The resulting addition to the normalized 95% emittance in one second can be estimated from

$$\Delta\epsilon_{(x,y)second} = \frac{d_f d_w f_r}{\sqrt{2\pi}\sigma_y}\frac{3\beta_{(x,y)}}{\beta^3\gamma}\frac{1}{L_{rad}}\left(\frac{0.0141}{0.938}\right)^2[\pi] \tag{B.14}$$

where $\beta_{(x,y)}$ is the (x, y) lattice beta function at the target location, β and γ are the usual relativistic factors and $L_{rad} = 18.8$ cm is the radiation length of the target material. It is useful to parameterize the resulting total emittance growth in terms of the total pion statistics N_π,

$$\Delta\epsilon_{(x,y)tot} = \frac{3\beta_{(x,y)}}{\beta^3\gamma}\frac{1}{L_{rad}}\left[\frac{0.0141}{0.938}\right]^2\frac{N_\pi}{N_p}\left[\frac{A_w}{\rho N_A A_{nucl}}\right]\frac{1}{\delta\sigma}[\pi]\,. \tag{B.15}$$

With the relations given above we estimate the event rates and measuring times. These are listed in Table B.2. We used a 5 μg/cm^2 carbon ribbon target, a pion momentum bite of 0.1, at $x_F = 0.6$, and $p_T = 0.8$ GeV/c. We have assumed a total statistics of 10^4 pions in the polarimeter to obtain a 7% error

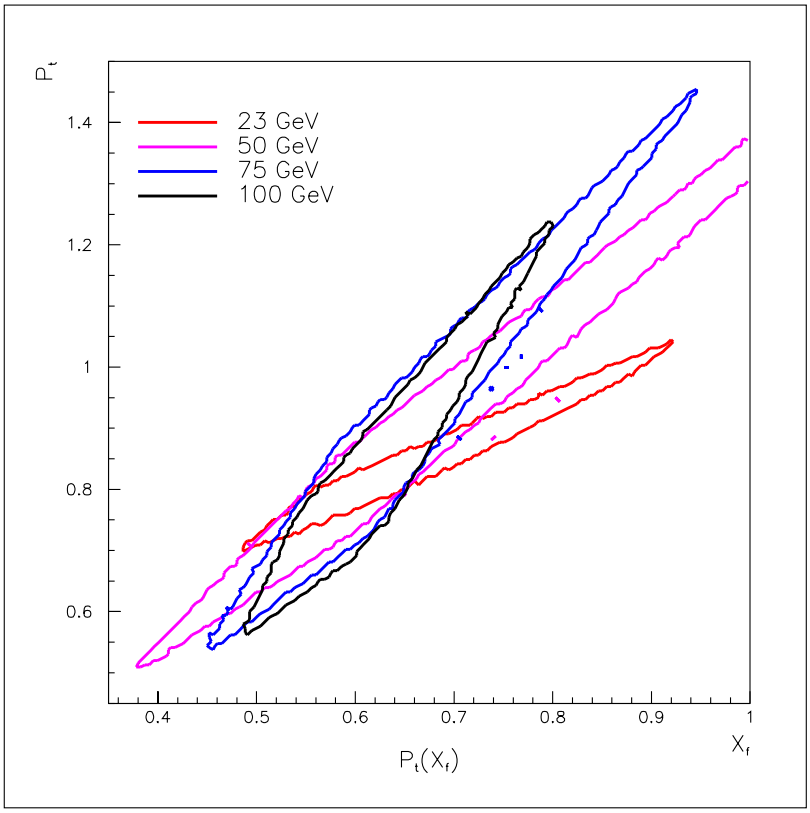

Figure B.8: Polarimeter acceptance for 23 GeV/c, 50 GeV/c, 75 GeV/c and 100 GeV/c using respective magnet settings found in Table B.1.

p_π (GeV/c)	$\delta\Omega$ (μster)	$\delta\sigma$ (nb)	T_{meas} (sec)	$\Delta\epsilon_x$ ($\Delta\epsilon_y$) (π mm mrad)
60	6.4	231	1.9	0.0028 (0.0032)
13.8	26.1	49.7	~ 18	0.22 (0.33)

Table B.2: Acceptance and rate estimates for the pion polarimeter. Also includes expected emittance dilution due to multiple scattering for collecting 10^4 pions. The following parameters were assumed: $\epsilon_N = 20\pi$ mm mrad, protons/fill = 120 bunches at 2×10^{11} protons/bunch, $d_f = 2.5 \times 10^{-8}$ m, $p_T = 0.8$ GeV/c, $\delta p/p = 0.1$

1st hodoscopes	3-4 × 5 cm	X
2nd hodoscopes	3-4 × 7 cm	X
3rd hodoscopes	8-10 × 4 cm	X,Y
4th hodoscopes	10 × 10 cm	X,Y

Table B.3: Sizes of the four hodoscopes.

in polarization. The emittance growth at 23 GeV/c is about 1% for the measurement, and there is much less growth for higher energy. Thus, the measurements can be parasitic. As can be seen from the table, measurement times are quite reasonable. The acceptance, and number of bunches used (for example, for commissioning) will be optimized, since these choices depend on the number of stored protons, rates in the detector, and the desired polarization error. In year-one commissioning, the number of bunches will be about 60, and the intensity of each bunch is estimated as half of the designed value: 1×10^{11} protons/bunch. The measuring time and emittance blow up are estimated as 72 s and 0.8π mm-mrad, respectively for the injection energy.

B.3.4 Polarimeter Detectors

The detectors will determine the (x_F, p_T) for each particle, and crudely measure the energy of each particle. If π^+ measurement becomes necessary in the low intensity situation, a Cerenkov counter will be used to identify pions. The (x_F, p_T) measurement will allow selection of pions with high analyzing power. We will want to choose pions with $x_F > 0.47$ and $p_T > 0.6$ GeV/c. The acceptance of the dipoles extends to lower (x_F, p_T) where pion production is significantly larger (see Fig. B.8) and the analyzing power lower. Therefore, the lower edge of (x_F, p_T) for the selected pions must be sharply defined. Four scintillator hodoscopes modified from AGS E925 will be used (see Table B.3). Each element is 6 mm wide scintillator and two staggered, overlapping layers of the scintillator provides 2 mm wide segments. There are two hodoscopes between the third and fourth dipoles, and the other two hodoscopes are after the fifth dipole. In addition, there are three trigger scintillators near hodoscopes 2-4. Since a large analyzing power for π^- production at the RHIC injection energy has been found in AGS E925, we expect to use only π^-. We plan to use tracking to measure (x_F, p_T) and, in addition, hadron calorimeters to provide a cruder but independent measurement of the pion energy. The calorimeters will be built with existing modules.

An important detector issue is to isolate the detectors out of the line of sight of the target. For year-one operation, the intensity is low and simulation shows that the direct particles are not a problem. To reconstruct the pion trajectories we use the target/beam location as an upstream point, and we measure the deflection (r) and track angle (Θ_{meas}) after the bending in the dipoles (see Fig. B.3).

Resolution, with $\delta x = 1$ mm from the hodoscopes, is $\delta p/p = 1.1\%$ with no multiple scattering (1.5% with scattering), and $\delta\Theta/\Theta = 0.5\%$. This is good enough to be used to select higher x_F and p_T for good analyzing power, and to match the acceptance of E925 to use A_N measured there. The separation of Θ (basically given by the position at hodoscope 1) and momentum (basically the difference between positions

at hodoscope 3 and hodoscope 4) is also nice in that matrix logic can be used as a clean trigger to eliminate the low analyzing power region.

It is important to have a deadtimeless data acquisition. Otherwise, we blow up the beam with the target, and do not get as much data as we need. We can take advantage of the small amount of data per measurement and place all the data into memory, reading it out after 10^4 pions have been recorded. A LeCroy 2367 with 3 MByte memory, and internal logic to trigger with a lower x_F and p_T cut would allow 0.5 million events to be stored by using two units (there are 57 input/output lines available per unit).

B.4 p-Carbon CNI Polarimeter

Small angle elastic scattering of hadrons in the Coulomb-Nuclear Interaction (CNI) region has long been advocated for polarimetry. The predicted asymmetry is significant and largely independent of energy for energies above a few GeV. The prediction rests on hadronic spin flip being small, which is expected for high energies. The CNI process has been proposed for RHIC polarimetry using a hydrogen jet target and in collider mode using the *pp*2*pp* experiment. Both would be *pp* CNI. It is also possible to use a carbon target, pC CNI, which is simpler and cheaper than a hydrogen jet, and can be installed in the individual rings, as opposed to requiring collision of both rings as for the *pp*2*pp* experiment. The analyzing power for pC CNI is similar to *pp* CNI (both about 0.04) and the cross section is high, giving a very large figure of merit NA^2. However, for pC CNI, the proton scattered forward is not easily detectable (it stays within the beam), and the energy of the recoil carbon nucleus is 100-400 keV. The low energy carbon would stop in most targets. The pC CNI polarimeter became feasible with the development of very thin ribbon carbon targets at IUCF[67]. The slowness of the recoil carbon also makes detection difficult. However, the arrival time of the carbon can be set to be in between RHIC bunches, avoiding prompt background.

Elastic scattering in the small angle CNI region is predicted to have a calculable analyzing power of about 3-5%[68] as well as a large cross section over the whole RHIC energy range from 23 GeV/c to 250 GeV/c. The analyzing power is given by

$$A_N = \frac{G t_0 t \sqrt{t}}{m_p(t^2 + t_0^2)}, \tag{B.16}$$

where G is the anomalous magnetic moment of the proton(1.7928), m_p the proton mass, and $t_0 = \frac{8\pi\alpha Z}{\sigma_{tot}}$. The total cross section σ_{tot} is only weakly energy dependent over the relevant energy range. Fig. B.9 shows the calculated analyzing power for a hydrogen target ($Z = 1$, $\sigma_{tot} = 35$ mb) and a carbon target($Z = 6$, $\sigma_{tot} = 330$ mb[69]) as a function of $(-t)$. The uncertainty from a hadronic spin flip amplitude has been estimated to be smaller than 10% of the analyzing power from CNI. Using a carbon target will result in the high luminosity required for fast polarization measurements. The sizable analyzing power, the large cross section and the advantages of a solid ribbon target makes this process ideal for a fast primary polarimeter for RHIC.

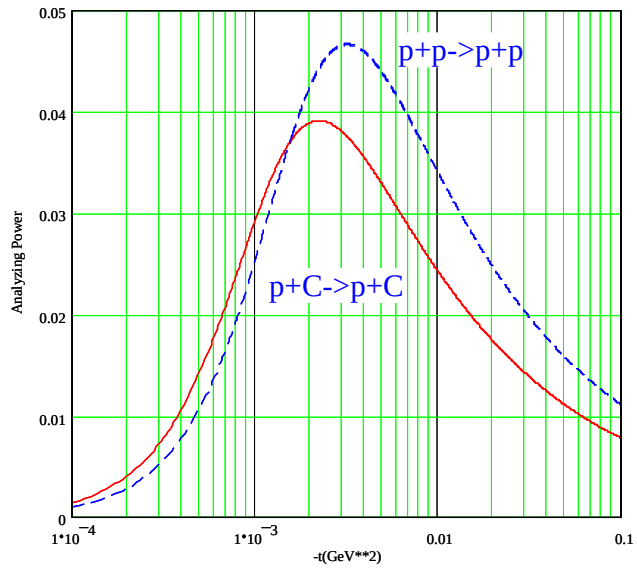

Figure B.9: Coulomb-Nuclear interference analyzing power for pp and pC scattering.

A typical $(-t)$ value of 0.002 to 0.01 GeV^2 results at high energy in a very small angle of the forward scattered proton relative to the beam direction and also a very low kinetic energy of the Carbon recoil of about 0.5 MeV. It will be impossible to measure the forward scattered proton without drastically reducing the beam divergence at the target which would severely reduce the scattering rate and also cause unacceptable beam emittance growth. It will therefore be necessary to rely only on the measurement of the recoil Carbon nucleus to identify elastic scattering.

Direct measurement of the 0.1 to 1 MeV recoil Carbon nucleus is only possible for a very thin Carbon target. The detector for the recoil carbon must be compact with recoil arms about 10 cm long, and in the beam vacuum. The detector will be silicon strip detector (SSD) and/or micro-channel plate (MCP) with sizes of the order of centimeters. Very thin micro-ribbon carbon targets are needed to allow the recoils to exit.

The determination of elastic scattering will be done by measuring both the energy and angle of the recoil Carbon. In addition, the time-of-flight will be measured to discriminate against target fragments. Fig. B.10 shows the expected energy-angle correlation for the recoil Carbon. The horizontal lines show the expected angular straggling from the target ribbon. Also shown is the kinematic range for producing the first excited Carbon state at 4.4 MeV. Elastics are well separated. Another background would be forward production of N^* which needs to be evaluated. The kinematics of the recoil system will not separate this background.

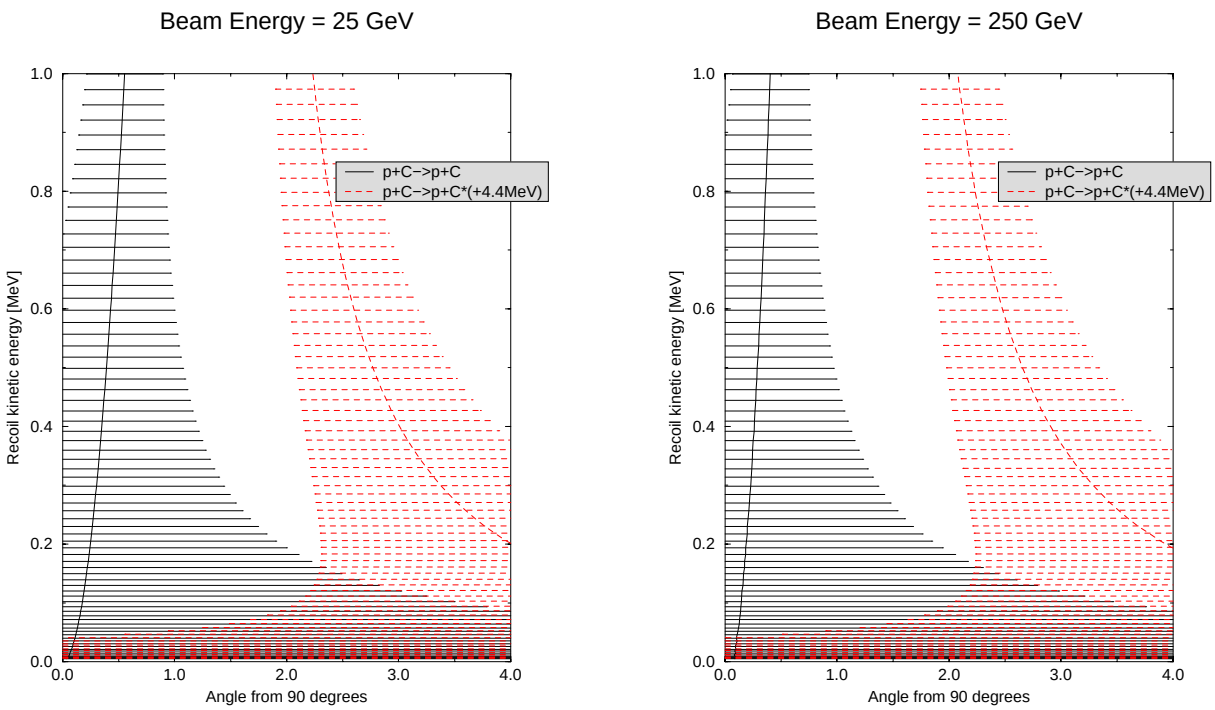

Figure B.10: Energy-angle correlation for the elastic and inelastic recoil Carbon nucleus at 25 GeV (left) and 250 GeV (right).

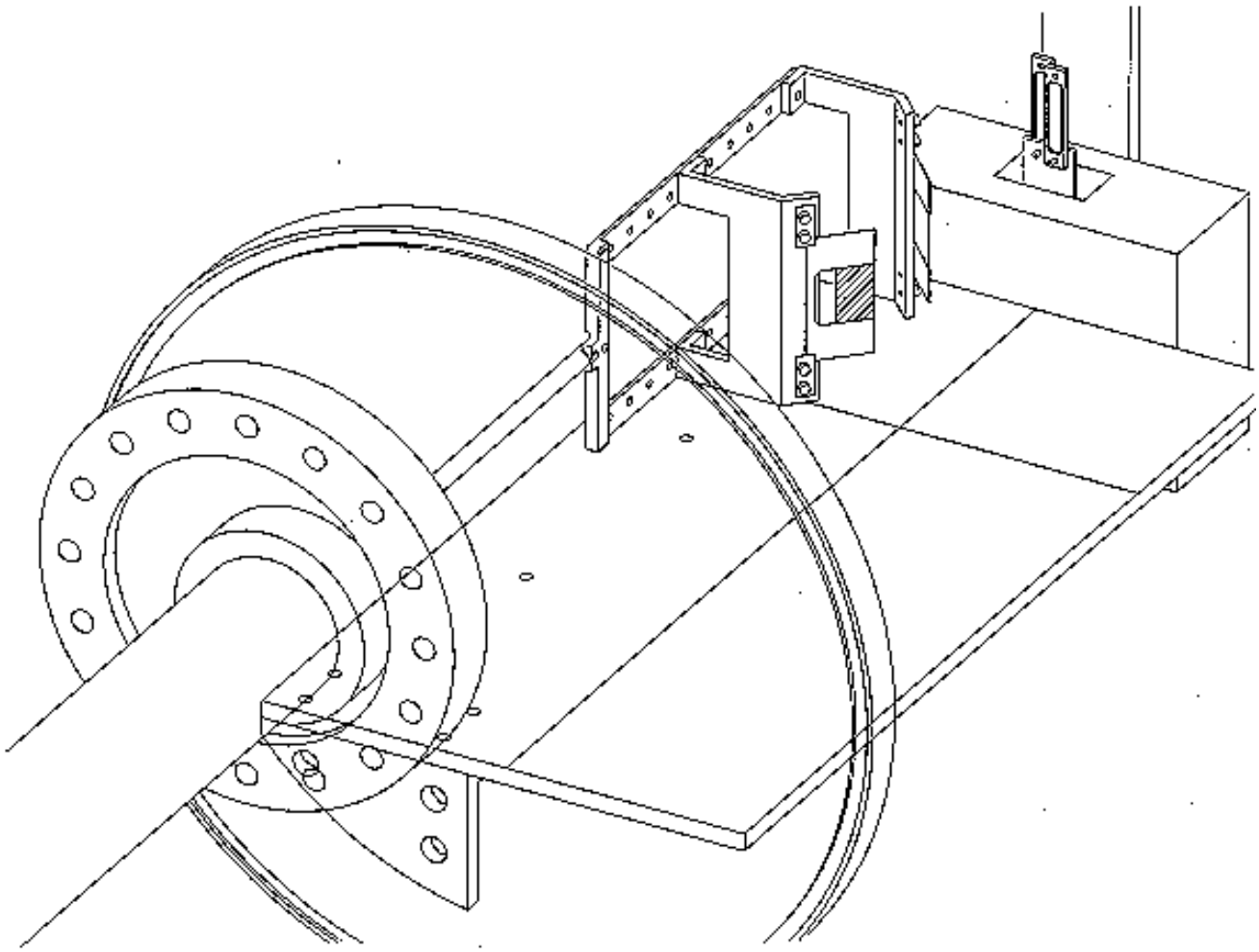

Figure B.11: The layout of the IUCF 200 MeV small angle elastic p-carbon scattering experiment. The two silicon detectors are mounted on the far side, and the foil (near) and ribbon (far) targets are mounted on the movable fork. The beam passes between the two targets, from right to left in this figure.

A proposal[83] was presented and approved by IUCF to carry out tests of such a polarimeter using silicon detectors which had its first successful run in March 1998. The layout of this test is shown in Fig. B.11. For low energy and kinematics where the recoil carbon is 0.1 to 1 MeV, the forward proton scatters to a large angle, and can be seen by the Meyer forward detector system at IUCF[71]. Fig. B.12 shows the results from the March test. The energy in the silicon is shown in (a), the correlation between the forward proton scattering angle and carbon energy in (b), the correlation between time of flight at the silicon (the start time used for this was the rf time) is shown in (c), and the projection of the proton plane onto a plane transverse to the beam is shown in (d) after an energy cut on the silicon has been applied. The carbon energy range for this silicon detector was 150-400 keV. For the data in (a), (b) and (d), the proton detector was used to trigger (half the detector, as can be seen from (d)). We also successfully triggered

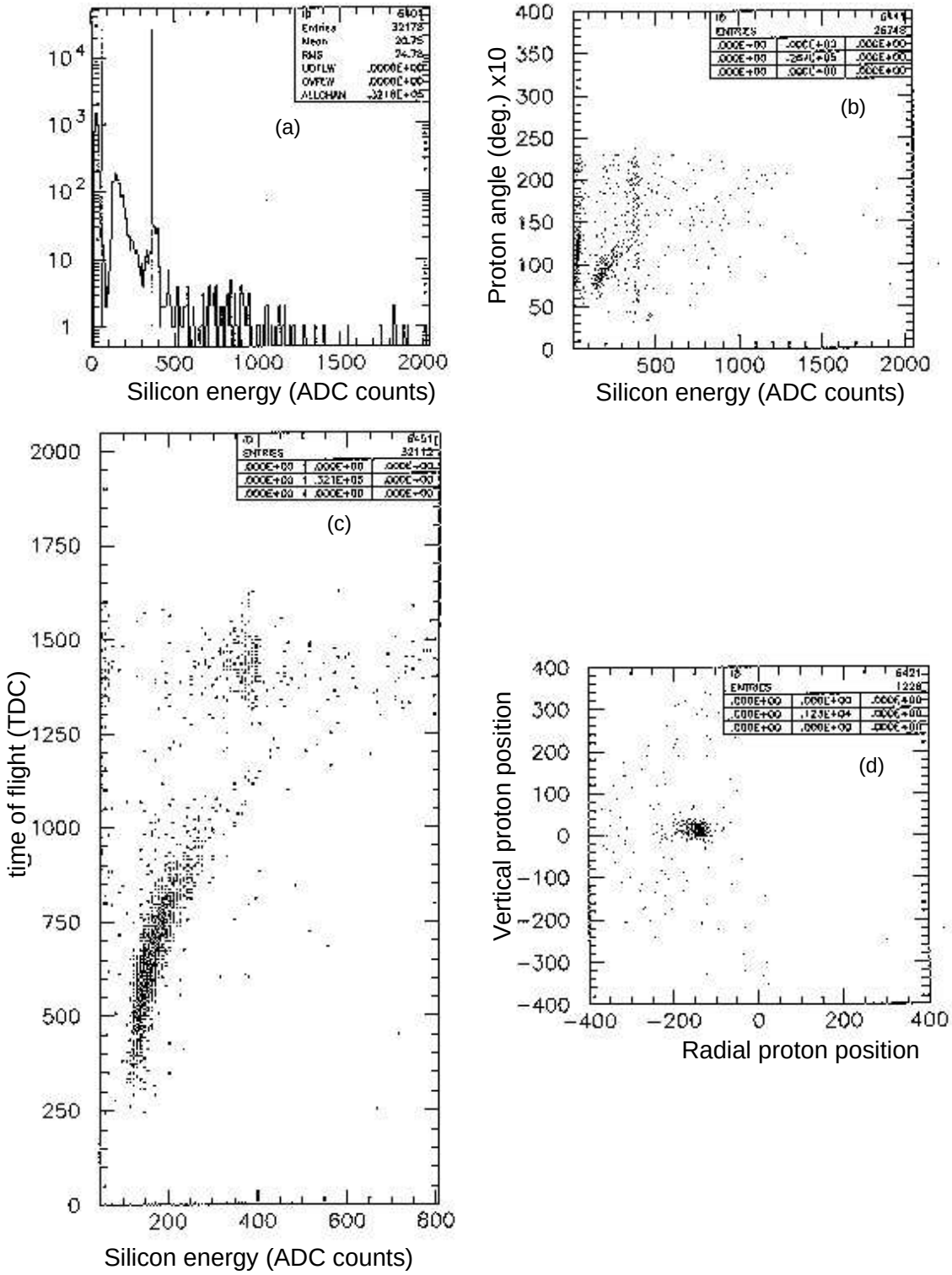

Figure B.12: Results from IUCF *pC* test run. (a) Top left, energy in silicon detectors. (b) Top right, forward proton energy and carbon energy correlation. (c) Bottom left, time of flight correlation. (d) Bottom right, space projection of elastically scattered protons.

on only the silicon detector energy (e), with the difficulty that a higher threshold was necessary (300 keV) due to noise background. This is one of the issues we are continuing to study.

Simultaneously, our collaborators at Kyoto University and RIKEN are conducting similar tests using Micro Channel Plate (MCP) detectors at the Kyoto 10 MeV proton Van de Graaff.[84] The first test used a micro channel plate to directly observe the recoil carbon. Time of flight is used to give the carbon energies, shown in Fig. B.13. The forward proton is observed and the predicted energy for each histogram is indicated. The second test used an electrostatic mirror, as shown in Fig. B.14. Electrons emitted from the surface of the silicon were collected in the MCP. The silicon was not read out. Results are shown in Fig. B.15. For carbon below 400 keV, the efficiency for electron emission from silicon was poor. A new test this fall will use a thin carbon foil to emit secondary electrons, with the goal of reaching lower energy (100-200 keV). The setup is shown in Fig. B.16. This would be our ideal detector: a coincidence between the MCP (time and angle) and silicon (energy and angle).

Our next plan is to install such a polarimeter in the AGS for the upcoming run in February 1999. This will be used to measure A_N for the RHIC injection energy and to test the technique at higher energy. If this is a success, we plan to install a two-arm pC CNI detector for the commissioning of RHIC in FY2000. The pC CNI and pion polarimeters would use the same carbon ribbon target.

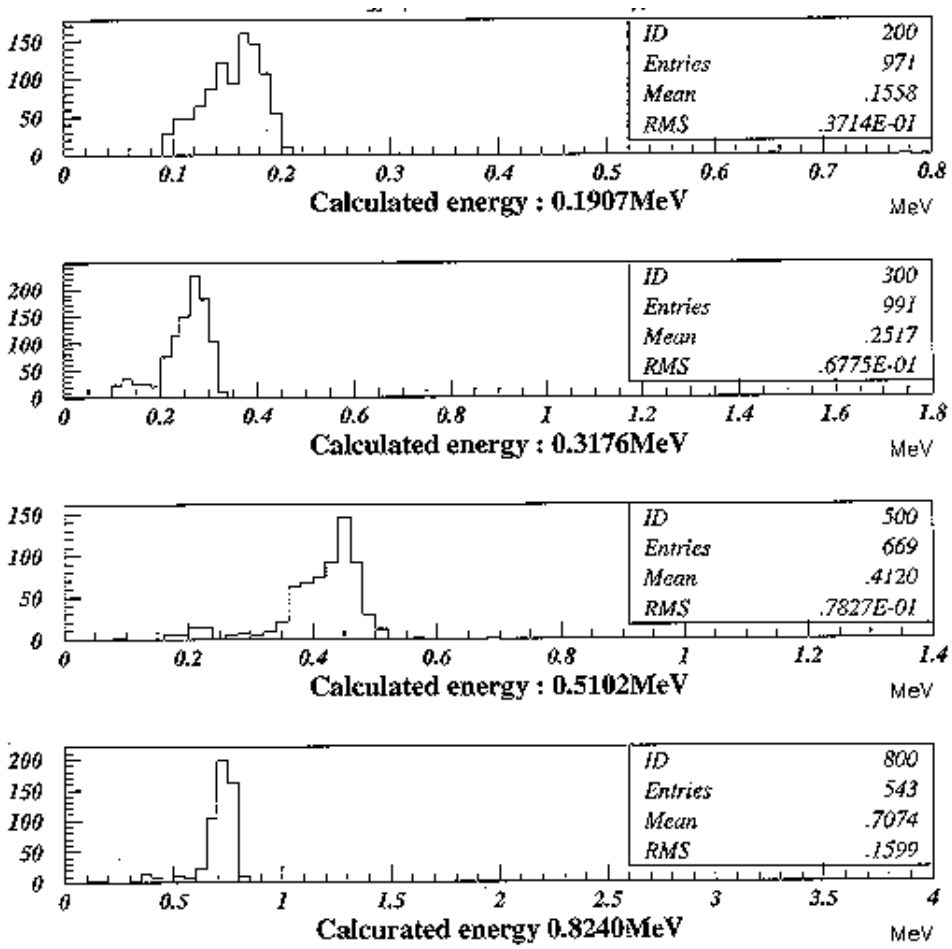

Figure B.13: The experiment data from Kyoto University Van de Graaff with only MCP used.

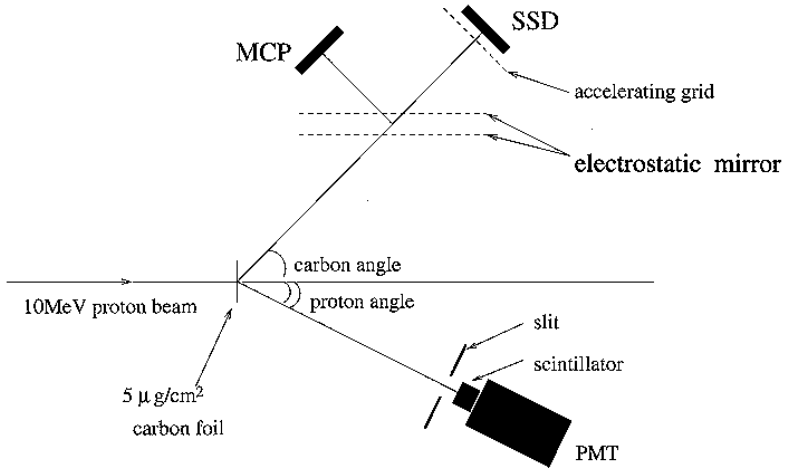

Figure B.14: The experiment layout at Kyoto University Van de Graaff.

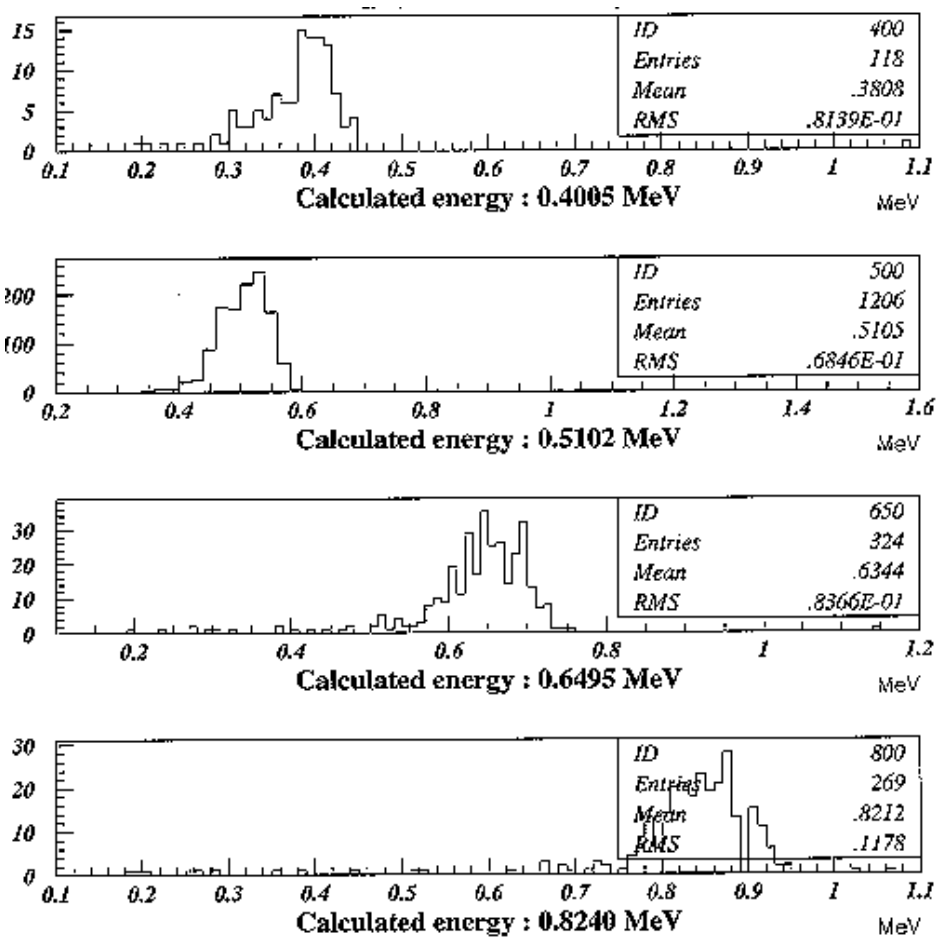

Figure B.15: The experiment data from Kyoto University Van de Graaff with both MCP and SSD used (see Fig. B.14).

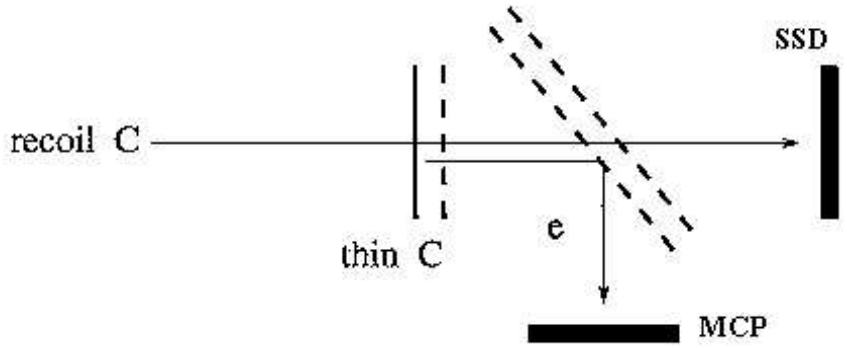

Figure B.16: The detector system to be tested in the future.

Appendix C

Bibliography

Bibliography

[1] "RHIC Design Manual," Brookhaven National Laboratory. 1

[2] Proposal on Spin Physics Using the RHIC Polarized Collider (R5), submitted to the BNL PAC August 1992; update September 1993. 1

[3] K. Abe et al. (E143 Collaboration) Phys. Rev. Lett. 74, 346 (1995); D. Adams et al. (SMC) Phys. Lett. B329, 399 (1994). 2, 5

[4] V.W. Hughes et al., "Roundtable of Future Measurements of the Polarized Gluon Distribution in the Nucleon," to be published in the proceedings of the Spin96 Symposium, Amsterdam, 1996. 2

[5] L.H. Thomas, Phil. Mag. **3**, 1 (1927); V. Bargmann, L. Michel, V.L. Telegdi, Phys. Rev. Lett. **2**, 435 (1959). 6

[6] M. Froissart and R. Stora, Nucl. Instr. Meth., **1**, 297 (1960). 7, 51

[7] T. Khoe et al., Part. Accel. **6**, 213 (1975); J.L. Laclare et al., J. Phys. (Paris), Colloq. **46**, C2-499 (1985); H. Sato et al., Nucl. Inst. Meth., Phys. Res. Sec A**272**, 617 (1988); F.Z. Khiari, et al., Phys. Rev. D**39**, 45 (1989). 7

[8] Ya.S. Derbenev et al., Part. Accel. **8**, 115 (1978). 7

[9] T. Roser, AIP Conf. Proc. No. 187, ed. K.J. Heller p.1442 (AIP, New York, 1988). 7

[10] Proposal on Spin Physics Using the RHIC Polarized Collider (R5), submitted to the BNL PAC October 1992. 8

[11] J.G. Alessi et al., AIP Conf. Proc. No. 187, p. 1221 (1988). 13

[12] Y. Mori, K. Ikegami, Z. Igarashi, A. Takagi, S. Fukumoto, in Polarized Proton Sources (Vancouver, 1983), AIP Conf. Proc. No. 117, p.123. 13

[13] M. Kinsho, K. Ikegami, A. Takagi, Y. Mori, Proc. 6th International Conf. on Ion Sources (Whistler, Sept. 1995), Rev. Sci. Instrum. 67, 1362 (1996). 14

[14] C.D.P. Levy and A.N. Zelenski, Proc. 7th International Conf. on Ion Sources (Taormina, Sept. 1997), Rev. Sci. Instrum. 69, 732 (1998). 14

[15] C.D.P. Levy, K. Jayamanna, M. McDonald, P.W. Schmor, W.T.H. van Oers, J. Welz, G.W. Wight, G. Dutto, A.N. Zelenski, T. Sakae, Proc. 6th International Conf. on Ion Sources (Whistler, Sept. 1995), Rev. Sci. Instrum. 67, 1291 (1996). 15

[16] F.Z.Khiari et al., Phys. Rev. D39, 45 (1989). 16

[17] T.Roser, AIP Conf. Proc. No. 187, p.1442 (1988). 16

[18] H.Huang et al., Phys. Rev. Lett. **73**, 2982 (1994). 16

[19] M.Bai et al., Phys. Rev. Lett. **80**, 4673 (1998). 19

[20] T.Roser, Proceedings of the 10th International Symposium on High Energy Spin Physics, Nagoya, 429 (1992). 19

[21] T. Roser, M. Syphers, E. Courant, L. Ratner, M. Okamura, "Helical Partial Snake for the AGS," BNL Internal Report AGS/RHIC/SN-072, March, 1998. 19

[22] S.Y.Lee and E.D.Courant, BNL Technical Note AD/RHIC-63. 19, 23, 26

[23] J.Claus and H.Foelsche, Beam Transfer from AGS to RHIC, RHIC 47, 1988. 23

[24] N.Tsoupas, E.Rodger, J.Claus, H.W.Foelsche and P. Wanderer BNL Design and B-field measurements of a Lambertson injection magnet for the RHIC machine. Proceedings of PAC 1995 v.2 p. 1352. 25

[25] N.Tsoupas, H.W.Foelsche, J.Claus, and R.Thern Closed orbit calculations at AGS and extraction beam parameters at H13. AD/RHIC/RD-75. 26, 27

[26] S.B.Kowalski and H.A.Enge The ion-optical program RAYTRACE NIM A258 (1987) p407. 27

[27] V.I.Ptitsin and Yu.M.Shatunov, Helical Spin Rotators and Snakes, Proc. Third Workshop on Siberian Snakes and Spin Rotators (A.Luccio and Th.Roser Eds.) Upton, NY, Sept. 12-13,1994, Brookhaven National Laboratory Report BNL-52453, p.15. 35, 36

[28] A.U.Luccio, Program SNIG, unpublished, and SNIG Formalism Proc. Third Workshop on Siberian Snakes, loc. cit., p. 193. Also: Numerical Optimization of Siberian Snakes and Spin Rotators for RHIC. Proc. Adriatico Conf. Trieste, Italy, Dec. 1995, World Scientific, and: Spin Note AGS/RHIC/SN008. 36

[29] A.U.Luccio, Optimization of Spin Angles from a Helix Field Map. Spin Note AGS/RHIC/SN042, Upton, Nov.5, 1996. 36

[30] E. Courant, "Orbit Matrices for Helical Snakes," BNL Internal Report RHIC/AP/47, November, 1994. 37

[31] F. Pilat, "Linear Coupling Effect of the Helical Snakes and Rotators in RHIC," BNL Internal Report RHIC/AP/56, February, 1995. 37

[32] M. J. Syphers, "Closed Orbit Errors from Helical Dipole Magnets," BNL Internal Report AGS/RHIC/SN-016, January, 1996. 37

[33] M. J. Syphers, "Total Pitch Specification for RHIC Helical Dipole Magnets," BNL Internal Report AGS/RHIC/SN-058, August, 1997. 42, 83

[34] M. Okamura, "Optimization of Rotation Angle of the Helical Dipole Magnets," BNL Internal Report AGS/RHIC/SN-061, August, 1997. 42, 79, 83

[35] A. K. Jain, "Estimation of Rotation Angle in the Full Length Helical Dipole Based on Data in the Half-Length Prototype HRC001," BNL Internal Report AGS/RHIC/SN-062, September, 1997. 42, 78

[36] M. J. Syphers, "Field Quality Issues for RHIC Helical Dipole Magnets," BNL Internal Report AGS/RHIC/SN-015, January, 1996. 42

[37] T. Katayama, "Multipole Field Expansion of Helical Magnet," BNL Internal Report AGS/RHIC/SN-038, September, 1996. 42

[38] W. Fischer, "Preliminary Tracking Results with Helical Magnets in RHIC," BNL Internal Report AGS/RHIC/SN-034, August, 1996. 42

[39] B. Autin and Y. Marti, "Closed Orbit Correction of Alternating Gradient Machines using a small Number of Magnets," CERN/ISR-MA/73-17, CERN, 1973. 46

[40] J. Wei, "Magnet Quality and Collider Performance Prediction," BNL Internal Report RHIC/AP/117, November, 1996. 46

[41] S.Y.Lee and S.Tepikian, Phys. Rev. Lett. 56, 1635 (1986). 48

[42] C. Ohmori et al., "Observation of a Second Order Depolarizing Resonance," Phys. Rev. Lett. 75 (1995) 1931. 49

[43] J. E. Goodwin, et al., Phys. Rev. Lett. **73**, 2779 (1990). 49

[44] L. D. Bozano, "Optimization of a Nominal 4-Helix Snake at Various Beam Energies," BNL Internal Report AGS/RHIC/SN-050, December, 1996. 51

[45] A.U.Luccio, Spin Tracking in RHIC (Code Spink). Proc. Adriatico Conf. Trieste, Italy, Dec. 1995, World Scientific. 51

[46] F.Ch.Iselin and J.Niederer, The Mad Program. User's Reference Manual. CERN/LEP-TH/88, July 13, 1988 (and later additions). 51

[47] H.Huang, T.Roser and A.Luccio, Spin Tracking Study of the AGS. AGS/RHIC/SN043, Upton, Nov. 6, 1996. 52

[48] M. Okamura, "The Hall Probe Measurement and Calculation of the Half Length Helical Dipole Magnet," BNL Internal Report AGS/RHIC/SN-060, August, 1997. 75

[49] G. H. Morgan, "End Design of a Helically-Wound Magnet for RHIC," Proc. 17th Int. Cryo. Eng. Conf., July 14-17, 1998, Bournemouth, UK. 75

[50] M. Okamura, "Optimization of Rotation Angle of the Helical Dipole Magnets," BNL Internal Report AGS/RHIC/SN-061, August, 1997. 83

[51] P.R. Cameron et.al., "RHIC Beam Position Monitor Assemblies," 1993 IEEE PAC, p.2328. 88, 89

[52] P.R. Cameron et.al., "RHIC Beam Position Monitor Characterization," 1995 IEEE PAC, p. 2458. 88, 89

[53] W.A. Ryan et.al., "A Sampling Detector for the RHIC BPM Electronics," 1995 IEEE PAC, p. 2455. 88

[54] D. Trbojevic et.al., "Alignment and Survey of the Elements in RHIC," 1995 IEEE PAC, p.2099. 89

[55] P.R. Cameron and M. Morvillo, "Thermal Behavior of RHIC BPM Cryogenic Signal Cables," RHIC/AP/68, January, 1996. 89

[56] R.E. Schafer, "Beam Position Monitoring," AIP 212, Brookhaven, 1989, p. 26-58. 89

[57] L.Ratner, private communication. 93

[58] Y. Batygin, T. Katayama, to appear in Phys. Rev. E58 (1998). 96

[59] A.Luccio and M. Syphers, "Effects of Beam-beam Interaction on Spin Motion," BNL Internal Report AGS/RHIC/SN-068, November, 1997. 96

[60] T.Roser, Spin Rotators and Split Siberian Snakes, NIM **A342** (1994) 343. 99

[61] D.D. Caussyn, et al., Phys. Rev. Lett. **73**, 2857 (1994). 99

[62] R.A.Phelps, "Spin Flipping a Stored Polarized Proton Beam in the Presence of Siberian Snakes," Third Workshop on Siberian Snakes, loc. cit., p. 225. 100

[63] M.Bai et al., Phys. Rev. E56, 6002 (1997). 100

[64] Final Report of the Polarization Measurement Working Group on RHIC Polarimeters, July 31st, 1996.

[65] The original idea of using toroidal magnets for polarimetry at RHIC is due to Dave Underwood, Private Communication. 103, 107, 137 103, 137

[66] W. Guryn, Proceedings of Workshop on Jet Targets at RHIC, January, 2000. 104

[67] W.R. Lozowski and J.D. Hudson, NIM in Physics Research A334, 173(1993). 105, 150

[68] N.H. Buttimore et al., Phys. Rev. D 18, 694(1978); N.H. Buttimore, AIP Conf. Proc.95,(AIP, New York, 1983), p. 634 105, 150

[69] J.L. Rosen, AIP Conf. Proc.26,(AIP, New York, 1975), p. 287. 105, 150

[70] D. Fields, *RHIC Spin Physics*, Proceedings of RIKEN BNL Research Center Workshop, Vol.7, April 27-29, 1998, BNL-65615. 105

[71] H.O. Meyer, et al., Phys. Rev. C 23, 616(1981). 105, 153

[72] K. Imai, *Physics of Polarimetry at RHIC*, Proceedings of RIKEN BNL Research Center Workshop, Vol.10, August 4-7, 1998, BNL-65926. 105

[73] J. Tojo, et al., *Measurement of the Analyzing Power for Proton-Carbon Elastic Scattering in the CNI Region with a 22 GeV/c Polarized Proton Beam*, Proceedings of SPIN2000, Osaka, Japan. 107

[74] H. Wang and H. Huang, RHIC Polarimeter Impedance Analysis with MAFIA, RHIC/AP/178(October,1999). 110

[75] J. Bosser, at al., PAC IEEE Proceedings, CH2387-9, 783 (1987). 111, 145

[76] W.W. Mackay, et al., *Super-conducting Helical Snake Magnets: Design and Construction*, p.163, DESY-PROC-1999-03. 113

[77] M.J. Syphers and F.G. Mariam, Effects of Leakage Fields from Polarimeter Toroid Magnets, AGS/RHIC/ SN No. 031 (1996). 129

[78] Private communications (1996). 134

[79] D.L.Adams et al., Phys. Lett. B264, 462 (1991). 137, 138

[80] Dragoset et al., Phys. Rev. D 18, 3939 (1976). 138

[81] L.G. Ratner et al., Proc. of the Rochester Meeting APS/DPF, Rochester, p. 99 (1971). 139, 147

[82] V. Kanavets, Private communications (1998). 145

[83] D.Fields, et al., Proposal CE75, IUCF, Bloomington, IN, (1997). 153

[84] K. Imai et al., Kyoto University, (unpublished). 155